

# REPORT DOCUMENTATION PAGE

AFOSR-TR-97

Public reporting burden for this collection of information is estimated to average 1 hour per response, including gathering and maintaining the data needed, and completing and reviewing the collection of information. Send collection of information, including suggestions for reducing this burden to Washington Headquarters Service, Davis Highway, Suite 1204, Arlington, VA 22202-4302, and to the Office of Management and Budget, Paper

0350

1. AGENCY USE ONLY (Leave blank)		2. REPORT DATE June 30, 1997	3. REPORT TYPE AND DATES COVERED Jan. 1, 1994- April 30, 1997	
4. TITLE AND SUBTITLE Nonlinear, Rotational-Acoustic Processes in Solid Rocket Engines			5. FUNDING NUMBERS PE-61102F PR-2305 SA-AS G-F49620-94-1-0042	
6. AUTHOR(S) D. R. Kassoy				
7. PERFORMING ORGANIZATION NAMES(S) AND ADDRESS(ES) Center for Combustion Research Mechanical Engineering Department, CB-427 University of Colorado Boulder, CO 80309			8. PERFORMING ORGANIZATION REPORT NUMBER	
9. SPONSORING / MONITORING AGENCY NAMES(S) AND ADDRESS(ES) AFOSR/NA, 110 Duncan Ave. # B115 Bolling AFB DC 20332-0001			10. SPONSORING / MONITORING AGENCY REPORT NUMBER	
11. SUPPLEMENTARY NOTES				
19971003 068				
a. DISTRIBUTION / AVAILABILITY STATEMENT unlimited: approved for public release			12. DISTRIBUTION CODE	
<div style="border: 1px solid black; padding: 5px; text-align: center;"> <b>DISTRIBUTION STATEMENT A</b>              Approved for public release              Distribution Unlimited           </div>				
13. ABSTRACT (Maximum 200 words)  Solid rocket motor chamber fluid dynamics are modeled using the full Navier-Stokes equations. Mass injection from the sidewall of a cylinder simulates the propellant gasification. Prescribed boundary disturbances in velocity or pressure induce acoustic waves and other transients into the chamber geometry. Vorticity is generated on the sidewall from an inviscid interaction between transient pressure gradients and the fluid injected from the surface. Axisymmetric and three dimensional solutions obtained from analysis and computation are used to predict the dynamics of the co-existing acoustic and rotational flows. Results suggest that intense transient vorticity is present throughout much of the chamber during a firing as long as acoustic transients are present. The rotational flow component is associated with intense transient shear stresses on the sidewall. Meanflow profiles and RMS intensity distributions are similar to those found in traditional turbulent pipe flows with injection. Traditional acoustic stability theory, based on purely irrotational flow assumptions, may describe the pressure variations in chamber models, but cannot describe the rotational component of the flow found in the present model.				
14. SUBJECT TERMS			15. NUMBER OF PAGES 15	
			16. PRICE CODE	
17. SECURITY CLASSIFICATION OF REPORT unclassified	18. SECURITY CLASSIFICATION OF THIS PAGE unclassified	19. SECURITY CLASSIFICATION OF ABSTRACT unclassified	20. LIMITATION OF ABSTRACT UL	

# **NONLINEAR ROTATIONAL-ACOUSTIC PROCESSES IN SOLID ROCKET ENGINES**

**Grant No. F49620-94-I-0042**

**Final Technical Report**

**prepared for**

**Dr. Mitat Birkan**

**Air Force Office of Scientific Research**

**D. R. Kassoy**

**Center for Combustion Research  
Department of Mechanical Engineering  
University of Colorado, Boulder  
Boulder, CO. 80309-0427**

**June 30, 1997**

**DTIC QUALITY INSPECTED 3**

## Table of Contents

1. Abstract
2. Project Objectives, Status and Accomplishments
3. Bibliography
4. Project Personnel
5. Publications
6. Appendices
  - a. Q. Zhao, "Nonlinear Acoustic Processes in Solid Rocket Engines", PhD Thesis, University of Colorado, Boulder, CO. 1994 [Abstract only].
  - b. K. Kirkkopru, D. R. Kassoy and Q. Zhao, "Unsteady Vorticity Generation and Evolution in a Model of a Solid Rocket Motor: Sidewall Mass Addition Transients", AIAA #95-0603, Aerospace Sciences Meeting, Reno, NV., 1995.
  - c. M. Wang and D. R. Kassoy, "Nonlinear Acoustic Oscillations in a Resonant Gas Column; An Initial - Boundary Value Study", SIAM J. Applied Math., 55:923-915, 1995
  - d. K. Kirkkopru, D. R. Kassoy and Q. Zhao, "Unsteady Vorticity Generation and Evolution in a Model of a Solid Rocket Motor", J. Propulsion and Power, 12, #4, 646-654, 1996.
  - e. D. R. Kassoy, P. L. Staab, T. Y. Chang and A. M. Hegab, "Co-Exisiting Acoustic-Rotational Disturbances in a Coldflow Model of a Solid Rocket Motor", AIAA #97-0697, Aerospace Sciences Meeting, Reno, NV., 1997.
  - f. P. L. Staab and D. R. Kassoy, "Three Dimensional, Unsteady, Acoustic-Shear Flow Dynamics in a Cylinder with Sidewall Mass Addition", accepted for publication in the Physics of Fluids, 1997.
  - g. Q. Zhao and D. R. Kassoy, "Acoustically Generated Vorticity in an

Internal Flow", resubmitted to the J. Fluid Mechanics, 1997.

- h. P. L. Staab and D. R. Kassoy, "Co-Existing Acoustic-Rotational Disturbances in a Coldflow Model of a Solid Rocket Motor," AIAA #97-2066, Fluid Dynamics Conference, Snowmass, CO., 1997.



## 1. ABSTRACT

Solid rocket motor chamber fluid dynamics are modeled using the full Navier-Stokes equations. Mass injection from the sidewall of a cylinder simulates the propellant gasification. Prescribed boundary disturbances in velocity or pressure induce acoustic waves and other transients into the chamber geometry. Vorticity is generated on the sidewall from an inviscid interaction between transient pressure gradients and the fluid injected from the surface. Axisymmetric and three dimensional solutions obtained from analysis and computation are used to predict the dynamics of the co-existing acoustic and rotational flows. Results suggest that intense transient vorticity is present throughout much of the chamber during a firing as long as acoustic transients are present. The rotational flow component is associated with intense transient shear stresses on the sidewall. Meanflow profiles and RMS intensity distributions are similar to those found in traditional turbulent pipe flows with injection. Traditional acoustic stability theory, based on purely irrotational flow assumptions, may describe the pressure variations in chamber models, but cannot describe the rotational component of the flow found in the present model.

## 2. PROJECT OBJECTIVES, STATUS AND ACCOMPLISHMENTS

Our project has focused on the modeling of the transient flow dynamics that occur in coldflow and thermally active versions of a motor chamber. The results provide new perspectives about the physical processes occurring in these systems. Their application to the design process should foster the development of more reliable motors with predictable performance.

The substance of our work can be divided broadly into two major tasks:

- (i) Analysis and numerical simulation of an injected internal flow when equal magnitude acoustics and vorticity co-exist.*

Our numerical simulations of coldflow processes describe instantaneous velocity and pressure distributions in a model motor chamber, including the development and convection of vorticity from the sidewall, where time-dependent normal injection is imposed. The results predict the characteristics of a high Reynolds and low Mach number flow with co-existing, equal magnitude acoustic and rotational flow fields. Uniquely, we have separated the acoustic and rotational components of the complete numerical velocity response to the imposed transient sidewall disturbance. We use turbulent flow data reduction techniques to describe the spatial characteristics of the mean flow, and the RMS-intensity of the combined acoustic and rotational fluctuating flow fields. The results can be compared with relevant experiments and with turbulent flow models involving various closure schemes (k- $\epsilon$ , k- $\omega$  and full Reynolds stresses). Comparison of mean and instantaneous axial shear stresses at the injection surface enable us to determine if the former are helpful for predicting where erosive burning might occur, or if one must focus on the impact of the transient surface stress, which is considerably larger than the mean stress, on propellant burning.

- (ii) Non-axisymmetric , transient flow dynamics in a coldflow model chamber.*

An analytical method has been developed to describe three-dimensional transient flows in a cylindrical chamber with steady sidewall injection and a time-dependent disturbance on the headend

that varies azimuthally and radially. The results show that nonaxisymmetric flow dynamics exist only in a limited portion of the chamber adjacent to the headend, and that azimuthal and radial velocities decay swiftly in the axial direction over a few cylinder radii. Further downstream, in a high aspect ratio chamber, only axisymmetric disturbances appear. The results are in excellent agreement with a numerically intensive, three dimensional turbulence model by Sabnis et. al<sup>(1)</sup>. Our three-dimensional analysis is also used to evaluate the impact of transient, azimuthally dependent sidewall injection on the co-existing acoustic and rotational flow field in a high aspect ratio cylinder. In this case, the time-dependent injection distribution emulates non-axisymmetric propellant burning. We are not aware of any comparable numerical or experimental studies, where explicit transient propellant burning emulation is used as the source of the flow dynamics in the chamber.

Each of these research efforts will now be described in more detail.

- (I) Analysis and numerical simulation of an injected internal flow when equal magnitude acoustics and vorticity co-exist.

Our numerical simulations of the transient flow response to prescribed boundary disturbances<sup>(2-4)</sup> have been used to study the generation and evolution of intense transient vorticity in a cylinder with sidewall injection. The complete axial velocity is divided into the numerical analog of the steady Culick<sup>(5)</sup> profiles, and transient responses for the co-existing, equal magnitude acoustic and rotational flow fields. The latter is used to describe the time-varying spatial distribution of vorticity in the cylinder. Ref.3 (see Appendices for copies of papers by this group) contains examples of the instantaneous, rotational axial velocity distribution at a specified axial location, and the vorticity distribution throughout the cylinder at a specified time.

Our numerical data has also be analyzed in terms of mean flow and fluctuating flow properties<sup>(6)</sup>, so that comparisons with more traditional turbulent flow modeling can be carried out. Liou and Lien<sup>(7)</sup> summarize many important contributions to chamber flow turbulence modeling, based on  $k-\epsilon$ ,  $k-\omega$  and full Reynolds stress methods. In general, the modeling results often tend to predict larger turbulent intensities, and fuller mean velocity profiles than found in experiment. It is suggested the Navier-Stokes based DNS's will require far fewer assumptions about flow injection boundary

conditions imposed on the chamber sidewall, and may give more accurate representations of the turbulent properties of the flow. Results of DNS calculations for flow in a large aspect ratio channel are reported in Ref. 7 for mean flow profiles, transition to turbulence and turbulent intensity distributions. The injection speed,  $v'_w = O(1 \text{ m./s.})$ , is unusually large, the Reynolds number,  $Re = O(10^6)$ , and the axial Mach number in the downstream half of the channel takes on significant subsonic values. The calculations are run for about 15 axial acoustic time scales. Comparisons of mean flow and turbulent intensity predictions with experiments appear to be better than those of the traditional turbulence models. The results are significantly affected by compressibility, so that the mean flow evolution differs significantly from that predicted by the Culick<sup>(5)</sup> profile, which is valid only for an incompressible flow. The turbulent intensity shows a single peak across the channel, with the location of the peak moving toward the sidewall with increasing downstream location. It is recognized that such an effect may enhance erosive burning on the downstream section of a solid propellant. The authors do not specify the specific initial and boundary conditions used in the DNS. It is difficult to know what types of disturbances are used to drive the solution, or whether the DNS resolves acoustic phenomena that may be present. No instantaneous profiles are displayed.

Our low Mach number, high Reynolds number numerical simulation of injected flow in a cylindrical geometry is based on the parabolized Navier-Stokes equations and imposed disturbances on the sidewall<sup>(3,8)</sup>. We generate a flow with co-existing, equal amplitude acoustics and vorticity, and a pressure disturbance field that is between 1% and 10% of the reference static pressure. A methodology is developed for separating these two transient flow fields. Thus, we can consider the contribution of acoustics alone, the vorticity alone and the explicit interaction between the two flow fields.

A comparison of the mean flow and instantaneous axial velocity profiles for  $Re = 10^4$ ,  $M = 0.02$  and an aspect ratio of 20 is given in Ref. 6. One notes the former does not hint at the spatial variations of the axial velocity shown in the latter. In particular, the relatively large wall shear stress in the instantaneous profile (which varies in time between positive and negative values) is not reflected in the mean flow value. The latter alone, may not be a useful measure of the "scouring" effect arising from a time dependent, rapidly varying

wall shear stress on the fizz-foam surface layer of a decomposing solid propellant.

The RMS intensity distribution in the cylinder is also given in Ref 6. The result includes the effects of both the rotational and acoustic transients. One notes several local peaks across the radius, with the largest value near the sidewall. In general, the amplitude increases, and the local peaks move toward the sidewall with increasing axial distance downstream. The single peak results described in Ref. 7 are qualitatively similar. Our multiple peaks arise from vorticity generation driven by axial acoustic waves in the cylinder. The latter may not be present in any of the turbulence models discussed in Ref. 7 or in the DNS discussed there.

We have extended our numerical simulations to a variety of Mach and Reynolds number values, and to other frequency ranges<sup>(9)</sup>. The boundary condition representation has been improved by using ingoing and outgoing characteristic relationships. This permits a more accurate description of wave behavior at the headwall, sidewall and exit plane.

By driving the co-existing acoustic and rotational flow transients with explicit boundary disturbances, we establish a clear cause and effect relationship between the transient internal flow dynamics and the imposed conditions on the endwall or sidewall. Forcing on the latter boundary is particularly relevant to simulating unsteady propellant burning. Our numerical simulation involves fewer assumptions than those needed in more traditional turbulence modeling<sup>(7)</sup>(e.g., closure models), and may provide considerable insights into the transient dynamics of weakly viscous, low Mach number, compressible flows with co-existing acoustics and vorticity.

An understanding of oscillatory, intense axial shear stress on the sidewall will be useful for developing physically viable boundary conditions at the decomposing interface of a burning solid propellant. The idea here is account for the "scouring" effect of oscillatory shear stress on the fizz-foam zone thought to exist at the gas-propellant interface. Although the axial velocity in the combustion zone may be small, the results of the coldflow studies in Refs. 2-4, 8,10 and 14 suggest that the velocity gradient will be relatively large, and hence can be a source of axial deformation, and perhaps stripping of easily deformable surface material.

## (II) Non-axisymmetric transient flow dynamics in a coldflow model chamber

Our initial analysis of three dimensional unsteady flow dynamics in a model chamber<sup>(11)</sup> was motivated by the computational result of Sabnis et. al<sup>(1)</sup>, showing that nonaxisymmetric effects disappear entirely within about two cylinder diameters in axial distance from a cross-section on which asymmetric distributions of velocity and pressure are imposed. This observation from a turbulent numerical solution suggests that certain type of imposed boundary conditions or forcing cannot produce sustained tangential disturbances in a long, narrow motor configuration.

To test this hypothesis, and to confirm the result in Ref. 1, we developed an asymptotic analysis of the three dimensional Navier-Stokes equations for a transient flow in a cylinder of length  $L'$  and radius  $R'$  ( $L'/R' \gg 1$ ), with steady sidewall injection<sup>(6,11)</sup>. An asymmetric transient, axial velocity disturbance is imposed on the headend cross-section. The entire flow response in most of the cylinder must be axisymmetric<sup>(10)</sup>., and is not compatible with the asymmetric head end condition. We find that three dimensional flow exists only in a confined transition layer adjacent to the headend, with axial extent  $O(R')$ . There, the describing equation is inviscid and incompressible, so that no acoustic response occurs for the driving frequencies associated with the lower order axial modes. Solutions for the pressure and axial velocity show exponential decay of all three dimensional effects as the edge of the layer is approached. The radial and azimuthal velocities decay similarly. The remaining time dependent terms drive the axisymmetric disturbances found in Ref. 10.

The asymmetric transverse velocity field on a cylinder cross-section is given in Ref. 11 for a specific headend disturbance. One notes the asymmetric character of the flow with respect to the diameter between  $\theta = -\pi/2$  and  $\theta = \pi/2$ , and the horizontal flow across the cylinder axis. Other quantitative results show that the amplitude of the three dimensional pressure effect has decreased to about 1% of the overall value at an axial distance of about  $2.5R'$ . The agreement with the numerical result in Ref. 1 is very satisfying. Hence, we have a viable explanation for the rapid disappearance of transient asymmetric disturbances, associated with the idea that certain types of acoustic modes cannot propagate in particular wave



guides.

The three dimensional solutions described above do not satisfy the no-slip conditions on the endwall and sidewall. We have derived a rotational, inviscid, incompressible solution valid in a thin sublayer adjacent to the former. Due the oscillatory and large injection associated with the disturbance boundary condition, a no-slip condition is compatible with an inviscid, but rotational process<sup>(15)</sup>.

Weakly viscous solutions in a boundary layer next to the sidewall describe the transition to zero axial velocity. Here again, large injection concepts must be used to understand the three dimensional process in the layer, including two large components of intense, transient vorticity( axial and azimuthal).

Azimuthally-dependent propellant burning transients are being simulated in more recent and ongoing work<sup>(6)</sup> by imposing a transient sidewall injection rate that varies with the angular variable  $\theta$  as well as with time and axial location. Both standing and traveling waves can be imposed on the interior circumference of the cylinder. Solutions for standing wave sidewall disturbances show that only axial, planar acoustic waves are driven in a large aspect ratio cylinder. However, there is also a non-acoustic time-dependent three dimensional flow induced in the chamber. Non-axisymmetric cross-sectional flow is described in Refs. 6 and 11, where one observes a non-zero velocity across the axis of the cylinder.

The axial and azimuthal pressure gradients associated with the transient response to the boundary disturbance interact with the fluid injected from the sidewall to produce two components of intense transient vorticity at the sidewall surface. In addition to the familiar azimuthal vorticity component found in axisymmetric flows, we now have in addition an axial component of similar magnitude. This means that an oscillatory shear stress will "scour" the circumference of the cylinder.

The non-axisymmetric vorticity front shape can be calculated from first principles as part of our analysis. Results in Ref. 16 show instantaneous configurations for two different distributions of the azimuthally dependent injection rate. Our solutions show that for times large compared to the axial acoustic time in the chamber, the front shape approaches an axisymmetric configuration.

There are, of course, other means for generating transverse disturbances in the largely inviscid shear flow that exists in a steady, sidewall injected chamber flow. For example, our group has shown that refraction of axial acoustic modes by a shear flow in a channel can produce surprisingly asymmetric acoustic responses<sup>(12, 13)</sup>. This early analytical work demonstrates explicitly that axial acoustic waves can be distorted by refraction to generate purely transverse, and even oblique waves in the channel. This type of acoustic wave-shear flow interaction is a "higher order" effect in a low Mach number asymptotic expansion, so that the amplitude of the asymmetric response is smaller than that of the axial mode itself. Hence these types of asymmetries are smaller than those driven by boundary disturbances.



### 3.BIBLIOGRAPHY

1. Sabnis, J.S., Gibeling, H.J. and McDonald, H., J. Propulsion, **5**, 657, (1989).
2. Kirkkopru, K., Kassoy, D.R., and Zhao, Q., AIAA 95-0603, Aerospace Sciences Meeting, Reno, NV, (1995).
3. Kirkkopru, K., Kassoy, D.R., and Zhao, Q., J. Propulsion and Power, **12**, #4, 646-654,(1996).
4. Kirkkopru, K., Kassoy, D.R., and Zhao, Q., to be submitted, Phys. of Fluids, (1997).
5. Culick, F.E.C., AIAA J. **4**, 1462, (1966).
6. Kassoy, D. R., Staab, P. L., Chang, T. Y. and Hegab, A. M., "Co-Existing Acoustic-Rotational Disturbances in a Coldflow Model of a Solid Rocket Motor", AIAA #97-0697, Aerospace Sciences Meeting, Reno, NV.,(1997).
7. Liou, T.M. and Lien, W. Y., J. Propulsion and Power, **11**, 600, (1995).
8. Zhao, Q., PhD Thesis, University of Colorado, Boulder, CO. (1994).
9. Hegab, A. M., PhD Thesis, University of Colorado, Boulder, CO., in progress (1997).
- 10 Zhao, Q., Kassoy, D. R. and Kirkkopru, K., resubmitted, J. Fluid Mechanics, (1996).
11. Staab, P. and Kassoy, D. R., "Three Dimensional, Unsteady, Acoustic-Shear Flow Dynamics in a Cylinder with Sidewall Mass Addition", accepted for publication in the Physics of Fluids, (1997).
12. Wang, M. and Kassoy, D. R., J. Fluid Mechanics, **238**, 509, (1992).
13. Wang, M. and Kassoy, D. R., AIAA J., **30**, 1708, (1992).
14. Zhao, Q. and Kassoy, D. R., AIAA 94-0779, Aerospace Sciences Meeting, Reno, NV., (1994).
15. Cole, J. D. and Aroesty, J., Int. J. Heat Mass Transfer, **11**, 1167-1183, (1968).
16. Staab, P. L. and Kassoy, D. R., "Co-Existing Acoustic-Rotational Disturbances in a Coldflow Model of a Solid Rocket Motor," AIAA #97-2066, Fluid Dynamics Conference, Snowmass, CO., (1997).

#### **4. PROJECT PERSONNEL**

- a. D. R. Kassoy is a Professor of Mechanical Engineering at the University of Colorado at Boulder. He is the author of more than 90 published papers. Much of his recent work has focused on the modeling of low and high speed reactive systems, including flame combustion, detonations and explosions, as well as acoustic-vorticity dynamics in rocket motor chambers. Kassoy has been the recipient of a Guggenheim Fellowship, a Fulbright Research Award, a Fellowship from the Japan Society for the Promotion of Science, and is a Fellow of the American Physical Society (Division of Fluid Dynamics). He is currently the Interim Assoc. Vice-President for Technology at the University of Colorado System.
- b. Kadir Kirkkopru, PhD, was a Research Associate through December 1994. He is an Assoc. Professor of Mechanical Engineering at the Istanbul Technical University in Turkey.
- c. Tae Chang, PhD, was a Research Associate from June 1995 to June 1996. He is employed by Lockheed-Martin Corporation in Denver Colorado.
- d. Qing Zhao completed his PhD in Mechanical Engineering at the University of Colorado, Boulder in August 1994. He is employed by Applicon in Boulder Colorado.
- e. Peter Staab is a Research Assistant. He is completing his PhD in Applied Mathematics at the University of Colorado, Boulder
- f. Abdel Karim Hegab is a Visiting Scholar from Menoufia University in Egypt, supported by the Egyptian government. He is completing his PhD research work at the University of Colorado and will receive his degree from Menoufia University.

## 5. PUBLICATIONS

1. Q. Zhao, "Nonlinear Acoustic Processes in Solid Rocket Engines", PhD Thesis, University of Colorado, Boulder, CO. 1994 [Abstract only].
2. K. Kirkkopru, D. R. Kassoy and Q. Zhao, "Unsteady Vorticity Generation and Evolution in a Model of a Solid Rocket Motor: Sidewall Mass Addition Transients", AIAA #95-0603, Aerospace Sciences Meeting, Reno, NV., 1995.
3. M. Wang and D. R. Kassoy, "Nonlinear Acoustic Oscillations in a Resonant Gas Column; An Initial - Boundary Value Study", SIAM J. Applied Math., 55:923-915, 1995
4. K. Kirkkopru, D. R. Kassoy and Q. Zhao, "Unsteady Vorticity Generation and Evolution in a Model of a Solid Rocket Motor", J. Propulsion and Power, 12, #4, 646-654, 1996.
5. D. R. Kassoy, P. L. Staab, T. Y. Chang and A. M. Hegab, "Co-Exisiting Acoustic-Rotational Disturbances in a Coldflow Model of a Solid Rocket Motor", AIAA #97-0697, Aerospace Sciences Meeting, Reno, NV., 1997.
6. P. L. Staab and D. R. Kassoy, "Three Dimensional, Unsteady, Acoustic-Shear Flow Dynamics in a Cylinder with Sidewall Mass Addition", accepted for publication in the Physics of Fluids, 1997.
7. Q. Zhao and D. R. Kassoy, "Acoustically Generated Vorticity in an Internal Flow", resubmitted to the J. Fluid Mechanics, 1997.
8. P. L. Staab and D. R. Kassoy, "Co-Existing Acoustic-Rotational Disturbances in a Coldflow Model of a Solid Rocket Motor," AIAA #97-2066, Fluid Dynamics Conference, Snowmass, CO., 1997.

## **6. APPENDICES**

NONLINEAR ACOUSTIC PROCESSES IN SOLID  
ROCKET ENGINES

by

QING ZHAO

Bachelor of Science,

University of Science and Technology of China,

Hefei, China, 1987

A thesis submitted to the  
Faculty of the Graduate School of the  
University of Colorado in partial fulfillment  
of the requirements for the degree of  
Doctor of Philosophy  
Department of Mechanical Engineering

1994

Zhao, Qing (Ph.D., Mechanical Engineering.)

Nonlinear Acoustic Processes in Solid Rocket Engines

Thesis directed by Professor David R. Kassoy

A study is made of flow dynamics in a model solid rocket engine chamber flow induced by strong sidewall mass injection. The system is subjected to either a large endwall transient disturbance, or a to large sidewall transient disturbance which mimics unsteady mass addition due to irregular propellant burning.

Perturbation methods are used to derive systematic approximations to the complete compressible Navier-Stokes equations. An initial-boundary value approach is used to formulate a generalized unsteady mathematical model capable of describing both non-resonant and resonant time histories of solutions. Fourier series representations of the velocity and pressure are obtained in terms of eigenfunctions that satisfy all the prescribed boundary conditions. Finite difference schemes have been adopted to solve the final nonlinear diffusive equations in order to obtain the explicit results. In addition, in the case of endwall forcing, systems of truncated, time dependent, nonlinear coupled ordinary differential equations have been solved to evaluate the validity of the modal approach for different frequencies.

Axial waves, generated directly by an endwall forcing or indirectly by a sidewall forcing, propagate through the basically inviscid shear flow field, and perhaps unexpectedly, create significant vorticity at the surface of the porous cylinder. The radial component of the injected flow field carries vorticity into the entire cylinder.

The formulation and analysis describe the transport and time-history

of the spatial distribution of vorticity within the cylinder on the time scale for axial acoustic waves to traverse the cylinder length. Finally, results show that transient rotational flow effects are crucial to the evolution and stability of internal fluid dynamics when the characteristic cylinder Reynolds number ( $Re$ ) and axial Mach number ( $M$ ) are very large and small, respectively.



**AIAA 97-2066**

**Co-Existing Acoustic-Rotational Disturbances  
in a Coldflow Model of a Solid Rocket Motor**

**P. L. Staab**

Department of Applied Mathematics  
University of Colorado, Boulder

**D. R. Kassoy**

Department of Mechanical Engineering  
University of Colorado, Boulder

**28th AIAA Fluid Dynamics Conference  
4th AIAA Shear Flow Control Conference**

**June 29 - July 2, 1997**

**Snowmass Village, CO**



# CO-EXISTING ACOUSTIC-ROTATIONAL DISTURBANCES IN A COLDFLOW MODEL OF A SOLID ROCKET MOTOR

P. L. Staab

Department of Applied Mathematics, B-526  
University of Colorado, Boulder, CO 80309-0526

D. R. Kassoy

Center for Combustion Research,  
Mechanical Engineering Department, B-427  
University of Colorado, Boulder, CO 80309-0427

## Abstract

Analytical and numerical modeling methods are used to predict the transient flow dynamics generated by time-dependent boundary conditions in a solid rocket motor chamber model. Non-axisymmetric, time-dependent boundary forcing on a sidewall of the cylinder, which emulates unsteady propellant gasification, is used to establish asymmetric, three-dimensional flow in a model chamber. An asymptotic analysis is used to reduce the full Navier-Stokes equations to a simpler set of equations, which describe the acoustic processes and the vorticity in the cylinder. The results show that the presence of a non-axisymmetric time-dependent boundary condition drives planar axial acoustic waves and a non-axisymmetric flow response throughout the chamber. The interaction of the three-dimensional flow response to the non-axisymmetric boundary condition with the injected fluid produces two vector components of vorticity along the sidewall of the cylinder of magnitude  $O(M^{-1})$ . The vorticity is convected into the cylinder by the injected flow field.

## I Introduction

Internal flow dynamics in a cylinder with mass addition from the sidewall are studied as an analogue to flows within solid fuel rocket motors. The mass addition models the gasification of the burning propellant in the rocket motor.

The work presented here is related to that of Staab and Kassoy<sup>1</sup>, which describes a three-dimensional study of the flow in a cylinder with sidewall mass addition. The primary interest is to determine the influence of a non-axisymmetric, axial velocity boundary condition, applied to the closed endwall of the cylinder, on the internal flow process. Staab and

Kassoy<sup>1</sup> show that a non-axisymmetric core flow is present adjacent to the endwall, within an axial length scale on the order of the cylinder radius. Within the region, the flow is incompressible and inviscid, and the non-axisymmetric velocity field decays exponentially fast in the downstream direction. A viscous boundary layer exists near the sidewall of the cylinder. All three components of the vorticity exist within the boundary layer. The axial and azimuthal components of vorticity have a magnitude on the order of  $O(M^{-1})$ .

The present analysis is also similar to the work of Zhao et. al.<sup>2</sup> which models the axisymmetric flow within a solid rocket motor, by imposing an axisymmetric radial velocity boundary condition along the sidewall of the model cylinder. The results of the analysis reveal the structure of the vorticity. The interaction of acoustic waves with the sidewall mass addition generates vorticity of magnitude of order  $O(M^{-1})$ . The vorticity is convected away from the sidewall. Weak viscous effects diffuse the vorticity on a fine radial scale of order  $O(M)$  as it approaches the centerline.

The objective of the present work is to describe the characteristics of the three-dimensional flow induced in the cylinder by a non-axisymmetric sidewall boundary condition, in contrast to the non-axisymmetric endwall boundary condition used in Staab and Kassoy<sup>1</sup>.

## Mathematical Formulation

The objective of the present work is to model a wall injected, semi-confined internal flow driven by a non-axisymmetric, time-dependent velocity disturbance on the sidewall. The flow occurs in a cylinder of length  $L'$ , and radius,  $R'$ , with a pressure node at the open end as shown in Figure 1. The primes represent dimensional variables.

Fluid is injected steadily through the sidewall with a characteristic velocity  $V'_{r0}$  and induces an axial flow characterized by  $V'_{z0}$ . The mathematical model is based on the following non-dimensional Navier Stokes equations:

$$\frac{\partial \rho}{\partial t} + M \left[ \frac{1}{r} \frac{\partial}{\partial r} (r \rho V_r) + \epsilon \frac{1}{r} \frac{\partial}{\partial \theta} (\rho V_\theta) + \frac{\partial}{\partial z} (\rho V_z) \right] = 0, \quad (1)$$

$$\rho \left[ \frac{DV_r}{Dt} - M \epsilon^2 \frac{V_\theta^2}{r} \right] = -\frac{\delta^2}{\gamma M} \frac{\partial P}{\partial r} + \frac{M \delta^2}{Re} S_r, \quad (2)$$

$$\rho \left[ \frac{DV_\theta}{Dt} + M \frac{V_r V_\theta}{r} \right] = -\frac{\delta^2}{\gamma \epsilon M} \frac{1}{r} \frac{\partial P}{\partial \theta} + \delta^2 \frac{M}{Re} S_\theta, \quad (3)$$

$$\rho \frac{DV_z}{Dt} = -\frac{1}{\gamma M} \frac{\partial P}{\partial z} + \delta^2 \frac{M}{Re} S_z, \quad (4)$$

$$\begin{aligned} \rho C_V \frac{DT}{Dt} &= -M(\gamma - 1) P \nabla \cdot \bar{V} \\ &+ \frac{M^3(\gamma - 1)\gamma}{Re} \Phi + \frac{M}{Pr Re} \nabla \cdot (\kappa \nabla T), \quad (5) \\ P &= \rho T, \quad (6) \end{aligned}$$

where

$$\nabla \cdot \bar{V} = \frac{\partial V_r}{\partial r} + \frac{V_r}{r} + \frac{\epsilon}{r} \frac{\partial V_\theta}{\partial \theta} + \frac{\partial V_z}{\partial z},$$

$$\frac{D}{Dt} = \frac{\partial}{\partial t} + M \left( V_r \frac{\partial}{\partial r} + \epsilon \frac{1}{r} V_\theta \frac{\partial}{\partial \theta} + V_z \frac{\partial}{\partial z} \right),$$

$S_r, S_\theta, S_z$  are viscous terms, and  $\Phi$  is the dissipation function. Equations (1)–(6) are non-dimensionalized using the following definitions:

$$\begin{aligned} V_r &= \frac{V'_r}{V'_{r0}}, \quad V_\theta = \frac{V'_\theta}{V'_{\theta0}}, \quad V_z = \frac{V'_z}{V'_{z0}}, \\ \rho &= \frac{\rho'}{\rho'_0}, \quad P = \frac{P'}{P'_0}, \quad T = \frac{T'}{T'_0}, \quad \mu = \frac{\mu'}{\mu'_0}, \quad C_V = \frac{C'_V}{C'_{V0}}, \\ r &= \frac{r'}{R'}, \quad z = \frac{z'}{L'}, \quad t = \frac{t'}{t'_a}, \quad \kappa = \frac{\kappa'}{\kappa'_0}, \end{aligned}$$

where  $P'_0$  is the initial static pressure in the cylinder, and  $\rho'_0$  and  $T'_0$  are the density and temperature of the fluid being injected from the sidewall. The aspect ratio is given by  $\delta = \frac{L'}{R'}$ , where  $\delta \gg 1$ . The induced characteristic axial velocity and the characteristic endwall velocity disturbance  $V'_{z0}$  is defined with respect to the injection reference sidewall velocity,  $V'_{r0}$  by overall mass conservation,  $\frac{V'_{z0}}{V'_{r0}} = \delta$ . The

size of the initially unknown reference azimuthal velocity  $V'_{\theta0}$  is related to  $V'_{r0}$  by  $\frac{V'_{\theta0}}{V'_{r0}} = \epsilon$ . Later, it is shown that  $\epsilon = 1$ .

The time is non-dimensionalized using the axial acoustic time scale,  $t'_a = \frac{L'}{C'_0}$ , where  $C'_0 = (\gamma \mathcal{R}' T'_0)^{\frac{1}{2}}$  is the speed of sound,  $\mathcal{R}'$  is the gas constant, and  $\gamma$  is the ratio of specific heats. The thermal diffusivity, viscosity, and specific heat for constant volume,  $\kappa'_0, \mu'_0$ , and  $C'_{V0}$  are characteristic properties of the injected fluid. Also the Reynolds number, Prandtl number, and Mach number are defined as

$$Re = \frac{\rho' V'_{z0} L'}{\mu'_0}, \quad Pr = \frac{\mu'_0 C'_{V0}}{\kappa'_0}, \quad M = \frac{V'_{z0}}{C'_0},$$

where  $Re \gg 1, M \ll 1$ , and  $Pr = O(1)$ .

Initially, a steady flow is generated by the sidewall injection,  $V_r = -1$ . At  $t = 0^+$ , the radial speed on the sidewall begins to oscillate with a non-dimensionalized sinusoidal variation,  $V_r = -1 + F(\theta, z) \sin \omega t$ , where  $\omega = O(1)$ .

The full boundary conditions are:

$$z = 0; \quad V_z = 0 \quad (7)$$

$$z = 1; \quad P = 1, \quad (8)$$

$$r = 0; \quad P, \rho, T, V_r, V_\theta, V_z \text{ finite}, \quad (9)$$

$$r = 1; \quad V_r = \begin{cases} -1 & t \leq 0 \\ -1 + F(\theta, z) \sin \omega t, & t > 0 \end{cases} \quad (10)$$

$$r = 1; \quad V_z = V_\theta = 0, \quad (11)$$

and solutions must be periodic in  $\theta$ .

## II Steady Solution

In general, solutions to (1)–(6), with boundary conditions (7)–(11), are found in terms of the dependent variables, written as

$$(V_r, V_\theta, V_z, P, \rho, T) = (V_{rs}, V_{\theta s}, V_{zs}, P_s, \rho_s, T_s) + (\tilde{V}_r, \tilde{V}_\theta, \tilde{V}_z, \tilde{P}, \tilde{\rho}, \tilde{T}),$$

where the subscript "s" represents the steady part of the flow and ( $\tilde{\phantom{x}}$ ) represents the unsteady flow. The steady parts of the solutions satisfy the condition  $V_{rs} = -1$  at  $r = 1$  for all  $t$ . As a result of the axisymmetric boundary conditions, the steady solution is axisymmetric.

The steady variables are expanded as

$$(V_{rs}, V_{\theta s}, V_{zs}) \sim \sum_{i=0} M^i (V_{ris}, V_{\theta is}, V_{zis}),$$

$$(P_s, \rho_s, T_s) \sim 1 + \sum_{i=0} M^{i+2} (P_{is}, \rho_{is}, T_{is}),$$

for the limit  $M \rightarrow 0$ .

The solutions to the first-order steady equations,

$$V_{r0s} = -\frac{1}{r} \sin\left(\frac{\pi}{2} r^2\right), \quad (12)$$

$$V_{\theta 0s} = 0, \quad (13)$$

$$V_{z0s} = \pi z \cos\left(\frac{\pi}{2} r^2\right), \quad (14)$$

$$P_{0s} = \gamma \frac{\pi^2}{2} (1 - z^2), \quad (15)$$

are those derived by Culick<sup>3</sup> and Taylor<sup>4</sup>.

The initial conditions for the unsteady flow are given by the steady solution profiles. In terms of the unsteady variables, at  $t = 0$ ,

$$(\tilde{V}_r, \tilde{V}_\theta, \tilde{V}_z, \tilde{P}, \tilde{\rho}, \tilde{T}) = 0. \quad (16)$$

### III Three-dimensional Unsteady Flow

The unsteady flow in the cylinder is described in terms of asymptotic expansions

$$(\rho, P, T) \sim 1 + \sum_{i=1} M^{i+1} (\tilde{\rho}_i, \tilde{P}_i, \tilde{T}_i),$$

$$(V_r, V_\theta, V_z) \sim (V_{r0s}, V_{\theta 0s}, V_{z0s}) + \sum_{i=0} M^i (\tilde{V}_{ri}, \tilde{V}_{\theta i}, \tilde{V}_{zi}) \quad (17)$$

valid in the limit  $M \rightarrow 0$ .

To resolve the flow structure, a multiple spatial scale analysis is required. The first spatial scale,  $r_1 = 1 - r$ , is the cylinder radius, and the second,  $r_2 = \frac{1-r}{M}$  is needed to resolve the fine scale structure of the vorticity. The radial gradients in (1)–(6) are replaced by

$$\frac{\partial}{\partial r} = -\frac{\partial}{\partial r_1} - \frac{1}{M} \frac{\partial}{\partial r_2}, \quad (18)$$

$$\frac{\partial^2}{\partial r^2} = \frac{\partial^2}{\partial r_1^2} + \frac{2}{M} \frac{\partial^2}{\partial r_1 \partial r_2} + \frac{1}{M^2} \frac{\partial^2}{\partial r_2^2}.$$

### Leading Order Mathematical Model

The unsteady expansions in (17) and the multiple radial scales in (18) are substituted into (1)–(6), and

the leading order equations are found with  $M \rightarrow 0$ ,  $\frac{\delta^2}{Re} \ll 1$ , and  $\delta = \frac{k}{M}$ . The first asymptotic relationship is the hard-blowing condition and the second relationship is used to simplify the analysis. The aspect ratio,  $\delta$  and the Reynolds number,  $Re$ , will be written in terms of the Mach number. The aspect ratio is taken to be  $\delta = \frac{k}{M}$ , where  $k$  is an order one constant. Although this relationship is done to simplify the mathematics, it is also physically relevant. In real solid rocket motors, the aspect ratio is between 15 and 50 and within the core of the motor chamber and upstream of the nozzle, the Mach number is between 0.05 and 0.3.

After considerable technical manipulation like that used in Zhao et. al.<sup>2</sup> one finds,

$$\frac{\partial \tilde{V}_{r0}}{\partial r_2} = 0, \quad (19)$$

$$\frac{\partial \tilde{\rho}_0}{\partial t} - (\tilde{V}_{r0} + V_{r0s}) \frac{\partial \tilde{\rho}_0}{\partial r_2} = \frac{1}{r} \frac{\partial (r \tilde{V}_{r0})}{\partial r_1} + \frac{1}{r} \frac{\partial (r \tilde{V}_{r1})}{\partial r_2} - \frac{\epsilon}{r} \frac{\partial \tilde{V}_{\theta 0}}{\partial \theta} - \frac{\partial \tilde{V}_{z0}}{\partial z}, \quad (20)$$

$$\frac{\partial \tilde{P}_0}{\partial r_2} = 0, \quad (21)$$

$$\frac{\partial \tilde{P}_0}{\partial r_1} + \frac{\partial \tilde{P}_1}{\partial r_2} = 0, \quad (22)$$

$$\frac{\partial \tilde{P}_1}{\partial r_1} + \frac{\partial \tilde{P}_2}{\partial r_2} = 0, \quad (23)$$

$$\frac{\partial \tilde{V}_{r0}}{\partial t} = \frac{k^2}{\gamma} \left( \frac{\partial \tilde{P}_2}{\partial r_1} + \frac{\partial \tilde{P}_3}{\partial r_2} \right), \quad (24)$$

$$\frac{\partial \tilde{P}_0}{\partial \theta} = \frac{\partial \tilde{P}_1}{\partial \theta} = 0, \quad (25)$$

$$\frac{\partial \tilde{V}_{\theta 0}}{\partial t} - (V_{r0s} + \tilde{V}_{r0}) \frac{\partial \tilde{V}_{\theta 0}}{\partial r_2} = -\frac{k^2}{\epsilon \gamma r} \frac{\partial \tilde{P}_2}{\partial \theta}, \quad (26)$$

$$\frac{\partial \tilde{V}_{z0}}{\partial t} - (V_{r0s} + \tilde{V}_{r0}) \frac{\partial \tilde{V}_{z0}}{\partial r_2} = -\frac{1}{\gamma} \frac{\partial \tilde{P}_0}{\partial z}, \quad (27)$$

$$\frac{\partial \tilde{T}_0}{\partial t} - (V_{r0s} + \tilde{V}_{r0}) \frac{\partial \tilde{T}_0}{\partial r_2} = \frac{\gamma - 1}{\gamma} \frac{\partial \tilde{P}_0}{\partial t}, \quad (28)$$

$$\tilde{P}_0 = \tilde{\rho}_0 + \tilde{T}_0. \quad (29)$$

Equations (19) and (20) are found from the conservation of mass, (1). The radial momentum equation (2) gives rise to (21)–(24). Equations (25) and (26) are first-order approximations of (3). Equations (21)–(23), and (25) arise due to the large aspect ratio of the motor. Equations (27)–(29) are leading order versions of (4)–(6).

A further division of the variables is used to describe the acoustic and rotational parts of the flow field, written as

$$\begin{aligned}\bar{\rho}_0 &= \bar{\rho}_0(z, t) + \hat{\rho}_0(r_1, r_2, \theta, z, t), \\ \bar{T}_0 &= \bar{T}_0(z, t) + \hat{T}_0(r_1, r_2, \theta, z, t), \\ \bar{P}_0 &= \bar{P}_0(z, t), \\ \bar{P}_1 &= \bar{P}_1(z, t), \\ \bar{P}_2 &= \bar{P}_2(r_1, \theta, z, t), \\ \bar{V}_{z0} &= \bar{V}_{z0}(z, t) + \hat{V}_{z0}(r_1, r_2, \theta, z, t), \\ \bar{V}_{\theta 0} &= \bar{V}_{\theta 0}(r_1, z, \theta, t) + \hat{V}_{\theta 0}(r_1, r_2, \theta, z, t), \\ \bar{V}_{r0} &= \bar{V}_{r0}(r_1, \theta, z, t),\end{aligned}\quad (30)$$

where a (  $\bar{\phantom{x}}$  ) refers to irrotational acoustics and a (  $\hat{\phantom{x}}$  ) refers to the rotational component of the flow.

The leading order pressures,  $\bar{P}_0$  and  $\bar{P}_1$  contain only the irrotational term, which depends only on  $z$  and  $t$ . This will be shown later. The irrotational part of the leading order temperature, density, and axial velocity ( $\bar{T}_0$ ,  $\bar{\rho}_0$ , and  $\bar{V}_{z0}$ ) are related to  $\bar{P}_0$  as will also be shown later. Similarly, the irrotational parts of  $\bar{V}_{\theta 0}$ ,  $\bar{V}_{r0}$  are related to  $\bar{P}_2$ .

The irrotational variables and the pressure describe the acoustics within the chamber, and the rotational parts describe the vorticity.

### Irrotational Equations

The expansions in (30) are substituted into (19)–(29) to form two sets of equations. The irrotational equations are

$$\frac{\partial \bar{\rho}_0}{\partial t} = \frac{1}{r} \frac{\partial (r \bar{V}_{r0})}{\partial r_1} - \frac{\epsilon}{r} \frac{\partial \bar{V}_{\theta 0}}{\partial \theta} - \frac{\partial \bar{V}_{z0}}{\partial z}, \quad (31)$$

$$\frac{\partial \bar{V}_{\theta 0}}{\partial t} = -\frac{k^2}{\gamma \epsilon r} \frac{\partial \bar{P}_2}{\partial \theta}, \quad (32)$$

$$\frac{\partial \bar{V}_{z0}}{\partial t} = -\frac{1}{\gamma} \frac{\partial \bar{P}_0}{\partial z}, \quad (33)$$

$$\frac{\partial \bar{T}_0}{\partial t} = \frac{\gamma - 1}{\gamma} \frac{\partial \bar{P}_0}{\partial t}, \quad (34)$$

$$\bar{P}_0 = \bar{\rho}_0 + \bar{T}_0, \quad (35)$$

The irrotational conservation of mass (31), can be further divided into two equations,

$$\frac{\partial \bar{\rho}_0}{\partial t} + \frac{\partial \bar{V}_{z0}}{\partial z} = \frac{1}{\pi} \int_{-\pi}^{\pi} F(\theta, z) \sin \omega t, \quad (36)$$

$$-\frac{1}{r} \frac{\partial (r \bar{V}_{r0})}{\partial r_1} + \frac{\epsilon}{r} \frac{\partial \bar{V}_{\theta 0}}{\partial \theta} = -\frac{1}{\pi} \int_{-\pi}^{\pi} F(\theta, z) \sin \omega t. \quad (37)$$

Integrating (31) over the cross-section of the cylinder, and using the sidewall boundary condition in (10), yields (36). This equation only depends on  $z$  and  $t$ . The second equation, (37) is found by the difference between (31) and (36), and depends on  $z$ ,  $t$ ,  $r_1$  and  $\theta$ .

Equations (33)–(35) and (36), can be combined to yield an axial wave equation,

$$\frac{\partial^2 \bar{P}_0}{\partial t^2} - \frac{\partial^2 \bar{P}_0}{\partial z^2} = -\frac{\gamma}{\pi} \int_{-\pi}^{\pi} F(\theta, z) \omega \cos \omega t \, d\theta, \quad (38)$$

with boundary/initial conditions:

$$\begin{aligned}\frac{\partial \bar{P}_0}{\partial z} &= 0, \quad z = 0; \quad \bar{P}_0 = 0, \quad z = 1, \\ \bar{P}_0 &= \frac{\partial \bar{P}_0}{\partial t} = 0, \quad t = 0.\end{aligned}$$

Standard techniques can be used to find the solution:

$$\bar{P}_0 = \sum_{n=0}^{\infty} \frac{2\gamma \omega a_n}{b_n^2 - \omega^2} (\cos \omega t - \cos b_n t) \cos b_n z, \quad (39)$$

where  $a_n = -\frac{1}{\pi} \int_0^1 \int_{-\pi}^{\pi} F(z, \theta) \cos b_n z \, d\theta \, dz$  and  $b_n = (n + \frac{1}{2})\pi$ . The solution above is valid for  $\omega \neq b_n$ ,  $n = 0, 1, 2, \dots$  in order to avoid resonance, which is not studied in the present work.

The leading order velocity, found from (33), is

$$\bar{V}_{z0} = \sum_{n=0}^{\infty} \frac{2a_n b_n}{b_n^2 - \omega^2} \left( \frac{\omega}{b_n} \sin b_n t - \sin \omega t \right) \sin b_n z. \quad (40)$$

The above results indicate that the pressure and axial velocity contain both the driving frequency of the sidewall as well as all eigenfunctions associated with the cylinder length.

### Higher Order Pressure Terms

Because the solution to the leading order pressure in (39) does not depend on  $r_1$ , the second order pressure satisfies  $\frac{\partial \bar{P}_1}{\partial r_2} = 0$  from (22). An integration of the third-order conservation of radial momentum, (23), gives

$$\bar{P}_2 = -r_2 \frac{\partial \bar{P}_1}{\partial r_1} + G_2(r_1, \theta, z, t). \quad (41)$$

The secular growth term in  $r_2$  must be suppressed, therefore  $\frac{\partial \bar{P}_1}{\partial r_1} = 0$ . Consequently, the first- and second-order pressure terms are dependent only on  $z$  and  $t$ . Also, the third-order pressure,  $\bar{P}_2$ , cannot depend on  $r_2$ , from (23).

Similarly, an integration of (23) with respect to  $r_2$  yields

$$\bar{P}_3 = r_2 \left( \frac{\gamma}{k^2} \frac{\partial \bar{V}_{r0}}{\partial t} - \frac{\partial \bar{P}_2}{\partial r_1} \right) + G_3(r_1, \theta, z, t), \quad (42)$$

since neither  $\bar{V}_{r0}$  nor  $\bar{P}_2$  depend on  $r_2$ . Suppressing the secular growth in  $r_2$  results in

$$\frac{\partial \bar{V}_{r0}}{\partial t} = \frac{k^2}{\gamma} \frac{\partial \bar{P}_2}{\partial r_1}. \quad (43)$$

### First-Order Transverse Flow

Equations (31), (32), and (43) can be combined to give a Poisson equation of the form:

$$\frac{k^2}{r} \frac{\partial}{\partial r} \left( r \frac{\partial \bar{P}_2}{\partial r} \right) + \frac{k^2}{r^2} \frac{\partial^2 \bar{P}_2}{\partial \theta^2} = \frac{\gamma \omega}{\pi} \int_{-\pi}^{\pi} F(\theta, z) d\theta \cos \omega t, \quad (44)$$

where the original radial variable  $r$  is used instead of  $r_1$ . The boundary conditions are:

$$\begin{aligned} r = 0, \quad \bar{P}_2 \text{ finite}, \\ r = 1, \quad \frac{\partial \bar{P}_2}{\partial r} = \gamma \omega F(\theta, z) \cos \omega t, \end{aligned} \quad (45)$$

with  $\bar{P}_2$  periodic in  $\theta$ .

The solution to (44) is

$$\begin{aligned} \bar{P}_2 = & \frac{\gamma \omega}{k^2} \cos \omega t \left[ \frac{r^2}{2} F(\theta, z) + A_0(z) \right. \\ & + \sum_{n=1}^{\infty} r^n (A_n(z) \cos n\theta + B_n(z) \sin n\theta) \\ & \left. + \sum_{n=1}^{\infty} r^2 (a_n(z) \cos n\theta + b_n(z) \sin n\theta) \right], \quad (46) \end{aligned}$$

where

$$a_n(z) = -\frac{1}{2\pi} \int_{-\pi}^{\pi} F(\theta, z) \cos n\theta d\theta,$$

$$b_n(z) = -\frac{1}{2\pi} \int_{-\pi}^{\pi} F(\theta, z) \sin n\theta d\theta,$$

$$A_n(z) = -\frac{2}{n} a_n(z) \quad (47)$$

$$B_n(z) = -\frac{2}{n} b_n(z)$$

and  $A_0(z)$  is an unknown function to be determined. Equations (32) and (43), can be used to show that

$$\begin{aligned} \bar{V}_{r0} = & \sin \omega t \left[ -r F(\theta, z) \right. \\ & - \sum_{n=1}^{\infty} n r^{n-1} (A_n(z) \cos n\theta + B_n(z) \sin n\theta) \\ & \left. - \sum_{n=1}^{\infty} 2r (a_n(z) \cos n\theta + b_n(z) \sin n\theta) \right], \quad (48) \end{aligned}$$

$$\begin{aligned} \bar{V}_{\theta 0} = & \frac{1}{\epsilon} \sin \omega t \left[ -\frac{r}{2} \frac{\partial F(\theta, z)}{\partial \theta} \right. \\ & + \sum_{n=1}^{\infty} n r^{n-1} (A_n(z) \sin n\theta - B_n(z) \cos n\theta) \\ & \left. + \sum_{n=1}^{\infty} n r (a_n(z) \sin n\theta - b_n(z) \cos n\theta) \right]. \quad (49) \end{aligned}$$

In the absence of a time derivative in (44), the pressure solution in (46) cannot satisfy the initial condition. If one looks at the problem for  $t = O(M)$ , the radial acoustic time scale, a hyperbolic equation for  $\bar{P}_2$  is recovered, for which an acoustic solution satisfying the initial condition can be found. In contrast to the axial velocity in (40), the solutions in (46), (48), and (49) are time-dependent non-acoustic responses of the flow to the sidewall boundary condition.

Figure 2 shows a cross-section of the vector field for the boundary condition  $F(\theta, z) = \cos \frac{\pi z}{2} \sin^2 \frac{\theta}{2}$ . The vector field consists only of the vector sum of the leading-order radial velocity,  $V_{r0s} + \bar{V}_{r0}$  and the azimuthal velocity,  $\bar{V}_{\theta 0}$ . The values  $z = \frac{1}{2}$ ,  $t = \frac{\pi}{4}$  and  $\omega = 1$  are chosen for the plot, which reveals a flow from right to left across the centerline. The boundary condition contains a non-zero Fourier coefficient,  $A_1(z)$ , which will be shown to be an indicator of cross-axis flow.

### Determination of the Parameter $\epsilon$

The parameter  $\epsilon$  in the definition of  $\epsilon = \frac{V'_{\theta 0}}{V'_{r0}}$  can be found by examining the flow at the centerline of the

cylinder. The magnitude of the flow here can only depend on  $z$  and not  $\theta$ . Values of the radial and azimuthal velocities along the axis of the cylinder are

$$\bar{V}_{\theta 0}|_{r \rightarrow 0} = \frac{1}{\epsilon}(A_1(z) \sin \theta - B_1(z) \cos \theta) \sin \omega t, \quad (50)$$

$$\bar{V}_{r 0}|_{r \rightarrow 0} = (A_1(z) \sin \theta + B_1(z) \cos \theta) \sin \omega t. \quad (51)$$

The magnitude of the transverse velocity vector along the centerline is

$$\begin{aligned} \bar{V}_{r 0}^2|_{r \rightarrow 0} + \bar{V}_{\theta 0}^2|_{r \rightarrow 0} &= \sin^2 \omega t \\ &\left[ \left( \sin^2 \theta + \frac{\cos^2 \theta}{\epsilon^2} \right) A_1^2(z) \right. \\ &+ \left( 2 - \frac{2}{\epsilon^2} \right) A_1(z) B_1(z) \sin \theta \cos \theta \\ &\left. + \left( \cos^2 \theta + \frac{\sin^2 \theta}{\epsilon^2} \right) B_1^2(z) \right] \end{aligned}$$

and does not depend on  $\theta$  if  $\epsilon = 1$ . The square of the speed transverse to the cylinder axis is

$$\bar{V}_{r 0}^2|_{r \rightarrow 0} + \bar{V}_{\theta 0}^2|_{r \rightarrow 0} = (A_1^2(z) + B_1^2(z)) \sin^2 \omega t.$$

This result demonstrates that if  $A_1(z)$  or  $B_1(z)$  is non zero then there is flow across the centerline of the cylinder. Flow across the axis of the cylinder occurs only when the coefficients  $A_1(z)$  and  $B_1(z)$  are nonzero. These are the coefficients for the eigenfunctions  $\sin \theta$  and  $\cos \theta$  given in (47). These are the only  $\theta$ -dependent eigenfunctions which are not symmetric about the center of the cylinder.

### Rotational Equations

The solutions to the irrotational velocities in (40), (48), and (49) describe the acoustic and non-acoustic response characteristics of the flow. In contrast, the rotational equations contain vortical characteristics. An analogous procedure to that used to find the irrotational equations is now employed to find the rotational equations. The expansions in (30) are substituted into (26)–(29) to give the leading order rotational equations,

$$\frac{\partial \hat{V}_{\theta 0}}{\partial t} - (V_{r 0 s} + \bar{V}_{r 0}) \frac{\partial \hat{V}_{\theta 0}}{\partial r_2} = 0, \quad (52)$$

$$\frac{\partial \hat{V}_{z 0}}{\partial t} - (V_{r 0 s} + \bar{V}_{r 0}) \frac{\partial \hat{V}_{z 0}}{\partial r_2} = 0, \quad (53)$$

$$\frac{\partial \hat{T}_0}{\partial t} - (V_{r 0 s} + \bar{V}_{r 0}) \frac{\partial \hat{T}_0}{\partial r_2} = 0, \quad (54)$$

$$\hat{\rho}_0 + \hat{T}_0 = 0. \quad (55)$$

The latter two equations can be combined to show that the rotational part of the density is described by

$$\frac{\partial \hat{\rho}_0}{\partial t} - (V_{r 0 s} + \bar{V}_{r 0}) \frac{\partial \hat{\rho}_0}{\partial r_2} = 0. \quad (56)$$

Equation (56) and the rotational part of the conservation of mass (20) can be used to derive an incompressible rotational conservation of mass,

$$\frac{\partial \hat{V}_{r 1}}{\partial r_2} - \frac{1}{r} \frac{\partial \hat{V}_{\theta 0}}{\partial \theta} - \frac{\partial \hat{V}_{z 0}}{\partial z} = 0. \quad (57)$$

Boundary conditions along the sidewall for (52)–(56) are found from the no-slip boundary condition (11) and the known values of the axial and azimuthal velocities in (40) and (49). The density and the temperature on the sidewall can be found from (31) and (35). The boundary conditions for (52)–(56) are

$$\begin{aligned} r_1 = r_2 = 0, \quad \hat{V}_{\theta 0} &= -\bar{V}_{\theta 0}(r = 1, z, t), \\ r_1 = r_2 = 0, \quad \hat{V}_{z 0} &= -\bar{V}_{z 0}(z, t), \\ r_1 = r_2 = 0, \quad \hat{T}_0 &= -\bar{T}_0(z, t), \\ r_1 = r_2 = 0, \quad \hat{\rho}_0 &= -\bar{\rho}_0(z, t). \end{aligned} \quad (58)$$

Equation (53) can be written,

$$\frac{d \hat{V}_{z 0}}{dt} = 0, \quad (59)$$

along a characteristic surface  $\xi = \xi(r_1, r_2, \theta, z, t)$  defined by

$$\frac{dr_2}{dt} = -(V_{r 0 s} + \bar{V}_{r 0}), \quad (60)$$

where the derivative is taken with  $r_1$ ,  $\theta$ , and  $z$  constant. The equations (52)–(54) and (56) can be written in the form (59). Each of these equations have the form of a one-dimensional wave equation. The solutions of these equations will each be waves traveling toward the center of the cylinder and convected by the radial injection velocity,  $\bar{V}_{r 0} + V_{r 0 s}$ .

Using (12) and (48), (60) can be solved for  $r_2$ ,

$$\xi + r_2 = t \frac{\sin(\frac{\pi}{2}(1 - r_1)^2)}{1 - r_1}$$

$$\begin{aligned}
& + \left( \frac{1 - \cos \omega t}{\omega} \right) [(1 - r_1) F(\theta, z) \\
& + \sum_{n=1}^{\infty} n(1 - r_1)^{n-1} (A_n(z) \cos n\theta + B_n \sin n\theta) \\
& + \sum_{n=1}^{\infty} 2(1 - r_1) (a_n(z) \cos n\theta + b_n(z) \sin n\theta) ] ,
\end{aligned} \quad (61)$$

where  $r_1$ ,  $\theta$ , and  $z$  are taken as parameters. The rotational parts of the azimuthal velocity, axial velocity, temperature and density can be written as

$$\begin{aligned}
\hat{V}_{\theta 0} &= \hat{V}_{\theta 0}(\xi; r_1, \theta, z), \quad \hat{V}_{z 0} = \hat{V}_{z 0}(\xi; r_1, \theta, z), \\
\hat{T}_0 &= \hat{T}_0(\xi; r_1, \theta, z), \quad \hat{\rho}_0 = \hat{\rho}_0(\xi; r_1, \theta, z).
\end{aligned}$$

Each value of  $\xi = \text{constant}$  in (61), describes a surface in  $(t, r_1, r_2)$  for  $z$  and  $\theta$  parameters. The physical front of the vorticity,  $\xi = 0$  is found from the intersection of the surface with the plane  $r_1 = Mr_2$ .

Figures 3 and 4 show a series of cross-sections of the vorticity front for two different boundary conditions. The curves represent the boundary between the rotational unsteady flow and the unsteady irrotational and steady rotational flow, for times,  $t = 2, 4, 8, 12$ , and  $16$ . The largest curve represents the sidewall of the cylinder. The front closest to the sidewall corresponds to  $t = 2$  and they become smaller as time increases.

The plot in Figure 3 shows cross-sectional projections of the vorticity front for the radial boundary condition  $V_r = -1 + \cos^2 \frac{\theta}{2} \cos \frac{\pi}{2} z \sin \omega t$  for  $z = \frac{1}{4}$  and  $\omega = \frac{1}{2}$ . The plot reveals that the front shifts to the left for  $t = 4, 8$ , and  $12$ . The maximum of the offset occurs as  $t = 2\pi$ . It is also noted that as time increases, the vorticity front becomes more axisymmetric.

The plot in Figure 4 shows cross-sectional projections of the vorticity front for the radial boundary condition  $V_r = -1 + \cos^2 3\theta \cos \frac{\pi}{2} z \sin \omega t$  for  $z = \frac{1}{4}$  and  $\omega = \frac{1}{2}$ . The effect of the non-axisymmetric boundary condition is evident for the fronts at  $t = 2$  and  $t = 4$ . The shape of the vorticity fronts remains nearly axisymmetric for  $t \geq 8$ .

#### IV Vorticity

The vorticity,  $\Omega = (\Omega_r, \Omega_\theta, \Omega_z)$  along the sidewall,  $r = 1$ , is calculated by examining the leading order azimuthal and axial momentum equations (26) and (27). The no-slip boundary condition applied at the sidewall is  $\hat{V}_{\theta 0} = \hat{V}_{z 0} = 0$ . The result is that

the radial velocity gradients are proportional to the pressure gradients, which are known.

$$\begin{aligned}
\frac{\partial \hat{V}_{\theta 0}}{\partial r_2} &= \frac{k^2}{\gamma r} \frac{1}{V_{r0s} + \bar{V}_{r0}} \frac{\partial \bar{P}_2}{\partial \theta}, \\
\frac{\partial \hat{V}_{z 0}}{\partial r_2} &= \frac{1}{\gamma} \frac{1}{V_{r0s} + \bar{V}_{r0}} \frac{\partial \bar{P}_0}{\partial z}.
\end{aligned}$$

The vorticity on the sidewall can be calculated using the pressure gradients (39) and (46) and the radial injection boundary condition (10).

$$\begin{aligned}
\Omega_\theta &\sim \frac{1}{M} \frac{\partial \hat{V}_{z 0}}{\partial r_2} \\
&= \frac{\sum_{n=0}^{\infty} \frac{2\omega a_n b_n}{b_n^2 - \omega^2} (\cos \omega t - \cos b_n t) \sin b_n z}{M(-1 + F(\theta, z) \sin \omega t)}, \\
\Omega_z &\sim -\frac{1}{M} \frac{\partial \hat{V}_{\theta 0}}{\partial r_2} \\
&= -\frac{\omega}{M} \cos \omega t \left( \frac{1}{2} \frac{\partial F(\theta, z)}{\partial \theta} \right. \\
&\quad \left. - \sum_{n=1}^{\infty} n(A_n(z) \sin n\theta - B_n(z) \cos n\theta) \right. \\
&\quad \left. - \sum_{n=1}^{\infty} n(a_n(z) \sin n\theta - b_n(z) \cos n\theta) \right) \\
&\quad \left/ \left( -1 + F(\theta, z) \cos \omega t \right) \right., \\
\Omega_r &\sim O(1).
\end{aligned}$$

The azimuthal component of vorticity is  $O(M^{-1})$ , as found by Zhao et. al.<sup>2</sup> This component of vorticity contains both a time-dependent response to the boundary condition as well as all eigenfunctions. A large axial component of vorticity,  $O(M^{-1})$  exists due to the nonaxisymmetric boundary condition. It contains only the time-dependent response associated with the boundary condition.

#### V Higher Order Equations

A higher order analysis must be done to resolve the effect of the second radial scale on the rotational variables. The procedure used in section III is employed here to divide the higher-order velocities, density and temperature into irrotational and rotational parts, using the following expansions:



$$\begin{aligned}
\hat{V}_{z1} &= \bar{V}_{z1}(z, t) + \hat{V}_{z1}(r_1, r_2, \theta, z, t), \\
\hat{p}_1 &= \bar{p}_1(z, t) + \hat{p}_1(r_1, r_2, \theta, z, t) \\
\hat{V}_{\theta 1} &= \bar{V}_{\theta 1}(r_1, \theta, z, t) + \hat{V}_{\theta 1}(r_1, r_2, \theta, z, t), \\
\hat{T}_1 &= \bar{T}_1(z, t) + \hat{T}_1(r_1, r_2, \theta, z, t)
\end{aligned} \tag{62}$$

The second order rotational azimuthal and axial momentum equations are found by substituting (17) and (62) into (3) and (4), using  $\delta = \frac{k}{M}$  and  $Re = \frac{1}{C M^*}$ , where  $C = O(1)$ . Similar to the aspect ratio, the Reynolds number is written in terms of the Mach number to simplify the model. This particular relationship is chosen to include a weak viscous effect for the first-order velocities.

Additional equations that describe the effect of the shorter length scale,  $r_2$ , are found by suppressing terms on the right hand side of (63) and (64) that cause secular growth in  $\hat{V}_{\theta 1}$  and  $\hat{V}_{z1}$ . These equations will not be discussed in the present work, but a set of nonlinear convection-diffusion equations, which are similar but more general than those found by Zhao et. al.<sup>2</sup>, is expected.

$$\begin{aligned}
\frac{\partial \hat{V}_{\theta 1}}{\partial t} - (V_{r0s} + \bar{V}_{r0}) \frac{\partial \hat{V}_{\theta 1}}{\partial r_2} &= \frac{k^2}{\gamma} \frac{1}{r} \bar{p}_0 \frac{\partial \bar{P}_2}{\partial \theta} + (V_{r0s} + \bar{V}_{r0}) \frac{\partial \hat{V}_{\theta 0}}{\partial r_2} - \hat{V}_{r1} \frac{\partial \hat{V}_{\theta 0}}{\partial r_2} + Ck^2 \frac{\partial^2 \hat{V}_{\theta 0}}{\partial r_2^2} \\
&+ \frac{1}{r} \hat{V}_{\theta 0} \frac{\partial \bar{V}_{\theta 0}}{\partial \theta} + \frac{1}{r} \bar{V}_{\theta 0} \frac{\partial \hat{V}_{\theta 0}}{\partial \theta} + \frac{1}{r} \hat{V}_{\theta 0} \frac{\partial \hat{V}_{\theta 0}}{\partial \theta} + \hat{V}_{z0} \frac{\partial \bar{V}_{z0}}{\partial z} \\
&+ (V_{z0s} + \bar{V}_{z0} + \hat{V}_{z0}) \frac{\partial \hat{V}_{\theta 0}}{\partial z} + \frac{1}{r} (V_{r0s} + \bar{V}_{r0}) \hat{V}_{\theta 0}, \tag{63}
\end{aligned}$$

$$\begin{aligned}
\frac{\partial \hat{V}_{z1}}{\partial t} - (V_{r0s} + \bar{V}_{r0}) \frac{\partial \hat{V}_{z1}}{\partial r_2} &= \frac{1}{\gamma} \frac{\partial \bar{P}_0}{\partial z} + (V_{r0s} + \bar{V}_{r0}) \frac{\partial \hat{V}_{z0}}{\partial r_1} + \hat{V}_{r1} \frac{\partial \hat{V}_{z0}}{\partial r_2} + Ck^2 \frac{\partial^2 \hat{V}_{z0}}{\partial r_2^2} \\
&+ \bar{V}_{r0} \frac{\partial V_{z0s}}{\partial r_1} - \frac{1}{r} (\bar{V}_{\theta 0} + \hat{V}_{\theta 0}) \frac{\partial \hat{V}_{z0}}{\partial \theta} - V_{z0s} \left( \frac{\partial \bar{V}_{z0}}{\partial z} + \frac{\partial \hat{V}_{z0}}{\partial z} \right) \\
&- (\bar{V}_{z0} + \hat{V}_{z0}) \left( \frac{\partial V_{z0s}}{\partial z} + \frac{\partial \bar{V}_{z0}}{\partial z} \right) - \hat{V}_{z0} \frac{\partial \hat{V}_{z0}}{\partial z}. \tag{64}
\end{aligned}$$

### Conclusion

Three-dimensional flow dynamics in a cylinder with sidewall mass addition have been studied to examine the effect of a time-harmonic, non-axisymmetric, radial velocity sidewall boundary condition with a driving frequency close to that of the first few axial modes of the cylinder. The results show that the flow is dominated by an axial velocity that consists of irrotational acoustics containing all axial eigenfunctions when the exit boundary condition is a pressure node. Non-axisymmetric, non-

acoustic radial and azimuthal velocities are time-dependent responses to the boundary condition.

The two largest components of vorticity are the azimuthal and axial parts, and each are of the order  $O(M^{-1})$ . Each component arises from an interaction between either the axial irrotational acoustics in (40) or the azimuthal component of the transverse velocity in (49) with the radial injection on the sidewall.

Finally, a higher order analysis is done to describe the effect of the shorter radial variable. A set of nonlinear convection-diffusion equations are expected which includes the effect of viscosity.

### References

1. Staab, P. L., and Kassoy, D. R. 1997, Three-Dimensional, Unsteady, Acoustic-Shear Flow Dynamics in a Cylinder with Sidewall Mass Addition, *Physics of Fluids*, to appear.
2. Zhao, Q., Kassoy, D. R., Kirkkopru, 1997, Acoustically Generated Vorticity in an Internal Flow, submitted, *J. Fluid Mech.*
3. Culick, F. E. C., 1966, Rotational Axisymmetric Mean Flow and Damping of Acoustic Waves in Solid Propellant Rocket Motors, *AIAA J.*, 4, 1462-1464.
4. Taylor, G. I., 1956, *Proc. Royal Soc. Lond.*, A 234, 456-475.



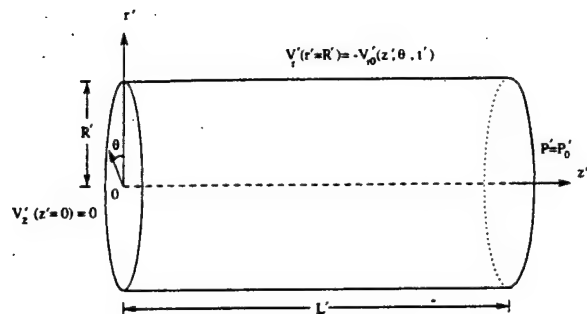


Figure 1: A solid rocket motor is modeled by a cylinder of length  $L'$  and radius  $R'$ . A pressure node,  $P' = P_0'$  exists at the open end,  $z' = L'$ . A non-axisymmetric radial velocity is imposed. The aspect ratio is  $\delta = \frac{L'}{R'} \gg 1$ .

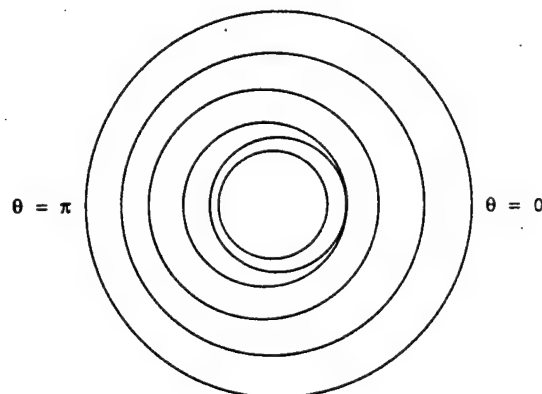


Figure 3: The plot is a series of cross-sections of the vorticity front for radial velocity boundary condition,  $V_r = -1 + \cos^2 \frac{\theta}{2} \cos \frac{\pi}{2} z \sin \omega t$  for  $z = \frac{1}{4}$  and  $\omega = \frac{1}{2}$ . The outer curve is the boundary of the cylinder and the inner curves are the cross-sections for  $t = 2, 4, 8, 12$ , and  $16$ .

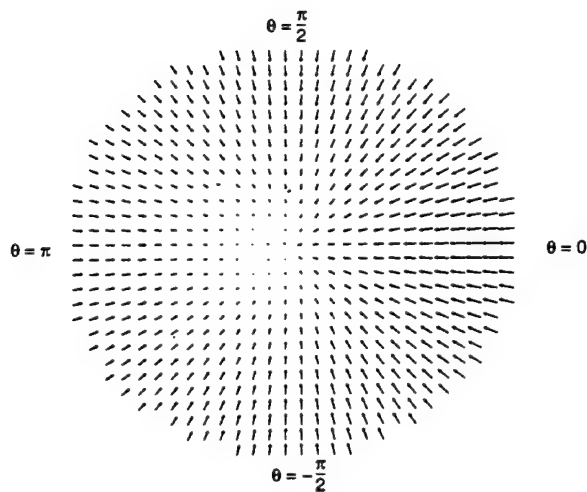


Figure 2: The plot of a projection of the velocity vector field onto a cross-sectional plane at  $z = 1/2$  for  $t = \pi/4$ . The field consists of the vector sum of the radial,  $V_{r0s} + \bar{V}_{r0}$ , and azimuthal,  $\bar{V}_{\theta 0}$  velocities. The function  $F(z, \theta) = \cos(\pi z/2) \sin^2(\theta/2)$  is used for the sidewall velocity boundary condition.

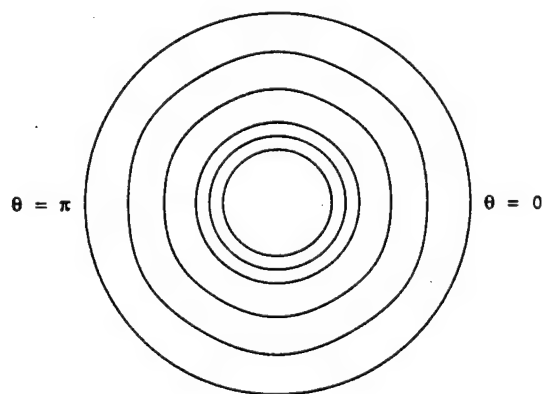


Figure 4: This plot is a series of cross-sections of an example vorticity front for radial velocity boundary condition,  $V_r = -1 + \cos^2 3\theta \cos \frac{\pi}{2} z \sin \omega t$  for  $z = \frac{1}{4}$  and  $\omega = \frac{1}{2}$ . The outer curve is the boundary of the cylinder and the inner curves are the cross-sections of the vorticity front for  $t = 2, 4, 8, 12$ , and  $16$ .



**AIAA 97-0697**

**Co-Existing Acoustic-Rotational  
Disturbances in a Coldflow Model  
of a Solid Rocket Motor**

D. R. Kassoy, P. L. Staab, T. Y. Chang,  
and A. M. Hegab

Center for Combustion Research  
University of Colorado, Boulder

**35th Aerospace Sciences  
Meeting & Exhibit  
January 6-10, 1997 / Reno, NV**

# CO-EXISTING ACOUSTIC-ROTATIONAL DISTURBANCES IN A COLDFLOW MODEL OF A SOLID ROCKET MOTOR

D. R. Kassoy, P. L. Staab, T. Y. Chang, and A. M. Hegab

Center for Combustion Research

Mechanical Engineering Department, B-427

University of Colorado, Boulder, CO 80309-0427

## Abstract

Numerical and analytical modeling methods are used to predict the transient flow dynamics generated by time-dependent boundary conditions in a solid rocket motor chamber model. First, nonaxisymmetric boundary forcing on the endwall is used to establish asymmetric, three-dimensional flow in a model chamber. Results of an asymptotic analysis provide an understanding of why such a flow is confined to a limited spatial region, and why most of the flow away from the endwall is axisymmetric.

Prescribed time-dependent sidewall mass addition is used to simulate irregular burning rates that characterize motor instabilities. The flow field consists of co-existing, equal magnitude acoustic (irrotational) and vorticity (rotational) fields present across the entire diameter of the cylindrical chamber. The numerical flow data is used to calculate mean flow and fluctuating flow properties, including RMS-values.

## I Non-Axisymmetric Flow in a Model Solid Rocket Motor

Most studies of rocket motor flow dynamics are focused on the behavior and impact of axial acoustic disturbances. In principle, azimuthally dependent, time varying burning rates could be the source of non-axisymmetric acoustic disturbances that initiate three-dimensional motor chamber flow transients. Sabnis et. al.<sup>1</sup> describe a three-dimensional numerical solution to a turbulent flow model, driven by an imposed non-axisymmetric pressure disturbance on a cross section of a long, narrow cylinder. The results show that the nonaxisymmetric portion of the flow exists only within two diameters from the cross section on which the pressure disturbance is imposed.

The flow dynamics in a solid-rocket chamber are modeled mathematically in the present work by using a cylinder with uniform sidewall mass injection. The unsteady flow is generated by a nonaxisymmetric oscillation of the axial velocity on the endwall. Asymptotic analysis, using a perturbation series in small Mach number, is used to find approximate solutions to the Navier-Stokes equations for a high aspect ratio rocket motor and a high Reynolds number. Except near the endwall, the flow is characterized by axisymmetric properties. A thin, three-dimensional incompressible flow transition layer exists between the endwall and the downstream axisymmetric region. The unsteady components of the radial and azimuthal velocities vanish as one moves downstream toward the edge of the layer as does all  $r$  and  $\theta$  dependence of the axial velocity and pressure. The basic result is in excellent agreement with that described by Sabnis et. al.<sup>1</sup>, and is valid for driving frequencies similar to those associated with the first few acoustic normal modes in the cylinder.

## Mathematical Formulation

The flow occurs in a cylinder of length  $L'$ , and radius,  $R'$ , with a pressure node at the open end as shown in Figure 1. Fluid is injected steadily through the sidewall with a characteristic velocity  $V'_{r0}$  and induces an axial flow characterized by  $V'_{z0}$ . The imposed axial velocity on the endwall also has a characteristic velocity  $V'_{z0}$ . The mathematical model is based on the following non-dimensional Navier Stokes equations:

$$\frac{\partial \rho}{\partial t} + M \left[ \frac{1}{r} \frac{\partial}{\partial r} (r \rho V_r) + \epsilon \frac{1}{r} \frac{\partial}{\partial \theta} (\rho V_\theta) + \frac{\partial}{\partial z} (\rho V_z) \right] = 0, \quad (1)$$

$$\rho \left[ \frac{DV_r}{Dt} - M \epsilon^2 \frac{V_\theta^2}{r} \right] = -\frac{\delta^2}{\gamma M} \frac{\partial P}{\partial r} + \frac{M \delta^2}{Re} S_r, \quad (2)$$

$$\rho \left[ \frac{DV_\theta}{Dt} + M \frac{V_r V_\theta}{r} \right] = -\frac{\delta^2}{\gamma \epsilon M} \frac{1}{r} \frac{\partial P}{\partial \theta} + \delta^2 \frac{M}{Re} S_\theta, \quad (3)$$

$$\rho \frac{DV_z}{Dt} = -\frac{1}{\gamma M} \frac{\partial P}{\partial z} + \delta^2 \frac{M}{Re} S_z \quad (4)$$

$$\rho C_V \frac{DT}{Dt} = -M(\gamma - 1) P \nabla \cdot \bar{V} + \frac{M^3(\gamma - 1)\gamma}{Re} \Phi + \frac{M \delta^2}{Pr Re} \nabla \cdot (\kappa \nabla T), \quad (5)$$

$$P = \rho T, \quad (6)$$

where

$$\nabla \cdot \bar{V} = \frac{\partial V_r}{\partial r} + \frac{V_r}{r} + \frac{\epsilon}{r} \frac{\partial V_\theta}{\partial \theta} + \frac{\partial V_z}{\partial z},$$

$$\frac{D}{Dt} = \frac{\partial}{\partial t} + M \left( V_r \frac{\partial}{\partial r} + \epsilon \frac{V_\theta}{r} \frac{\partial}{\partial \theta} + V_z \frac{\partial}{\partial z} \right),$$

$S_r, S_\theta, S_z$  are viscous terms, and  $\Phi$  is the dissipation function. Equations (1)–(6) are non-dimensionalized using the following definitions:

$$V_r = \frac{V'_r}{V'_{r0}}, \quad V_\theta = \frac{V'_\theta}{V'_{\theta0}}, \quad V_z = \frac{V'_z}{V'_{z0}},$$

$$\rho = \frac{\rho'}{\rho'_0}, \quad P = \frac{P'}{P'_0}, \quad T = \frac{T'}{T'_0}, \quad \mu = \frac{\mu'}{\mu'_0}, \quad C_V = \frac{C'_V}{C'_{V0}},$$

$$r = \frac{r'}{R'}, \quad z = \frac{z'}{L'}, \quad t = \frac{t'}{t'_a}, \quad \kappa = \frac{\kappa'}{\kappa'_0},$$

where  $P'_0$  is the initial static pressure in the cylinder, and  $\rho'_0$  and  $T'_0$  are the density and temperature of the fluid being injected from the sidewall. The aspect ratio is given by  $\delta = \frac{L'}{R'}$ , where  $\delta \gg 1$ . The induced characteristic axial velocity and the characteristic endwall velocity disturbance  $V'_{z0}$  is defined with respect to the injection reference sidewall velocity,  $V'_{r0}$  by overall mass conservation,  $\frac{V'_{z0}}{V'_{r0}} = \delta$ . The size of the initially unknown reference azimuthal velocity  $V'_{\theta0}$  is related to  $V'_{r0}$  by  $\frac{V'_{\theta0}}{V'_{r0}} = \epsilon$ . Physically meaningful solution on the axis,  $r = 0$ , are found only if  $\epsilon = 1$ .

The time is non-dimensionalized using the axial acoustic time scale,  $t'_a = \frac{L'}{C'_0}$ , where  $C'_0 = (\gamma R' T'_0)^{\frac{1}{2}}$  is the speed of sound,  $R'$  is the gas constant, and  $\gamma$  is the ratio of specific heats. The thermal diffusivity, viscosity, and specific heat for constant volume,  $\kappa'_0, \mu'_0$ , and  $C'_{V0}$  are characteristic properties of the injected fluid. Also the Reynolds number, Prandtl number, and Mach number are defined as

$$Re = \frac{\rho' V'_{z0} L'}{\mu'_0}, \quad Pr = \frac{\mu'_0 C'_{V0}}{\kappa'_0}, \quad M = \frac{V'_{z0}}{C'_0},$$

where  $Re \gg 1, M \ll 1$ , and  $Pr = O(1)$ .

Initially, a steady flow is generated by the sidewall injection,  $V_r = -1$ . At  $t = 0^+$ , the endwall begins oscillating with the non-dimensionalized sinusoidal axial velocity,  $V_z = F(r, \theta) \sin \omega t$ .

The full boundary conditions are:

$$z = 0; \quad V_z = F(r, \theta) \sin \omega t, \quad t > 0, \quad (7)$$

$$z = 1; \quad P = 1, \quad (8)$$

$$r = 0; \quad P, \rho, T, V_z, V_\theta, V_r \text{ finite}, \quad (9)$$

$$r = 1; \quad V_r = -1, \quad (10)$$

$$r = 1; \quad V_z = V_\theta = 0, \quad (11)$$

and solutions must be periodic in  $\theta$ .

In general, solutions to (1)–(6), with boundary conditions (7)–(11), are found in terms of the dependent variables, written as  $(V_r, V_\theta, V_z, P, \rho, T) = (V_{rs}, V_{\theta s}, V_{zs}, P_s, \rho_s, T_s) + (\tilde{V}_r, \tilde{V}_\theta, \tilde{V}_z, \tilde{P}, \tilde{\rho}, \tilde{T})$ , where the subscript "s" represents the steady part of the flow and ( $\tilde{\phantom{x}}$ ) represents the unsteady flow. The steady parts of the solutions satisfy the endwall condition  $V_z = 0$  at  $z = 0$  for  $t \leq 0$ . As a result of the axisymmetric boundary conditions, the steady solution is axisymmetric.

The steady variables are expanded as

$$(V_{rs}, V_{\theta s}, V_{zs}) \sim \sum_{i=0} M^i (V_{ris}, V_{\theta is}, V_{zis})$$

$$(P_s, \rho_s, T_s) \sim 1 + \sum_{i=0} M^{i+2} (P_{is}, \rho_{is}, T_{is})$$

for the limit  $M \rightarrow 0$ .

The solutions to the first order steady equations,

$$V_{r0s} = -\frac{1}{r} \sin\left(\frac{\pi}{2} r^2\right) \quad (12)$$

$$V_{\theta0s} = 0 \quad (13)$$

$$V_{z0s} = \pi z \cos\left(\frac{\pi}{2} r^2\right) \quad (14)$$

$$P_{0s} = \gamma \frac{\pi^2}{2} (1 - z^2) \quad (15)$$

are those derived by Culick<sup>2</sup>.

The initial conditions for the unsteady flow are given by the steady solution profiles. In terms of the unsteady variables, at  $t = 0$ ,

$$(\bar{V}_r, \bar{V}_\theta, \bar{V}_z, \bar{P}, \bar{\rho}, \bar{T}) = 0. \quad (16)$$

### Three-dimensional Unsteady Flow

The unsteady flow field is driven by the non-axisymmetric boundary condition in (7), which is a generalization of the purely time dependent disturbance considered by Zhao et. al.<sup>3</sup> Their results describe axisymmetric, co-existing acoustic and rotational flow fields where the radial extent of the vorticity depends on the magnitude of the sidewall blowing. If  $\frac{M^2 Re}{\delta^2} \ll 1$  a purely acoustic core can be described away from the sidewall. A viscous transition layer containing vorticity is present adjacent to the sidewall, thicker than a traditional acoustic boundary layer, but small compared to the cylinder radius. The transition layer is described by two length scales. The smaller is on the order of the radial distance traveled by an injected fluid particle during one period of oscillation of the endwall velocity and the larger is a viscous damping length.

If  $\frac{M^2 Re}{\delta^2} \sim O(1)$ , then the transition layer grows to fill the entire cylinder. For this parameter regime, no purely acoustic core exists as in the previous case. Instead, distinct acoustic (irrotational) and rotational flows co-exist. Acoustic waves driven by the endwall disturbance interact inviscidly with fluid injected from the wall to create vorticity. Subsequently, the rotational flow is convected into the cylinder by the injected flow field. Weak viscosity diffuses the vorticity on a short radial length scale,  $O(MR')$  and weak nonlinear effects alter the flow in the axial direction. The Zhao et. al.<sup>3</sup> results are valid for  $0 \leq z \leq 1$ . A numerical solution for a related problem is given by Kirkkopru et. al.<sup>4</sup>

For the present work, the condition  $\frac{M^2 Re}{\delta^2} \ll 1$  is used, and we expect a sidewall transition layer as in Zhao et. al.<sup>3</sup>

#### Core Flow: Region I

Certain essential results of Zhao et. al.<sup>3</sup> are red-erived from the three-dimensional equations. If the velocities and thermodynamic variables in region I are expanded as

$$\begin{aligned} (V_r, V_\theta, V_z) &\sim (V_{r0s}, V_{\theta0s}, V_{z0s}) \\ &+ \sum_{i=0} M^i (\bar{V}_{ri}, \bar{V}_{\theta i}, \bar{V}_{zi}), \quad (17) \\ (P, \rho, T) &\sim 1 + \sum_{i=0} M^{i+1} (\bar{P}_i, \bar{\rho}_i, \bar{T}_i) \end{aligned}$$

then the leading order equations can be found in a manner similar to that of Zhao et. al.,<sup>3</sup>. The leading order acoustic solutions are found by substituting (17) into (1)–(6). It follows from the limit,  $M \rightarrow 0$ , with the hard blowing condition,  $\frac{\delta^2}{Re} \ll 1$ , and the large aspect ratio assumption,  $\delta \gg 1$  that the acoustic core equations have the form,

$$\frac{\partial \bar{\rho}_0}{\partial t} = -\frac{\partial \bar{V}_{z0}}{\partial z}, \quad (18)$$

$$\bar{P}_0 = \bar{P}_0(z, t), \quad (19)$$

$$\frac{\partial \bar{V}_{z0}}{\partial t} = -\frac{1}{\gamma} \frac{\partial \bar{P}_0}{\partial z}, \quad (20)$$

$$\frac{\partial \bar{T}_0}{\partial t} = \frac{\gamma - 1}{\gamma} \frac{\partial \bar{P}_0}{\partial t}, \quad (21)$$

$$\bar{P}_0 = \bar{\rho}_0 + \bar{T}_0. \quad (22)$$

Equation (19) arises because the radial and azimuthal pressure gradients are vanishingly small in the chosen limit. The large aspect ratio condition causes the pressure in (19) to vary only in the axial direction. This is consistent with the acoustic core of the solution found in Zhao et. al.<sup>3</sup>. One can combine (19) with boundary conditions on  $r = 1$ ;  $\bar{V}_{r0} = 0$  and  $\bar{V}_{\theta0} = 0$ , to show that the radial and azimuthal velocities are zero. The injection boundary condition,  $V_r = -1$  at  $r = 1$  is satisfied by the steady solution cited in (12). Equations (18)–(22) yield the familiar wave equation:

$$\frac{\partial^2 \bar{V}_{z0}}{\partial t^2} = \frac{\partial^2 \bar{V}_{z0}}{\partial z^2}. \quad (23)$$

The solution to this equation will consist only of planar acoustic waves in the  $z$  direction due to the form of  $\bar{P}_0$  in (19) and  $\bar{V}_{z0}$  in (20). This equation is valid away from the endwall, where the oscillating  $r$ -, and  $\theta$ -dependent endwall condition, (7) is imposed and away from the sidewall where the no-slip boundary condition in (11) prevails. It appears that a region (denoted by  $\Pi$  in Figure 2) near the endwall,  $z = 0$ , must exist where a transition occurs from a three-dimensional to a one-dimensional flow. One must find the appropriately scaled axial variable in the transitional layer.

## Endwall Core: Region II

The radial and azimuthal pressure gradients, lost in the limiting form of the momentum equations in region I, can be restored by using the following rescaled variables,

$$\begin{aligned} z &= \frac{1}{\delta} \hat{z}, \\ P &= 1 + M \bar{P}_{00}(t) + \frac{M}{\delta} \hat{P}_0, \\ V_r &= V_{r0s} + \delta \hat{V}_{r0}, \\ V_\theta &= V_{\theta 0s} + \delta \hat{V}_{\theta 0}, \\ V_z &= V_{z0s} + \hat{V}_{z0} \end{aligned} \quad (24)$$

in order to get physically meaningful equations in the limit  $M \rightarrow 0$ . The  $(\hat{\cdot})$  denote variables in region II, and the  $\bar{P}_{00}(t)$  term is needed to obtain a proper matching of the pressures in regions I and II. The above expansions can be used in (1)–(4), to find the first order unsteady equations:

$$0 = \frac{1}{r} \frac{\partial}{\partial r} (r \hat{V}_{r0}) + \frac{1}{\epsilon r} \frac{\partial \hat{V}_{\theta 0}}{\partial \theta} + \frac{\partial \hat{V}_{z0}}{\partial \hat{z}}, \quad (25)$$

$$-\frac{1}{\gamma} \frac{\partial \hat{P}_0}{\partial r} = \frac{\partial \hat{V}_{r0}}{\partial t}, \quad (26)$$

$$-\frac{1}{\gamma \epsilon r} \frac{\partial \hat{P}_0}{\partial \theta} = \frac{\partial \hat{V}_{\theta 0}}{\partial t}, \quad (27)$$

$$-\frac{1}{\gamma} \frac{\partial \hat{P}_0}{\partial \hat{z}} = \frac{\partial \hat{V}_{z0}}{\partial t}, \quad (28)$$

in the limit,  $M \rightarrow 0$ , with  $\delta \gg 1$ ,  $M\delta \ll 1$ ,  $\frac{\delta^2}{Re} \ll 1$ . The second inequality ensures that the equations are linear. The incompressible form of the continuity equation, (25) implies that acoustic propagation does not occur in region II. This means that the flow in region II responds to the imposed time-dependent axial velocity in (7), without downstream signal propagation. The result is valid for  $\omega = O(1)$  on the time scale  $t = O(1)$ .

Equations (25)–(28) can be combined to show that

$$\frac{\partial^2 \hat{P}_0}{\partial r^2} + \frac{1}{r} \frac{\partial \hat{P}_0}{\partial r} + \frac{1}{r^2} \frac{\partial^2 \hat{P}_0}{\partial \theta^2} + \frac{\partial^2 \hat{P}_0}{\partial \hat{z}^2} = 0. \quad (29)$$

The boundary conditions:

$$\hat{z} = 0; \quad \frac{\partial \hat{P}_0}{\partial \hat{z}} = -\gamma \omega F(r, \theta) \cos \omega t, \quad (30)$$

$$r = 0; \quad \hat{P}_0 \text{ finite}, \quad (31)$$

$$r = 1; \quad \frac{\partial \hat{P}_0}{\partial r} = 0, \quad (32)$$

are found from (7), (9), the unsteady component of (10), (26) and (28). In addition,  $\hat{P}_0$  must be periodic in  $\theta$ . Given that the unsteady flow in region I depends only on the axial variable, then the pressure matching condition between regions I and II implies that

$$\hat{z} \rightarrow \infty, \quad \hat{P}_0 \sim \bar{P}_0(\hat{z}, t). \quad (33)$$

This condition, (26), and (27) together with the initial condition,  $\hat{V}_{\theta 0} = \hat{V}_{r0} = 0$  at  $t = 0$ , implies that the radial and azimuthal velocities vanish as  $\hat{z} \rightarrow \infty$ . The full three dimensional time-dependent solution to (29)–(33), found using standard separation of variables techniques, is

$$\begin{aligned} \hat{P}_0(r, \theta, \hat{z}, t) &= A_0(t) - \gamma \omega \cos \omega t \left( a_{00} \hat{z} + \sum_{m=1}^{\infty} a_{m0} e^{-\mu_{m0} \hat{z}} J_0(\mu_{m0} r) + \sum_{m=1}^{\infty} \sum_{n=1}^{\infty} e^{-\mu_{mn} \hat{z}} \right. \\ &\quad \left. \times J_n(\mu_{mn} r) (a_{mn} \cos n\theta + b_{mn} \sin n\theta) \right) \end{aligned} \quad (34)$$

where

$$\begin{aligned} a_{mn} &= \lambda_{mn} \int_0^1 \int_{-\pi}^{\pi} F(r, \theta) r J_n(\mu_{mn} r) \cos n\theta \, d\theta \, dr, \\ b_{mn} &= \lambda_{mn} \int_0^1 \int_{-\pi}^{\pi} F(r, \theta) r J_n(\mu_{mn} r) \sin n\theta \, d\theta \, dr, \\ a_{m0} &= \frac{\lambda_{mn}}{2} \int_0^1 \int_{-\pi}^{\pi} F(r, \theta) r J_0(\mu_{m0} r) \, d\theta \, dr, \\ a_{00} &= \frac{1}{\pi} \int_0^1 \int_{-\pi}^{\pi} F(r, \theta) r \, d\theta \, dr, \\ \nu_{mn} &= \int_0^1 r J_n^2(\mu_{mn} r) \, dr, \end{aligned} \quad (35)$$

$\lambda_{mn} = -1/(\pi \mu_{mn} \nu_{mn})$ , and  $\mu_{mn}$  is the  $m^{\text{th}}$  zero of  $J'_n(r)$ , which is needed to satisfy (32). The first few values for  $\mu_{mn}$  are  $\mu_{m0} \approx 3.83171, 7.01559, 10.1735, \dots$ ,  $\mu_{m1} \approx 1.84118, 5.33144, 8.53632, \dots$  and  $\mu_{m2} \approx 3.05424, 6.70613, 9.96947, \dots$ . The  $\mu$ 's for larger  $n$  satisfy  $\mu_{m1} > 3$  for  $m \geq 3$ . Thus the smallest eigenvalue is 1.84118. It is noted that the terms decay quickly as  $n$  and  $m$  increase. The solution is dominated by the first few terms in (34), and

these solutions are valid for  $\omega$  not equal to any of the resonance frequencies ( $b_n = (n + \frac{1}{2})\pi$  for  $n \geq 0$ ) of the cylinder.

The function  $A_0(t)$  in (34) is as yet undetermined. It will be found when the region I solution is obtained. It may be noted from (34) that the  $r$  and  $\theta$ -dependence of  $\tilde{P}_0$  decays exponentially fast as  $\hat{z} \rightarrow \infty$ . At the edge of the transition layer,

$$P|_{\hat{z} \rightarrow \infty} \sim 1 + M\tilde{P}_{00}(t) + \frac{M}{\delta} (A_0(t) - a_{00}\hat{z}\gamma\omega \cos \omega t). \quad (36)$$

The velocities in region II are found from the pressure field in (34) using (26)–(28) and the initial condition (16),

$$\begin{aligned} \hat{V}_{z0} = \sin \omega t \left[ a_{00} - \sum_{m=1}^{\infty} a_{m0} \mu_{m0} e^{-\mu_{m0}\hat{z}} J_0(\mu_{m0}r) \right. \\ \left. - \sum_{m=1}^{\infty} \sum_{n=1}^{\infty} \mu_{mn} e^{-\mu_{mn}\hat{z}} J_n(\mu_{mn}r) \right. \\ \left. \times (a_{mn} \cos n\theta + b_{mn} \sin n\theta) \right], \quad (37) \end{aligned}$$

$$\begin{aligned} \hat{V}_{r0} = \sin \omega t \left[ \sum_{m=1}^{\infty} a_{m0} \mu_{m0} e^{-\mu_{m0}\hat{z}} J'_0(\mu_{m0}r) \right. \\ \left. + \sum_{m=1}^{\infty} \sum_{n=1}^{\infty} \mu_{mn} e^{-\mu_{mn}\hat{z}} J'_n(\mu_{mn}r) \right. \\ \left. \times (a_{mn} \cos n\theta + b_{mn} \sin n\theta) \right], \quad (38) \end{aligned}$$

$$\begin{aligned} \hat{V}_{\theta 0} = \frac{1}{\epsilon} \sin \omega t \left[ \sum_{m=1}^{\infty} \sum_{n=1}^{\infty} n e^{-\mu_{mn}\hat{z}} \frac{1}{r} J_n(\mu_{mn}r) \right. \\ \left. \times (-a_{mn} \sin n\theta + b_{mn} \cos n\theta) \right]. \quad (39) \end{aligned}$$

Here again, one may observe exponential decay of the  $r$  and  $\theta$  solution dependence as  $\hat{z} \rightarrow \infty$ . As a result, the amplitude of the axial speed at the downstream edge of the transitional layer depends on the endwall mass addition through the coefficient  $a_{00}$  defined in (35). The azimuthal and axial velocities (39) and (37) do not satisfy the no-slip condition (11). A viscous boundary layer, adjacent to the sidewall,  $r = 1$ , is considered in a fuller study of this problem.<sup>5</sup> Also, the solution does not satisfy a no-slip boundary condition on the endwall ( $z = 0$ ). A viscous layer thinner than region II must exist adjacent to

the endwall in order to satisfy the no-slip condition on the radial and azimuthal velocities. This region will not be described in the present work.

The decay of all non-axisymmetric flow occurs within region II. The dimensional length scale of the region,  $\frac{1}{\delta}L' = R'$ , is the radius of the cylinder. In the non-axisymmetric numerical calculation of Sabinis et. al.<sup>1</sup>, it is noted that the asymmetry of the flow exists in a region about two diameters upstream of the exit plane, where a non-axisymmetric pressure boundary condition is imposed. The analytical results in the present work appears to provide an explanation for the local character of the three-dimensional flow found in the numerical solution.

### Solution to the Region I Wave Equation

The solution to the acoustic flow in region I, described by (23) can now be found. The initial/boundary conditions are:

$$t = 0; \quad \tilde{V}_{z0} = \frac{\partial \tilde{V}_{z0}}{\partial t} = 0, \quad (40)$$

$$z = 1; \quad \frac{\partial \tilde{V}_{z0}}{\partial z} = 0, \quad (41)$$

A condition at  $z = 0$  comes from the matching of the solution between regions I and II. The condition is derived by taking the limit of (37) as  $\hat{z} \rightarrow \infty$ .

$$z = 0; \quad \tilde{V}_{z0} = a_{00} \sin \omega t. \quad (42)$$

The solution to (23) with (40)–(42) is:

$$\tilde{V}_{z0} = a_{00} \left[ \sin \omega t + \right. \quad (43)$$

$$\left. \sum_{n=0}^{\infty} \frac{2\omega}{b_n^2 - \omega^2} \left\{ \frac{\omega}{b_n} \sin \omega t - \sin b_n t \right\} \sin b_n z \right], \quad (44)$$

where  $b_n = (n + \frac{1}{2})\pi$ .

The coefficient  $a_{00}$  in (35) represents a non-dimensional instantaneous mass addition due to the velocity endwall condition. Waves will propagate in region I only if  $a_{00} \neq 0$ . The pressure field in region I is found by using (44), (28) and the pressure node boundary condition, (8),

$$\begin{aligned} \tilde{P}_0(z, t) = -a_{00} [(z-1)\gamma\omega \cos \omega t + \\ \sum_{n=0}^{\infty} \frac{2\gamma\omega}{b_n^2 - \omega^2} \left\{ \frac{\omega^2}{b_n^2} \cos \omega t - \cos b_n t \right\} \cos b_n z]. \quad (45) \end{aligned}$$



The pressure in region I near the edge of region II is

$$P|_{z \rightarrow 0} = 1 + Ma_{00} [\gamma\omega \cos \omega t - \sum_{n=0}^{\infty} \frac{2\gamma\omega}{b_n^2 - \omega^2} \left( \frac{\omega^2}{b_n^2} \cos \omega t - \cos b_n t \right)] - M[a_{00} z \gamma\omega \cos \omega t] + O(z^2). \quad (46)$$

The unknown function  $\bar{P}_{00}(t)$  in the expansion of  $P$  in (24) can now be found by matching the order  $M$  terms of the pressure between regions I and II, using (36) and (46)

$$\bar{P}_{00}(t) = a_{00} [\gamma\omega \cos \omega t - \sum_{n=0}^{\infty} \frac{2\gamma\omega}{b_n^2 - \omega^2} \left( \frac{\omega^2}{b_n^2} \cos \omega t - \cos b_n t \right)]. \quad (47)$$

The term  $A_0(t)$  can be found from a higher order solution in region I and matching terms at order  $\frac{M}{\delta}$ . If this is done, it is found that  $A_0(t) = 0$ .

The composite solution for the pressure can now be found using (24), (47), and (34),

$$P(r, \theta, z, t) = 1 + Ma_{00} [-(z-1)\gamma\omega \cos \omega t - \frac{2\gamma\omega}{b_n^2 - \omega^2} \left( \frac{\omega^2}{b_n^2} \cos \omega t - \cos b_n t \right) \cos b_n z] + \frac{M}{\delta} \gamma\omega \cos \omega t \left[ \sum_{n=1}^{\infty} a_{m0} e^{-\mu_{m0}\delta z} J_0(\mu_{m0}r) + \sum_{m=1}^{\infty} \sum_{n=1}^{\infty} e^{-\mu_{mn}\delta z} J_n(\mu_{mn}r) \times (a_{mn} \cos n\theta + b_{mn} \sin n\theta) \right] + O(M^2). \quad (48)$$

The results in Figures 4, 5, and 6 are computed using a 20 term truncated Taylor series of (37)–(39) for the case  $F(r, \theta) = r^2(1-r)^2 \sin^2(\frac{\theta}{2})$ , corresponding to the endwall axial velocity shown in Figure 3 at  $t = \frac{\pi}{2}$ . The series is alternating, hence the error is bounded by the coefficient of the next term, which is bounded by  $10^{-3}$ .

Figure 4 shows a two-dimensional cross-section of the velocity vector field in region II at a fixed axial location  $\hat{z} = 0.01$  for  $t = \frac{\pi}{2}$ . Only the  $r$  and  $\theta$  components of the velocities are represented and the dimensional lengths of the arrow vectors are  $V'_{z0}(\hat{V}_{\theta 0}^2 + \hat{V}_{r0}^2)^{\frac{1}{2}}$ . The flow in Figure 4 is symmetric

with respect to a horizontal diameter of the cylinder from  $\theta = 0$  to  $\theta = \pi$ , but there is flow from the left to right side of the cylinder. The source of the flow appears to be located at  $r = \frac{1}{2}$  and  $\theta = \pi$ . The source corresponds to the point of highest velocity of Figure 3. A pattern similar to the vector field of Figure 4 appears for larger  $\hat{z}$ , however with a smaller amplitude. The field is dominated by the first few terms of the Taylor series in (38) and (39), hence the amplitude of the vector field lines decrease exponentially.

Figure 5 shows an axial cross-section of the velocity vector field in region II for fixed azimuthal location  $\theta = 0$  and  $\theta = \pi$ . The variable  $y$  is defined as  $y = r$  for  $\theta = 0$  and  $y = -r$  for  $\theta = \pi$ . Only the  $r$  and  $z$  components of the velocities are shown, with the dimensional magnitude of the vector field,  $V'_{z0}(\hat{V}_{z0}^2 + \hat{V}_{r0}^2)^{\frac{1}{2}}$ . The plot in Figure 5 shows that there is flow across the centerline from the bottom to the top. There is flow across the centerline of the cylinder due to the asymmetry of the endwall velocity. The maximum velocity at the horizontal line  $y = -\frac{1}{2}$ , corresponds to the region of high velocity of the endwall condition at  $r = \frac{1}{2}$  and  $\theta = \pi$  of Figures 3 and 4.

Figure 6 shows an axial cross-section of the velocity vector field in region II for the fixed azimuthal location  $\theta = \frac{\pi}{2}$  and  $\theta = -\frac{\pi}{2}$ , perpendicular to that in Figure 5. The variable  $y$  is defined as  $y = r$  for  $\theta = \frac{\pi}{2}$  and  $y = -r$  for  $\theta = -\frac{\pi}{2}$ . As with the results in Figure 5, only the  $r$  and  $z$  components of the velocities are shown, and the dimensional magnitude is the same. However, since the length of the lines in each figure is scaled to the maximum cross-sectional velocity, the absolute magnitude of the velocity fields in Figures 5 and 6 are different. The symmetry of the vector field across the centerline at  $y = 0$  is due to the symmetry of the endwall condition. As with the results in Figure 5, the vector field near the line  $\hat{z} = 1$ , is composed essentially of an axial velocity because the radial and azimuthal velocities have decayed away exponentially fast.

## II Turbulence Characteristics of Solid Rocket Motor Flow

Kirkkopru et. al.<sup>4</sup> describe a computational model for high Reynolds number flow in a cylinder with transient sidewall mass addition. The parabolized Navier-Stokes equations are solved using a 4th-order accurate MacCormack scheme to predict transient



flow characteristics driven by a harmonically varying, positive wall injection speed that varies in the axial direction. In particular, the solution is used to study the generation and evolution of intense transient vorticity in the flow field, arising from an acoustic wave interaction with the fluid leaving the porous surface.

The complete axial velocity is divided into the numerical analogues of the steady Culick<sup>2</sup> profile, and of the transient responses for the co-existing, equal magnitude acoustic and rotational flow fields discussed by Zhao.<sup>6</sup> The latter is used to describe the time-varying spatial distribution of vorticity in the cylinder. It is shown that the radial gradients of vorticity occur on a length scale ( $MR'$ ), where the Mach number  $M \ll 1$ .

Asymptotic methods (Zhao<sup>6</sup>, Zhao and Kassoy<sup>7</sup>, and Zhao et. al.<sup>3</sup>), have been used to show that the flow physics are only weakly viscous. Irrotational acoustic disturbances arise from the transient sidewall injection. The vorticity is generated by an inviscid interaction between the acoustic waves and fluid exiting the sidewall and convected into the cylinder by the radial component of the injection velocity field. The only role of viscosity is to diffuse the vorticity on the short  $O(MR')$  length scale.

High Reynolds number and low Mach number internal flows driven by injection, described either by asymptotic or numerical solutions, have several features in common with a turbulent flow field. They are essentially transient, primarily inviscid and contain vorticity distributions that have a length scale small compared to the overall geometry. In this sense, it is illustrative to examine the relationship between results obtained from traditional studies of turbulence in injection driven tubes and channels, and those found in our direct numerical simulations.

Liou and Lien<sup>8</sup>, hereafter L&L, summarize many important contributions to chamber flow turbulence modeling, based on  $k-\epsilon$ ,  $k-\omega$  and full Reynolds stress methods. In general, the modeling results over predict turbulence levels and are not very successful in predicting the radial location of the turbulent intensity peak. It is suggested that Navier-Stokes based DNS's require far fewer assumptions about the turbulence properties of the injected fluid and may give more accurate representations of the turbulent properties of the flow.

The L&L DNS calculations for flow in a large aspect ratio channel are carried out for an injection speed,  $v'_w = O(1 \text{ m./s.})$ , and an axial Reynolds num-

ber,  $Re = O(10^6)$ . The axial Mach number in the downstream half of the channel takes on significant subsonic values. The calculations are run for about 15 axial acoustic time scales. Comparisons of mean flow and turbulent intensity predictions with experiments appear to be better than those of the traditional turbulence models. The results are significantly affected by compressibility particularly in the downstream portion of the flow. The turbulent intensity shows a single peak across the channel, with the location of the peak moving toward the sidewall with increasing downstream location. It is recognized that such an effect may enhance erosive burning on the downstream section of a solid propellant.

Linear stability theory for a channel with sidewall injection has been studied by Varapaev and Yagodkin<sup>9</sup>. They find that for a specified injection Reynolds number  $Re_s$ , based on the channel width and wall injection speed, disturbances will grow when the axial Reynolds number  $Re_c$ , based on the center-line speed and the channel width, reaches a critical value. This is interpreted to mean that for a given  $Re_s$ , instability will occur in a sufficiently long duct.

Transition of the mean flow profile from a laminar to a turbulent shape occurs even further downstream, meaning a larger value of  $Re_c$ . Beddini<sup>10</sup> summarizes experimental results from numerous sources to show that the transition process occurs over a distance that is invariant to the value of the injection Reynolds number when  $Re_s > 100$ . His computational model drives the turbulence with a prescribed value of the RMS injection velocity fluctuation at the porous surface. Predictions for axial location of a fully turbulent profile, identified from a study of the momentum-flux coefficient variation with axial location, can be made compatible with experiments if appropriate magnitudes of the RMS value are employed. L&L indicate that such values have not been related to conditions in relevant experiments.

The DNS reported here is for a cylindrical geometry, and is based on the parabolized Navier-Stokes equations with an imposed sidewall injection speed  $V_w = -1 - 0.4 \cos(\frac{\pi x}{2})(1 - \cos(\omega t))$ . The parameter values are  $Re = 4 \times 10^5$ ,  $M = 0.02$ ,  $\delta = 20$ . The predicted flow contains co-existing, equal amplitude acoustics and vorticity, and a pressure disturbance field that is between 1% and 10% of the reference static pressure. A methodology borrowed from the asymptotic analyses is employed to separate the two

transient flow fields. Hence, one can consider the contribution of acoustics alone, the vorticity alone and the explicit interaction between the two flow fields. This separation enables us to differentiate the RMS values associated with the acoustic field from those of the rotational field, not possible in a more traditional turbulence study.

The parameter values for the Reynolds and Mach number cited above can be reinterpreted in terms of the injection and axial Reynolds numbers used in the stability and transition literature. In particular the former  $Re_s \approx 2.5 \times 10^3$  and the latter  $Re_c \approx 5 \times 10^4$ . This point on the stability diagram lies above the neutral stability line but below the region for which a fully transitioned mean flow can be expected. Our aspect ratio of twenty is not large enough to enable a fully turbulent mean flow to develop in the cylinder. It is also noted that the analogue to the RMS injection velocity fluctuation used by Beddini varies between 0.343 and zero as one moves from the head-end to the exit of the cylinder. This variation occurs because the time-dependent part of the injection distribution, cited above, varies in the axial direction.

A comparison of the time-averaged mean flow ( $\langle V_z \rangle$ ) and instantaneous axial velocity ( $V_z - \langle V_z \rangle$ ) profiles for  $Re = 4 \times 10^4$ ,  $M = 0.02$  and an aspect ratio of 20 is shown in Figure 7. The results are given at four axial locations for  $t = 30$ . The smooth shape of the mean flow does not hint at the spatial variations present in the instantaneous profiles. In particular, the relatively large wall gradient in the latter is not reflected in the former. Similar results at other values of time show that the instantaneous wall gradient fluctuates between positive and negative values. In this sense, the mean flow wall gradient may not be a useful measure of the "scouring" effect arising from a time dependent, rapidly varying wall shear stress on the fizz-foam surface layer of a decomposing solid propellant.

Figure 8 shows the distribution of the RMS fluctuation intensity for the axial velocity in the cylinder, where  $V_z = \langle V_z \rangle + u'_p + u'_v$ ,  $u'_p$  is the acoustic fluctuation and  $u'_v$  is the rotational fluctuation. The axial fluctuation intensity can be decomposed into three parts: pure acoustics, acoustic-rotational interaction, and pure rotational. The ramp-like surface near  $r = 0$  shows the contribution from the pure acoustics alone, since the vorticity generated at the sidewall has not yet reached the centerline when  $t = 30$ . One notes several local peaks across the radius, with the largest value near the sidewall.

In general, the amplitude increases, and the local peaks move toward the sidewall with increasing axial distance downstream. The single peak results described in L&L are qualitatively similar. Our multiple peaks arise from vorticity generation driven by axial acoustic waves in the cylinder. The latter may not be present in any of the turbulence models discussed in L&L or in the DNS discussed there.

The contribution from the pure rotational effect is shown in Figure 9 where the surface is less wrinkled than Figure 8. The rotational fluctuation intensity is larger near the sidewall and the exit. Contributions from the acoustic-rotational interaction effect and the pure rotational effect, of similar magnitude, are responsible for the corrugated surface in Figure 8.

The fluctuation intensity of the radial velocity is shown in Figure 10. The radial fluctuation is larger near the sidewall and closed endwall where the sidewall injection is stronger. The radial fluctuation intensity is smaller in magnitude than axial fluctuation intensity as predicted in a theory by Zhao<sup>6</sup>.

Results of the kind described here may help to identify high heat transfer and erosional burning locations in motor chambers. An understanding of oscillatory, intense axial shear stress on the sidewall will be useful for developing physically viable boundary conditions at the decomposing interface of a burning solid propellant. The idea here is account for the "scouring" effect of oscillatory shear stress on the fizz-foam zone thought to exist at the gas-propellant interface. Although the axial velocity in the combustion zone may be small, the results of these coldflow studies suggest that the velocity gradient will be relatively large, and hence can be a source of axial deformation, and perhaps stripping of easily deformable surface material.

## References

1. Sabnis, J. S., Gibeling, H. J., and McDonald, H. 1989, Navier-Stokes Analysis of Solid Propellant Rocket Motor Internal Flows, *J. Prop. Power*, 5, 657-664.
2. Culick, F.E.C., 1966, Rotational Axisymmetric Mean Flow and Damping of Acoustic Waves in Solid Propellant Rocket Motors, *AIAA J.*, 4, 1462-1464.
3. Zhao, Q., Kassoy, D. R., Kirkkopru, 1996, Acoustically Generated Vorticity in an Internal Flow, submitted, *J. Fluid Mech.*

4. Kirkkopru, K., Kassoy, D. R., and Zhao, Q. 1996, Unsteady Vorticity Generation and Evolution in a Model of a Solid Rocket Motor, *J. Prop. Power*, **12**, 646-654.
5. Staab, P. L., *Ph.D. Thesis*, in progress, 1996.
6. Zhao, Q. 1994, *Ph.D. Thesis*, Dept. of Mechanical Engineering, University of Colorado at Boulder.
7. Zhao, Q. and Kassoy, D.R., 1994, The Generation and Evolution of Unsteady Vorticity in a Solid Rocket Engine Chamber, *AIAA 94-0779*, 32nd Aerospace Sciences Meeting,.
8. Liou and Lien(1995) Liou, T-M. and Lien, W-Y., 1995, Numerical Simulations of Injection-Driven Flows in a Two-Dimensional Nozzleless Solid-Rocket Motor, *J. Prop. Power*, **11**, 600-605.
9. Varapaev, V.N. and Yagodkin, V.I., 1969, Flow Stability in a Channel With Porous Walls, *Izv. A. N. SSSR, Mekhanika Zhidkosti i Gaza*, **4**, 91-95.
10. Beddini, R. A. 1986, Injection-Induced Flows in Porous Walled Ducts, *AIAA J.*, **24**, 1766-1773.

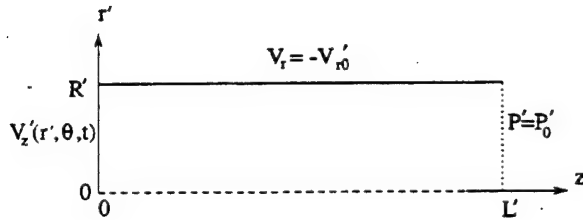


Figure 1: A radial cut through a cylinder of length  $L'$  and radius  $R'$ . There is a  $(r', \theta, t')$ -dependent axial velocity disturbance at the endwall  $z' = 0$ . A pressure node is imposed at the open end,  $z' = L'$ . On the sidewall  $r' = R'$ , fluid is injected at a constant speed  $V_{r0}'$ . The aspect ratio is  $\delta = \frac{L'}{R'} \gg 1$ .

II Inviscid, Incompressible, Irrotational	I: Core (Acoustic Waves) + Rotational Flow Transition Layer or Chamber Filled Vorticity
--	--

$z = 0$

$z = 1$

Figure 2: The regions of the cylindrical vessel investigated in this work. Zhao et. al. studied region I. This region is characterized by co-existing rotational and planar acoustic flow. Regions II and III are studied here.

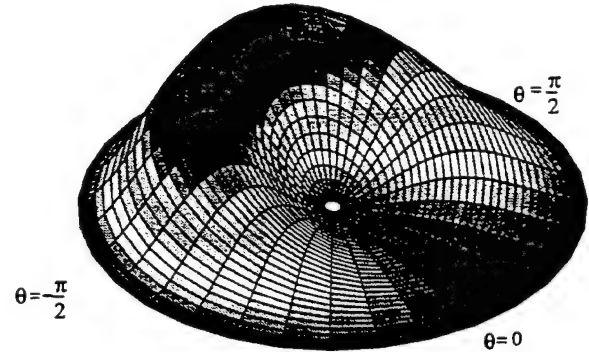


Figure 3: Example endwall condition with  $V_z = r^2(1-r)^2 \sin^2(\frac{\theta}{2}) \sin \omega t$ , with  $\omega = 1$  at  $t = \frac{\pi}{2}$ .

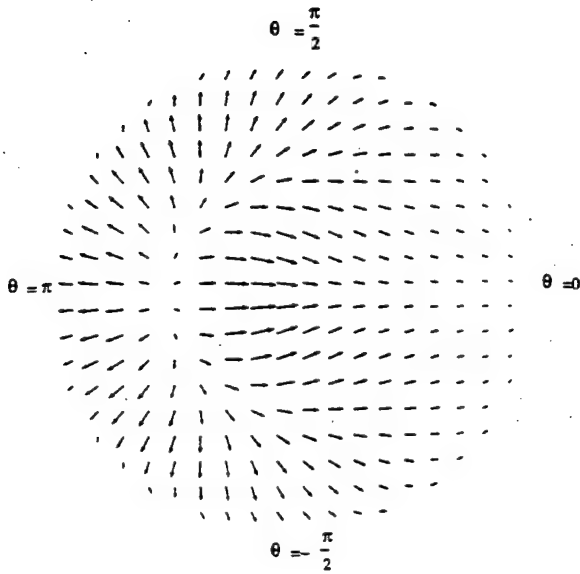


Figure 4: Two-dimensional vector field plot showing only the radial and azimuthal velocities. The cross-section is taken along the plane  $\hat{z} = 0.01$  and for the endwall velocity condition:  $V_z = r^2(1-r)^2 \sin^2(\frac{\theta}{2}) \sin \omega t$  and for  $\omega = 1$  when  $t = \frac{\pi}{2}$ . The symmetry about a line connecting  $\theta = 0$  and  $\theta = \pi$ , corresponds to the symmetry in the endwall velocity condition. There is net flow from the left to right side of the line connecting  $\theta = \frac{\pi}{2}$  and  $\theta = -\frac{\pi}{2}$ .

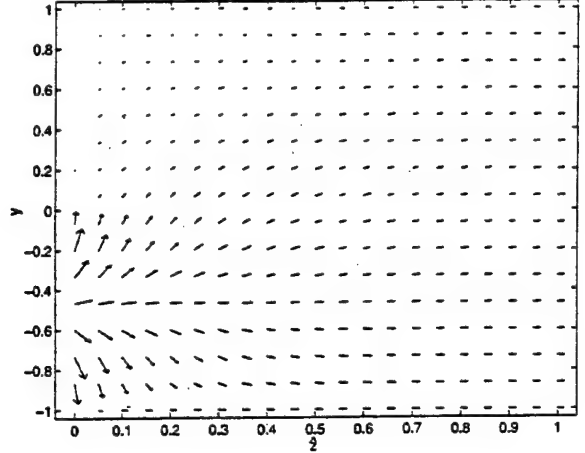


Figure 5: Two-dimensional vector field plot showing only the radial and axial velocities. The cross-section is taken axially with  $\theta = 0$ , (for values  $y > 0$ ,  $y = r$ ), and  $\theta = \pi$ , (for values  $y < 0$ ,  $y = -r$ ). The endwall velocity condition, as in Figure 4 is  $V_z = r^2(1-r)^2 \sin^2(\frac{\theta}{2}) \sin \omega t$ , for  $\omega = 1$  and  $t = \frac{\pi}{2}$ . There is net flow from the bottom to the top of the plot, representing flow across the centerline. The region of high velocity near  $y = -0.5$  is due to the high flow region at  $\theta = \pi$  and  $r = \frac{1}{2}$  of Figure 3. The flow near  $\hat{z} = 1$  is nearly planar.

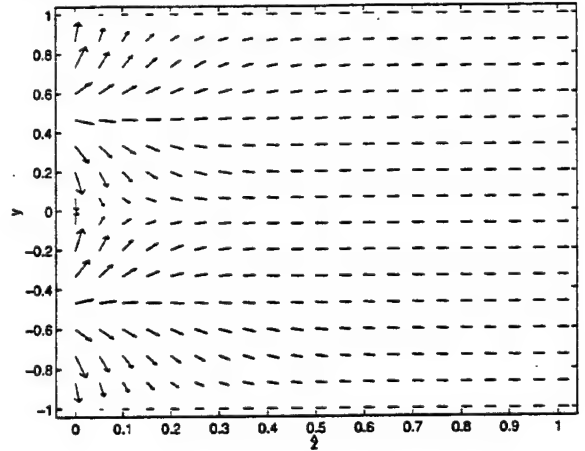


Figure 6: Two-dimensional vector field plot showing only the radial and axial velocities. The cross-section shown is for  $\theta = -\frac{\pi}{2}$ , ( $y < 0$ ,  $y = -r$ ), and  $\theta = \frac{\pi}{2}$ , ( $y > 0$ ,  $y = r$ ). Again, the endwall velocity condition used is  $V_z = r^2(1-r)^2 \sin^2(\frac{\theta}{2}) \sin \omega t$ , for  $\omega = 1$  and  $t = \frac{\pi}{2}$ . The symmetry with respect to the centerline in this plot is due to the symmetry of the endwall velocity condition in Figure 3. The flow near  $\hat{z} = 1$  is nearly planar.

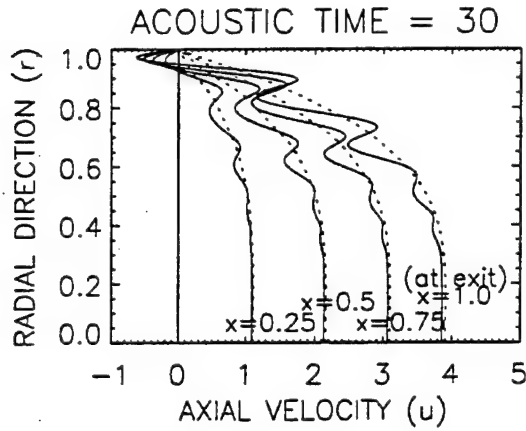


Figure 7: A radial profile of axial velocity at four different axial locations. The dotted lines are mean velocity and the solid lines are instantaneous velocity. The sidewall is at  $r = 1$  and the centerline is at  $r = 0$ . The closed endwall and the exit are located at  $x = 0$  and  $x = 1$ , respectively. Parameter values are  $Re = 4 \times 10^5$ ,  $M = 0.02$ ,  $\omega = 1$ , and  $\delta = 20$ .

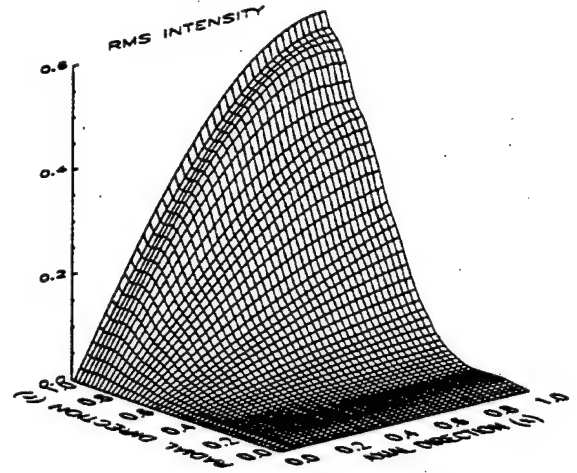


Figure 9: The pure rotational part of RMS axial velocity fluctuation,  $[(u'_v u'_v)]^{1/2}$ .

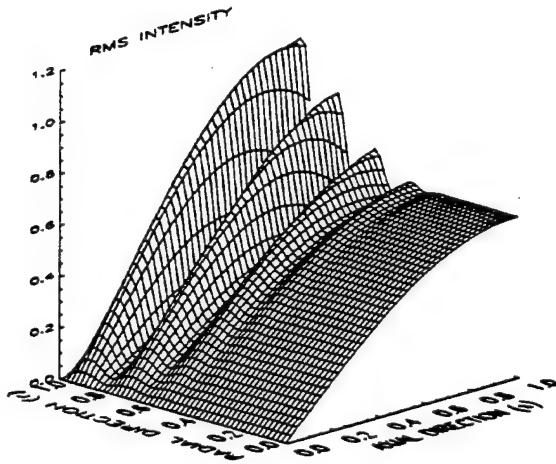


Figure 8: RMS axial velocity fluctuation intensities defined as  $[(\langle u'_p + u'_v \rangle)(\langle u'_p + u'_v \rangle)]^{1/2} = [\langle u'_p u'_p \rangle + 2\langle u'_p u'_v \rangle + \langle u'_v u'_v \rangle]^{1/2}$ , where  $u'_p$  is the pure acoustic fluctuation velocity,  $u'_v$  is the pure rotational fluctuation velocity, and  $\langle \rangle$  denotes the time averaging.

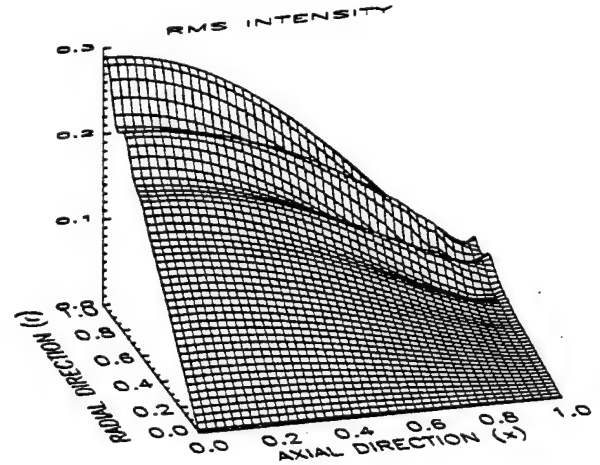


Figure 10: RMS radial velocity fluctuation intensity defined as  $[(\langle v' v' \rangle)]^{1/2}$  where  $v'$  is the radial velocity fluctuation.

# Three-Dimensional, Unsteady, Acoustic-Shear Flow Dynamics in a Cylinder with Sidewall Mass Addition

P. L. Staab\* and D. R. Kassoy†

Three-dimensional internal flow dynamics are studied in a cylinder with mass injection from the sidewall. A time-dependent, harmonic, non-axisymmetric axial velocity disturbance is imposed on the endwall of the cylinder to create a non-axisymmetric velocity field. An asymptotic analysis is used to reduce the Navier-Stokes equations to more elementary forms in two regions adjacent to the endwall with distinct physical characteristics: an incompressible, inviscid and irrotational core near the endwall, and an incompressible viscous boundary layer containing all three components of vorticity adjacent to the sidewall. Solutions to these equations for disturbance frequencies associated with the lowest order axial acoustic modes show that the non-axisymmetric nature of the flow is confined to the core region adjacent to the endwall with a characteristic axial dimension on the order of the cylinder radius. Within the region, axial, radial, and azimuthal velocities exist. These non-axisymmetric effects decay exponentially fast so that only axisymmetric acoustic modes exist further downstream. These results are valid for driving frequencies below the "cut-off" value that one would find in a duct.

---

\*Graduate Student, Department of Applied Mathematics, CB-526, University of Colorado, Boulder, CO 80309.

†Professor. Mechanical Engineering Department, CB-427, University of Colorado, Boulder, CO 80309.

## I. INTRODUCTION

Internal flow dynamics in a cylinder with mass addition from the sidewall are studied as an analogue to flows within solid fuel rocket motors. Mass addition models the gasification of burning propellant in the rocket motor.

Most previous modeling, whether analytical, numerical or experimental, has employed axisymmetry to simplify the problem. Experimental work by Brown et al. [1] is based on axisymmetric oscillatory wave motion and mean flow response. Smith et al. [2], employ numerical techniques to model the experiments of Brown. Baum [3], and Vuillot and Avalon [4] also use numerical methods to investigate acoustic wave processes and flow dynamics in an axisymmetric internal flow. Beddini [5], develops computational solutions for a turbulence model of an internal flow in a symmetric duct with sidewall injection.

Culick's [6] linear stability analysis for three-dimensional disturbances does not provide specific non-axisymmetric flow results. Sabnis et al. [7] use numerical experiments to describe turbulent axisymmetric and non-axisymmetric flows. One example includes an azimuthally and radially dependent boundary condition on a cylinder cross-section, used to force non-axisymmetric flow in a portion of the internal flow. The computational results show that the flow becomes fully axisymmetric within an axial distance of about two diameters away from the plane on which the boundary condition is imposed.

The work presented here is an extension of Zhao [8] and Zhao et al. [9] These papers contain asymptotic analyses for the axisymmetric Navier-Stokes equations that describe low Mach number, high Reynolds number and high aspect ratio flows with acoustic waves and vorticity. In the present work a study is made of non-axisymmetric flow in a region adjacent to the closed endwall of the cylinder where a radially and azimuthally-dependent, harmonically-varying velocity boundary condition is imposed. The driving frequency is on the order of the inverse of the axial acoustic time scale,  $t'_A = L'/C'_0$ , where  $L'$  is the length of the cylinder and  $C'_0$  is the reference speed of sound. Radial and azimuthal velocities are found



to vanish exponentially fast in the downstream direction within the core zone adjacent to the endwall, with a characteristic axial dimension measured by the cylinder radius  $R'$ . Hence, axisymmetric flow persists in most of the cylinder. A thinner inviscid layer is needed for the solution to satisfy the no-slip condition on the endwall. These results provide an analytical explanation of those found from computational analysis by Sabnis et al. [7] Non-axisymmetric flow near the endwall contains cross-sectional velocity patterns that include flow across the cylinder axis. A viscous boundary layer adjacent to the sidewall and near the endwall is studied to find the transition between the transient core flow and the no-slip condition on the sidewall. It is found, as in Zhao et al. [9], that the azimuthal component of the vorticity is proportional to the inverse of the Mach number. In addition, the axial component of the vorticity driven by the non-axisymmetric boundary condition at the endwall is also found to be proportional to the the inverse of the Mach number.

## II. FORMULATION OF THE PROBLEM

The objective of the present work is to model a wall injected, semi-confined internal flow driven by a non-axisymmetric, time-dependent velocity disturbance on the closed upstream endwall. The flow occurs in a cylinder of length  $L'$ , and radius  $R'$ , with a pressure node at the open end as shown in Figure 1. Fluid is injected steadily through the sidewall with a characteristic velocity  $V'_{r0}$  and induces an axial flow characterized by  $V'_{z0}$ . The imposed axial velocity on the endwall also has a characteristic velocity  $V'_{z0}$ . The mathematical model is based on the following non-dimensional Navier-Stokes equations:

$$\begin{aligned} \frac{\partial \rho}{\partial t} + M \left[ \frac{1}{r} \frac{\partial}{\partial r} (r \rho V_r) + \epsilon \frac{1}{r} \frac{\partial}{\partial \theta} (\rho V_\theta) + \frac{\partial}{\partial z} (\rho V_z) \right] &= 0, \\ \rho \left[ \frac{DV_r}{Dt} - M \epsilon^2 \frac{V_\theta^2}{r} \right] &= -\frac{\delta^2}{\gamma M} \frac{\partial P}{\partial r} + \frac{M \delta^2}{Re} \left\{ 2 \frac{\partial}{\partial r} \left[ \mu \left( \frac{\partial V_r}{\partial r} - \frac{1}{3} \nabla \cdot \bar{\mathbf{V}} \right) \right] \right. \\ &\quad \left. + \frac{1}{r} \frac{\partial}{\partial \theta} \left[ \mu \left( \frac{1}{r} \frac{\partial V_r}{\partial \theta} + \epsilon \frac{\partial V_\theta}{\partial r} - \epsilon \frac{V_\theta}{r} \right) \right] \right\} \end{aligned} \quad (1)$$



$$+ \frac{\partial}{\partial z} \left[ \mu \left( \frac{1}{\delta^2} \frac{\partial V_r}{\partial z} + \frac{\partial V_z}{\partial r} \right) \right] + 2 \frac{\mu}{r} \left[ \frac{\partial V_r}{\partial r} - \frac{\epsilon}{r} \frac{\partial V_\theta}{\partial \theta} - \frac{V_r}{r} \right] \Big\}, \quad (2)$$

$$\begin{aligned} \rho \left[ \frac{DV_\theta}{Dt} + M \frac{V_r V_\theta}{r} \right] = & - \frac{\delta^2}{\gamma \epsilon M} \frac{1}{r} \frac{\partial P}{\partial \theta} + \frac{M \delta^2}{Re \epsilon} \left\{ 2 \frac{\partial}{\partial \theta} \left[ \mu \left( \frac{\epsilon}{r} \frac{\partial V_\theta}{\partial \theta} - \frac{1}{3} \nabla \cdot \bar{\mathbf{V}} \right) \right] \right. \\ & + \frac{\partial}{\partial z} \left[ \mu \left( \frac{1}{r} \frac{\partial V_z}{\partial \theta} + \frac{\epsilon}{\delta^2} \frac{\partial V_\theta}{\partial z} \right) \right] + \frac{\partial}{\partial r} \left[ \mu \left( \frac{1}{r} \frac{\partial V_r}{\partial \theta} + \epsilon \frac{\partial V_\theta}{\partial r} - \epsilon \frac{V_\theta}{r} \right) \right] \\ & \left. + \frac{\mu}{r} \left[ \frac{1}{r} \frac{\partial V_r}{\partial \theta} + \epsilon \frac{\partial V_\theta}{\partial r} - \epsilon \frac{V_\theta}{r} \right] \right\}, \end{aligned} \quad (3)$$

$$\begin{aligned} \rho \frac{DV_z}{Dt} = & - \frac{1}{\gamma M} \frac{\partial P}{\partial z} + 2 \frac{M}{Re} \frac{\partial}{\partial z} \left[ \mu \left( \frac{\partial V_z}{\partial z} - \frac{1}{3} \nabla \cdot \bar{\mathbf{V}} \right) \right] \\ & + \delta^2 \frac{M}{Re} \left\{ \frac{1}{r} \frac{\partial}{\partial r} \left[ \mu \left( \frac{1}{\delta^2} \frac{\partial V_r}{\partial z} + \frac{\partial V_z}{\partial r} \right) \right] \right. \\ & \left. + \frac{1}{r} \frac{\partial}{\partial \theta} \left[ \mu \left( \frac{1}{r} \frac{\partial V_z}{\partial \theta} + \frac{\epsilon}{\delta^2} \frac{\partial V_\theta}{\partial z} \right) \right] \right\}, \end{aligned} \quad (4)$$

$$\begin{aligned} \rho C_V \frac{DT}{Dt} = & -M(\gamma-1)P \nabla \cdot \bar{\mathbf{V}} + \frac{M^3(\gamma-1)\gamma}{Re} \Phi \\ & + \frac{M}{Pr Re} \left[ \frac{1}{r} \frac{\partial}{\partial r} \left( r \kappa \frac{\partial T}{\partial r} \right) + \frac{1}{r^2} \frac{\partial}{\partial \theta} \left( \kappa \frac{\partial T}{\partial \theta} \right) + \frac{\partial}{\partial z} \left( \kappa \frac{\partial T}{\partial z} \right) \right], \end{aligned} \quad (5)$$

$$P = \rho T, \quad (6)$$

where

$$\nabla \cdot \bar{\mathbf{V}} = \frac{\partial V_r}{\partial r} + \frac{V_r}{r} + \frac{\epsilon}{r} \frac{\partial V_\theta}{\partial \theta} + \frac{\partial V_z}{\partial z},$$

$$\frac{D}{Dt} = \frac{\partial}{\partial t} + M \left( V_r \frac{\partial}{\partial r} + \epsilon \frac{1}{r} V_\theta \frac{\partial}{\partial \theta} + V_z \frac{\partial}{\partial z} \right),$$

and  $\Phi$  is the dissipation function. Equations (1)–(6) are non-dimensionalized using the following definitions:

$$\rho = \frac{\rho'}{\rho'_0}, \quad P = \frac{P'}{P'_0}, \quad T = \frac{T'}{T'_0}, \quad V_r = \frac{V'_r}{V'_{r0}}, \quad V_\theta = \frac{V'_\theta}{V'_{\theta 0}}, \quad V_z = \frac{V'_z}{V'_{z0}},$$

$$r = \frac{r'}{R'}, \quad z = \frac{z'}{L'}, \quad t = \frac{t'}{t'_a}, \quad \kappa = \frac{\kappa'}{\kappa'_0}, \quad \mu = \frac{\mu'}{\mu'_0}, \quad C_V = \frac{C'_V}{C'_{V0}},$$

where  $P'_0$  is the initial static pressure in the cylinder, and  $\rho'_0$  and  $T'_0$  are the density and temperature of the fluid being injected from the sidewall. The induced characteristic axial

velocity and the characteristic endwall velocity disturbance  $V'_{z0}$  is defined with respect to the injection reference sidewall velocity,  $V'_{r0}$  by overall mass conservation,  $\frac{V'_{z0}}{V'_{r0}} = \delta$ . The size of the initially unknown reference azimuthal velocity  $V'_{\theta 0}$  is related to  $V'_{r0}$  by  $\frac{V'_{\theta 0}}{V'_{r0}} = \epsilon$ . Later, it is shown that  $\epsilon = 1$ .

The time is non-dimensionalized using the axial acoustic time scale,  $t'_a = \frac{L'}{C'_0}$ , where  $C'_0 = (\gamma \mathcal{R}' T'_0)^{\frac{1}{2}}$  is the speed of sound,  $\mathcal{R}'$  is the gas constant, and  $\gamma$  is the ratio of specific heats. The thermal diffusivity, viscosity, and specific heat at constant volume,  $\kappa'_0$ ,  $\mu'_0$ , and  $C'_{V0}$  respectively are characteristic properties of the injected fluid. Also the Reynolds number, Prandtl number, and Mach number are defined as

$$Re = \frac{\rho' V'_{z0} L'}{\mu'_0}, \quad Pr = \frac{\mu'_0 C'_{p0}}{\kappa'_0}, \quad M = \frac{V'_{z0}}{C'_0},$$

where  $Re \gg 1$ ,  $M \ll 1$ , and  $Pr = O(1)$ .

The Mach number is chosen as a small parameter to model the small magnitude found in a typical rocket motor chamber, as opposed to the rocket nozzle where larger values are possible. The aspect ratio,  $\delta = \frac{L'}{R'} \gg 1$ , is taken to be a large parameter because many chambers have aspect ratios between 15 and 50. Finally, it is assumed that the hard blowing condition,  $\frac{\delta^2}{Re} \ll 1$  (Cole and Aroesty [10]) prevails.

Initially, a steady flow is generated by the sidewall injection,  $V_r = -1$ . At  $t = 0^+$ , the endwall begins oscillating with the non-dimensionalized sinusoidal axial velocity,  $V_z = F(r, \theta) \sin \omega t$ , for  $\omega = O(1)$ . The magnitude of  $\omega$  is compatible with the first few axial acoustic modes observed in high aspect ratio chambers.

The full boundary conditions are:

$$z = 0; \quad V_z = \begin{cases} 0, & t \leq 0, \\ F(r, \theta) \sin \omega t, & t > 0, \end{cases} \quad (7)$$

$$z = 0; \quad V_r = V_\theta = 0, \quad (8)$$

$$z = 1; \quad P = 1, \quad (9)$$

$$r = 0; \quad P, \rho, T, V_r, V_\theta, V_z \text{ finite}, \quad (10)$$

$$r = 1; \quad V_r = -1, \quad (11)$$

$$r = 1; \quad V_z = V_\theta = 0, \quad (12)$$

and solutions must be periodic in  $\theta$ .

In general, solutions to (1)–(6), with boundary conditions (7)–(12), are found in terms of the dependent variables, written as

$$(V_r, V_\theta, V_z, P, \rho, T) = (V_{rs}, V_{\theta s}, V_{zs}, P_s, \rho_s, T_s) + (\tilde{V}_r, \tilde{V}_\theta, \tilde{V}_z, \tilde{P}, \tilde{\rho}, \tilde{T}),$$

where the subscript “s” represents the steady part of the flow and  $(\tilde{\phantom{x}})$  represents the unsteady flow. The steady parts of the solutions satisfy the endwall condition  $V_{zs} = 0$  at  $z = 0$  for all  $t$ . As a result of the axisymmetric boundary conditions, the steady solution is axisymmetric.

The steady variables are expanded as

$$\begin{aligned} (V_{rs}, V_{\theta s}, V_{zs}) &\sim \sum_{i=0} M^i (V_{ris}, V_{\theta is}, V_{zis}), \\ (P_s, \rho_s, T_s) &\sim 1 + \sum_{i=0} M^{i+2} (P_{is}, \rho_{is}, T_{is}), \end{aligned}$$

for the limit  $M \rightarrow 0$ .

Culick [11] derived solutions to the first-order steady equations:

$$V_{r0s} = -\frac{1}{r} \sin\left(\frac{\pi}{2} r^2\right), \quad (13)$$

$$V_{\theta 0s} = 0, \quad (14)$$

$$V_{z0s} = \pi z \cos\left(\frac{\pi}{2} r^2\right), \quad (15)$$

$$P_{0s} = \gamma \frac{\pi^2}{2} (1 - z^2). \quad (16)$$

Initial conditions for the unsteady flow are given by the steady solution profiles. In terms of the unsteady variables, at  $t = 0$ ,

$$(\tilde{V}_r, \tilde{V}_\theta, \tilde{V}_z, \tilde{P}, \tilde{\rho}, \tilde{T}) = 0. \quad (17)$$

### III. UNSTEADY SOLUTION

The unsteady flow field is driven by the non-axisymmetric boundary condition in (7), which is a generalization of the purely time dependent disturbance considered by Zhao et al. [9]. Their results describe axisymmetric, co-existing acoustic and rotational flow fields where the radial extent of the vorticity depends on the magnitude of the sidewall blowing. If  $\frac{M^2 Re}{\delta^2} \ll 1$ , a purely acoustic core can be described away from the sidewall. A weakly viscous transition layer containing vorticity is present adjacent to the sidewall, thicker than a traditional acoustic boundary layer, but small compared to the cylinder radius. The transition layer is described by two length scales. The smaller is on the order of the radial distance traveled by an injected fluid particle during one period of oscillation of the endwall velocity and the larger is a viscous damping length.

If  $\frac{M^2 Re}{\delta^2} \sim O(1)$ , then the transition layer grows to fill the entire cylinder. For this parameter regime, no purely acoustic core exists as in the previous case. Instead, distinct acoustic (irrotational) and rotational flows co-exist. Acoustic waves driven by the endwall disturbance interact inviscidly with fluid injected from the wall to create vorticity. Subsequently, the rotational flow is convected into the cylinder by the injected flow field. Weak viscosity diffuses the vorticity on a short radial length scale,  $O(MR')$  and weak nonlinear effects alter the flow in the axial direction. The Zhao et al. [9] results are valid for  $0 \leq z \leq 1$ .

For the present work, the condition  $\frac{M^2 Re}{\delta^2} \ll 1$  is used, and we expect a transition layer as in Zhao et al. [9]

#### A. Core Flow: Region I

Certain essential results of Zhao et al. [9] are rederived from the three-dimensional equations. If the velocities and thermodynamic variables in region I are expanded as

$$(V_r, V_\theta, V_z) \sim (V_{r0s}, V_{\theta 0s}, V_{z0s}) + \sum_{i=0} M^i (\tilde{V}_{ri}, \tilde{V}_{\theta i}, \tilde{V}_{zi}), \quad (18)$$

$$(P, \rho, T) \sim 1 + \sum_{i=0} M^{i+1} (\tilde{P}_i, \tilde{\rho}_i, \tilde{T}_i),$$

then the leading-order equations can be found in a manner similar to that of Zhao et al. [9] The basic acoustic solutions are found by substituting (18) into (1)–(6). It follows from the limit,  $M \rightarrow 0$ , with the hard blowing condition,  $\frac{\delta^2}{Re} \ll 1$ , and the large aspect ratio assumption,  $\delta \gg 1$  that the acoustic core equations have the form,

$$\frac{\partial \tilde{\rho}_0}{\partial t} = -\frac{\partial \tilde{V}_{z0}}{\partial z}, \quad (19)$$

$$\tilde{P}_0 = \tilde{P}_0(z, t), \quad (20)$$

$$\frac{\partial \tilde{V}_{z0}}{\partial t} = -\frac{1}{\gamma} \frac{\partial \tilde{P}_0}{\partial z}, \quad (21)$$

$$\frac{\partial \tilde{T}_0}{\partial t} = \frac{\gamma - 1}{\gamma} \frac{\partial \tilde{P}_0}{\partial t}, \quad (22)$$

$$\tilde{\rho}_0 + \tilde{T}_0 = \tilde{P}_0. \quad (23)$$

Equation (20) arises because the radial and azimuthal pressure gradients are vanishingly small in the chosen limit. The large aspect ratio condition causes the pressure in (20) to vary only in the axial direction. This is consistent with the acoustic core of the solution found in Zhao et al. [9] One can combine (20) with boundary conditions on  $r = 1$ ;  $\tilde{V}_{r0} = 0$  and  $\tilde{V}_{\theta 0} = 0$  to show that the radial and azimuthal velocities are zero. The injection boundary condition,  $V_r = -1$  on  $r = 1$  is satisfied by the steady solution cited in (13). Equations (19)–(23) yield the familiar wave equation:

$$\frac{\partial^2 \tilde{V}_{z0}}{\partial t^2} = \frac{\partial^2 \tilde{V}_{z0}}{\partial z^2}. \quad (24)$$

The solution to this equation will consist only of planar acoustic waves in the  $z$  direction due to the form of  $\tilde{P}_0$  in (20) and  $\tilde{V}_{z0}$  in (21). This equation is valid away from the endwall, where the oscillating  $r$  and  $\theta$ -dependent endwall condition (7) is imposed, and away from the sidewall where the no-slip boundary condition (12) prevails. It appears that a region

(denoted by II in Figure 2) near the endwall,  $z = 0$ , must exist where a transition occurs from a three-dimensional to a one-dimensional flow. One must also find the appropriately scaled axial variable in the transitional sidewall layer.

### B. Endwall Core: Region II

The radial and azimuthal pressure gradients, lost in the limiting form of the momentum equations in region I, can be restored by using the following rescaled variables,

$$\begin{aligned} z &= \frac{1}{\delta} \hat{z}, \\ P &= 1 + M \hat{P}_{00}(t) + \frac{M}{\delta} \hat{P}_0, \\ V_r &= V_{r0s} + \delta \hat{V}_{r0}, \\ V_\theta &= V_{\theta 0s} + \delta \hat{V}_{\theta 0}, \\ V_z &= V_{z0s} + \hat{V}_{z0}, \end{aligned} \tag{25}$$

in order to get physically meaningful equations in the limit  $M \rightarrow 0$ . The  $(\hat{\phantom{x}})$  denote variables in region II, and the  $\hat{P}_{00}(t)$  term is needed to obtain proper matching of the pressures in regions I and II. There is no need to rescale the axial velocity given the boundary condition in (7). The imposed axial velocity induces radial and azimuthal velocities of the same dimensional magnitude, which accounts for the scaling factor,  $\delta$  in the third and fourth equations in (25). The pressure disturbance consists of two distinct terms. The lower order term ( $O(M)$ ) represents a spatially homogeneous pressure transient. The higher order term ( $O(\frac{M}{\delta})$ ) describes the explicit response to the non-axisymmetric boundary condition in (7). The above expansions can be used in (1)–(4), to find the first order unsteady equations:

$$0 = \frac{1}{r} \frac{\partial}{\partial r} (r \hat{V}_{r0}) + \frac{1}{\epsilon r} \frac{\partial \hat{V}_{\theta 0}}{\partial \theta} + \frac{\partial \hat{V}_{z0}}{\partial \hat{z}}, \tag{26}$$

$$-\frac{1}{\gamma} \frac{\partial \hat{P}_0}{\partial r} = \frac{\partial \hat{V}_{r0}}{\partial t}, \tag{27}$$

$$-\frac{1}{\gamma} \frac{1}{\epsilon r} \frac{\partial \hat{P}_0}{\partial \theta} = \frac{\partial \hat{V}_{\theta 0}}{\partial t}, \quad (28)$$

$$-\frac{1}{\gamma} \frac{\partial \hat{P}_0}{\partial \hat{z}} = \frac{\partial \hat{V}_{z 0}}{\partial t}, \quad (29)$$

in the limit,  $M \rightarrow 0$ , with  $\delta \gg 1$ ,  $M\delta \ll 1$ ,  $\frac{\delta^2}{Re} \ll 1$ . The incompressible form of the continuity equation, (26) implies that acoustic propagation does not occur in region II. This means that the flow in region II responds to the imposed axial velocity on the endwall, in (7), without downstream signal propagation. Equations (17) and (27)–(29) imply that the flow is irrotational. The result is valid for  $\omega = O(1)$  on the time scale  $t = O(1)$ .

The asymptotic relationship  $M\delta \ll 1$  is needed to ensure that the leading-order equations are linear. If this relationship is relaxed to  $M\delta \sim O(1)$ , then (26)–(29) will be the full incompressible Euler equations.

Equations (26)–(29) can be combined to show that the scaled pressure,  $\hat{P}_0$ , satisfies Laplace's equation,

$$\frac{\partial^2 \hat{P}_0}{\partial r^2} + \frac{1}{r} \frac{\partial \hat{P}_0}{\partial r} + \frac{1}{r^2} \frac{\partial^2 \hat{P}_0}{\partial \theta^2} + \frac{\partial^2 \hat{P}_0}{\partial \hat{z}^2} = 0. \quad (30)$$

The boundary conditions:

$$\hat{z} = 0; \quad \frac{\partial \hat{P}_0}{\partial \hat{z}} = -\gamma \omega F(r, \theta) \cos \omega t, \quad (31)$$

$$r = 0; \quad \hat{P}_0 \text{ finite}, \quad (32)$$

$$r = 1; \quad \frac{\partial \hat{P}_0}{\partial r} = 0, \quad (33)$$

are found from (7), (10), the unsteady component of (11), and using (27) and (29). In addition,  $\hat{P}_0$  must be periodic in  $\theta$ . Given that the unsteady flow in region I depends only on the axial variable, then the pressure matching condition between regions I and II implies that

$$\hat{z} \rightarrow \infty, \quad \hat{P}_0 \sim \hat{P}_0(\hat{z}, t). \quad (34)$$

This condition, (27), and (28) together with the initial condition,  $\hat{V}_{\theta 0} = \hat{V}_{r 0} = 0$  at  $t = 0$ , implies that the radial and azimuthal velocities vanish as  $\hat{z} \rightarrow \infty$ . The full three-dimensional

time-dependent solution to (30)–(34), found using standard separation of variables techniques, is

$$\begin{aligned} \hat{P}_0(r, \theta, \hat{z}, t) = & A_0(t) - \gamma\omega \cos \omega t \left( a_{00}\hat{z} + \sum_{m=1}^{\infty} a_{m0}e^{-\mu_{m0}\hat{z}}J_0(\mu_{m0}r) \right. \\ & \left. + \sum_{m=1}^{\infty} \sum_{n=1}^{\infty} e^{-\mu_{mn}\hat{z}}J_n(\mu_{mn}r)(a_{mn} \cos n\theta + b_{mn} \sin n\theta) \right), \end{aligned} \quad (35)$$

where

$$\begin{aligned} a_{mn} &= -\frac{1}{\pi\mu_{mn}\nu_{mn}} \int_0^1 \int_{-\pi}^{\pi} F(r, \theta) r J_n(\mu_{mn}r) \cos n\theta \, d\theta \, dr \quad \text{for } m \geq 1, n \geq 1, \\ b_{mn} &= -\frac{1}{\pi\mu_{mn}\nu_{mn}} \int_0^1 \int_{-\pi}^{\pi} F(r, \theta) r J_n(\mu_{mn}r) \sin n\theta \, d\theta \, dr \quad \text{for } m \geq 1, n \geq 1, \\ a_{m0} &= -\frac{1}{2\pi\mu_{m0}\nu_{m0}} \int_0^1 \int_{-\pi}^{\pi} F(r, \theta) r J_0(\mu_{m0}r) \, d\theta \, dr \quad \text{for } m \geq 1, \\ a_{00} &= \frac{1}{\pi} \int_0^1 \int_{-\pi}^{\pi} F(r, \theta) r \, d\theta \, dr, \\ \nu_{mn} &= \int_0^1 r J_n^2(\mu_{mn}r) \, dr. \end{aligned} \quad (36)$$

and  $\mu_{mn}$  is the  $m^{\text{th}}$  zero of  $J'_n(r)$ , which comes from (33). The first few values for  $\mu_{mn}$  are  $\mu_{m0} \approx 3.83171, 7.01559, 10.1735, \dots$ ,  $\mu_{m1} \approx 1.84118, 5.33144, 8.53632, \dots$  and  $\mu_{m2} \approx 3.05424, 6.70613, 9.96947, \dots$ . The  $\mu$ 's for large  $m$  satisfy  $\mu_{m1} > 3$  for  $m \geq 3$ . Thus the smallest eigenvalue is 1.84118. It is noted that the terms decay quickly as  $n$  and  $m$  increase. The solution is dominated by the first few terms in (35), and these solutions are valid for  $\omega$  not equal to any of the resonance frequencies ( $b_n = (n + \frac{1}{2})\pi$  for  $n \geq 0$ ) of the cylinder.

The function  $A_0(t)$  is as yet undetermined. It will be found when the region I solution is obtained. It may be noted from (35) that the  $r$ - and  $\theta$ -dependence of  $\hat{P}_0$  decays exponentially fast as  $\hat{z} \rightarrow \infty$ . At the edge of the transitional layer,

$$P|_{\hat{z} \rightarrow \infty} \sim 1 + M\hat{P}_{00}(t) + \frac{M}{\delta} (A_0(t) - a_{00}\hat{z}\gamma\omega \cos \omega t). \quad (37)$$

The velocities in region II are found from the pressure field in (35) using (27)–(29), and the initial condition (17),



$$\hat{V}_{z0} = \sin \omega t \left[ a_{00} - \sum_{m=1}^{\infty} a_{m0} \mu_{m0} e^{-\mu_{m0} \hat{z}} J_0(\mu_{m0} r) - \sum_{m=1}^{\infty} \sum_{n=1}^{\infty} \mu_{mn} e^{-\mu_{mn} \hat{z}} J_n(\mu_{mn} r) (a_{mn} \cos n\theta + b_{mn} \sin n\theta) \right], \quad (38)$$

$$\hat{V}_{r0} = \sin \omega t \left[ \sum_{m=1}^{\infty} a_{m0} \mu_{m0} e^{-\mu_{m0} \hat{z}} J'_0(\mu_{m0} r) + \sum_{m=1}^{\infty} \sum_{n=1}^{\infty} \mu_{mn} e^{-\mu_{mn} \hat{z}} J'_n(\mu_{mn} r) (a_{mn} \cos n\theta + b_{mn} \sin n\theta) \right], \quad (39)$$

$$\hat{V}_{\theta 0} = \frac{1}{\epsilon} \sin \omega t \left[ \sum_{m=1}^{\infty} \sum_{n=1}^{\infty} n e^{-\mu_{mn} \hat{z}} \frac{1}{r} J_n(\mu_{mn} r) (-a_{mn} \sin n\theta + b_{mn} \cos n\theta) \right]. \quad (40)$$

Here again, one may observe exponential decay of the  $r$  and  $\theta$  solution dependence as  $\hat{z} \rightarrow \infty$ . As a result, the amplitude of the axial speed at the downstream edge of the transitional layer depends on the endwall mass addition through the coefficient  $a_{00}$  defined in (36). The azimuthal and axial velocities (40) and (38) do not satisfy the no-slip condition (12). A viscous boundary layer exists along the sidewall,  $r = 1$ , and will be investigated later. Also, the solution does not satisfy the no-slip boundary condition on the endwall,  $z = 0$ . An inviscid, rotational layer, thinner than region II, exists adjacent to the endwall which provides a transition from the irrotational velocities in (39) and (40) to the no-slip condition at  $\hat{z} = 0$ . This region will also be described later.

The decay of all non-axisymmetric flow in region II occurs over the dimensional length region  $\frac{1}{\delta} L' = R'$ , the radius of the cylinder. In the non-axisymmetric numerical calculation of Sabnis et al. [7], it is noted that the asymmetry of the flow persists only in a region less than two diameters upstream of the exit plane, where a non-axisymmetric pressure boundary condition is imposed.

### C. Solution to the Region I Wave Equation

Equation (24) can now be used to find the acoustic flow solution in region I, subject to the initial and boundary conditions;

$$t = 0; \quad \tilde{V}_{z0} = \frac{\partial \tilde{V}_{z0}}{\partial z} = 0, \quad (41)$$

$$z = 1; \quad \frac{\partial \tilde{V}_{z0}}{\partial z} = 0. \quad (42)$$

A condition at  $z = 0$  is derived by matching the solutions in regions I as  $z \rightarrow 0$  and II as  $\hat{z} \rightarrow \infty$ . Equation (38) can be used in the limit  $\hat{z} \rightarrow \infty$  to derive

$$z = 0; \quad \tilde{V}_{z0} = a_{00} \sin \omega t. \quad (43)$$

The solution to (24) with (41)–(43) is:

$$\tilde{V}_{z0} = a_{00} \left[ \sin \omega t + \sum_{n=0}^{\infty} \frac{2\omega}{b_n^2 - \omega^2} \left\{ \frac{\omega}{b_n} \sin \omega t - \sin b_n t \right\} \sin b_n z \right]. \quad (44)$$

where  $b_n = (n + \frac{1}{2})\pi$ , and  $a_{00}$ , defined in (36), represents a non-dimensional instantaneous mass addition due to the velocity endwall condition. It is noted that waves will propagate in region I only if  $a_{00} \neq 0$ . Equations (21) and (44) and the pressure node boundary condition, (9), can be used to find the pressure field in region I,

$$\tilde{P}_0 = -a_{00} \left[ (z-1)\gamma\omega \cos \omega t + \sum_{n=0}^{\infty} \frac{2\gamma\omega}{b_n^2 - \omega^2} \left\{ \frac{\omega^2}{b_n^2} \cos \omega t - \cos b_n t \right\} \cos b_n z \right]. \quad (45)$$

The pressure in region I near the edge of region II, found from (25) and (45),

$$\begin{aligned} P|_{z \rightarrow 0} = 1 + M a_{00} & \left[ \gamma\omega \cos \omega t - \sum_{n=0}^{\infty} \frac{2\gamma\omega}{b_n^2 - \omega^2} \left( \frac{\omega^2}{b_n^2} \cos \omega t - \cos b_n t \right) \right] \\ & - M [a_{00} z \gamma\omega \cos \omega t] + O(z^2). \end{aligned} \quad (46)$$

can be compared with (37) to find the unknown function  $\hat{P}_{00}(t)$  by matching the order  $M$  terms, (46),

$$\hat{P}_{00}(t) = a_{00} \left[ \gamma\omega \cos \omega t - \sum_{n=0}^{\infty} \frac{2\gamma\omega}{b_n^2 - \omega^2} \left( \frac{\omega^2}{b_n^2} \cos \omega t - \cos b_n t \right) \right]. \quad (47)$$

Finally, the term  $A_0(t)$  in (35) can be found from a higher order solution in region I and matching terms at order  $\frac{M}{\delta}$ . It follows that  $A_0(t) = 0$ .

The composite asymptotic solution is constructed from (25), (35), and (47),

$$\begin{aligned}
P(r, \theta, z, t) = & 1 + Ma_{00} \left[ -(z-1)\gamma\omega \cos \omega t - \frac{2\gamma\omega}{b_n^2 - \omega^2} \left( \frac{\omega^2}{b_n^2} \cos \omega t - \cos b_n t \right) \cos b_n z \right] \\
& + \frac{M}{\delta} \gamma\omega \cos \omega t \left[ \sum_{n=1}^{\infty} a_{m0} e^{-\mu_{m0}\delta z} J_0(\mu_{m0}r) \right. \\
& \left. + \sum_{m=1}^{\infty} \sum_{n=1}^{\infty} e^{-\mu_{mn}\delta z} J_n(\mu_{mn}r) (a_{mn} \cos n\theta + b_{mn} \sin n\theta) \right] + O(M^2). \quad (48)
\end{aligned}$$

#### D. Determination of $\epsilon$

Equations (38)–(40) can be used to find the unsteady speed on the cylinder axis ( $r = 0$ ),

$$\begin{aligned}
||\tilde{\mathbf{V}}||^2 &= \tilde{V}_{z0}^2 + \delta^2 \tilde{V}_{r0}^2 + \delta^2 \tilde{V}_{\theta 0}^2 \\
&= \sin^2 \omega t \left[ D(\hat{z}) + \delta^2 (A^2(\hat{z}) \cos^2 \theta + 2A(\hat{z})B(\hat{z}) \sin \theta \cos \theta + B^2(\hat{z}) \sin^2 \theta) \right. \\
&\quad \left. + \frac{\delta^2}{\epsilon^2} (A^2(\hat{z}) \sin^2 \theta - 2A(\hat{z})B(\hat{z}) \sin \theta \cos \theta + B^2(\hat{z}) \cos^2 \theta) \right],
\end{aligned}$$

where

$$\begin{aligned}
A(\hat{z}) &= \frac{1}{2} \sum_{m=1}^{\infty} a_{m1} \mu_{m1} e^{-\mu_{m1}\hat{z}}, \\
B(\hat{z}) &= \frac{1}{2} \sum_{m=1}^{\infty} b_{m1} \mu_{m1} e^{-\mu_{m1}\hat{z}}, \\
D(\hat{z}) &= a_{00} - \sum_{m=1}^{\infty} a_{m0} \mu_{m0} e^{-\mu_{m0}\hat{z}}.
\end{aligned}$$

On the axis, the fluid speed must be independent of  $\theta$ , therefore  $\epsilon = \frac{V'_{\theta 0}}{V'_{r0}}$  must be such that the speed at the centerline is only a function of  $\hat{z}$ . A  $\theta$ -independent function along the cylinder axis results only if  $\epsilon = 1$ , such that

$$||\tilde{\mathbf{V}}||^2 = \sin^2 \omega t (D^2(\hat{z}) + A^2(\hat{z}) + B^2(\hat{z}))$$

This result demonstrates that if  $A(\hat{z})$  and  $B(\hat{z})$  are nonzero then there is flow across the centerline of the cylinder. The function  $D(\hat{z})$  corresponds to flow in the  $z$ -direction. Flow across the axis of the cylinder occurs only when  $a_{m1}$  and  $b_{m1}$  are nonzero. The corresponding eigenfunctions,  $\sin \theta$  and  $\cos \theta$ , in (36) and (38)–(40) are the only  $\theta$ -dependent eigenfunctions which are not symmetric about the center of the cylinder as shown in Figure 3.

### E. Example of a Flow with a $\theta$ - and $r$ -Dependent Endwall Condition

A specific endwall condition is chosen in (7) to examine more closely the structure of the flow in this region. The function  $F(r, \theta) = r^2(1 - r)^2 \sin^2(\frac{\theta}{2})$  has a zero radial derivative at both  $r = 0$  and  $r = 1$  which permits fast convergence of its Fourier Bessel series, and the azimuthal part,  $\sin^2(\frac{\theta}{2})$  is positive everywhere and non-axisymmetric. It follows that  $a_{00} \neq 0$  and waves will propagate in region I. Figure 4 depicts the endwall condition for  $\omega = 1$  at  $t = \frac{\pi}{2}$ .

Figure 5 shows the decaying part of the pressure in (35), defined as  $P_D$ , at four axial locations within region II. All  $r$  and  $\theta$  dependence of the unsteady pressure is contained in the terms in  $P_D$ . These terms directly relate to the radial and azimuthal velocities as in (27) and (28). The plot shows that the decay of  $P_D$  is very rapid. The absolute value of  $P_D$  when  $\hat{z} = 1$  is 84% lower than analogous pressure at  $\hat{z} = 0.01$ .

Figures 6, 7, and 8 show two-dimensional projections of the largest asymptotic approximation to the velocity vector fields on either the cross-sectional or an axial-radial plane. The dimensional velocities are written as

$$\begin{aligned} V'_z &\sim (V_{z0s} + \tilde{V}_{z0})V'_{z0} \sim \hat{V}_{z0}V'_{z0} + V_{z0s}V'_{z0} \sim \hat{V}_{z0}V'_{z0} + O(\frac{1}{\delta}), \\ V'_r &\sim (V_{r0s} + \tilde{V}_{r0})V'_{r0} \sim \left(\frac{V_{r0s}}{\delta} + \hat{V}_{r0}\right)V'_{z0} \sim \hat{V}_{r0}V'_{z0} + O(\frac{1}{\delta}), \\ V'_\theta &\sim \tilde{V}_{\theta0}V'_{\theta0} \sim \hat{V}_{\theta0}V'_{z0} + O(M), \end{aligned}$$

where the steady velocities are asymptotically smaller than their unsteady counterparts, scaled with respect to  $V'_{z0}$ . The axial steady velocity is small due to the linear  $z$  dependence in (13), where  $z \sim \frac{1}{\delta}$  in region II. In comparison, the radial steady velocity is on the order of  $V'_{r0}$ , which is  $O(\frac{1}{\delta})$  smaller than  $V'_{z0}$ , the scale of the unsteady radial velocity.

The plots in Figures 6, 7, and 8 are based on a 20 term truncated, alternating Fourier series expansion of (38)–(40), is bounded by  $10^{-3}$ .

Figure 6 shows a two-dimensional projection of the vector field in region II onto the cross-

sectional plane where  $\hat{z} = 0.01$ . Only the  $r$  and  $\theta$  components of the velocities are represented and the dimensional lengths of the arrow vectors in the plot is  $V'_{z0}(\hat{V}_{\theta 0}^2 + \hat{V}_{r0}^2)^{\frac{1}{2}}$ . Figure 6 shows that the flow is symmetric with respect to a horizontal diameter of the cylinder from  $\theta = 0$  to  $\theta = \pi$ , but not symmetric from the left to right side of the cylinder. The source of the flow, located at  $r = \frac{1}{2}$  and  $\theta = \pi$ , corresponds to the point of highest velocity of Figure 4. A pattern similar to the vector field of Figure 6 appears for larger  $\hat{z}$ , however with a smaller amplitude. The field is dominated by the first mode of the Fourier series in (39) and (40), hence the amplitude of the vector field lines decrease exponentially.

Figure 7 is a two-dimensional projection of the vector field in region II onto a plane containing the axis of the cylinder at the location  $\theta = 0$  and  $\theta = \pi$ . The variable  $y$  is defined as  $y = r$  for  $\theta = 0$  and  $y = -r$  for  $\theta = \pi$ . Only the  $r$  and  $z$  components of the velocities are shown, with the dimensional magnitude of the vector field,  $V'_{z0}(\hat{V}_{z0}^2 + \hat{V}_{r0}^2)^{\frac{1}{2}}$ . Figure 7 shows that there is flow across the centerline from the bottom to the top. There is flow across the centerline of the cylinder due to the asymmetry of the endwall velocity as discussed earlier in this section and in Figure 3. The maximum velocity at the horizontal line  $y = -\frac{1}{2}$ , corresponds to the region of high velocity of the endwall condition at  $r = \frac{1}{2}$  and  $\theta = \pi$  of Figure 4.

Figure 8 shows a two-dimensional projection of the velocity vector field onto a plane containing the cylinder axis at the location  $\theta = \frac{\pi}{2}$  and  $\theta = -\frac{\pi}{2}$ . The variable  $y$  is defined as  $y = r$  for  $\theta = \frac{\pi}{2}$  and  $y = -r$  for  $\theta = -\frac{\pi}{2}$ . As in Figure 7, only the  $r$  and  $z$  components of the velocities are shown, and the dimensional magnitude is the same. However, since the length of the lines in each plot is scaled with respect to the maximum velocity in the plot, the actual magnitude of the velocity fields in Figures 7 and 8 differ. The symmetry of the vector field across the centerline at  $y = 0$  results from the symmetry of the endwall condition. As with Figure 7, the vector field near the line  $\hat{z} = 1$ , is composed only of an axial velocity because the radial and azimuthal velocities decay exponentially.

### F. Region III: Viscous Boundary Layer

The solutions in (38) and (40) do not satisfy the no-slip condition in (12) along the sidewall. It follows that a viscous boundary layer must exist adjacent to the sidewall in region II.

Region III is similar to the sidewall transition layer of Zhao et al. [9], when the sidewall blowing condition  $\frac{M^2 Re}{\delta^2} \ll 1$  is used. The boundary layer here must be resolved using a multiple scale analysis, where one scale is on the order of the distance a fluid particle moves during one cycle of the endwall oscillation, and the other scale is associated with a viscous damping scale.

The following transformations and expansions,

$$\begin{aligned}
 z &= \frac{\hat{z}}{\delta}, \\
 r_1 &= \frac{1-r}{M}, \quad \text{and} \quad r_2 = \frac{1-r}{\beta}, \\
 V_r &\sim -1 + M\delta\bar{V}_{r0} + \dots, \\
 V_\theta &\sim \delta\bar{V}_{\theta0} + \frac{M\delta}{\beta}\bar{V}_{\theta1} + \dots, \\
 V_z &\sim \bar{V}_{z0} + \frac{M}{\beta}\bar{V}_{z1} + \dots, \\
 P &\sim 1 + M\hat{P}_{00}(t) + \frac{M}{\delta}\bar{P}_0 + \dots, \\
 \rho &\sim 1 + \frac{M}{\delta}\bar{\rho}_0 + \dots,
 \end{aligned} \tag{49}$$

are employed to find the boundary layer equations, where  $\beta = \frac{M^2 Re}{\delta^2}$ ,  $\hat{P}_{00}(t)$  is defined in (47), and  $(-)$  represents variables in region III. It is important to recognize the limitation  $M \ll \beta \ll 1$  ensures that the viscous damping length scale is larger than the second scale associated with the Mach number. The relationship  $M\delta \ll 1$  is the same as in region II, and arises to ensure that the leading order equations are linear.

A balance of pressure and convective terms is used to find the  $O(M)$  scaling for  $r_1$  while a balance between second-order convective terms with the leading-order viscous term generates

the definition of  $\beta$ . Equation (49) can be used in (1)–(4), with the limit  $M \rightarrow 0$ , to find the leading order equations in region III,

$$-\frac{\partial \bar{V}_{r0}}{\partial r_1} + \frac{\partial \bar{V}_{\theta 0}}{\partial \theta} + \frac{\partial \bar{V}_{z0}}{\partial \hat{z}} = 0, \quad (50)$$

$$\frac{\partial \bar{P}_0}{\partial r_1} = \frac{\partial \bar{P}_0}{\partial r_2} = 0, \quad (51)$$

$$\frac{\partial \bar{V}_{\theta 0}}{\partial t} + \frac{\partial \bar{V}_{\theta 0}}{\partial r_1} = -\frac{1}{\gamma} \frac{\partial \bar{P}_0}{\partial \theta}, \quad (52)$$

$$\frac{\partial \bar{V}_{\theta 1}}{\partial t} + \frac{\partial \bar{V}_{\theta 1}}{\partial r_1} = -\frac{\partial \bar{V}_{\theta 0}}{\partial r_2} + \frac{\partial^2 \bar{V}_{\theta 0}}{\partial r_1^2}, \quad (53)$$

$$\frac{\partial \bar{V}_{z0}}{\partial t} + \frac{\partial \bar{V}_{z0}}{\partial r_1} = -\frac{1}{\gamma} \frac{\partial \bar{P}_0}{\partial \hat{z}}, \quad (54)$$

$$\frac{\partial \bar{V}_{z1}}{\partial t} + \frac{\partial \bar{V}_{z1}}{\partial r_1} = -\frac{\partial \bar{V}_{z0}}{\partial r_2} + \frac{\partial^2 \bar{V}_{z0}}{\partial r_1^2}. \quad (55)$$

Equations (50) and (51) are derived from (1) and (2) respectively. Equations (52) and (54) are the leading-order versions of (3) and (4), while (53) and (55) are the corresponding second-order approximations. The boundary conditions are found from (11) and (12),

$$r_1 = r_2 = 0 \quad \bar{V}_{z0} = \bar{V}_{\theta 0} = \bar{V}_{r0} = 0. \quad (56)$$

The region III solutions in the limit  $r_1 \rightarrow \infty$  must match with the region II solutions as  $r \rightarrow 1$ ,

$$r_1 \rightarrow \infty; \quad \bar{V}_{z0} \rightarrow \hat{V}_{z0}|_{r \rightarrow 1}, \quad \bar{V}_{\theta 0} \rightarrow \hat{V}_{\theta 0}|_{r \rightarrow 1}, \quad \bar{V}_{r0} \rightarrow \hat{V}_{r0}|_{r \rightarrow 1}. \quad (57)$$

Equation (50) shows that the boundary layer flow is incompressible, as in region II. Equation (51) implies that the boundary layer pressure is equal to that at its edge. Therefore

$$\bar{P}_0(\hat{z}, \theta, t) = \lim_{r \rightarrow 1} \hat{P}_0 = -\gamma \omega \cos \omega t H(\hat{z}, \theta), \quad (58)$$

where

$$\begin{aligned} H(\hat{z}, \theta) = & a_{00} \hat{z} + \sum_{m=1}^{\infty} a_{m0} e^{-\mu_{m0} \hat{z}} J_0(\mu_{m0}) \\ & + \sum_{m=1}^{\infty} \sum_{n=1}^{\infty} e^{-\mu_{mn} \hat{z}} J_n(\mu_{mn}) (a_{mn} \cos n\theta + b_{mn} \sin n\theta) \end{aligned}$$

is obtained by taking the limit of (35) as  $r \rightarrow 1$ .

The quasi-steady solution of (52) will not satisfy the initial condition, but can be used to find the general properties of the boundary layer structure. The complex form of (58) can be used in (52), with  $\bar{V}_{\theta 0} = F_{\theta}(r_1, r_2, \theta, \hat{z})e^{i\omega t}$  to find

$$i\omega F_{\theta} + \frac{\partial F_{\theta}}{\partial r_1} = -\omega \frac{\partial H}{\partial \theta}. \quad (59)$$

This equation is compatible with the no-slip boundary condition in (56), and the solution is given by

$$F_{\theta} = C_1(r_2, \theta, \hat{z})e^{-i\omega r_1} + i \frac{\partial H}{\partial \theta}. \quad (60)$$

The smaller radial-scale behavior of  $\bar{V}_{\theta 0}$  is found using (53). The form  $\bar{V}_{\theta 1} = G(r_1, r_2, \theta, \hat{z})e^{i\omega t}$  and (60) is used in (53) to yield

$$i\omega G_{\theta} + \frac{\partial G_{\theta}}{\partial r_1} = -\frac{\partial}{\partial r_2} C_1(r_2, \theta, \hat{z})e^{-i\omega r_1} - \omega^2 C_1(r_2, \theta, \hat{z})e^{-i\omega r_1} \quad (61)$$

Secular growth of the solution is avoided by setting the right hand side of (61) to zero:

$$\frac{\partial C_1}{\partial r_2} + \omega^2 C_1 = 0. \quad (62)$$

The solution to (62) is,

$$C_1 = C_2(\theta, \hat{z})e^{-\omega^2 r_2}. \quad (63)$$

It follows from the definition,  $\bar{V}_{\theta 0} = F_{\theta}e^{i\omega t}$ , (60), and (63) and the boundary condition (56) that

$$\bar{V}_{\theta 0} = \text{Re} \left\{ i e^{i\omega t} \frac{\partial H}{\partial \theta} \left( \exp(-\omega^2 r_2 - i\omega r_1) - 1 \right) \right\}, \quad (64)$$

where Re is the real part of the solution. Similarly, the solution to (54) is given by

$$\bar{V}_{z 0} = \text{Re} \left\{ i e^{i\omega t} \frac{\partial H}{\partial \hat{z}} \left( \exp(-\omega^2 r_2 - i\omega r_1) - 1 \right) \right\}. \quad (65)$$



The  $\frac{\partial H}{\partial \theta}$  term in (64) is equivalent to the azimuthal region II velocity in (40) as  $r \rightarrow 1$ , and the  $\frac{\partial H}{\partial z}$  term in (65) is equivalent to the region II axial velocity as  $r \rightarrow 1$ .

Finally from (50),

$$\bar{V}_{r0} = \text{Re} \left\{ i e^{i\omega t} \left( \frac{\partial^2 H}{\partial \theta^2} + \frac{\partial^2 H}{\partial \tilde{z}^2} \right) \left( \frac{\exp(-\omega^2 r_2 - i\omega r_1) - 1}{-i\omega} - r_1 \right) \right\}. \quad (66)$$

Region III contains a transition between the region II azimuthal, radial and axial velocities and the no-slip boundary condition that exists at the sidewall  $r = 1$ . In the limit  $r_1 \rightarrow \infty$ , (at the edge of the boundary layer),  $\bar{V}_{r0} \sim r_1$ . The edge of the boundary layer acts like a source or sink on the fluid in region II.

The exponential decay effect in (64)–(66) can be written in terms of the radial variable  $r$  by using (49) and the definition of  $\beta$ ;

$$\exp[-\omega^2 r_2] = \exp \left[ -\frac{\omega^2 \delta^2}{M^2 Re} (1 - r) \right]$$

The boundary layer thickness is proportional to the parameter  $M^2 Re / \omega^2 \delta^2$ . For a fixed value of  $r$  close to the sidewall, the boundary layer thickness decreases when  $Re$ ,  $M$ , and  $\omega$  decrease, and  $\delta$  increases. In contrast, the thickness of a non-injected viscous acoustic boundary layer will increase with a decrease in  $Re$ .

Interaction of the sidewall injection and axial pressure gradients arising from endwall velocity oscillation produces vorticity in region III. All three components of vorticity exist here. Azimuthal and axial components, proportional to the inverse of the Mach number, provide the largest contributions, while the smaller radial component is  $O(1)$ . The unsteady part of the vorticity in region III, denoted  $\bar{\Omega}$ , decays exponentially away from the sidewall, and is analogous to the behavior found in Zhao et al. [9],

$$\begin{aligned} \bar{\Omega}_\theta &\sim \frac{1}{M} \frac{\partial \bar{V}_{z0}}{\partial r_1} = \frac{1}{M} \text{Re} \left\{ \omega e^{i\omega t} \frac{\partial H}{\partial \tilde{z}} \exp(-\omega^2 r_2 - i\omega r_1) \right\}, \\ \bar{\Omega}_z &\sim -\frac{1}{M} \frac{\partial \bar{V}_{\theta 0}}{\partial r_1} = -\frac{1}{M} \text{Re} \left\{ \omega e^{i\omega t} \frac{\partial H}{\partial \theta} \exp(-\omega^2 r_2 - i\omega r_1) \right\}, \\ \bar{\Omega}_r &\sim O(1), \end{aligned}$$

where (64) and (65) have been employed.

Figures 9 and 10 show the azimuthal velocity profiles near the sidewall at several values of time. The graphs reveal the multiple scale structure of the boundary layer where a typical spatial oscillation wavelength is about 0.05 radial units. These oscillations in  $\bar{V}_{\theta 0}$  arise from the harmonic variation in the endwall velocity as can be seen from the  $i\omega r_1$  term in (40). The viscous damping is sensitive to the frequency  $\omega$ . For example, when  $\omega = 1.0$  the boundary layer thickness is about 18% of the radius. In contrast, when  $\omega = 0.8$ , the spatial oscillations persist to about 25% of the radius. The results in Figures 9 and 10 also imply that the  $\theta$ -component of the wall shear stresses varies significantly in amplitude and direction during the time period shown. A similar result is found from the axial wall shear stress.

### G. Satisfying the No-Slip Boundary Condition on the Endwall

The radial and azimuthal velocities in (39) and (40) do not satisfy the no-slip boundary condition in (8) on the endwall  $z = \hat{z} = 0$ . One might expect to discover a classical “acoustic” boundary layer between the wall and region II ( $z = O(1/\delta)$ ) which provides a transition from the irrotational solution in (39) and (40) to the no-slip condition. However, in this problem with “hard” injection from the endwall viscous effects are very weak. It is found that the no-slip condition can be satisfied by a three-dimensional rotational solution to an inviscid equation (Cole and Aroesty [10]) in a thin transition layer of axial thickness  $z = O(M) \ll O(1/\delta)$ .

The fluid dynamics in the thin layer are described by incompressible Euler equations to a first approximation. Radial and azimuthal pressure gradients, derived from (35) in the limit  $\hat{z} \rightarrow 0$ , drive the radial and azimuthal momentum equations respectively. Solutions for the radial and azimuthal velocities satisfy matching conditions obtained from (39) and (40) in the limit  $\hat{z} \rightarrow 0$  and the no-slip condition on the endwall. These solutions are derived from first-order wave equations with coefficients that vary harmonically in time. The characteristics

for these equations,  $\eta = \text{constant}$ , are described by

$$z = M \frac{F(r, \theta)}{\omega} (1 - \cos \omega t - \eta). \quad (67)$$

The axial location of the vorticity front,  $\eta = 0$ , is confined to a region  $z \leq 2 \frac{M}{\omega} \max F(r, \theta)$ , given the harmonic time-dependence in (67). Beyond the front the flow is always irrotational.

Axial gradients of the radial and azimuthal rotational velocity components exhibit non-uniformities when  $\omega t = 0, \pi, 2\pi, \dots$ . This implies that a thinner fundamentally viscous sublayer is needed to resolve the weak singularity.

The rotational analysis near the endwall shows that the irrotational results in Figure 6 at  $\hat{z} = 0.01$  are downstream of the vorticity front as long as  $M\delta < 0.08$ . There are similar implications for the results in Figures 7-10.

#### IV. CONCLUSION

Three-dimensional flow dynamics in a cylinder with sidewall mass addition have been studied to examine the effect of a time-harmonic, non-axisymmetric, axial velocity endwall boundary condition when the driving frequency is close to those of the first few axial acoustic modes. The Navier-Stokes equations have been reduced to a form that can be solved analytically. An asymptotic analysis based on a small axial flow Mach number, compatible with a large aspect ratio cylinder and a large Reynolds number, is used to derive the simplified equations. The non-axisymmetric boundary condition induces a three-dimensional flow that is confined to a region near the endwall of the cylinder. The region's axial length scale is on the order of the cylinder radius. The flow in this core region is incompressible, inviscid, and irrotational. Due to the incompressibility, an acoustic flow does not exist in this region for  $\omega = O(1)$ . The solutions to the reduced form of the Navier-Stokes equations show that;

1. The unsteady radial and azimuthal velocities vanish exponentially fast and the flow becomes planar at the edge of the region.

2. The time-dependent behavior of the axial velocity solution at the downstream edge of the three-dimensional core region drives the planar acoustic waves found farther down the cylinder,
3. A viscous boundary layer exists adjacent to the sidewall. Similar to the flow in the interior core, the boundary layer is incompressible. It is also weakly viscous and contains all three components of vorticity.
4. A very thin inviscid, rotational layer exists adjacent to the endwall. The solution for the radial and azimuthal velocities satisfy the no-slip boundary condition.

The analysis performed here is similar to that describing compact vortex sound. [12] There is an analogy between region II and the incompressible source region of a vortex, where the length scale of the source region is much smaller than that of the acoustic wavelength.

Future work involves studying three-dimensional flow arising from a transient sidewall blowing condition that is  $\theta$ -dependent.

## V. REFERENCES

---

- [1] R. S. Brown and A. M. Blackner. "Coupling Between Acoustic Velocity Oscillations and Solid Propellant Combustion," *Journal of Propulsion and Power*, **2**, 428-437 (1986).
- [2] T. M. Smith, R. L. Roach, and G. A. Flandro. "Numerical Study of the Unsteady Flow in a Simulated Solid Rocket Motor," in *31st Aerospace Sciences Meeting*, AIAA 93-0112 (1993).
- [3] J. D. Baum. "Investigation of Flow Turning Phenomenon," In *27th Aerospace Sciences Meeting*, AIAA 89-0297, (1989).

- [4] F. Vuillot and G. Avalon. "Acoustic Boundary Layers in Solid Propellant Rocket Motors Using Navier-Stokes Equations," *Journal of Propulsion and Power*, **7**, 231–239, (1991).
- [5] R. A. Beddini. "Injection-Induced Flows in Porous-Walled Ducts," *AIAA Journal*, **24**, 1766–1773 (1986).
- [6] F. E. C. Culick. "Stability of Three-Dimensional Motions in a Combustion Chamber," *Combustion Science and Technology*, **10**, 109–124, (1975).
- [7] J. S. Sabnis, H. J. Gibeling, and H. McDonald. "Navier-Stokes Analysis of Solid Rocket Motor Internal Flow," *Journal of Propulsion and Power*, **5**, 657–664 (1989).
- [8] Q. Zhao. "Nonlinear Acoustic Processes in Solid Rocket Engines," *PhD thesis*, University of Colorado at Boulder, (1994).
- [9] Q. Zhao, D. R. Kassoy, and K. Kirkkopru. "Acoustically Generated Vorticity in an Internal Flow," *submitted*, *J. Fluid Mechanics*, 1995.
- [10] J. D. Cole and J. Aroesty. "The Blowhard Problem—Inviscid Flows with Surface Injection," *Int. J. Heat Mass Transfer*, **11**, 1167–1183 (1968).
- [11] F. E. C. Culick. "Rotational Axisymmetric Mean Flow and Damping of Acoustic Waves in a Solid Propellant," *AIAA J.*, **4**, 1462–1463 (1966).
- [12] S. C. Crow. "Aerodynamic Sound Emission as a Singular Perturbation Problem," *Stud. Appl. Math.*, **49**, 21–44 (1970).
- [13] Q. Zhao, D. R. Kassoy, and K. Kirkkopru. "Nonlinear Vorticity Generation in a Cold Flow Model of a Solid Rocket Motor," *submitted to J. Fluid. Mech.*, (1997).

FIG. 1. A radial cut through a cylinder of length  $L'$  and radius  $R'$ . There is a  $(r', \theta, t')$ -dependent axial velocity disturbance at the endwall  $z' = 0$ . A pressure node is imposed at the open end,  $z' = L'$ . On the sidewall  $r' = R'$ , fluid is injected at a constant speed  $V'_{r0}$ . The aspect ratio is  $\delta = \frac{L'}{R'} \gg 1$ .

FIG. 2. Flow regions within the cylindrical vessel investigated in this work. Zhao et al.[9] studied region I, characterized by co-existing rotational and planar acoustic flow. Regions II and III are studied in the present work.

FIG. 3. A graphical representation of the eigenfunctions  $\sin \theta$  and  $\sin 2\theta$  in the region II of the tube. The eigenfunction  $\sin \theta$  is not symmetric about the center of the tube because no diameter can be drawn which crosses only "+" regions or only "-" regions. The eigenfunction  $\cos \theta$  is also not symmetric. On the other hand,  $\sin 2\theta$  is symmetric, as are  $\sin n\theta$ , and  $\cos n\theta$ ,  $n \geq 2$ . The only flows with mass across the centerline as those with a nonzero  $\sin \theta$  or  $\cos \theta$  component, ( $a_{m1}$  or  $b_{m1}$  nonzero).

FIG. 4. Example endwall condition:  $V_z = r^2(1 - r)^2 \sin^2(\frac{\theta}{2}) \sin \omega t$ , for  $\omega = 1$  at  $t = \frac{\pi}{2}$ .

FIG. 5. Axial cross sections of the pressure for  $\omega = 1$  and  $t = \frac{\pi}{4}$ . Only the decaying part of the pressure in (35), defined as  $P_D$ , is plotted at axial locations  $\hat{z} = 0.01, 0.1, 0.25$  and  $1.0$ . The maximum absolute value of  $P_D$  at  $\hat{z} = 1.00$  is about 14% of the analogous value at  $\hat{z} = 0.01$ . The parameter values are  $\delta = 20$ ,  $Re = 10^6$ , and  $M = 0.01$ , which give a viscous length scale at the endwall of  $O(10^{-3})$ .

FIG. 6. Two-dimensional vector field plot showing only the radial and azimuthal velocities. A cross-section is taken along the plane  $\hat{z} = 0.01$  for the endwall velocity condition:  $V_z = r^2(1 - r)^2 \sin^2(\frac{\theta}{2}) \sin \omega t$  with  $\omega = 1$  and  $t = \frac{\pi}{2}$ . The symmetry about a line connecting  $\theta = 0$  and  $\theta = \pi$ , corresponds to the symmetry in the endwall velocity condition. There is net flow from the left to right side of the line connecting  $\theta = \frac{\pi}{2}$  and  $\theta = -\frac{\pi}{2}$ .

FIG. 7. Two-dimensional vector field plot showing only the radial and axial velocities. A cross-section is taken axially with  $\theta = 0$ , (for values  $y > 0$ ,  $y = r$ ), and  $\theta = \pi$ , (for values  $y < 0$ ,  $y = -r$ ), and velocity condition,  $V_z = r^2(1 - r)^2 \sin^2(\frac{\theta}{2}) \sin \omega t$ , for  $\omega = 1$  and  $t = \frac{\pi}{2}$ . There is net flow from the bottom to the top of the plot, representing flow across the centerline. There is a region of high velocity near  $y = -0.5$ , which is due to the high flow region at  $\theta = \pi$  and  $r = \frac{1}{2}$  of Figure 4. Nearly planar flow is found near  $\hat{z} = 1$ .

FIG. 8. Two-dimensional vector field plot showing only the radial and axial velocities. The cross-section shown is for  $\theta = -\frac{\pi}{2}$ , ( $y < 0$ ,  $y = -r$ ), and  $\theta = \frac{\pi}{2}$ , ( $y > 0$ ,  $y = r$ ) Again, the endwall velocity condition used is  $V_z = r^2(1 - r)^2 \sin^2(\frac{\theta}{2}) \sin \omega t$ , for  $\omega = 1$  and  $t = \frac{\pi}{2}$ . Symmetry with respect to the centerline in this plot is due to the symmetry of the endwall velocity condition in Figure 4. The flow near  $\hat{z} = 1$  is nearly planar.

FIG. 9. Azimuthal velocity profiles near the sidewall,  $r = 1$ , at  $t = 6, 7.5, 9, 10.5, 12$ , for  $\omega = 1$ ,  $Re = 10^5$ ,  $\delta = 20$ ,  $M = 0.01$ ,  $\hat{z} = 0.01$  and  $\theta = \frac{\pi}{2}$ . The plot shows the boundary layer structure through almost a full cycle of the velocity boundary condition in 7.

FIG. 10. Azimuthal velocity profiles near the sidewall,  $r = 1$ , at  $t = 6, 7.5, 9, 10.5, 12$ , for  $\omega = 0.8$ ,  $Re = 10^5$ ,  $\delta = 20$ ,  $M = 0.01$ ,  $\hat{z} = 0.01$  and  $\theta = \frac{\pi}{2}$ . The plot shows the boundary layer structure through three-quarters of a cycle of the velocity boundary condition in (7). It is noted that the boundary layer thickness is larger than that in Figure 9, where  $\omega = 1$ .

Figure 1: Staab and Kassoy

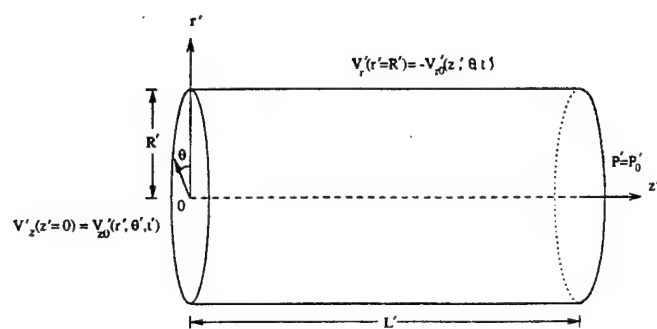




Figure 2: Staab and Kassoy

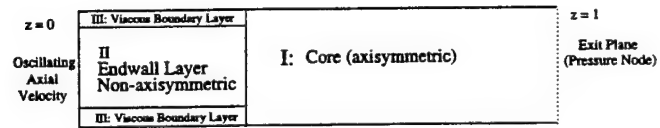


Figure 3: Staab and Kassoy

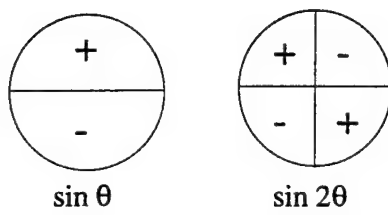


Figure 4: Staab and Kasoy

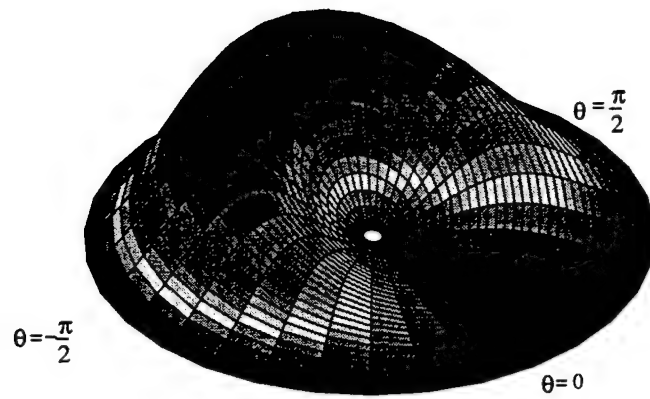


Figure 5: Staab and Kassoy

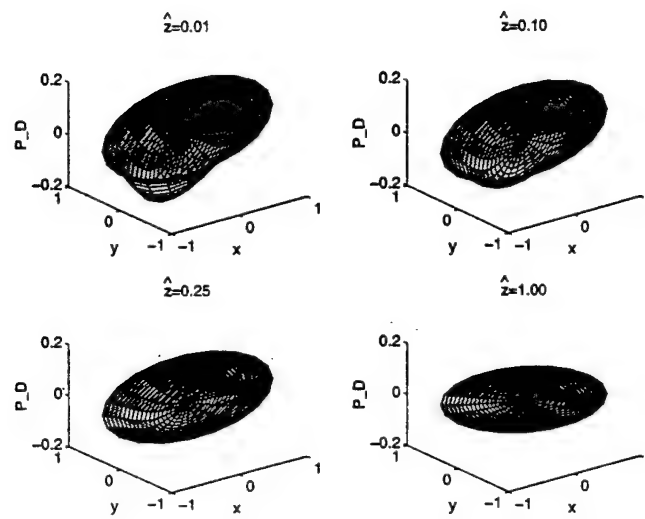


Figure 6: Staab and Kassoy

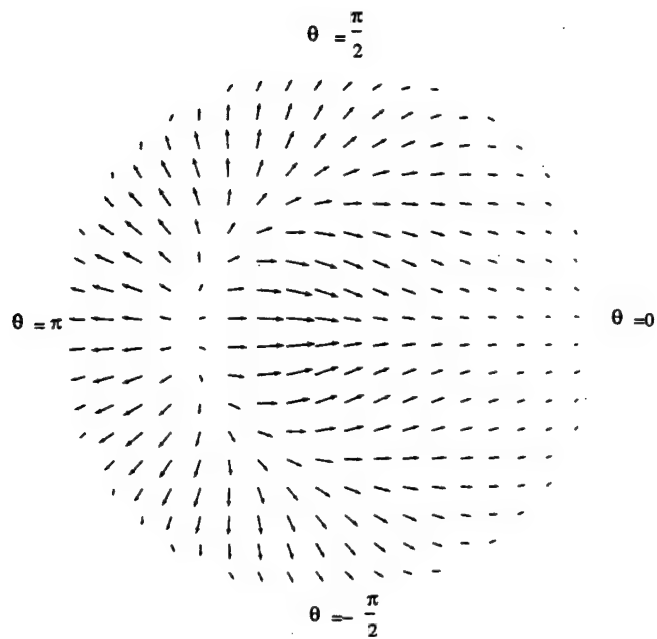


Figure 7: Staab and Kassoy

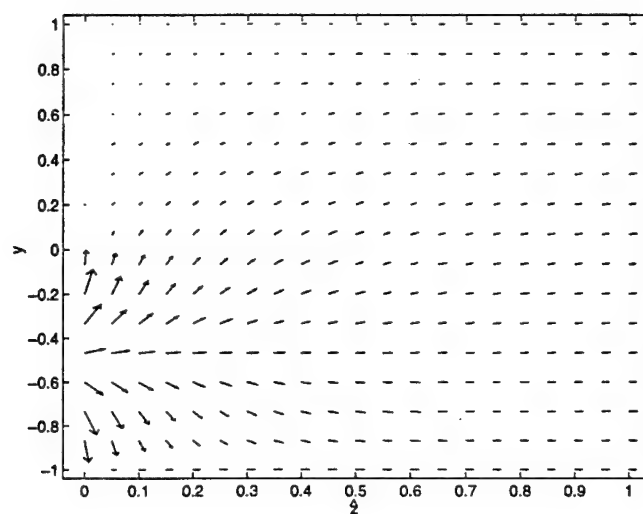


Figure 8: Staab and Kassoy

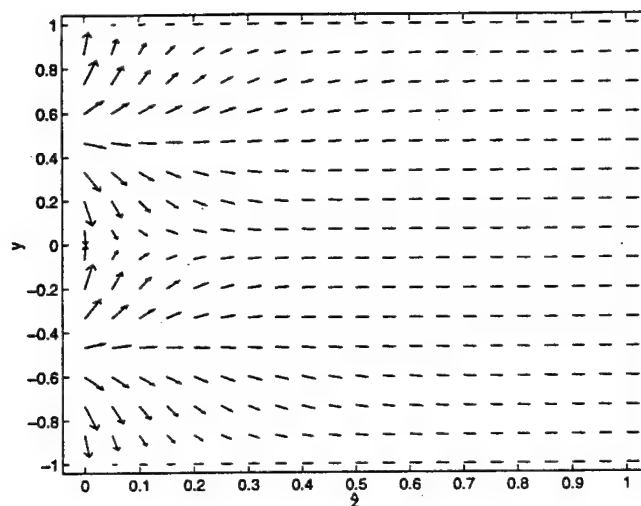


Figure 9: Staab and Kassoy

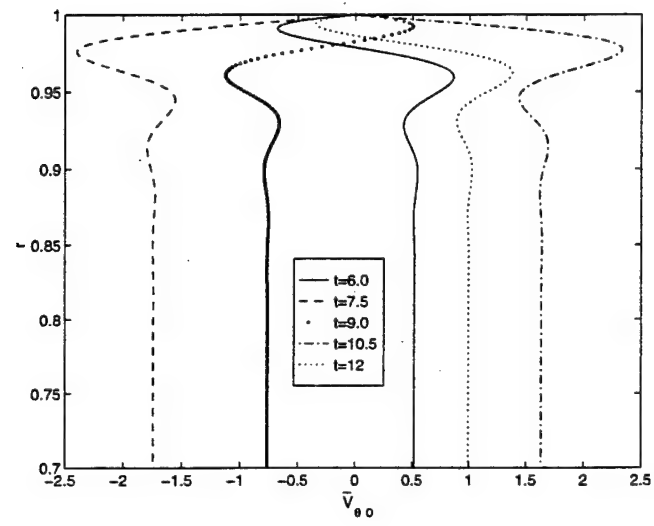
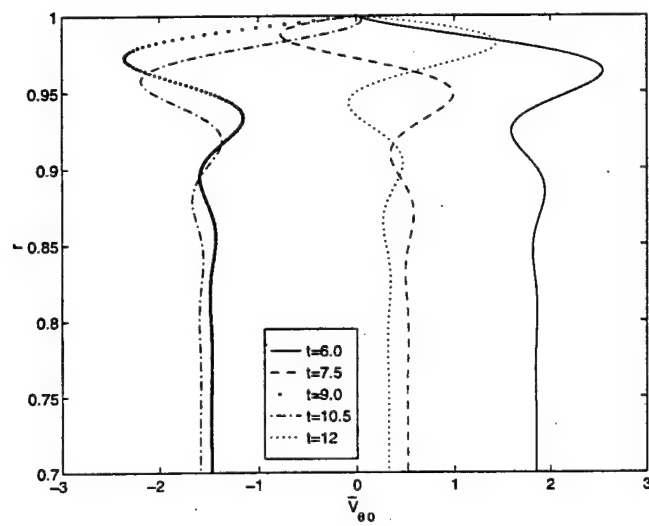




Figure 10: Staab and Kasoy



# Acoustically Generated Vorticity in an Internal Flow\*

Q. Zhao<sup>†</sup>, D. R. Kassoy<sup>‡</sup> and K. Kirkkopru

Mechanical Engineering Department;

Center for Combustion Research

University of Colorado at Boulder; Boulder, CO 80309-0427

## Abstract

A mathematical model is formulated to describe the initiation and evolution of intense unsteady vorticity in a low Mach number ( $M$ ), weakly viscous internal flow sustained by mass addition through the side wall of a long, narrow cylinder. An  $O(M)$  axial acoustic velocity disturbance, generated by a prescribed harmonic transient endwall velocity, interacts with the basically inviscid rotational steady injected flow to generate time dependent vorticity at the side wall. The steady radial velocity component convects the vorticity into the flow. The axial velocity associated with the vorticity field varies across the cylinder radius and in particular has an instantaneous oscillatory spatial distribution with a characteristic wave length  $O(M)$  smaller than the radius. Weak viscous effects cause the vorticity to diffuse on the small radial length scale as it is convected from the wall toward the axis. The magnitude of the transient vorticity field is larger by  $O(M^{-1})$  than that in the steady flow.

An initial-boundary value formulation is employed to find nonlinear unsteady solutions when a pressure node exists at the downstream exit of the cylinder. The complete velocity consists of a superposition of the steady flow, an acoustic (irrotational) field and the rotational component, all of the same magnitude.

---

\*Research is supported by the Air Force Office of Scientific Research through AFOSR 89-0023

<sup>†</sup>Mailing address: Applicon Inc; 6260 Lookout Rd; Boulder, CO 80301

<sup>‡</sup>Mailing address: Office of Academic Affairs B-40; University of Colorado, Boulder, CO 80309

# 1 Introduction

Intense transient vorticity can be generated in a tubular internal flow by an interaction between a forced acoustic field and fluid injected normally from the cylinder sidewall. At a given axial location, the transient axial gradient of the acoustic pressure drives time-dependent wall shear stress variations. The resulting radial gradient in the axial speed is convected into the cylinder by the injected flow field so that one finds coexisting irrotational and rotational disturbances of the same magnitude.

The spatial distribution and time-history of the vorticity depend upon the characteristic amplitude of the wall injection speed ( $V'_{r0}$ ), the length ( $L'$ ) and radius ( $R'$ ) of the cylinder, the frequency of the acoustic forcing ( $\omega'$ ), and the fluid properties. It follows that the crucial nondimensional parameters include, the flow Reynolds (Re) and Mach (M) numbers along with the aspect ratio ( $\delta$ ) and a frequency ( $\omega$ ), all defined below.

The intense transient vorticity is confined to a viscous acoustic boundary layer, small in transverse dimension with respect to the cylinder radius, when the wall injection speed is sufficiently small. As the injection rate increases, the boundary layer thickness grows and the importance of viscous forces is reduced, relative to the axial pressure gradient effect. Eventually, the boundary layer concept is invalid, the flow is only weakly viscous and transient vorticity is present throughout the cylinder. The objective of the present work is to describe a mathematical formulation based on perturbation methods, valid for wall injection rates sufficiently large to preclude the viability of the viscous acoustic boundary layer model. Solutions to the model describe the time-history of the coexisting acoustic and rotational flow fields.

Flandro (1974) provides an early assessment of the importance of vorticity in an acoustic boundary layer. He studies the impact of a small axial pressure gradient, varying harmonically in time, on the viscous processes occurring adjacent to a surface from which a steady, spatially uniform transverse injection occurs. A linear equation for axial velocity contains a balance of convection, pressure gradient forces and viscous diffusion. The solution describes a shear wave convecting away from the wall, with an amplitude that is damped by viscous effects. One finds intense, transient vorticity in the boundary layer, relative to the weaker steady vorticity associated with the inviscid, rotational Culick (1966) solution valid beyond the boundary layer. The solution is valid only when the small injection Mach number  $M_b = O(R_A^{-1/2})$  where  $R_A \gg 1$  is the appropriate acoustic Reynolds number for the chamber. Related work has been described by Tien (1972) and Flandro (1986).

Important extensions of Flandro's concepts have been developed by Zinn and coworkers (Hegde et. al., 1986, Hegde and Zinn, 1986, Sankar et. al., 1988a,b, Chen et. al., 1990, Matta and Zinn 1993) in the context of acoustic boundary layers that are thin relative to the transverse dimension of the internal flow. These research efforts are motivated by the need to understand how energy is transferred from the axial acoustic field to the fluid injected from the sidewall as the latter is turned toward the axial flow direction from its initially transverse motion (flow turning). Hegde et. al. (1986) recognized explicitly that for sufficiently large injection rates, "...the boundary layer may encompass a significant portion of the duct..." and that in this case "...viscous effects must then be included in the analysis of the (entire chamber)". However, there was no specific modeling of this particular situation.

The pervasive presence of rotational disturbances throughout an injected internal flow was first demonstrated in the experiments of Brown et. al. (1986a,b), Brown (1986) and, Brown and Schaeffer (1992). They injected gas through the porous side-

wall of a cylinder/nozzle configuration. A periodic mass injection technique is used to induce single frequency disturbances into the system. Hot wire measurements of the time-averaged axial velocity field at numerous axial and radial locations are used to show that large, local radial gradients of the time-averaged axial velocity are present across the entire cylinder cross section, with a characteristic length scale far smaller than the radius. The associated radial spatial oscillations in the axial speed are not compatible with profiles predicted by a traditional acoustic analysis, (Culick and Yang 1992), although associated pressure variations appear to be purely acoustic in character. The experimental observations suggest that the need for a mathematical model of the disturbed, sidewall injected flow system that can deal with coexisting acoustic and rotational flow processes throughout the chamber geometry, as well as resolve transverse flow processes on radial length scales short with respect to the overall transverse dimension of the chamber geometry.

Vuillot and Avalon (1991) and Vuillot (1995) have repeatedly emphasized the importance of vorticity in these injected internal unsteady flows. They point out that the assumptions built into the acoustic stability theory reviewed extensively by Culick and Yang (1992) have the effect of "... cancelling all trace of vorticity of the flows". In particular, the velocity perturbation is proportional to the gradient of the pressure perturbation. Clearly, an irrotational formulation cannot account for the highly rotational, unsteady flow field observed in experiments, and seen in the computational results described below.

Flandro and Roach (1992) describe an initial attempt at developing an analytically based model of the Brown and coworker experiments. A more complete version is given in Flandro (1995a) where a theory is developed for coexisting transient vorticity and acoustic waves throughout a cylindrical chamber. The steady, inviscid rotational Culick (1966) solution, associated with a uniform injection Mach number  $M_b \ll 1$ , is disturbed by a smaller  $O(\epsilon)$  acoustic velocity that varies harmonically in time. Perturbation methods valid for  $M_b \rightarrow 0$  and a linear stability approach are used to derive an inviscid, linear, small disturbance equation for the rotational part of the axial velocity, which is assumed to have quasi-steady time dependence.

The solution satisfies the no-slip condition on the sidewall, and symmetry conditions on the axis. The equation itself can be used to show that the amplitude of the vorticity generated at the sidewall surface is  $O(\epsilon/M_b^2)$  relative to the vorticity associated with the steady Culick profiles. Hence for sufficiently large values of  $\epsilon$  the transient vorticity can be more intense than is the steady field vorticity. The rotational axial velocity solution is characterized by shear waves of small radial length scale that are convected into the cylinder by the steady Culick velocity components. The time-averaged axial velocity variation with radius is qualitatively similar to the spatial oscillations observed experimentally by Brown and co-workers.

Flandro(1995a) notes that viscous effects will have a minor impact on the inviscid rotational solution for the vorticity distribution, using an argument based on his earlier viscous acoustic boundary layer theory, Flandro(1974). That work is valid mathematically only adjacent to the injection surface because the transverse speed is assumed to be constant. Hence it appears unlikely that the results can be applied to the entire cylinder, where the radial speed must vanish at the centerline.

A more systematic effort is made to consider the impact of viscosity in Flandro (1995b), in the context of small disturbance, linear stability theory. As in the previous paper the asymptotic methods, valid for  $M_b \rightarrow 0$ , are applied in an intuitive manner. It is not always apparent why terms in equations are included or neglected. The results of the linear analysis suggest that viscous effects are most important near the centerline of the cylinder, a result quite different from conclusions of the present work.

Majdalani and Van Moorhem (1996) also describe a small disturbance, linear stability theory that includes the impact of viscosity on the vorticity distribution. Their formulation is based on a limit of large acoustic Reynolds number with the injection Mach number,  $M_b$ , fixed. Solutions are assumed to have quasi-steady time dependence. The results can be interpreted to mean that vorticity is weak but pervasive throughout the cylindrical flow.

Significant efforts have been made to develop multidimensional computational models for wall injected internal flow including the resolution of the identifiable layers containing rotational flow. Baum and Levine (1987) used the Navier-Stokes (N.S.) equations to evaluate the internal flow response to imposed disturbances. Baum (1989, 1990) has used the Reynolds averaged compressible Navier-Stokes equations, including  $k - \epsilon$  model, to carry out initial value solutions for the transient flow in a cylindrical geometry. Sidewall injection is steady and uniform and disturbances are created by a prescribed harmonic variation of the axial speed on the endwall (piston effect). Results are obtained for  $R_A = 3(10^7)$  and  $M_b = 2.2(10^{-3})$ . Acoustic boundary layers adjacent to the injecting surface, containing significant radial gradients of the axial velocity, appear to be quite thin, usually confined to a few percent of the cylinder radius. In one case vorticity is seen as far as about 20% of the radius from the sidewall. These results are quite different from the experimental observations of Brown and co-workers which appear to include coexisting vorticity and acoustic waves across the entire cylinder. The difference likely rises from (a) the distribution of grid points across the cylinder (most are packed close to the sidewall in anticipation of traditional acoustic boundary layer behavior), and (b) short run times (not enough time has elapsed after the introduction of the disturbance to convect the vorticity generated at the sidewall very far out into the cylinder). The former condition implies that the computation can resolve the short length scale radial gradients only in the vicinity of the sidewall. Even if the vorticity convects beyond the region with sufficient grid resolution, its presence cannot be discriminated by the larger grids in the central portion of the cylinder.

Vuillot and Avalon (1991) use laminar Navier-Stokes equations to develop an initial value study for flow in a planar rectangular chamber where a prescribed harmonic disturbance in pressure is applied on the exit plane. The calculation is carried out for  $R_A = 3(10^4)$  and  $M_b = 0.0098$ , corresponding to a relatively viscous system. Here again the transverse gridding is packed near the wall, although a finer resolution is present further out into the field than in the Baum work. The computation times are long enough for the vorticity generated at the wall to reach the centerline. Significant transverse gradients in the axial velocity (vorticity) are found out to about 50% of the half height of the rectangle.

Smith, Roach and Flandro (1993) also find vorticity present in a large portion a cylindrical geometry. Their computation is done to simulate the Brown and co-worker experiments. Significant radial gradients in the axial velocity are seen about half way out toward the centerline. Here again, the run times are sufficiently long to move the vorticity well away from the injection surface, and the gridding distribution enables it to be resolved, at least part way out into the cylinder. The authors suggest that the spatial resolution may not be adequate further out into the cylinder.

Acoustic processes in a thermally active internal flow with combustion have been studied computationally by Tseng, et. al. (1994), based on the use of the compressible N.S. equations. Steady, spatially uniform injection of a propane-air mixture occurs at the porous sidewall of a planar, rectangular geometry. A small (2%,) time-dependent harmonic pressure disturbance is applied at either the head end (traveling wave solutions) or the exit plane (standing wave solutions) of the chamber. Vorticity, as

represented by large transverse gradients in the axial velocity, is found in a thin layer near the injecting surface, on the order of 10-15% of the channel half height. This confinement of the rotational flow distribution is due in part to short run times and in part to a coarse grid distribution in the central portion of the rectangle. It is important to note that flame resolution requires a significant number of points near the injection surface, and not surprisingly the vorticity is seen most strongly in this highly resolved region.

Roh and Yang (1995) have done a similar computation for combustion processes associated with double base propellants. Longer run times and better spatial resolution leads to the appearance of vorticity through 75% of the half height of the rectangular height.

The modelling in the present paper is described in terms of a quasi-analytical, asymptotic analysis for an initial-boundary value problem with imposed boundary disturbances of significant magnitude. In contrast to the previously cited small disturbance, linear stability-based theories with quasi-steady time dependence, we study an evolving fully transient flow including the complete acoustic field compatible with the cylindrical geometry and imposed boundary conditions.

Our work focuses on the fluid dynamics occurring in the finite length ( $L'$ ) cylinder of radius  $R'$  with one open end. Steady radial mass addition from the sidewall creates a primarily inviscid rotational internal flow which is affected weakly by viscosity (Taylor 1956, Culick 1966). The characteristic axial flow Reynolds number, and the axial flow Mach number are large and small respectively. The "large" or "massive" injection velocity needed to diminish the significance of viscosity near the sidewall has been considered in the context of injected boundary layer theory by Cole and Aroesty (1968).

Imposed time-dependent axial velocity disturbances on the closed end add transient energy to the internal flow and generate an acoustic field present throughout the cylinder. The characteristic magnitude of the imposed disturbance is chosen to be the same as that of the steady injection induced axial velocity in order to study a relatively large transient response of the system. Axial acoustic waves interact with injected fluid particles to create intense transient, axially distributed vorticity on the sidewall, far larger than that of the primarily inviscid steady rotational flow produced by the sidewall injection alone. The vorticity is convected into the cylinder along pathlines associated with the internal flow.

The transient vorticity is confined to a weakly viscous "transition layer" adjacent to the wall for sufficiently small values of the wall injection speed. This layer thickness is large compared to a viscous acoustic layer, but smaller than the cylinder radius. The convected vorticity is diffused on a transverse scale that is small compared to the transition layer dimension. However, over the latter scale, the accumulated impact of weak diffusion damps out the intense transient vorticity. Beyond the transition layer one finds a "core" flow consisting of the irrotational acoustic field and the less intense steady vorticity.

Transient vorticity is present throughout the cylinder when the wall injection speed is sufficiently large, as defined explicitly by the model. In this case the transient flow field is weakly viscous across the entire cylinder. Again, vorticity is diffused on a short length scale, but the accumulated viscous damping is not sufficient to prevent the eventual appearance of vorticity at all radial locations except on the axis, where symmetry requires a zero vorticity value.

The mathematical model is formulated in terms of an initial value problem with explicit time-dependent forcing conditions on the closed end of the cylinder. A multiple



scale approach is used to describe coexisting phenomena (steady, inviscid rotational flow field; planar, irrotational acoustic wave field; transient, weakly viscous rotational flow field) evolving simultaneously on two, disparate transverse dimensions.

Solutions for the transition layer/core model are given in analytical terms, based on asymptotic expansions in the small axial flow Mach number ( $M$ ). The planar acoustic pressure and axial velocity solutions are eigenfunction expansions appropriate to the geometry and prescribed boundary conditions. Both nonresonant and resonant cases are included. The axial speed in the transition layer depends upon two transverse variables of disparate size. A small scale variable is used to describe relative short wave length spatial oscillations embedded within the transition layer. The amplitude of the oscillations, dependent on the larger scale variable, vanishes exponentially fast as the transition layer edge is approached. Asymptotic properties of the solution are used to define the parameter conditions for which the transition layer/core concept fails, and for which vorticity can be present across the entire cylinder.

A multiple scale approach is used to formulate the model for the co-existing acoustic and rotational flow fields that evolve simultaneously in the cylinder when vorticity may be present at all radial locations. Planar acoustic solutions, composed of a forced mode and eigenmodes, are derived from a linear wave equation driven by a forced endwall boundary condition. The lowest order rotational part of the axial speed field is described by an inviscid, linear first order wave equation. The latter implies that vorticity generated at the sidewall by an axial pressure gradient/injected fluid interaction is convected toward the cylinder axis by the radial component of the injected flow field. For sufficiently small times a sharp front separates the intense transient vorticity initiated at the wall from the much weaker steady vorticity of the Culick (1966) solution. Eventually, the front location asymptotes to the cylinder axis and vorticity is present everywhere.

Although the lowest order vorticity transport process is described by an inviscid equation, a higher order analysis is used to prove that weak viscous and nonlinear effects are pervasive in the flow field for useful values of the significant parameters, including the relatively large boundary disturbance considered here. In particular, vorticity is diffused by viscosity on a length scale short compared with the cylinder radius. The complete initial value solution for the rotational part of the axial speed is derived from a nonlinear diffusion equation using both a truncated dynamical system (Wang and Kassoy 1990 a,b,c, 1992a,b, 1995) and direct numerical computations. Results are given for several parameter values and at various locations in the cylinder. In particular, one may understand how the energy input at the endwall is partitioned between the acoustic and rotational components of the flow field.

Evaluation and interpretation of the results show that a complex vorticity distribution is present throughout the cylinder sufficiently long after the disturbance is initiated at the endwall. In part the spatial variations result from the inclusion of numerous Fourier modes in the acoustic solutions that are responsible for the appearance of the vorticity. Fully computational methods are used by Kirkkopru et al. (1995, 1996a,b) to provide supporting evidence for the solutions found here by quasianalytical means.

## 2 Mathematical Formulation

An internal flow arising from time-invariant side wall mass addition in a cylindrical tube of length  $L'$  and diameter  $D'$  is shown schematically in Figure 1. The oscillatory end wall disturbance in the axial speed  $V_z$  is the source of acoustic waves in the cylinder. A pressure node boundary condition is assumed at the downstream end of the tube.

The complete non-dimensional equations describing the fluid dynamics and acoustics for an axisymmetric system can be written in the form

$$\frac{\partial \rho}{\partial t} + M \left[ \frac{1}{r} \frac{\partial(\rho r V_r)}{\partial r} + \frac{\partial(\rho V_z)}{\partial z} \right] = 0, \quad (1)$$

$$\begin{aligned} \rho \frac{DV_r}{Dt} = & -\delta^2 \frac{1}{\gamma M} \frac{\partial P}{\partial r} + \delta^2 \frac{M}{Re} \left\{ \frac{\partial}{\partial z} \mu \left[ \frac{1}{\delta^2} \frac{\partial V_r}{\partial z} + \frac{\partial V_z}{\partial r} \right] \right. \\ & \left. + 2 \frac{\partial}{\partial r} \mu \left[ \frac{\partial V_r}{\partial r} - \frac{1}{3} \left( \frac{1}{r} \frac{\partial(r V_r)}{\partial r} + \frac{\partial V_z}{\partial z} \right) \right] + \frac{2\mu}{r} \left[ \frac{\partial V_r}{\partial r} - \frac{V_r}{r} \right] \right\}, \end{aligned} \quad (2)$$

$$\begin{aligned} \rho \frac{DV_z}{Dt} = & -\frac{1}{\gamma M} \frac{\partial P}{\partial z} + \delta^2 \frac{M}{Re} \left\{ \frac{\mu}{r} \left[ \frac{1}{\delta^2} \frac{\partial V_r}{\partial z} + \frac{\partial V_z}{\partial r} \right] + \frac{\partial}{\partial r} \mu \left[ \frac{1}{\delta^2} \frac{\partial V_r}{\partial z} + \frac{\partial V_z}{\partial r} \right] \right\} \\ & + 2 \frac{M}{Re} \frac{\partial}{\partial z} \mu \left[ \frac{\partial V_z}{\partial z} - \frac{1}{3} \left( \frac{1}{r} \frac{\partial(r V_r)}{\partial r} + \frac{\partial V_z}{\partial z} \right) \right], \end{aligned} \quad (3)$$

$$\begin{aligned} \rho C_v \frac{DT}{Dt} = & -(\gamma - 1) M P \left[ \frac{1}{r} \frac{\partial(r V_r)}{\partial r} + \frac{\partial V_z}{\partial z} \right] \\ & + \frac{\delta^2 M}{Re} \frac{\gamma}{Pr} \left[ \frac{1}{\delta^2 r} \frac{\partial}{\partial z} \left( kr \frac{\partial T}{\partial z} \right) + \frac{1}{r} \frac{\partial}{\partial r} \left( kr \frac{\partial T}{\partial r} \right) \right] + \frac{M^3 \delta^2}{Re} \Phi, \end{aligned} \quad (4)$$

$$P = \rho T \quad (5)$$

where

$$\frac{D}{Dt} = \frac{\partial}{\partial t} + M \left( V_r \frac{\partial}{\partial r} + V_z \frac{\partial}{\partial z} \right),$$

and  $\Phi$  is the viscous dissipation function. The non-dimensional variables are defined in terms of dimensional quantities (with a prime) by

$$\begin{aligned} \rho = \frac{\rho'}{\rho_0}, P = \frac{p'}{p_0}, T = \frac{T'}{T_0}, V_r = \frac{V_r'}{V_{r0}}, V_z = \frac{V_z'}{V_{z0}}, \\ z = \frac{z'}{L'}, r = \frac{r'}{R'}, t = \frac{t'}{t_a}, k = \frac{k'}{k_0}, \mu = \frac{\mu'}{\mu_0}, C_v = \frac{C_v'}{C_{v0}}. \end{aligned} \quad (6)$$

The reference value  $p_0'$  is the initial static pressure in the cylinder, while the analogous density and temperature values  $\rho_0'$ ,  $T_0'$  respectively represent properties of the injected fluid. The known characteristic injection speed  $V_{r0}'$  is related to the derived characteristic axial speed  $V_{z0}'$  by the approximate mass conservation relationship  $V_{z0}' = \delta V_{r0}'$ . Here, the large aspect ratio  $\delta = \frac{L'}{R'} \gg 1$  and  $R'$  is the tube radius. Characteristic



length scales for the axial and radial variables are defined by  $L'$  and  $R'$  respectively. Time is nondimensionalized with respect to the axial acoustic time  $t'_a = \frac{L'}{C'_0}$ , where  $C'_0 = (\gamma R' T'_0)^{\frac{1}{2}}$  is the characteristic sound speed. The reference material properties  $k'_0$ ,  $\mu'_0$  and  $C'_{v0}$  are defined at temperature  $T'_0$ . The parameter  $\gamma$  is the ratio of specific heats and

$$Re = \frac{\rho'_0 V'_{z0} L'}{\mu'_0}, Pr = \frac{\mu'_0 C'_{p0}}{k'_0}, M = \frac{V'_{z0}}{C'_0}, \quad (7)$$

where typically the Prandtl number  $Pr = O(1)$ , the axial Mach number  $M \ll 1$  and the axial flow Reynolds number  $Re \gg 1$ . It is noted that the Reynolds number used here is  $O(M)$  smaller than the acoustic Reynolds number.

Initially, a steady flow exists in the cylinder, driven by spatially distributed normal injection from the wall where the no-slip condition is satisfied. Symmetry prevails along the axis. The mathematical form of the steady flow boundary conditions may be written as

$$r = 0; \quad V_r = \frac{\partial V_z}{\partial r} = 0, \quad r = 1; \quad V_r = -V_{rw}(z), \quad V_z = 0, \quad T = 1 \quad (8)$$

$$z = 0; \quad V_z = 0, \quad z = 1; \quad P = 1. \quad (9)$$

The steady flow is disturbed at  $z = 0$  by imposing a harmonic end wall axial velocity variation that is independent of the radial coordinate;

$$z = 0; \quad V_z = A \sin \omega t, \quad t \geq 0; \quad 0 \leq r \leq 1, \quad (10)$$

where the amplitude  $A = O(1)$ .

It should be noted that the imposed end wall disturbance, of the same order of magnitude as that of the steady axial speed, is the source of mechanical and thermodynamical disturbances of like magnitude in the gas. These relatively large variations are described by a weakly nonlinear theory that differs from the small disturbance theory used by Flandro (1995).

The sidewall injection is strong in the sense that  $V'_{r0} \gg \frac{V'_{z0}}{Re^{\frac{1}{2}}}$  (Cole and Aroesty 1968), which implies that the parameter combination seen in (2) and (3),  $\delta^2/Re \ll 1$ . The hard blowing condition implies that the flow is basically inviscid, even near the injecting surface, so that no acoustic boundary layer is expected.

### 3 Steady State Flow

The steady state flow generated by time independent mass addition on the side wall can be described in terms of the asymptotic expansions:

$$(P, \rho, T) \sim 1 + M^2(P_{0s}, \rho_{0s}, T_{0s}) + o(M^2), \quad (V_z, V_r) \sim (V_{z0s}, V_{r0s}) + o(1); \quad (11)$$

valid in the limit  $M \rightarrow 0$ . Equation (11) can be used in (1)–(5) to find the leading order equations describing an incompressible, inviscid, rotational flow that satisfies the

no-slip and injection boundary conditions on the side wall and symmetry conditions on the axis, given in (8) and (9)

$$\frac{1}{r} \frac{\partial(rV_{r0s})}{\partial r} + \frac{\partial V_{z0s}}{\partial z} = 0 \quad (12)$$

$$P_{0s} = P_{0s}(z) \quad (13)$$

$$V_{r0s} \frac{\partial V_{z0s}}{\partial r} + V_{z0s} \frac{\partial V_{z0s}}{\partial z} = -\frac{1}{\gamma} \frac{\partial P_{0s}}{\partial z}, \quad (14)$$

The transport terms are excluded from the leading order equations because  $\frac{\delta^2}{Re} \ll 1$ . Equation (13) arises because the aspect ratio  $\delta \gg 1$ . Solutions for the radial and axial velocity, as well as the pressure distribution can be written in the form

$$V_{r0s} = -\frac{V_{rw}(z)}{r} \sin\left(\frac{\pi}{2}r^2\right), \quad V_{z0s} = \left(\pi \int_0^z V_{rw}(\tau) d\tau\right) \cos\left(\frac{\pi}{2}r^2\right), \quad (15)$$

$$P_{0s} = \gamma\pi^2 \int_z^1 \left[ V_{rw}(\hat{z}) \int_0^{\hat{z}} V_{rw}(\tau) d\tau \right] d\hat{z}, \quad (16)$$

where  $-V_{rw}(z) \neq 0$  is an arbitrary time-independent side wall injection distribution. Related solutions can be found in Culick (1966). It should be noted that Balakrishnan et al.(1991) obtained a fully compressible solution valid for  $M = O(1) < 1$ .

## 4 Core/Transition Layer Solutions

Flandro's (1974) viscous acoustic boundary layer theory describes intense, transient vorticity generation and evolution in a layer of nondimensional thickness  $O(R_A^{-\frac{1}{2}})$  where the acoustic Reynolds number  $R_A \equiv Re/M \gg 1$ . The solution is valid formally for a small injection Mach number  $M_b = O(R_A^{-\frac{1}{2}})$ .

It is of interest to develop a theory for larger injection rates, when the transverse dimension of the layer containing vorticity remains smaller than the radius of the cylinder, but is larger than that permitted by Flandro's (1974) model. The conceptual approach focuses first on a central "core" region containing the weak vorticity of the steady solutions in (15) and (16) and irrotational, linear acoustic disturbances of the same magnitude, driven by the prescribed end wall disturbances in (10). The thinner transition layer contains the intense, transient vorticity. A multiple length scale asymptotic analysis, used to develop the solutions, describes how weak but pervasive viscosity affects the flow physics in the transition layer.

The asymptotic expansions for the unsteady core flow can be written as

$$(P, \rho, T) \sim 1 + M \sum_{n=0} M^n (P_n, \rho_n, T_n), \quad (V_z, V_r) \sim \sum_{n=0} M^n (V_{zn}, V_{rn}); \quad (17)$$

in the limit  $M \rightarrow 0$ . Equation (17) can be used in (1)–(5) to derive the lowest order equations, valid in the limit  $M \rightarrow 0$ , with  $\frac{\delta^2}{Re} \rightarrow 0$ ;

$$\frac{\partial \rho_0}{\partial t} + \frac{1}{r} \frac{\partial(rV_{r0})}{\partial r} + \frac{\partial(V_{z0})}{\partial z} = 0; \quad (18)$$

$$\frac{\partial V_{z0}}{\partial t} = -\frac{1}{\gamma} \frac{\partial P_0}{\partial z}, \quad P_0 = P_0(z, t); \quad (19)$$

$$\frac{\partial T_0}{\partial t} = (\gamma - 1) \frac{\partial \rho_0}{\partial t}; \quad (20)$$

$$\rho_0 = P_0 - T_0. \quad (21)$$

The velocity components in (18) are composed of both steady state and a transient parts of the same magnitude;  $(V_{z0}, V_{r0}) = (V_{z0s}, V_{r0s}) + (\tilde{V}_{z0}, \tilde{V}_{r0})$ . Subtraction of the steady state equations (12)-(14) from (18)-(21) provides the transient acoustic mathematical problem. The boundary condition in (10) implies that the radial speed,  $\tilde{V}_{r0} = 0$ .

#### 4.1 The Planar Acoustic Solution in the Core

The transient part of the leading order equations can be combined into a planar wave equation for the axial velocity component:

$$\frac{\partial^2 \tilde{V}_{z0}}{\partial t^2} = \frac{\partial^2 \tilde{V}_{z0}}{\partial z^2} \quad (22)$$

subject to the initial and boundary conditions;

$$t = 0, \quad \tilde{V}_{z0} = 0, \quad \frac{\partial \tilde{V}_{z0}}{\partial t} = 0, \quad (23)$$

$$z = 0, \quad \tilde{V}_{z0} = A \sin \omega t; \quad (24)$$

$$z = 1, \quad \frac{\partial \tilde{V}_{z0}}{\partial z} = 0. \quad (25)$$

where (25) is obtained from (9). The simplicity of the equation can be attributed to the large aspect ratio condition  $\delta \gg 1$ .

The general solution for  $\tilde{V}_{z0}$  is :

$$\begin{aligned} \tilde{V}_{z0}(z, t)/A &= \sin \omega t \\ &+ \sum_{n=0, n \neq n^*}^{\infty} \left\{ -\frac{2\omega}{b_n^2} \left[ \left( \frac{b_n^2}{b_n^2 - \omega^2} \right) \sin(b_n t) - \frac{b_n \omega}{b_n^2 - \omega^2} \sin(\omega t) \right] \right\} \sin(b_n z) \\ &- \left\{ \left( \frac{1}{b_{n^*}} \right) \sin(b_{n^*} t) + t \cos(b_{n^*} t) \right\} \sin(b_{n^*} z), \end{aligned} \quad (26)$$

where  $b_n = (n + \frac{1}{2})\pi$ . The last term describes a resonant effect present only when  $\omega = b_{n^*}$  and cannot be found from a quasi-steady analysis. The solution provides insight into the properties of the acoustical field compatible with the cylindrical geometry and prescribed boundary conditions.

- The first term itself and the second part of the nonresonant Fourier series represent quasi-steady motion at the driving frequency. The other Fourier series terms can each be decomposed into two counter-propagating planar travelling waves.

- If  $\omega$  is very close to one of the natural frequencies, then beats will appear due to the interaction between the quasi-steady motion and one pair of travelling waves.
- Resonance occurs when  $\omega = b_n$ , and the amplitude of one mode grows linearly with time.

Table 1 contains results for a system where  $t'_A = 10^{-3}$  s, so that dimensional frequencies can be considered. When  $\omega' \approx 159$  Hz, the response shown in Figure 2 for  $\tilde{V}_{z0}$  at  $z = 0.5$  is bounded and the contributions are primarily from the first few forced modes and the first few axial travelling modes. A beat is observed in Figure 3 when  $\omega' \approx 238$  Hz. The period of the beat, about 90 time units, arises from the interaction between the driven frequency  $\omega = 1.5$  and the first eigenfunction  $b_0 = \pi/2$ . Linear monotonic amplitude growth seen in Figure 4 is primarily from the resonant axial mode in (26) when  $\omega' = 250$  Hz ( $\omega = b_0 = \pi/2$ ).

The pressure solution  $P_0(z, t)$  can be obtained from a first integral of the unsteady part of (18) and the isentropic relationship  $P_0 = \gamma p_0$ .

## 4.2 Transition Layer Solution

The leading order core acoustic solution in (26) does not satisfy the no-slip boundary condition. Under certain conditions to be defined quantitatively, the transition to zero axial velocity at the wall occurs in a relatively thin transition layer which has a multiple scale structure that differs fundamentally from a traditional viscous acoustic boundary layer (Flandro, 1974). In particular the overall radial thickness of the layer is defined by weak viscous considerations. But within it there is a smaller length scale associated with the distance traveled by an injected fluid particle on the time scale  $t'_A = \frac{L'}{C_0}$ .

The hard injection condition  $V'_{r0} \gg V'_{z0}/Re^{\frac{1}{2}}$  implies that the transition layer is inviscid and rotational in the first approximation. Viscous stresses appear in a higher order description, but are essential to finding the complete solution, as might be expected in a multiple scale analysis.

The multiple scale structure is defined in terms of stretched variables that measure distance from the tube wall;

$$\xi = \frac{1-r}{M}, \quad \eta = \frac{1-r}{\beta}, \quad (27)$$

where  $\beta = M^2/(\delta^2/Re)$  if the core/transition layer concept is valid. In order for the total layer thickness to be large compared to the smaller scale feature but small compared to the tube radius,  $M \ll \beta \ll 1$ . The partial derivatives with respect to  $r$  must be replaced by

$$\left(\frac{\partial}{\partial r}\right) = -\frac{1}{M} \left(\frac{\partial}{\partial \xi}\right) - \frac{1}{\beta} \left(\frac{\partial}{\partial \eta}\right), \quad (28)$$

$$\left(\frac{\partial^2}{\partial r^2}\right) = \frac{1}{M^2} \left(\frac{\partial^2}{\partial \xi^2}\right) + \frac{2}{M\beta} \left(\frac{\partial^2}{\partial \eta \partial \xi}\right) + \frac{1}{\beta^2} \left(\frac{\partial^2}{\partial \eta^2}\right). \quad (29)$$

The variables, represented by the asymptotic expansions

$$(P, \rho, T) \sim 1 + \sum_{n=0} M^{n+1} (P_n, \rho_n, T_n), \quad (30)$$

$$V_z \sim V_{z0} + \frac{M}{\beta} V_{z1} + o\left(\frac{M}{\beta}\right), \quad V_r \sim -V_{rw}(z) + o(1), \quad (31)$$

valid in the limit  $M \rightarrow 0$ , are used with (28) and (29) in (1)-(5) to find the first two approximate equation systems for the transition layer.

The lowest order version is,

$$\frac{\partial V_{z0}}{\partial t} + V_{rw} \frac{\partial V_{z0}}{\partial \xi} = -\frac{1}{\gamma} \frac{\partial P_0}{\partial z}; \quad P_0 = P_0(z, t). \quad (32)$$

where  $V_{rw}(z)$  is known from (8) and  $P_0(z, t)$  is the acoustic pressure field obtained from (18) and (26). Equation (32) describes an inviscid rotational flow which can satisfy the no-slip boundary condition on the wall. In particular, an evaluation of (32) on the wall  $\xi = \eta = 0$  shows that the transient vorticity distribution created there,

$$\left( \frac{\partial V_{z0}}{\partial \xi} \right)_w = -\frac{1}{\gamma V_{rw}(z)} \frac{\partial P_0(z, t)}{\partial z} \quad (33)$$

depends on both the local pressure gradient time variation and the local injection magnitude. This transition layer vorticity is  $O(M^{-1})$  larger than that associated with the steady solution in (15) and (16), given the stretching transformation in the first of (27).

The convective transport equation for the relatively intense transient vorticity,  $\partial V_{z0}/\partial \xi$ , can be obtained from a  $\xi$ -derivative of (32). In this case, the right hand side vanishes and one finds that vorticity is convected invariantly by the radial wall injection velocity  $V_{rw}$  along well defined characteristic lines,  $\varphi = t - (\frac{\xi}{V_{rw}})$ .

The second order momentum equation is obtained from terms of  $O(\frac{M}{\beta})$ ;

$$\frac{\partial V_{z1}}{\partial t} + V_{rw} \frac{\partial V_{z1}}{\partial \xi} = -V_{rw} \frac{\partial V_{z0}}{\partial \eta} + \frac{\partial^2 V_{z0}}{\partial \xi^2}, \quad (34)$$

where a viscous stress term associated with  $V_{z0}$  is present, and the pressure gradient is absent since  $\beta \ll 1$ .

The acoustic solution in the core must match with the transition layer solutions at the outer edge ( $\xi \rightarrow \infty, \eta \rightarrow \infty$ ), and the no-slip condition on the side wall provides an inner boundary condition for (32) and (34). The acoustic core solution in (26) shows that, all the terms can be classified into the following two forms:  $\bar{V}_{z0}(z)e^{i\Omega t}$  with  $\Omega = \omega$  or  $b_n$ ,  $\bar{V}_{z0}(z) = \sin b_n z$ , and  $-t \cos(b_n t) \sin(b_n z)$ . It follows that;

$$\xi = \eta = 0, \quad V_{z0} = 0; \quad (35)$$

$$\xi, \eta \rightarrow \infty; \quad V_{z0} \sim \bar{V}_{z0}(z, t). \quad (36)$$

with the latter from (26).

Equations (32)–(36) are used first to find quasi-steady solutions to each relevant frequency in the core solution. For any of the nonresonant modes  $\Omega = \omega$  or  $b_n$  but  $\omega \neq b_n$  for any integer  $n$ , the transition layer solutions can be written as

$$V_{z0} = F(\xi, \eta, z)e^{i\Omega t}; \quad V_{z1} = G(\xi, \eta, z)e^{i\Omega t}. \quad (37)$$

These solution forms can be substituted into (32) and (34) to determine  $F$  and  $G$ . The former found from (32), (35) and (36), is

$$F(\xi, \eta, z) = C(\eta, z) \exp\left(-\frac{i\Omega}{V_{rw}}\xi\right) + \bar{V}_{z0} \quad (38)$$

where the undetermined coefficient function  $C(\eta, z)$  must satisfy the conditions

$$\eta = 0; \quad C = -\bar{V}_{z0}(z), \quad (39)$$

$$\eta \rightarrow \infty; \quad C = 0. \quad (40)$$

Equation (34) can then be rewritten in terms of  $G$  and  $C$  as

$$\frac{\partial G}{\partial \xi} + \frac{i\Omega}{V_{rw}}G = -\exp\left(-\frac{i\Omega}{V_{rw}}\xi\right) \left[ \frac{\partial C}{\partial \eta} + \frac{\Omega^2}{V_{rw}^3}C \right] \quad (41)$$

where the second term in brackets arises from viscous effects.

In order to avoid secular growth of  $G$  with respect to the variable  $\xi$ , the quantities in the square bracket must be set to zero. Therefore,

$$\frac{\partial C}{\partial \eta} + \frac{\Omega^2}{V_{rw}^3}C = 0 \quad (42)$$

together with (39)–(40) are solved to find

$$C(\eta, z) = -\bar{V}_{z0} \exp\left(-\frac{\Omega^2}{V_{rw}^3}\eta\right). \quad (43)$$

It follows that the axial velocity variation in the transition layer for each frequency  $\Omega$  has the form:

$$V_{z0}(\xi, \eta, z, t) = -\sin(b_n z) \left\{ \exp\left[-\frac{\Omega^2}{V_{rw}^3(z)}\eta - \frac{i\Omega}{V_{rw}(z)}\xi\right] - 1 \right\} e^{i\Omega t} \quad (44)$$

where  $-V_{rw}(z)$  is the steady side wall injection velocity. The product of the exponential terms in (44) yields that part of the axial velocity component containing the intense transient vorticity of the transition layer;

$$\exp\left(-\frac{\Omega^2}{V_{rw}^3(z)}\eta\right) e^{i\Omega \varphi} \quad (45)$$

where  $\varphi = t - \frac{\xi}{V_{rw}}$  is the characteristic line for vorticity transport. The radial traveling speed for a constant  $\varphi$  line can be described by:

$$\left. \frac{\partial r}{\partial t} \right|_{\varphi} = -M \left. \frac{\partial \xi}{\partial t} \right|_{\varphi} = -MV_{rw}(z) \quad (46)$$

This shows explicitly that the vorticity is convected in the transition layer by the steady wall injection speed.

The first factor in (45) describes amplitude damping arising from viscous effects because the  $\eta$ -variable defined in (27) is scaled with respect to  $Re$ , in part. The second part describes harmonic spatial oscillations associated with the acoustic solution in the core.

When resonant driving is present  $\Omega = \omega = b_{n^*}$ , and the resonant mode representation of  $V_{z0}$  is found in a similar way to be;

$$\begin{aligned} V_{z0}(\xi, \eta, z, t) = & -t \sin(b_{n^*} z) \sin(b_{n^*} t) \\ & + \{ t [\sin(k\xi) \sin(b_{n^*} t) + b_{n^*} \cos(k\xi) \cos(b_{n^*} t)] \\ & - \left[ \frac{\eta}{(1 + b_{n^*})} \cos(k\xi) + \frac{b_{n^*} \xi}{2k^2(1 + b_{n^*})} \sin(k\xi) \right] \sin(b_{n^*} t) \\ & - \frac{1}{\omega} \left[ \frac{V_{rw}^2(z)}{2(1 + b_{n^*})} \xi \cos(k\xi) - \left( 1 - \frac{b_{n^*}^2}{1 + b_{n^*}} \right) \sin(k\xi) \right] \\ & \cos(b_{n^*} t) \} \frac{1}{b_{n^*}} \sin(b_{n^*} z) \exp\left(-\frac{b_{n^*}^2}{V_{rw}^3(z)} \eta\right) \end{aligned} \quad (47)$$

where  $k = \frac{b_{n^*}}{V_{rw}(z)}$ .

When  $\xi = \eta = 0$ , the solutions satisfy the no-slip boundary condition on the wall. On the other hand, when  $\xi$  and  $\eta \rightarrow \infty$ , the core solution is recovered in an oscillatory manner since the amplitude of the exponential term goes to zero harmonically. The effective thickness of the transition layer depends strongly on  $\Omega$  and  $V_{rw}$ . A large value of  $\Omega$  promotes relatively rapid exponential decay, implying that a high frequency disturbance is associated with a thinner transition layer. Alternatively, low frequency forcing fosters thick transition layers. Thus, higher order modes tend to be associated with effectively thinner transition layers. The same type of argument demonstrates that increasing the value of  $V_w(z)$  enhances the overall transition layer thickness.

A complete solution for the axial velocity in the transition layer consists of an infinite sum of terms obtained from (44) and (47); one for each frequency  $\omega$  and  $b_n$  in (26). The spatial structure of such a solution will be quite complex, given the oscillatory dependence on the value of  $\Omega$ . It is perhaps more illustrative to look at the results for a single frequency.

The reduced axial velocity inside the vortical layer,  $\frac{V_{z0}}{[-V_{z0}e^{i\Omega\eta}]}$  is plotted against  $\xi$  in Figure 5 with  $M = 0.01$ ,  $\beta = 0.1$  and  $V_{rw} = 1$  for  $\Omega = 2.5$  and  $\Omega = 3.0$ . The core solution is recovered at about  $\xi = 10$  for  $\Omega = 2.5$  which corresponds to  $r = 0.9$ . In contrast, the transition layer thickness is a little smaller for the higher frequency  $\Omega = 3.0$ . Of course the overall transition layer thickness is determined by the lowest mode in the system.

The viscous factors in (44) and (47) decay exponentially at the edge of the transition layer when  $\eta \rightarrow \infty$ . In dimensional terms, the layer thickness can be characterized by the decay length  $l'_D = (\beta V_{rw}^3 / \Omega^2) R'$  obtained from the dimensional form

of the argument of the exponential in (45) or the analogous term in (47). In order to assure the existence of a thin transition layer,  $l'_D/R' = \beta V_{rw}^3/\Omega^2 \ll 1$ . Given the definition of  $\beta$  below (27), and that the characteristic injection Mach number can be defined by  $M_b = M/\delta$ , it follows that  $\beta = M_b^3 R_A$ , where the acoustic Reynolds number  $R_A \equiv Re/M$ . This shows explicitly that an increase in the characteristic wall injection Mach number will eventually cause the transition layer to be as large as the cylinder radius,  $l'_D = O(R')$  or  $\beta = O(1)$ , so that the core/transition layer concept fails. Then a new multiple scale perturbation technique is needed to find solutions where rotational effects coexist with an acoustic field throughout the cylinder.

## 5 Co-existing Acoustic/Rotational Flow

The failure of the core/transition layer asymptotic model, described in Section 4, when  $\beta = O(1)$  implies that one must develop a mathematical model for coexisting acoustic and rotational disturbances of equal magnitude. Flandro(1995) describes a theoretical formulation for such a situation when the amplitude of the transients is smaller than that of the steady Culick(1966) profiles in (15) and (16). Perturbation methods valid for  $M_b \rightarrow 0$  are used to derive an inviscid, linear equation for the rotational part of the transient axial velocity component. Although the importance of a shorter radial length scale is recognized, a formal multiple length scale analysis is not employed. Further, an intuitive approach is used to determine which terms in the full equations are retained in the lowest order asymptotic analysis. The solution driven by a quasi-steady acoustic field, satisfies the no-slip condition on the sidewall and symmetry conditions at the cylinder axis. It is characterized by harmonically varying shear waves on the short length scale that are convected into the cylinder by the Culick(1966) steady velocity components. The viscous damping of Flandro's (1974) earlier work, like that observed in (44) or (45), is replaced by a nonviscous attenuation function associated with the axial dependence of the acoustic velocity field.

Here, an alternative formulation is developed based on a systematic, fully defined multiple scale analysis that includes the effects of weak viscosity. The asymptotic expansions for the velocity components and thermodynamic variables in the limit  $M \rightarrow 0$  are

$$V_z \sim V_{z0s}(z, r) + \sum_{n=0} M^n V_{zn}(z, r, t) \quad (48)$$

$$V_r \sim V_{r0s}(z, r) + \sum_{n=0} M^n V_{rn}(z, r, t) \quad (49)$$

$$(P, \rho, T) \sim 1 + M \sum_{n=0} M^n (P_n, \rho_n, \theta_n) \quad (50)$$

where the axial speed transient disturbances are as large as the Culick(1966) profiles.

It is recognized that two disparate length scales are important; the tube radius and a much shorter length associated with the radial distance traveled by a fluid particle on the acoustic timescale. A multiple scale analysis will be carried out in terms of the variables  $r_1$  and  $r_2$  defined by

$$r_1 = 1 - r; \quad r_2 = \int_0^{r_1} \frac{1}{-M V_{r0s}(\sigma)} d\sigma. \quad (51)$$



The second transformation includes an integral of the steady radial velocity field for the case of **constant steady wall injection**  $V_{rw} = 1$  which simplifies the describing equations considerably. It is noted that when the center line is approached  $r_1 \rightarrow 1$  the integral diverges and  $r_2 \rightarrow \infty$ .

Each of the dependent variables is written in terms of  $r_1$  and  $r_2$  instead of  $r$  alone. The partial derivatives with respect to  $r$  in equations (1)–(5) must be replaced by

$$\left(\frac{\partial}{\partial r}\right) = -\left(\frac{\partial}{\partial r_1}\right) + \frac{1}{MV_{r0s}} \left(\frac{\partial}{\partial r_2}\right), \quad (52)$$

$$\begin{aligned} \left(\frac{\partial^2}{\partial r^2}\right) &= \left(\frac{\partial^2}{\partial r_1^2}\right) - \left(\frac{2}{MV_{r0s}} \frac{\partial^2}{\partial r_1 \partial r_2}\right) \\ &\quad + \left(\frac{1}{MV_{r0s}}\right)^2 \left(\frac{\partial^2}{\partial r_2^2}\right) + \frac{1}{MV_{r0s}^2} \frac{\partial V_{r0s}}{\partial r_1} \left(\frac{\partial}{\partial r_2}\right). \end{aligned} \quad (53)$$

### 5.1 Lowest order mathematical model

The relations (48)–(50) can be substituted into (1)–(5) to find the leading order equations in the limit  $M \rightarrow 0$ . First, the spatially homogeneous boundary forcing in (10) and the condition  $\delta \gg 1$  imply that  $V_{r0} = 0$ . Then,

$$\frac{\partial R_0}{\partial t} + \frac{\partial R_0}{\partial r_2} = -\frac{\partial V_{z0}}{\partial z} - \left(\frac{1}{V_{r0s}}\right) \frac{\partial V_{r1}}{\partial r_2}, \quad (54)$$

$$\frac{\partial V_{z0}}{\partial t} + \frac{\partial V_{z0}}{\partial r_2} = -\frac{1}{\gamma} \frac{\partial P_0}{\partial z}, \quad (55)$$

$$\frac{\partial P_0}{\partial r_1} = \frac{\partial P_0}{\partial r_2} = 0, \quad (56)$$

$$\frac{\partial \theta_0}{\partial t} + \frac{\partial \theta_0}{\partial r_2} = \frac{(\gamma - 1)}{\gamma} \frac{\partial P_0}{\partial t}, \quad (57)$$

$$P_0 = R_0 + \theta_0. \quad (58)$$

Following a procedure related to that described by Lagerstrom(1964), and similar to that employed by Flandro (1995) the variables, except for  $P_0$ , are divided into coexisting irrotational planar and rotational nonplanar parts of equal magnitude,

$$V_{z0} = W_{0p}(z, t) + \hat{W}_0(z, t, r_1, r_2), \quad (59)$$

$$R_0 = R_{0p}(z, t) + \hat{R}_0(z, t, r_1, r_2), \quad (60)$$

$$\theta_0 = \theta_{0p}(z, t) + \hat{\theta}_0(z, t, r_1, r_2). \quad (61)$$

Equations (59)–(61) can be used in (54)–(58) to show that the planar functions are described by an irrotational acoustic system

$$\frac{\partial R_{0p}}{\partial t} = -\frac{\partial W_{0p}}{\partial z}, \quad (62)$$

$$\frac{\partial W_{0p}}{\partial t} = -\frac{1}{\gamma} \frac{\partial P_0}{\partial z}, \quad P_0 = P_0(z, t), \quad (63)$$

$$\frac{\partial \theta_{0p}}{\partial t} = \frac{\gamma - 1}{\gamma} \frac{\partial P_0}{\partial t}, \quad (64)$$

$$P_0 = R_{0p} + \theta_{0p}, \quad (65)$$

nearly identical to (18)—(21).

The initial/boundary conditions are:

$$t = 0, \quad W_{0p} = 0, \quad \frac{\partial W_{0p}}{\partial t} = 0, \quad (66)$$

$$z = 0, \quad W_{0p} = A \sin \omega t; \quad (67)$$

$$z = 1, \quad \frac{\partial W_{0p}}{\partial z} = 0. \quad (68)$$

in analogy to (23)—(25).

The nonresonant acoustic solution for the planar contribution is

$$W_{0p}(t, z)/A = - \sum_{n=1}^{\infty} a_n \left( \frac{\lambda_n}{\omega} \sin(\omega t) - \sin(\lambda_n t) \right) \sin(\lambda_n z), \lambda_n \neq \omega, \quad (69)$$

$$P_0(t, z)/A = \gamma \sum_{n=1}^{\infty} a_n (-\cos(\omega t) + \cos(\lambda_n t)) \cos(\lambda_n z), \lambda_n \neq \omega, \quad (70)$$

$$P_0 = \gamma R_{0p} \quad (71)$$

where  $a_n = -\frac{2\omega}{\lambda_n^2 - \omega^2}$  and  $\lambda_n = (n - \frac{1}{2})\pi$ . Equation (69) is equivalent to (26) for the nonresonant case. The first term in the sums of (69) and (70) arises from forcing at frequency  $\omega$ , and the second term describes the eigenfunction response. Only the nonresonant case will be considered in the present work.

The equations for the rotational components are

$$\frac{\partial \hat{R}_0}{\partial t} + \frac{\partial \hat{R}_0}{\partial r_2} = -\frac{\partial \hat{W}_0}{\partial z} - \left( \frac{1}{V_{r0s}} \right) \frac{\partial V_{r1}}{\partial r_2}, \quad (72)$$

$$\frac{\partial \hat{W}_0}{\partial t} + \frac{\partial \hat{W}_0}{\partial r_2} = 0, \quad (73)$$

$$\frac{\partial \hat{\theta}_0}{\partial t} + \frac{\partial \hat{\theta}_0}{\partial r_2} = 0, \quad (74)$$

$$\hat{R}_0 + \hat{\theta}_0 = 0. \quad (75)$$

Equations (74) and (75) can be combined to show that the leading order vortical flow is incompressible:

$$\frac{\partial \hat{R}_0}{\partial t} + \frac{\partial \hat{R}_0}{\partial r_2} = 0 \quad (76)$$

Therefore, (72) can be rewritten as

$$\frac{\partial \hat{W}_0}{\partial z} + \left( \frac{1}{V_{r0s}} \right) \frac{\partial V_{r1}}{\partial r_2} = 0, \quad (77)$$

which can be used to find  $V_{r1}$  once  $\hat{W}_0$  is known.

The relevant initial and boundary conditions are

$$t = 0; \quad \hat{W}_0 = 0, \quad \frac{\partial \hat{W}_0}{\partial t} = 0, \quad (78)$$

$$z = 0; \quad \hat{W}_0 = 0, \quad (79)$$

$$z = 1; \quad \frac{\partial \hat{W}_0}{\partial z} = 0, \quad (80)$$

$$r_1 = 1, \quad r_2 \rightarrow \infty; \quad \frac{\partial \hat{W}_0}{\partial r_2} = 0, \quad \frac{\partial \hat{\theta}_0}{\partial r_2} = 0, \quad (81)$$

$$r_1 = r_2 = 0; \quad \hat{W}_0 = -W_{0p}(t, z), \quad \hat{\theta}_0 = -\theta_{0p}(t, z) \quad (82)$$

The first of (81) can be combined with (73) and the initial condition (78) to prove that  $\hat{W}_0 = 0$  on the axis  $r_1 = 0$  for all  $t$ . Equation (82) corresponds to the no-slip condition and isothermal flow injection. Equations (73), (74) and (76) show that  $\hat{W}_0$ ,  $\hat{\theta}_0$  and  $\hat{R}_0$  are invariant on a characteristic line defined by

$$\eta = t - r_2, \quad (83)$$

but vary across the  $\eta$  lines. On the sidewall ( $r_2 = 0$ ), the  $\eta = 0$  line appears at  $t = 0^+$  and subsequently, at  $t = c > 0$ ,  $\eta = c$  appears. At a particular time  $T$ , constant  $\eta$  lines, which range in value from 0 to  $T$ , are transported toward the axis by convection at the local radial steady velocity, as found from a time derivative of (83) after using (51).

The inviscid equation in (73) can be combined with the first of (82) and (63) to show that vorticity is produced on the sidewall by the transient axial gradient of the acoustic pressure field,

$$\frac{\partial \hat{W}_0(t, z, 0, 0)}{\partial r_2} = -\frac{\partial \hat{W}_0}{\partial t} = \frac{\partial W_{0p}(t, z)}{\partial t} = -\frac{1}{\gamma} \frac{\partial P_0}{\partial z} \quad (84)$$

where  $W_{0p}$  and  $P_0$  are given in (69) and (70). Equation (84) is analogous to (33) in the core/transition layer description. It is noted that the largest unsteady nondimensional vorticity term is given by  $\Omega_\theta = (\frac{1}{M V_{r0s}}) \frac{\partial \hat{W}_0}{\partial r_2}$ . The parameter,  $\frac{1}{M}$ , arises from large gradients occurring in the spatially oscillatory velocity profile on the short length scale  $r_2$ . Equation (73) also shows that the vorticity generated at the wall is convected into the cylinder by the steady radial velocity field  $V_{r0s}(r)$ .

It should be noted that the inviscid equation for  $\hat{W}_0$  in (73) differs from Flandro's(1995) analogous equation which includes an axial convection term proportional

to  $\frac{\partial \hat{W}_0}{\partial z}$ . The latter is retained on the basis of an intuitive rather than a formal asymptotic argument.

In general, solutions to the inviscid first order hyperbolic equations in (73)–(75) can be written symbolically as,

$$\hat{W}_0 = \hat{W}_0(\eta, r_1, z), \quad \hat{\theta}_0 = \hat{\theta}_0(\eta, r_1, z) = -\hat{R}_0, \quad \eta = t - r_2 \quad (85)$$

If the no-slip and isothermal boundary conditions (see (8) and (82)) are satisfied, then one finds results on  $r_1 = 0$ ;

$$\hat{W}_0(\eta, 0, z) = -W_{0p}(\eta, z), \quad \hat{\theta}_0(\eta, 0, z) = -\frac{(\gamma - 1)}{\gamma} P_0(\eta, z), \quad (86)$$

where the quantities on the right hand side of the equality signs are given in (69) and (70). The results in (86) are essentially boundary conditions for higher order equations, which are used to find explicit functional dependence of the variables. Once  $\hat{W}_0$  is found, then the mass conservation equation (77) can be integrated with respect to  $r_2$  to find the radial velocity  $V_{r1}$ . The rotational temperature and density fields can be found using related methods.

## 5.2 Higher order consideration

Equations (48)–(50) can be combined with (1)–(5) to find the O(M) equation set in the limit  $M \rightarrow 0$ . The procedure used to find the leading order solution is employed so that the variables, except for  $P_1$ , are divided into irrotational planar and rotational nonplanar parts,

$$V_{z1} = W_{1p}(z, t) + \hat{W}_1(z, t, r_1, r_2), \quad (87)$$

$$R_1 = R_{1p}(z, t) + \hat{R}_1(z, t, r_1, r_2), \quad (88)$$

$$\theta_1 = \theta_{1p}(z, t) + \hat{\theta}_1(z, t, r_1, r_2). \quad (89)$$

The planar, acoustic equations,

$$\frac{\partial R_{1p}}{\partial t} = -\frac{\partial}{\partial z} [W_{1p} + R_{0p} W_{0p}], \quad (90)$$

$$\frac{\partial W_{1p}}{\partial t} = \frac{\partial}{\partial z} \left[ -\frac{1}{\gamma} (P_1 - P_{0s}) + \frac{R_{0p}^2}{2} - \frac{W_{0p}^2}{2} \right], \quad (91)$$

$$\frac{\partial \theta_{1p}}{\partial t} = \frac{\partial}{\partial t} \left[ (\gamma - 1) R_{1p} + \frac{(\gamma - 2)(\gamma - 1)}{2} R_{0p}^2 \right] \quad (92)$$

$$P_1 = R_{1p} + \theta_{1p} + R_{0p} \theta_{0p} \quad (93)$$

containing quadratic driving terms associated with lower order acoustics are not considered further here, although they may be important for studying acoustic streaming effects.

The largest possible viscous effect occurs when  $\beta = ReM^2/\delta^2 = O(1)$  (see (27)), in which case the higher order axial momentum equation for  $\hat{W}_1$  has the nonhomogeneous form

$$\begin{aligned} \frac{\partial \hat{W}_1}{\partial t} + \frac{\partial \hat{W}_1}{\partial r_2} = & \frac{1}{V_{r0s}^2} \frac{\partial^2 \hat{W}_0}{\partial r_2^2} + \frac{1}{\gamma} \hat{R}_0 \frac{\partial P_0}{\partial z} - (V_{z0s} + V_{z0}) \frac{\partial(V_{z0s} + V_{z0})}{\partial z} \\ & + V_{z0s} \frac{\partial V_{z0s}}{\partial z} + W_{0p} \frac{\partial W_{0p}}{\partial z} + V_{r0s} \frac{\partial(V_{z0s} + V_{z0})}{\partial r_1} \\ & - \left( \frac{V_{r1}}{V_{r0s}} \right) \frac{\partial V_{z0}}{\partial r_2} - V_{r0s} \frac{\partial V_{z0s}}{\partial r_1}. \end{aligned} \quad (94)$$

Equation (94), the higher order analogue to (73), provides additional information about the behaviour of the leading order axial speed solution.

The corresponding energy equation for  $\hat{\theta}_1$  analogous to (74) contains a conduction term. Thus, transport effects are important conceptually in the distribution and evolution of the rotational variables.

If the transformation of the coordinate system from  $(t, r_1, r_2, z)$  to  $(\eta, r_1, r_2, z)$  is made, then the derivatives with respect to  $t$  and  $r_2$  must be replaced by

$$\left( \frac{\partial}{\partial t} \right) = \left( \frac{\partial}{\partial \eta} \right)_{r_2}, \quad \left( \frac{\partial}{\partial r_2} \right) = \left( \frac{\partial}{\partial r_2} \right)_{\eta} - \left( \frac{\partial}{\partial \eta} \right)_{r_2}, \quad (95)$$

It follows that (94) can be written as

$$\begin{aligned} \left. \frac{\partial \hat{W}_1}{\partial r_2} \right|_{\eta} = & \frac{1}{V_{r0s}^2} \frac{\partial^2 \hat{W}_0}{\partial \eta^2} - V_{z0} \frac{\partial(V_{z0s} + \hat{W}_0)}{\partial z} \\ & - \hat{W}_0 \frac{\partial \hat{W}_0}{\partial z} - \frac{1}{V_{r0s}} \left[ \frac{\partial(V_{r1} \hat{W}_0)}{\partial r_2} - \frac{\partial(V_{r1} \hat{W}_0)}{\partial \eta} \right] \\ & - V_{z0s} \frac{\partial V_{z0}}{\partial z} - \hat{W}_0 \frac{\partial W_{0p}}{\partial z} + V_{r0s} \frac{\partial \hat{W}_0}{\partial r_1} + \frac{1}{\gamma} \hat{R}_0 \frac{\partial P_0}{\partial z}, \end{aligned} \quad (96)$$

An integration of (96) with respect to  $r_2$ , holding  $\eta$ ,  $r_1$  and  $z$  fixed will generate secular growth in  $r_2$  unless certain terms are suppressed. In considering the impact of each term, it is important to remember that the harmonic  $t$ -dependence of the planar acoustic solutions in (69)-(71) must be rewritten in terms of  $\eta$  and  $r_2$  by using (83). When written in the coordinate system  $(z, t, r_1, r_2)$  the suppressed terms take the form;

$$\frac{1}{V_{r0s}^2} \frac{\partial^2 \hat{W}_0}{\partial r_2^2} + V_{r0s} \frac{\partial \hat{W}_0}{\partial r_1} - \frac{\partial}{\partial z} [\hat{W}_0^2 + \hat{W}_0 V_{z0s}] = 0 \quad (97)$$

which is a nonlinear diffusion equation for the rotational axial velocity  $\hat{W}_0$  with a time-like variable  $r_1$ . The solution for  $\hat{W}_0$  must satisfy an "initial" condition from

(82)

$$\begin{aligned}
\hat{W}_0(t, z, r_1 = 0, r_2)/A &= -W_{0p}(\eta, z) & \eta > 0 \\
&= \sum_{n=1}^{\infty} a_n \left( \frac{\lambda_n}{\omega} \sin(\omega\eta) - \sin(\lambda_n\eta) \right) \sin(\lambda_n z), \lambda_n \neq \omega, \\
\hat{W}_0(t, z, r_1 = 0, r_2)/A &= 0 & \eta < 0
\end{aligned} \tag{98}$$

and a boundary condition at the center line from (81)

$$r_2 \longrightarrow \infty, \quad \frac{\partial \hat{W}_0}{\partial r_2} = 0. \tag{99}$$

In addition a condition must be specified on  $r_1 > 0, r_2 = 0$  which is compatible with (98) at the point  $r_1 = r_2 = 0$ . This is necessary because  $r_1$  and  $r_2$  are treated as independent variables in (102). The reasonable choice is given by

$$\hat{W}_0(t, z, r_1, r_2 = 0) = -W_{0p}(t, z). \tag{100}$$

The nonlinear term in (97),  $(\hat{W}_0^2)_z$  is present in our problem because the  $O(M)$  boundary disturbance is larger than that used in earlier, basically linear studies (Flandro 1974, 1995). Its presence suggests that wave steepening and other forms of instability may occur in the evolving flow field. If the imposed endwall disturbance is smaller, and/or axial variations are ignored, then a linear, viscous diffusion equation is derived, which is related to that used by Price and Flandro (1995).

The linear convection term in the diffusion equation (97), includes the axial convection effect,  $V_{z0s}(\hat{W}_0)_z$ , retained somewhat arbitrarily by Flandro (1995) in his analogue to (73). In the present multiple scale formulation, the asymptotic analysis itself leads to the conclusion that the effect properly belongs in the higher order diffusion equation, rather than in the lower order inviscid axial momentum equation in (73).

One solution approach is based on a finite difference approximation to (97)-(100). Solutions for  $\hat{W}_0(z, t, r_1, r_2)$  can be found by employing a second order accurate Adam-Bashforth/Crank-Nicolson scheme. Most of the results presented here (see Section 6) have been found in this way.

Given the forcing condition in (98), it is also possible to find solutions in terms of the eigenfunction set  $\{\sin(\lambda_n z)\}, n = 1, 2, \dots$ ;

$$\hat{W}_0(t, z, r_1, r_2) = \sum_{n=1}^{\infty} A_n(t, r_1, r_2) \sin(\lambda_n z) \tag{101}$$

Coupled partial differential equations for the Fourier coefficients  $A_n$ , are found by using (101) in (97) and invoking orthogonality conditions for the eigenfunction set on the interval  $[0, 1]$ . The results are;

$$\begin{aligned}
\frac{1}{V_{r0s}^3} \frac{\partial^2 A_n}{\partial r_2^2} + \frac{\partial A_n}{\partial r_1} - \frac{1}{V_{r0s}} \frac{\partial V_{z0s}}{\partial z} A_n - \frac{2}{V_{r0s}} \left( \sum_{n_1=1}^{\infty} \right. \\
\left. \left[ \sum_{n_2=1}^{\infty} a_{nn_1n_2} A_{n_1} A_{n_2} + \left( \frac{V_{z0s}}{z} \right) b_{nn_1} A_{n_1} \right] \right) = 0
\end{aligned} \tag{102}$$

and are subject to conditions obtained from (98) and (99).

(a) Initial Condition:

$$\begin{aligned} A_n(t, r_1 = 0, r_2)/A &= a_n \left( \frac{\lambda_n}{\omega} \sin \omega(t - r_2) - \sin \lambda_n(t - r_2) \right) \quad 0 < r_2 \leq t \\ &= 0 \quad r_2 > t \end{aligned} \quad (103)$$

(b) Boundary Conditions:

$$r_2 \longrightarrow \infty, \quad \frac{\partial A_n}{\partial r_2} = 0 \quad (104)$$

$$A_n(t, r_1, r_2 = 0)/A = a_n \left( \frac{\lambda_n}{\omega} \sin(\omega t) - \sin(\lambda_n t) \right) \quad (105)$$

where

$$a_{nn_1n_2} = 2\lambda_{n_2} \int_0^1 \sin(\lambda_{n_1} z) \cos(\lambda_{n_2} z) \sin(\lambda_n z) dz \quad (106)$$

$$b_{nn_1} = \lambda_{n_1} \int_0^1 z \cos(\lambda_{n_1} z) \sin(\lambda_n z) dz \quad (107)$$

Equation (102) is a coupled system of quasi-linear diffusion equations with a time like variable  $r_1$ , and nonlinear source terms. The physical time  $t$  is a parameter of the differential equations, appearing explicitly only in the boundary conditions. Solutions to (102)-(107) are described in Section 7. A truncation approach is used to reduce (102) to a finite "dynamical" system for a finite number of coefficients  $A_n$ .

## 6 Finite Difference Solutions for the Nonlinear System

Solutions to (97)-(100) for  $\hat{W}_0(z, t, r_1, r_2)$  have been found by using a finite difference method based on the second order accurate  $O(\delta r_1^2, \delta r_2^2)$  Adam-Bashforth/Crank-Nicolson scheme. This scheme is a semi-implicit and neutrally unstable in the sense that it works well if the nonlinear effect is moderate in comparison with the viscous effect. For example, instability results if the amplitude of the initial condition for a given  $\omega$  is larger than a threshold value.

The far end boundary condition for  $r_2 \rightarrow \infty$  is implemented by providing a sufficiently large number of grid points between the convected outer edge of the rotational layer and the finite location of the computational boundary with respect to  $r_2$ . A total of 1000 grid points in the  $r_2$  direction with  $\delta r_2 = 0.1$  is chosen. The function and derivatives must remain zero at a significant number of nodes in order to ensure that conditions at the computational boundary do not constrain the solution.

At each value of the "parameter"  $t$ , the integration is initiated with the initial conditions in (98), subject to the boundary conditions in (99). The spatial distribution of the solution with respect to  $r_2$  evolves as the "time-like" variable  $r_1$  increases. Integration is carried out to a sufficiently large value of  $r_1$  to ensure that adequate

data fields  $\hat{W}_0(z, t, r_1, r_2)$  are available on the locus curve relating  $r_1$  and  $r_2$  defined by (51). Then the physical solution  $\hat{W}_0(z, t, r)$  is found from the intersection of the surface defined by  $\hat{W}_0(z, t, r_1, r_2)$  and the vertical plane from the locus curve relating  $r_1$  and  $r_2$ . In general this curve does not coincide with the computational grid points. Hence cubic spline interpolations in  $r_2$  are employed at every chosen  $r_1$  value to obtain the desired real solution. The amplitude parameter in (26), is  $A=1$  in our computation unless otherwise noted.

The first case studied is for  $\omega = 1.0$ , which is a nonresonant frequency smaller than the first natural frequency  $\lambda_1 = \frac{\pi}{2}$ . This particular case allows us to develop a relatively simple solution with minimal computational time. The initial condition is obtained from (98) by using the first 20 Fourier modes.

It is important to resolve the solution in the axial direction by choosing a sufficiently large number of grid points in the  $z$ -direction,  $K_{max}$ . Solution comparisons for  $K_{max} = 9, 21$  and  $28$  at  $t = 40$ ,  $M=0.01$  and  $Z=0.25, 0.5$  and  $0.75$  show considerable variations between the first two values. Excellent comparisons for  $K_{max} = 21$  and  $28$  suggest that the former is adequate for  $\omega = 1.0$ .

The evolution of the vorticity generated at the sidewall, defined in (84), can be described by showing how the axial rotational velocity component  $\hat{W}_0$  varies with the radial variable  $r_1$  for a sequence of time values and at different axial locations. Figures 6, 7b and 8b give results at  $z = 0.5$  when  $t = 20, 30$  and  $40$ .

The profile at  $t = 20$  contains a little more than three complete spatial oscillations, comparable with the number of completed cycles of forcing at the endwall when  $\omega = 1$  and  $t = 20$ . These quasi-periodic changes occur because fluid exiting the sidewall is driven by the time-varying local axial gradient of the acoustic pressure (see 70), as described by (84). During periods of negative (positive) gradients the particles are accelerated downstream (upstream). As a result, near the wall one will observe alternating periods of positive and negative axial velocity. The steady radial velocity field carries these alternating regions of forward and reverse flow away from the wall toward the axis. Part of the fluid particle response is purely acoustic. The remainder is given by  $\hat{W}_0$ . In this sense the spatial pattern of the axial rotational velocity at fixed  $z$  reflects the historical behaviour of the local pressure gradient on the sidewall.

The  $O(M)$  length scale of the transverse spatial oscillations can now be explained easily since the approximately harmonic pressure gradient variation occurs on the acoustic time scale  $t'_A$  (for  $\omega=O(1)$ ) during which only limited radial motion is possible. The large local shear stresses occur on the short  $r_2$ -length scale, and represent the intense, transient vorticity as explained below (84).

The oscillations are terminated in the vicinity of the undiffused vorticity front, defined by  $\eta = 0$ , or  $r_{2e} = t$ , where the subscript  $e$  implies the existence of an "edge". One may employ (51) and (15) to show that the edge is located at

$$r_{1e}(t) = 1 - \frac{2}{\sqrt{\pi}} \left[ \tan^{-1}(e^{-M\pi t}) \right]^{\frac{1}{2}} \quad (108)$$

with respect to the  $r_1$ -coordinate in Figure 6 and is invariant to axial location for spatially uniform sidewall injection. The value for the conditions in Figure 6,  $r_{1e}(20) = 0.210$ , is marked by a dash. It compares very favorably with the diffused front location obtained from the complete numerical solution to (97), thus helping to verify the accuracy of the latter.

The undiffused front speed  $\left. \frac{\partial r}{\partial t} \right|_{\eta=0} = -MV_{r0s}(r)$ , obtained from the definition of  $\eta$



in (86) and the second of (51), defines the nondimensional radial speed of the “edge”, which asymptotes to zero as the axis is approached, given the result in (15).

At  $t = 30$  and  $40$ , in Figures 7b and 8b, one may observe that the front has moved further into the cylinder. Here again the undiffused edge locations  $r_{1e}(30) = 0.312$ ,  $r_{1e}(40) = 0.406$  are in excellent agreement with those from the computational solution. The growing number of spatial oscillations is compatible with the number of completed cycles of the endwall forcing.

One notes that the spatial oscillations are somewhat irregular in shape and amplitude, a combined result of the driving frequency and eigenvalues found in the “initial” condition in (98).

The amplitude of a given oscillation becomes smaller as is convected deeper into the cylinder. Local viscous and nonlinear effects have some influence on the amplitude reduction which must occur because the vorticity vanishes near the front and certainly at the axis  $r_1 = 1$ . Spatial oscillation wave lengths decrease as  $r_1$  increases toward the axis because the vorticity front speed declines as  $r_1$  increases.

The scaled vorticity distribution corresponding to conditions in Figure 8b, calculated from  $\frac{1}{V_{ros}(r)} \frac{\partial \hat{W}_0}{\partial r_2}$ , is given in Figure 9. The dimensionless vorticity  $\Omega_\theta$ , defined below (84) is  $O(M^{-1})$ . One should note the significant magnitude of the spatial variations in vorticity given the scaling factor  $\frac{1}{M}$ . The large amplitude is associated with the  $O(M)$  length scale of the axial speed gradient and the factor  $M^{-1}$ .

These results are quite different from those given by Flandro (1995) for a single forcing frequency in an assumed axial acoustic field. In particular, the present solutions are obtained from a nonlinear, diffusion equation where viscous effects cause the local shear stresses to diffuse on the short  $r_2$ -length scale as the injected fluid is transported into the cylinder and convected downstream. Flandro’s (1995) analogous result is entirely inviscid. The envelope of his spatial oscillations can be shown to be related directly to the axial dependence of the acoustic mode chosen and so has a characteristic shape not seen in the present  $\hat{W}_0$ -profiles.

A comparison of  $\hat{W}_0$  profiles at three axial locations  $z = 0.25, 0.5$  and  $0.75$  in Figures 7 and 8 shows considerable variation with the  $z$  variable, a result of the axial and time dependence of the wall vorticity defined in (84) with (70). The radial dependence of  $\hat{W}_0$  at a specified  $(z, t)$  combination arises from the time-history of many fluid particles that leave the sidewall from locations upstream of  $z$  and arrive at  $z$  at the specified  $t$  value. Each of these particles comes from a unique starting point and has experienced a unique time-history as it convects away from the initial location. Among the 6-plus spatial oscillations in Figures 8a-c one may note uniquely large negative amplitudes at  $z = 0.25$  and relatively smaller amplitudes at the downstream locations. The envelopes of the oscillations vary considerably among the axial locations. Flandro’s (1995) analytical result predicts similar shapes at every axial location.

The role of the nonlinear term in the diffusion equation in (97) has been assessed by carrying out a computation with  $\hat{W}_0^2$  reduced by a factor of  $10^{-5}$ . The results in Figure 10, corresponding to conditions in Figure 8, shows that the nonlinear term has a quantitative effect on the spatial distribution of  $\hat{W}_0$ , but does not fundamentally control the qualitative spatial oscillations. The nonlinear effect is more important in the fore end at  $z = 0.25$  than in the rear end at  $z = 0.75$  near the exit where nonlinear effect disappears because of the pressure node condition.

Figure 11 is the counterpart to Figure 8 with a reduced viscous effect. In this

case (97) is solved with the viscous term,  $\frac{1}{V_{r0}^2} \frac{\partial^2 \hat{W}_0}{\partial r^2}$ , multiplied by a factor of 0.25. The basic patterns of the complete solution in Figure 8 persist. One notes that the maximum oscillation amplitudes in Figure 11a,c are considerably larger than their analogues in Figure 8a, c, particularly away from the wall. Smaller differences are seen at  $z = 0.5$  in Figure 11b. In general, the impact of viscosity is greater at an axial location where the maximum oscillation amplitudes are relatively large.

The results presented for  $M = 0.01$  show that intense transient vorticity has filled a little more 40% of the cylinder radius at  $t = 40$ . Extended computational times at the small characteristic axial flow Mach number, are required to show further intrusion of the rotational flow into the cylinder. When  $M$  is larger, implying larger wall injection rates, the filling process is faster, so that less computational time is required.

Figures 12 and 13 are the counterparts of the nonlinear result in Figure 8b when  $M = 0.05$  and  $0.1$  respectively, and  $t = 40$ . The vorticity has filled nearly the entire cylinder for  $M = 0.05$ . The value of the undiffused front location from (108) is  $r_{1e}(40) = 0.951$ . This is expected because radial convection of vorticity occurs more quickly for a relatively larger steady radial velocity. At  $M = 0.1$ , where  $r_{1e}(40) = 0.998$ , vorticity is present everywhere in the cylinder, the value at the axis is zero, as explained below (82). It should be noted that the local velocity gradients are smaller in Figures 12 and 13 so that the magnitude of the unsteady vorticity is similarly reduced for higher Mach number systems as predicted by the definition of  $\Omega_\theta$  below (84).

The complete transient axial velocity response at a spatial location  $(z, r_1)$  in the cylinder arises from the superposition,  $W_{0p} + \hat{W}_0$ . Figure 14 provides results at  $z = 0.5, r_1 = 0.2$  for the time-variation of  $W_{0p}$ ,  $\hat{W}_0$  and their sum  $V_{z0}$ , defined in (59) with  $K_{max} = 21$  and  $M=0.01$ . The acoustic signal in Figure 14a is initiated at about  $t = 0.5$  to account for the wave travel from the endwall to the location  $z = 0.5$ . At  $r_1 = 0.2$  the rotational response appears after a delay of almost 18 axial acoustic time units, the time needed for the vorticity wave front initiated at the wall to convect out to the specified radial location. At the location  $r_1 = 0.2$ , phase differences between  $W_{0p}$  and  $\hat{W}_0$  are relatively small and the sum in Figure 14c shows a total response of significant amplitude. This amplitude actually increases as  $r_1$  decreases until locations very close to the wall are reached, where the impact of the no-slip condition at  $r_1 = r_2 = 0$  forces  $V_{z0} \rightarrow 0$ .

At higher driving frequencies one will find additional small scale structure in the  $\hat{W}_0$  profile arising from the shorter time scale for sign changes in the axial gradient of the acoustic pressure. Results for  $\omega = 2.5, M = 0.01, K_{max} = 21, A = 0.5$  are given in Figures 15a-c for  $t = 40$ . In this case there are about 10 spatial cycles, comparable with the number of completed cycles associated with the first eigenfrequency in (70),  $\lambda_1 = \pi/2$ , rather than the forcing frequency  $\omega = 2.5$ . The result points out the importance of retaining eigenfunctions in the acoustical theory. The results show that the spatial distribution curves for  $\omega = 1.0$  and  $2.5$  have similar characteristics although the smaller scale structure is much finer. Here again, one observes considerable variations in the axial direction.

The relative solution complexity for  $\omega = 2.5$  suggests that a more complex acoustic field, arising from multiple driving frequencies or perhaps sidewall injection oscillations, may initiate a relatively irregular rotational flow time-response. In this sense, one could ask whether "turbulent" responses observed in similar situations such as solid rocket chamber models are caused in part by wall generated vorticity that is

convected into the chamber by the injected field.

## 7 Modal Solutions to the Nonlinear System

The accuracy of finite difference solutions to (97) can be assessed in part by comparing results with those found using the modal analysis described earlier. Solutions found from (101)-(107) enable one to demonstrate how the energy is distributed among the Fourier modes. The coefficients  $A_n(r_1, r_2)$ ,  $n=1-N$  for specified  $N$ , have been found by using a finite difference method based on the Adam-Bashforth/Crank-Nicolson scheme described in Section 6. The procedure used previously to find  $\hat{W}_0$  on the real locus is applied to each  $A_n(r_1, r_2)$ . Once the  $A_n$ 's are known, the solution for  $\hat{W}_0$  is found by summing up  $N$  modal contributions according to (101). Careful attention must be given to the value of  $N$  in order to assure that the solutions are sufficiently accurate. In particular, solutions for  $\hat{W}_0$  based on  $N$  and  $N + L$  modes,  $L > 0$ , are compared until the results exhibit little appreciable change for an incremental  $L$  value. Valuable insights into the solution development for this problem have been found from the transient solution to a Fisher equation (Fisher, 1936) in terms of a Galerkin expansion. Details are given in Appendix A.

Figures 16-18 show  $\hat{W}_0$  results for  $M = 0.01$  and  $\omega = 1$  at  $z = 0.5, t = 40$  when  $N = 6, 8, 10$  respectively. The  $\hat{W}_0$  profile in each graph is obtained by using the sum of the last 6 modes, even though 8 and 10 modes were used in the numerical computation associated with Figures 17 and 18, respectively. A comparison of individual modes in the partial sum implies that the energy is concentrated primarily in the first two modes for  $\omega = 1$ . A comparison of results in Figures 16-18 with those in Figure 8b is striking, including the appearance of some irregular small scale structure in the second and fourth spatial waves above the sidewall. There is little difference between the best result in Figure 18 and that from a direct finite difference solution with  $K_{max} = 21$ . It is noted that the grid size in the axial direction for  $K_{max}=21$  is 0.05, just small enough to resolve the first six axial Fourier modes according to  $(\Delta z)_{max} = \frac{2\pi}{\lambda_6} \frac{1}{10}$ , where  $\lambda_6 = \frac{11}{2}\pi$ . Hence the most meaningful comparisons should be carried out with  $N = 6$ .

The six mode partial sum from the ten mode computation is closer to the finite difference result than the six mode summation from the six mode computation. A reasonable explanation of this observation may be based on the restricted energy transfer for modes near the truncation limit. Adding a few more modes permits realistic exchange between the lower modes. Hence a six mode partial sum from an  $N = 10$  calculation provides better results than the  $N = 6$  calculation alone. This effect occurs in related work by Wang and Kassoy (1995).

The smaller amplitude radial rotational velocity can be calculated by integrating (77),

$$V_{r1}(z, t, r_1, r_2) = -V_{r0s}(r_1) \int_0^{r_2} \frac{\partial \hat{W}_0(z, t, r_1, \tilde{r}_2)}{\partial z} d\tilde{r}_2 \quad (109)$$

where  $\hat{W}_0 = 0$ , for  $r_2 > r_{2e}(t)$  and  $r_{2e}$  is found from (52) and (108). The physical solution is found by intersection of  $V_{r1}$  with the locus curve relating  $r_1$  and  $r_2$ . One may note that for  $r_2 > r_{2e}(t)$ , the upper limit on the integral is fixed at  $r_{2e}$ , so that

the primary radial variation arises from the factor  $V_{r0s}$  defined in (15). The result in Figure 19 for  $M = 0.01, \omega = 1, z = 0.5, t = 40$  is a six mode partial sum for an  $N = 8$  computation. For  $0 \leq r \leq r_{2e}$  one observes spatial oscillations resulting from those in the  $\hat{W}_0$  profiles. The radial gradients in that region are far larger than those beyond the velocity front at  $r_{2e}$ . This point can be understood by using the multiple scale derivatives in (52) to find the physical radial gradient of  $V_{r1}$ ;

$$\frac{\partial V_{r1}}{\partial r_1} = \frac{\partial V_{r1}}{\partial r_1} + \frac{1}{M} \frac{\partial \hat{W}_0}{\partial z} \quad (110)$$

where (77) has been employed. The latter  $O(\frac{1}{M})$  term prevails between the sidewall and the vorticity front. Beyond the front, the second term in (110) is identically zero so that one should find the  $O(1)$  radial derivative observed in Figure 19.

The satisfying comparison between finite difference and modal solutions provides strong confidence in the characteristic solution properties. It is noted that CPU time requirement for direct finite difference computations is considerably less than that for modal solutions, given equivalent resolution requirements. However, the modal solutions can be used to obtain insights to the energy distribution at various length scales, not easy to find from finite difference calculations.

## 8 Energetics of the Internal Flow

The prescribed axial speed disturbance imposed on the endwall in (10) causes transient work to be done on the flow system. Acoustic disturbances originating at the end distribute the energy into the flow field. Simultaneously, energy is transferred from the acoustic field into the rotational flow field as vorticity is generated at the sidewall and redistributed in the internal flow. This partition of transient energy between the acoustic and rotational flows, is of interest in understanding the flow dynamics. It has been considered in terms of the concept of "flow turning" used in the solid rocket motor stability literature (Flandro, 1995, for example).

The endwall work input rate can be written in nondimensional form as

$$W_e(t) = MA \int_0^t P(0, t) \sin \omega t dt \quad (111)$$

where  $P(0, t)$  is obtained from (50) and (70) to  $O(M)$ . It follows that

$$\begin{aligned} \frac{W_e(t)}{MA} = & \frac{1}{\omega} (1 - \cos(\omega t)) \\ & + A\omega M \sum_{n=1}^{\infty} \frac{1}{(\lambda_n^2 - \omega^2)} \left\{ \frac{1 - \cos(2\omega t)}{2\omega} \right. \\ & \left. - \left[ \frac{(1 - \cos(\omega + \lambda_n)t)}{\omega + \lambda_n} + \frac{(1 - \cos(\omega - \lambda_n)t)}{\omega - \lambda_n} \right] \right\}, \end{aligned} \quad (112)$$

describes the time-history of the work input to  $O(M)$ . The long-time average,

$$\bar{W}_e = \lim_{T \rightarrow \infty} \frac{1}{T} \int_0^T W_e dt = MA \left[ \frac{1}{\omega} + MA \sum_{n=1}^{\infty} \frac{(3\omega^2 + \lambda_n^2)}{(\lambda_n^2 - \omega^2)^2} \right] \quad (113)$$

is positive definite and the series converges rapidly. This added energy must now be partitioned into the acoustic and rotational fields.

One may write the nondimensional total energy per unit mass of a fluid particle in the form

$$\begin{aligned}
E &= E' / \left( \frac{C_0'^2}{\gamma(\gamma-1)} \right) \\
&= \left\{ 1 + \frac{\gamma(\gamma-1)}{2} M^2 \left( V_{z0s}^2 + \frac{1}{\delta^2} V_{r0s}^2 \right) \right\} \\
&\quad + M\theta_0 \\
&\quad + M^2 \left\{ \theta_1 + \frac{\gamma(\gamma-1)}{2} \left( 2V_{z0s}(W_{0p} + \hat{W}_0) + (W_{0p} + \hat{W}_0)^2 + O(M, \frac{1}{\delta^2}) \right) \right\} \quad (114)
\end{aligned}$$

The first two terms (in curly brackets) represent steady flow energy, while the third includes both acoustic and rotational components defined in (61). The  $O(M)\theta_0$  term arises directly from the endwall disturbance and is larger than the biggest kinetic energy term of  $O(M^2)$  in this low Mach number flow. Energy in this thermal term and the analogous  $\theta_1$ -term cannot be evaluated until solutions are developed in a future paper. However, it is clear from the present formulation that a thermal accommodation layer will be present in order to satisfy an imposed wall temperature boundary condition (i.e. (8)), like those studied by Roh and Yang (1995).

The largest component of the unsteady kinetic energy,  $\Lambda$ , can be written in the nondimensional form;

$$\frac{\Lambda}{\gamma(\gamma-1)M^2} = V_{z0s}(W_{0p} + \hat{W}_0) + \frac{1}{2}(W_{0p} + \hat{W}_0)^2 \quad (115)$$

which includes both acoustic and rotational flow contributions. Equations (63) and (73) can then be employed to derive an expression for the rate of change of  $\Lambda$  for fluid particles entering the cylinder from the sidewall;

$$\frac{\partial \Lambda}{\partial t} + \frac{\partial \Lambda}{\partial r_2} = -M^2(\gamma-1)(V_{z0s} + W_{0p} + \hat{W}_0) \frac{\partial P_0}{\partial z} \quad (116)$$

Then a variable transformation employing  $\eta = t - r_2$  can be used to write a Lagrangian equation for  $\Lambda(t, \eta, r_1, z)$

$$\left. \frac{\partial \Lambda}{\partial t} \right|_{\eta} = -M^2(\gamma-1)(V_{z0s} + W_{0p} + \hat{W}_0) \frac{\partial P_0}{\partial z} \quad (117)$$

It follows that on a constant  $\eta$ -line the kinetic energy is altered by an interaction between the complete  $O(1)$  axial velocity and the axial gradient of the acoustic pressure.

One should note that the rotational field itself ( $\hat{W}_0$ ) affects the change in  $\Lambda$ .

One can integrate (117) by following a convecting fluid particle on a given  $\eta$ -line from the time it exits the side wall ( $t = \eta$ ) to any larger value of time. It follows that

$$\begin{aligned}
\Lambda &= \gamma(\gamma-1)M^2(W_{0p}(t, z) - W_{0p}(\eta, z)) \left[ V_{z0s} + \frac{W_{0p}(t, z) + W_{0p}(\eta, z)}{2} + \hat{W}_0 \right] \\
&\quad + \Lambda_0 \quad (118)
\end{aligned}$$

where  $\Lambda_0 \equiv \Lambda(\eta, \eta, r_1, z)$  is obtained from (115). Equation (118) describes the evolution of the fluid particle kinetic energy on a given  $\eta$  line. It is perhaps more illustrative to find the time-average of (118), in order to integrate away harmonic function variations. The result is that

$$\lim_{T \rightarrow \infty} \frac{1}{T} \int_0^T \Lambda dt = \gamma(\gamma - 1)M^2 \left\{ \lim_{T \rightarrow \infty} \frac{1}{T} \int_{\eta}^T \frac{W_{0p}^2}{2} dt + V_{z0s} \hat{W}_0 + \frac{\hat{W}_0^2}{2} \right\} \quad (119)$$

where the value of  $\Lambda_0$  has been used.

The first term on the right side of (119) describes the average acoustic kinetic energy and is positive definite. One can observe a form of long-time kinetic energy partitioning between the acoustic and rotational fields.

It is interesting to note that the long-time average of (117) on a constant  $\eta$ -line vanishes;

$$\lim_{T \rightarrow \infty} \frac{1}{T} \int_{\eta}^T \frac{\partial \Lambda}{\partial t} dt = 0 \quad (120)$$

This result and (117) imply that the kinetic energy increases in some intervals and decreases in others, with the average value on a constant  $\eta$ -line given by (119).

These issues are worthy of additional consideration in the future because the flow is fundamentally rotational in character. As a result, traditional acoustic intensity arguments cannot be employed to elucidate the fundamental energy partitioning processes.

## 9 Conclusions

Systematic asymptotic methods have been employed to formulate an initial-boundary value model for coexisting acoustic and rotational flow fields in a long, narrow cylinder. Boundary driven axial, planar acoustic waves interact with an inviscid, weakly rotational, injection induced steady flow to produce intense time dependent vorticity at the sidewall of the cylinder. The intense vorticity is convected into the entire chamber by the steady radial velocity field for appropriate ranges of Reynolds and Mach number and frequency. The amplitude and distribution of the vorticity is impacted by weak viscous and nonlinear effects.

It is also demonstrated that there are parameter ranges of Mach number (as it relates to injection rate), driving frequency and Reynolds number for which vorticity is really confined to weakly viscous acoustic boundary layers, thin compared to the radius of the cylinder, but larger than those discussed by Flandro (1974), Baum and Levine (1987). These structures can appear for relatively small injection rates, relatively high driving frequency and low Reynolds numbers, so that viscous damping of the vorticity amplitude is profound. Then, the cylinder core will contain the relatively weak vorticity of the steady Culick (1966) solution and irrotational acoustic waves driven by the boundary forcing.

There is now a considerable body of evidence in support of the presence of an unsteady vorticity distribution within an appropriately high Reynolds number wall injected flow in a cylinder. The experiments of Brown et al. (1986a, 1986b), the small disturbance, linear stability modeling of Flandro (1995a, 1995b) as well as Majdalani and Van Moorhem (1996), the computational solutions of Vuillot and Avalon (1991),



Smith et. al.(1993), and that of Kirkkopru et al. (1995, 1996a,b) as well as the current work show unequivocally that unsteady vorticity is generated at the cylindrical surface and is convected away by the injected fluid. The core of the cylinder is free of intense unsteady vorticity only during the very early phases of the transient process, prior to the arrival of a well defined unsteady vorticity front.

Unlike Flandro's recent work (1995a, 1995b) and that of Majdalani and Van Moorhem (1996), which employs quasi-steady, linear, small disturbance stability theory for explaining the observed presence of rotational flow throughout the cylinder, we have formulated an initial-boundary value theory for a weakly nonlinear and viscous flow process. A multiple length scale analysis, which is essential in forming a rational mathematical model, is used to demonstrate to the first order that the vorticity is generated at the surface by a fundamentally inviscid interaction between the acoustic pressure axial gradient and the injected fluid at the wall, and is convected away by a steady radial velocity field. Then, a higher order theory is used to prove that the basic vorticity is nonlinearized in the axial direction and viscously diffused on a small radial length scale. The latter result demonstrates that the weak viscosity is pervasive, although smaller in magnitude than the driving effect of the axial pressure gradient, and confirms the conjecture of Hedge et al.(1986). These results are a generalization of those by Flandro (1995b) and Majdalani and Van Moorhem (1996).

The amplitude of the transient vorticity distributions described by Kirkkopru et al.(1995), and in the present work are  $O(M^{-1})$  larger than that of the Culick(1966a) steady solution. It follows that there will be a relatively large transient axial shear stress on the cylinder surface, which can be calculated from equation (84), particularly for smaller  $M$  values. This result is important for applications of the theory to solid rocket motors.

One can speculate that the large transient shear stresses will impact the burning rate of a propellant which is the source of the "injected" fluid used in the present model. Perhaps there is a direct relationship between the effect of surface shear stress transients, predicted in the present work, and erosive burning concepts used in the solid rocket engineering literature (Williams,1985).

The linear acoustic pressure field in our theory is found independently of any vorticity distribution present in the cylinder. It is mathematically decoupled from the vorticity subsequently generated by the inviscid interaction between the axial pressure gradient and the fluid injected from the wall. As a result, the pressure field is determined from an irrotational formulation, using a homogeneous wave equation with nonhomogeneous boundary conditions. The solution, composed of a forced (Helmholtz) response and eigenfuctions (traveling waves) resembles what one measures in rocket motor models. However, the total axial velocity response arises from the coexisting acoustic and rotational flow fields of equal magnitude. The latter includes the "shear waves" or vorticity distribution. The associated radial gradient cannot be predicted from acoustic stability theory.

The conceptual approach used here has been extended by Kirkkopru et. al.(1996b) to disturbances driven by sidewall injection transients, rather than those applied at the closed endwall (Zhao(1994), Kirkkopru et al.(1995, 1996a)). The former type of disturbance emulates the effects of propellant burning rate variations in solid rocket motors. These methods have also proved effective for studying three dimensional flow responses to nonaxisymmetric boundary disturbances, Kassoy, et. al. (1997) and Staab and Kassoy (1996).

## 10 Acknowledgement

The authors would like to thank the Air Force Office of Scientific Research for continuing support through AFOSR 89-0023. A substantial discussion with Professor N. Riley of the University of East Anglia is much appreciated.

## 11 REFERENCES

- Balakrishnan, G., Liñán, A., and Williams, F., (1991) *AIAA J.* **29**, 2149-2154.
- Baum, J.D. (1989), "Investigation of Flow Turning Phenomenon; Effects of Frequency and Blowing Rate," AIAA-89-0293 27th Aerospace Sciences Meeting, Reno, NV., January 1989.
- Baum, J.D. (1990), "Energy Exchange Mechanisms Between the Mean and Acoustic Fields in a Simulated Rocket Combustor," AFOSR Contractors Meeting, Atlanta, GA, June.
- Baum, J.D. and Levine, J.N. (1987) *AIAA J.* **25**, 1577-1586
- Brown, R.S., Blackner, A.M., Willoughby, P.G., and Dunlap, R. (1986a), *J. Propulsion and Power*, **2**, 428-437.
- Brown, R.S., Blackner, A.M., Willoughby, P.G., and Dunlap, R. (1986b) "Coupling Between Velocity Oscillations and Solid Propellant Combustion," AIAA Paper 86-0531, 24th Aerospace Sciences Meeting, Reno, NV., January 1986.
- Brown, R.S. and Shaeffer, C.W. (1992) "Oscillatory Internal Flow Field Studies," AFOSR Contractors Meeting in Propulsion, LaJolla, California, June 1992.
- Chen, T., Hedge, U., and Zinn, B. (1990) "Driving of axial acoustic fields by sidewall stabilized diffusion flames," AIAA-90-0037, 28th Aerospace Science Meeting, Reno, NV., January 1990.
- Cole, J.D. and Aroesty, J. (1968) "The Blowhard Problem—Inviscid Flows with Surface Injection," *Int J. Heat Mass Transfer*, **11**, 1167-1183.
- Culick, F.E.C. (1966) *AIAA J.* **4**, 1462-1463.
- Culick, F.E.C. and Yang, V. (1992) "Prediction of the Stability of Unsteady Motions in Solid-Propellant Rocket Motors," Chap. 18, 719-779, in *Nonsteady Burning and Combustion Instability of Solid Propellants*, eds., L. DeLuca, E.W. Price and M. Summerfield, Prog. in Aero. and Astro., AIAA, Wash. D.C.
- Culick, F.E.C. (1966) *AIAA J.* **4**, 1462-1463.
- Culick, F.E.C. (1966) *AIAA J.* **4**, 1462-1463.
- Fisher, R.A. (1936) *Ann. Eugen.*, **7**, 355-369.
- Flandro, G.A. (1974) *J. Sound and Vibration*, **36**, 297-312.



- Flandro, G.A. (1986) J. Prop. Power, **2**, 206-214.
- Flandro, G.A. (1995a) J. Prop. Power, **11**, 607-625.
- Flandro, G.A. (1995b) "On Flow Turning", AIAA 95-2730, 31st AIAA/ASME/ASEE Joint Propulsion Conference, San Diego, CA. July 1995.
- Flandro, G.A. and Roach, R.L. (1992) *Effects of Vorticity Production on Acoustic Waves in a Combustion Chamber*. Final Technical Report AFOSR-90-0159
- Hegde, U.G., Chen, T., and Zinn, B.T. (1986), *AIAA J.* **24**, 1474-1482.
- Hegde, U.G. and Zinn, B.T. (1986), 21st Symp. (int'l.) Combust. 1993-2000
- Kasoy, D.R., Staab, P.L., Chang, T.Y. and Hegab A.M. (1997) "Co-Existing Acoustic Rotational Disturbances in a Cold Flow Model of a Solid Rocket Motor", AIAA 97-0697, 35th Aerospace Sciences Meeting, Reno, NV., January 1997.
- Kirkkopru, K., Kasoy, D.R. and Zhao, Q., (1995) "Unsteady Vorticity Generation and Evolution in a Model of a Solid Rocket Motor: Sidewall Mass Addition Transients" AIAA-95-0603, 33rd Aerospace Sciences Meeting, Reno, NV., January 1995.
- Kirkkopru, K., Kasoy, D.R. and Zhao, Q., (1996a) "Unsteady Vorticity Generation and Evolution in a Long Narrow Cylinder with Sidewall Injection", submitted to Physics of Fluids.
- Kirkkopru, K., Kasoy, D.R. and Zhao, Q., (1996b) "Unsteady Vorticity Generation and Evolution in a Model of a Solid Rocket Motor: Sidewall Mass Addition Transients", J. Propulsion and Power, **12**, 646-654.
- Lagerstrom, P.A. (1964) Theory of Laminar Flows, Section B, 90-92, Moore, F.K., ed., Princeton University Press, Princeton, NJ. .
- Matta, L.M. and Zinn, B.T. (1993) "Investigation of Flow Turning Loss in a Simulated Unstable Solid Propellant Rocket Motor," AIAA 93-0115, 31st Aerospace Sciences Meeting, Reno, NV., January 1993.
- Price, E.W. and Flandro, G.A. (1995) *Combustion Instability in Solid Propellant Rockets*. Book manuscript in preparation.
- Roh, T.S. and Yang, V. (1995), "Transient Combustion Responses of Solid Propellants to Acoustic Disturbances in Rocket Motors", AIAA 95-0602, 33rd Aerospace Sciences Meetings, Reno, NV., January 1995.
- Sankar, S.V., Hegde, U.G., Jagoda, J.I., and Zinn, B.T. (1988a), 22nd Symp. (int'l) on Combustion, 1865-1873
- Sankar, S.V., Jagoda, J.I., Daniel, B.R., and Zinn, B.T. (1988b), AIAA 88-0541, 26th Aerospace Sciences Meeting, Reno, NV., January 1988.
- Smith, T.M., Roach, R.L., Flandro, G.A. (1993), "Numerical Study of the Unsteady Flow in a Simulated Rocket Motor", AIAA 93-0112, 31st Aerospace Sciences Meeting, Reno, NV., January 1993.

- Staab, P.L. and Kassoy, D.R. (1996), "Three Dimensional, Unsteady, Acoustic-Shear Flow Dynamics in a Cylinder with Sidewall Mass Addition", submitted to The Physics of Fluids.
- Taylor, G.I.(1956), Proc. Royal Soc. Lond. **A 234**, 456-475.
- Tien, J.S. (1972) *Comb. Science and Tech.***5**, 47-54.
- Tseng, C., Tseng, I.S., Chu, W. and Yang, V.(1994), "Interactions Between Acoustic Waves and Premixed Flames in Porous Chambers", AIAA 94-3328, Joint Propulsion Conference, Indianapolis, IN., June 1994.
- Vuillot,F. (1995) *J. Propulsion and Power* **11**, 629-639.
- Vuillot,F. and Avalon,G. (1991) *J. Propulsion* **7**, 231-239.
- Wang, M. and Kassoy, D. R. (1990a) *J. Acoust. Soc. America* **87**,1466-1472
- Wang, M. and Kassoy, D. R. (1990b) *J. Fluid Mech.***220**, 267-292.
- Wang, M. and Kassoy, D. R. (1990c) *J. Fluid Mech.***221**, 23-52.
- Wang, M. and Kassoy, D. R. (1992a) *J. Fluid Mech.***238**, 509-536.
- Wang, M. and Kassoy, D. R.(1992b) *AIAA J.***30**, 1708-1715.
- Wang, M. and Kassoy, D. R.(1995) *SIAM J, Appl. Math.***55**, 924-951.
- Williams, F.A.(1985) *Combustion Theory*, Benjamin/Cummings, Menlo Park.
- Zhao, Q. (1994) "Nonlinear Acoustic Processes in Solid Rocket Motors", Ph.D. Thesis, Mechanical Engineering Department, University of Colorado.
- Zhao, Q., Kassoy, D.R. (1994) "The Generation and Evolution of Unsteady Vorticity in a Model of a Solid Rocket Engine Chamber", AIAA-94-0779, 32nd Aerospace Sciences Meeting, Reno, NV., January 1994.

## 12 Solution to a Related Model Problem

The nonlinear coupled system in (109) is sufficiently complex to require a computational solution. In order to develop an effective numerical approach, it is desirable to consider the solution to an elementary model problem with related properties. A simple Fisher equation (Fisher,1936) with appropriate periodic initial and boundary conditions can be used:

$$\frac{\partial U}{\partial z} = \frac{\partial^2 U}{\partial y^2} + \nu U^2, \quad y > 0, t > 0 \quad (121)$$

Initial Condition:

$$U(0, y) = -\sin(t - y) \quad \text{for } 0 \leq y \leq t; \quad (122)$$

$$U(0, y) = 0 \quad \text{for } y > t \quad (123)$$

Boundary Condition:

$$U(y = 0) = -\sin(t) \quad (124)$$

When the parameter  $t$  is increased, the nonzero portion of the initial condition is spread farther into the  $y$ -domain. In the spirit of (109), the multiple scale independent variables are related by  $y = \Omega^2 z$  and  $\Omega \gg 1$ .

An analytical solution for linear diffusion ( $\nu = 0$ ) is constructed for the odd extension of (118) and (119) for the domain  $0 < y < \infty$ :

$$U(z, y) = -\frac{1}{2\sqrt{\pi z}} \int_0^t \sin(t - y') \left[ e^{-\frac{(y-y')^2}{4z}} - e^{-\frac{(y+y')^2}{4z}} \right] dy' - \frac{y}{2\sqrt{\pi}} \int_0^z \frac{\sin(t)}{(z - z')^{\frac{3}{2}}} e^{-\frac{y^2}{4(z-z')}} dz', \quad y > 0 \quad (125)$$

A quasi-steady solution form  $U(y, z) = -\sin(t - y)e^{-z}$ ,  $y > 0$  can be recovered by taking the limits  $(\frac{y \pm t}{2\sqrt{z}}) \rightarrow \pm\infty$  and  $z \rightarrow 0^+$  simultaneously. Physically, this means that the solution has a quasi-steady form at a specific value of  $t$  if  $y$  lies between  $y=0$  and the inner edge of a diffusive boundary layer centered at  $y = t$  which is needed to smooth the discontinuous slope of the initial condition (118) and (119) at that location. Inside the diffusive layer, the solution is given by the full form of (121). The diffusive layer thickness is  $\delta \sim O(\frac{\sqrt{z}}{\Omega^2})$ . This linear result suggests that the assumed quasi-steady approximation employed by Price and Flandro (1993) is not uniformly valid in space.

The solution to (117)-(120) along the locus  $y = \Omega^2 z$ , for  $\nu = 1$  and  $\Omega^2 \approx 66$ , has been found from a computational analysis based on an elementary explicit finite difference method. The boundary condition (120) is enforced at  $y = 0$  for each integration step in  $z$  direction. The integration of  $U$  with respect to  $z$  is carried out for  $0 \leq z \leq 2.25$  with step size  $\delta z = 0.0015$ . The far end boundary condition is implemented in such a way that there are a sufficient number of grid points with zero value lying between the furthest grid point with nonzero value and the finite location of the computational boundary with respect to  $y$  after each integration in  $z$  direction. The dashed line in Figure 6 describes the linear solution when  $t = 100$  obtained from (121). An analogous numerical result ( $\nu = 0$ ) is indistinguishable from the analytical solution on the scale of the graph, thus verifying the numerical code. The linear solution shows regular, nearly harmonic spatial oscillations that decay until the diffusive layer is reached near  $z \approx 1.5$ . There the solution makes a rapid transition to a vanishingly small value for  $z > 1.5$ . In comparison the solid line represents the nonlinear numerical solution for  $\nu = 1$ . The frequency is nearly identical to the linear solution. However, the drift of the solution toward positive values of  $U$  is due to the positive definite source effect,  $\nu U^2$ . Again the deviation from the pattern of oscillations near  $z \approx 1.5$  is associated with the diffusive layer behavior. Given the parameters used in the calculation, the diffusive layer thickness with respect to the  $z$  coordinate is about 0.1. The analogous results for  $\nu = -1$ , corresponding to a nonlinear sink, are given in figure 7. There is no expectation of symmetry.

The basic properties of the model problem solution can be used to develop an effective numerical method for the solution of (109).

Table 1: Table 1: Acoustic Response Properties for Several Driving Frequencies

$\omega$	$\omega'$ (Hz)	Properties	Primary Response
1	159	stable	axial + quasi-steady modes
1.5	238	beats	quasi-steady modes with axial wave modulation
$\pi/2$	250	axial amplification	linear growth

## CAPTIONS

Figure 1: The cylindrical rocket engine chamber model of length  $L'$ , diameter  $D'$ , with endwall oscillations of frequency  $\omega$ .

Figure 2: The time response of the axial acoustic velocity  $\tilde{V}_{z0}$  at  $z=0.5$  and  $\omega = 1.0$ .

Figure 3: The time response (beats) of the axial acoustic velocity  $\tilde{V}_{z0}/30$  at  $z=0.5$  and  $\omega = 1.5$ .

Figure 4: The time response of the axial acoustic velocity  $\tilde{V}_{z0}$  at  $z=0.5$  and  $\omega = \pi/2$ , linear growth.

Figure 5: The axial velocity in the boundary layer as a function of the variable of  $\xi$  for  $M=0.01, \beta = 0.1$  when  $\Omega = 2.5$  and  $3.0$ . The boundary layer is thicker for the smaller frequency value.

Figure 6: The spatial variation of the rotational axial velocity component  $\hat{W}_0$  with the radial variable  $r_1$  at  $t=20$ . It can be seen that the front is about 23% of the way to the centerline and nearly 4 spatial oscillations have entered the cylinder.

Figure 7a,b,c: The spatial variation of the rotational axial velocity component  $\hat{W}_0$  at  $t=30$  for (a) $z=0.25$ , (b) $z=0.5$  (c) $z=0.75$  with the radial variable  $r_1$ . The front is about 35% of the way to the centerline and nearly 5.5 spatial oscillations have entered the cylinder. The amplitude of the oscillations near the front at this moment is noticeably smaller than those at  $t=20$ , an accumulative effect of viscosity on  $M$  scale.

Figure 8a: The spatial variation of the rotational axial velocity component  $\hat{W}_0$  with the radial variable  $r_1$  at  $t=40, z=0.25$ . The front is about 45% of the way to the centerline and nearly 7.5 spatial oscillations have entered the cylinder. Strong nonlinear effects alter the overall pattern.

Figure 8b: The spatial variation of the rotational axial velocity component  $\hat{W}_0$  with the radial variable  $r_1$  at  $t=40$ ,  $z=0.5$ . The front is about 45% of the way to the centerline and nearly 7.5 spatial oscillations have entered the cylinder. The amplitude of the oscillations near the front at this moment is substantially smaller than those at  $t=20$ , an accumulative effect of viscosity on  $M$  scale.

Figure 8c: The spatial variation of the rotational axial velocity component  $\hat{W}_0$  with the radial variable  $r_1$  at  $t=40$ ,  $z=0.75$ . It has the generic features as in Figure 8b.

Figure 9: The spatial variation of unsteady vorticity  $\Omega_\theta/100$ , with the radial variable  $r_1$ . The magnitude of  $\Omega_\theta$  is  $O(1/M)$  bigger than the steady vorticity and therefore dominant in the cylinder. The shear stress on the wall imposed by the unsteady vorticity is significant.

Figure 10a,b,c: The spatial variation of the rotational axial velocity component  $\hat{W}_0$  at  $t=40$  for (a) $z=0.25$ , (b) $z=0.5$ , (c) $z=0.75$ , with the radial variable  $r_1$  when the nonlinear term is suppressed. A comparison of these with Figures 8a,b,c demonstrates nonlinear effects are strong near the fore end, moderate at the middle, small at the rear end.

Figure 11a,b,c: The spatial variation of the rotational axial velocity component  $\hat{W}_0$  at  $t=40$  for (a) $z=0.25$ , (b) $z=0.5$ , (c) $z=0.75$ , with the radial variable  $r_1$  with the viscous term reduced by 50%. A comparison with Figures 8a,b,c demonstrates that local structure is altered by the reduction of viscosity.

Figure 12: The spatial variation of the rotational axial velocity component  $\hat{W}_0$  with the radial variable  $r_1$  at  $M=0.05$ ,  $z=0.5$ ,  $\omega=1.0$  and  $t=40$ . The larger  $M$  corresponds to stronger injection rate on the cylinder wall. As a result, almost all the cylinder has been filled with the rotational flow compared to only 45% in the case of  $M=0.01$  in Figure 8c.

Figure 13: The spatial variation of the rotational axial velocity component  $\hat{W}_0$  with the radial variable  $r_1$  at  $M=0.1$ ,  $z=0.5$ ,  $\omega=1.0$  and  $t=40$ . The larger  $M$  corresponds to a stronger injection rate on the cylinder wall.

Figure 14 a,b,c (from top to bottom): The time response of; (a) the axial acoustic

speed  $W_{0p}$ , (b) the rotational axial speed  $\hat{W}_0$  and (c) the complete axial speed  $V_{z0} = (W_{0p} + \hat{W}_0)$  for  $r_1=0.2, z=0.5, M=0.01$  and  $\omega = 1.0$ .

Figure 15a,b,c: The spatial variation of the rotational axial velocity component  $\hat{W}_0$  with the radial variable  $r_1$  at  $\omega = 2.5, t=40$  for (a) $z=0.25$ , (b) $z=0.5$ , (c) $z=0.75$  with the amplitude of the disturbance reduced by a half. More spatial oscillations are present in the structure due to the higher driving frequency, in comparison Figures 8a,b,c.

Figure 16: The spatial variation of the rotational axial velocity component  $\hat{W}_0$  with the radial variable  $r_1$  based on a 6 mode summation from a 6 mode, nonlinear computation ( $N=6$ ).

Figure 17: The spatial variation of the rotational axial velocity component  $\hat{W}_0$  with the radial variable  $r_1$  based on a 6 mode partial summation from an 8 mode, nonlinear computation ( $N=8$ ).

Figure 18: The spatial variation of the rotational axial velocity component  $\hat{W}_0$  with the radial variable  $r_1$  based on a 6 mode partial summation from a 10 mode, nonlinear computation ( $N=10$ ).

Figure 19: The spatial variation of the rotational radial velocity component  $\hat{V}_{r1}$  with the radial variable  $r_1$  based on the 6 mode partial summation from an 8 mode computation.

Figure 20: Solution  $U$  vs  $z$  for the nonlinear model problem on the locus curve  $y = \Omega^2 z$  with  $\Omega^2 \approx 66$  and  $\nu = 1$  The dashed line is the plot of  $U$  vs  $z$  from (A-5) on the same locus curve.

Figure 21: Solution  $U$  vs  $z$  for the nonlinear model problem on the locus curve  $y = \Omega^2 z$  with  $\Omega^2 \approx 66$  and  $\nu = -1$  The dashed line is the plot of  $U$  vs  $z$  from (A-5) on the same locus curve.

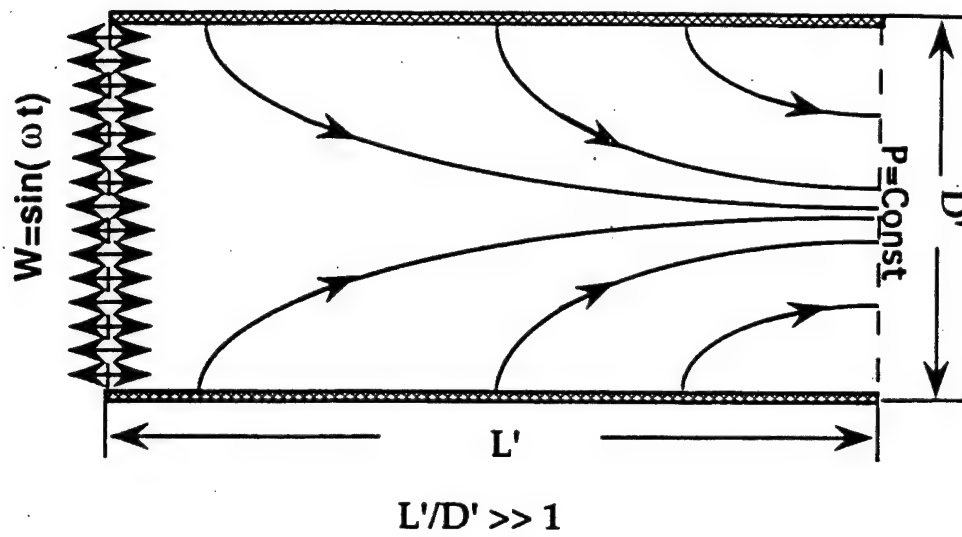
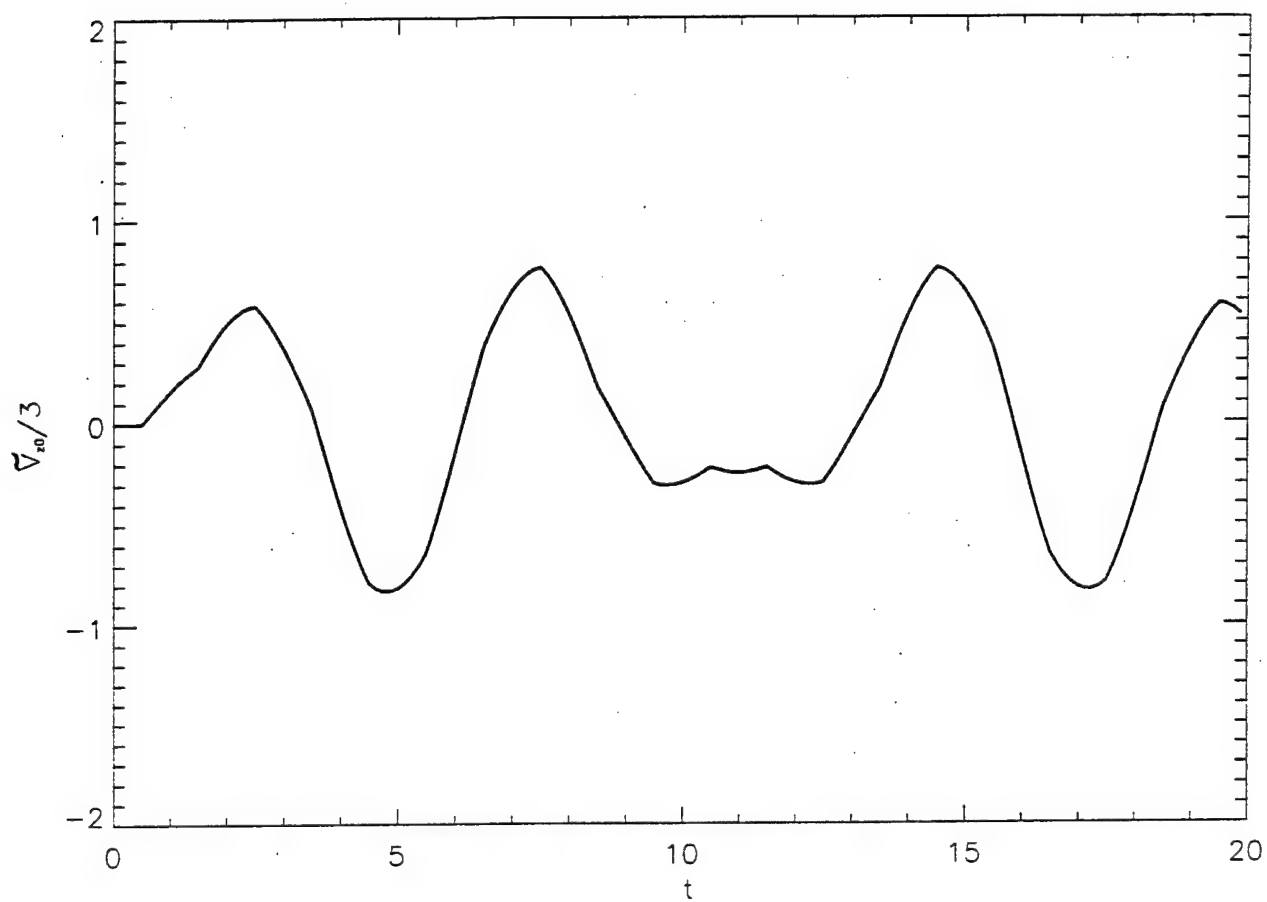


Figure 1: The cylindrical rocket engine chamber model of length  $L'$ , diameter  $D'$ , with endwall oscillations of frequency  $\omega$





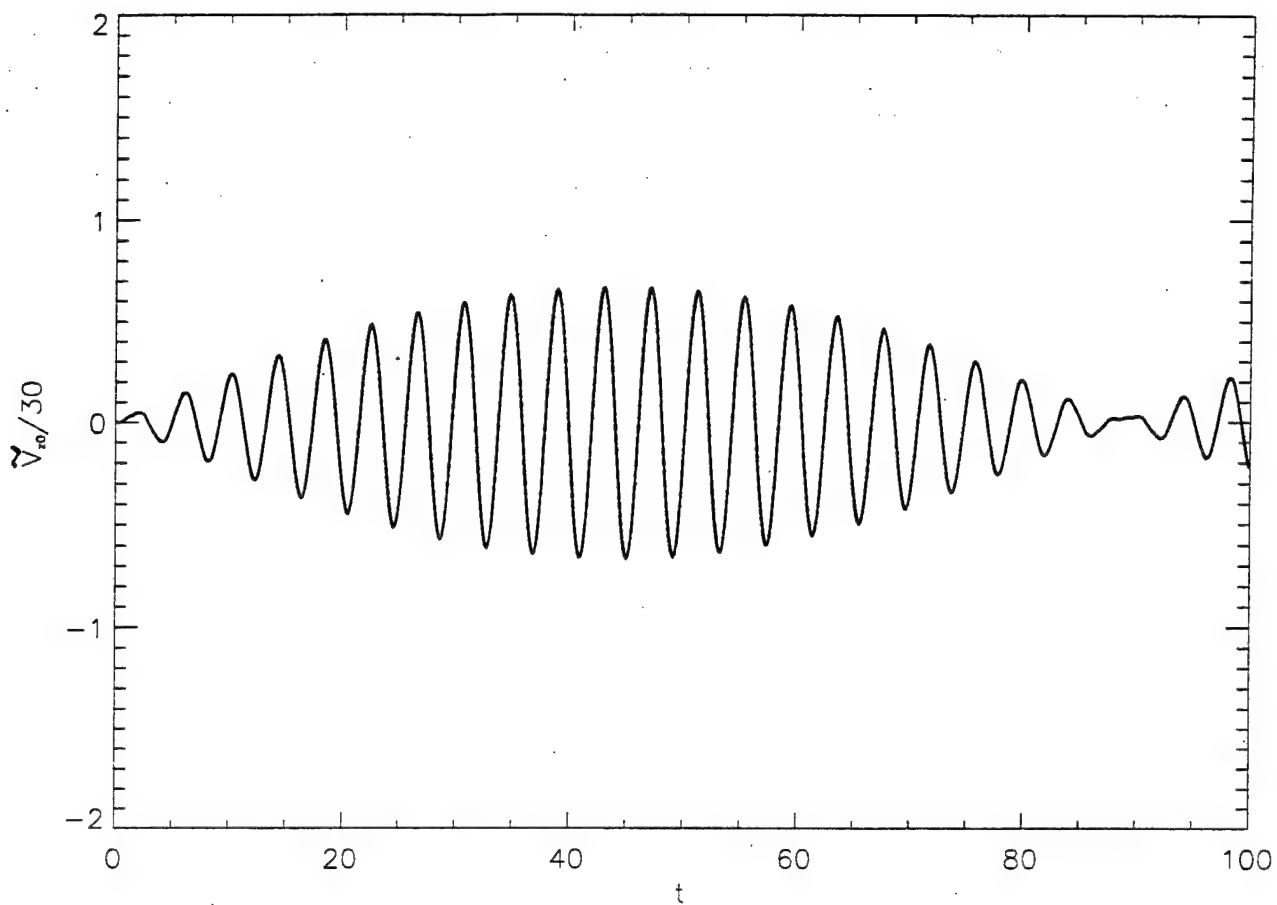


Fig. 3

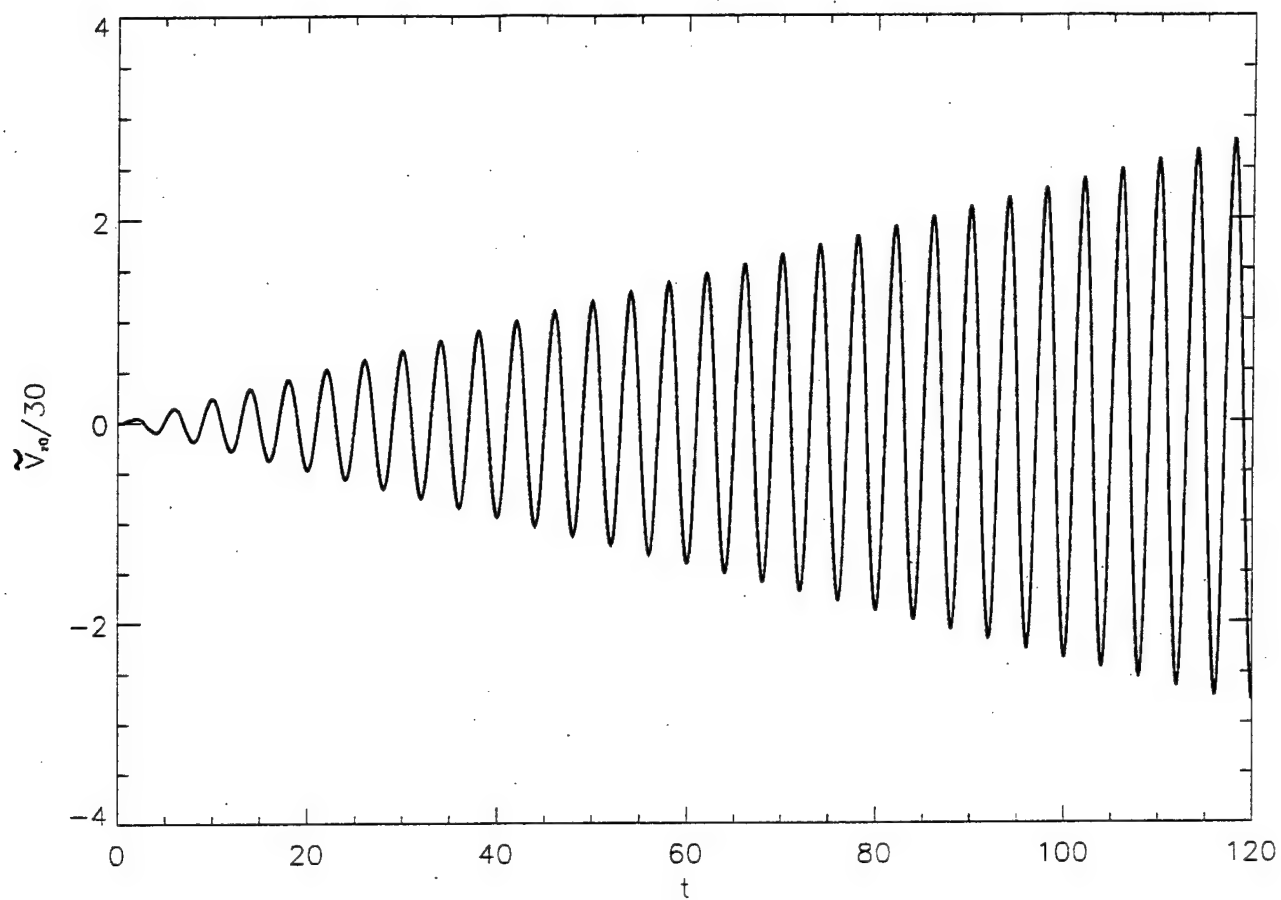


Fig. 4

2KK

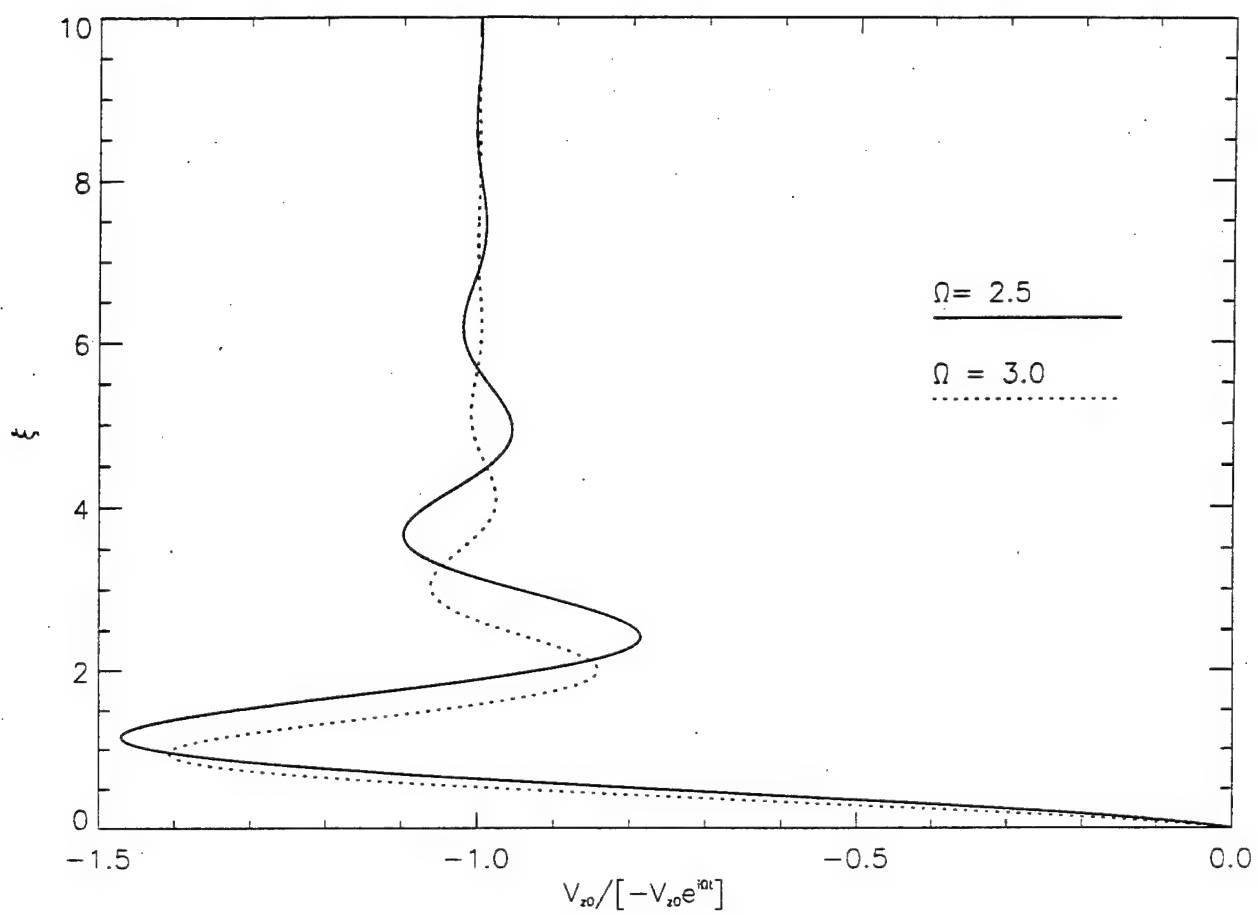


Fig. 5

ZKK

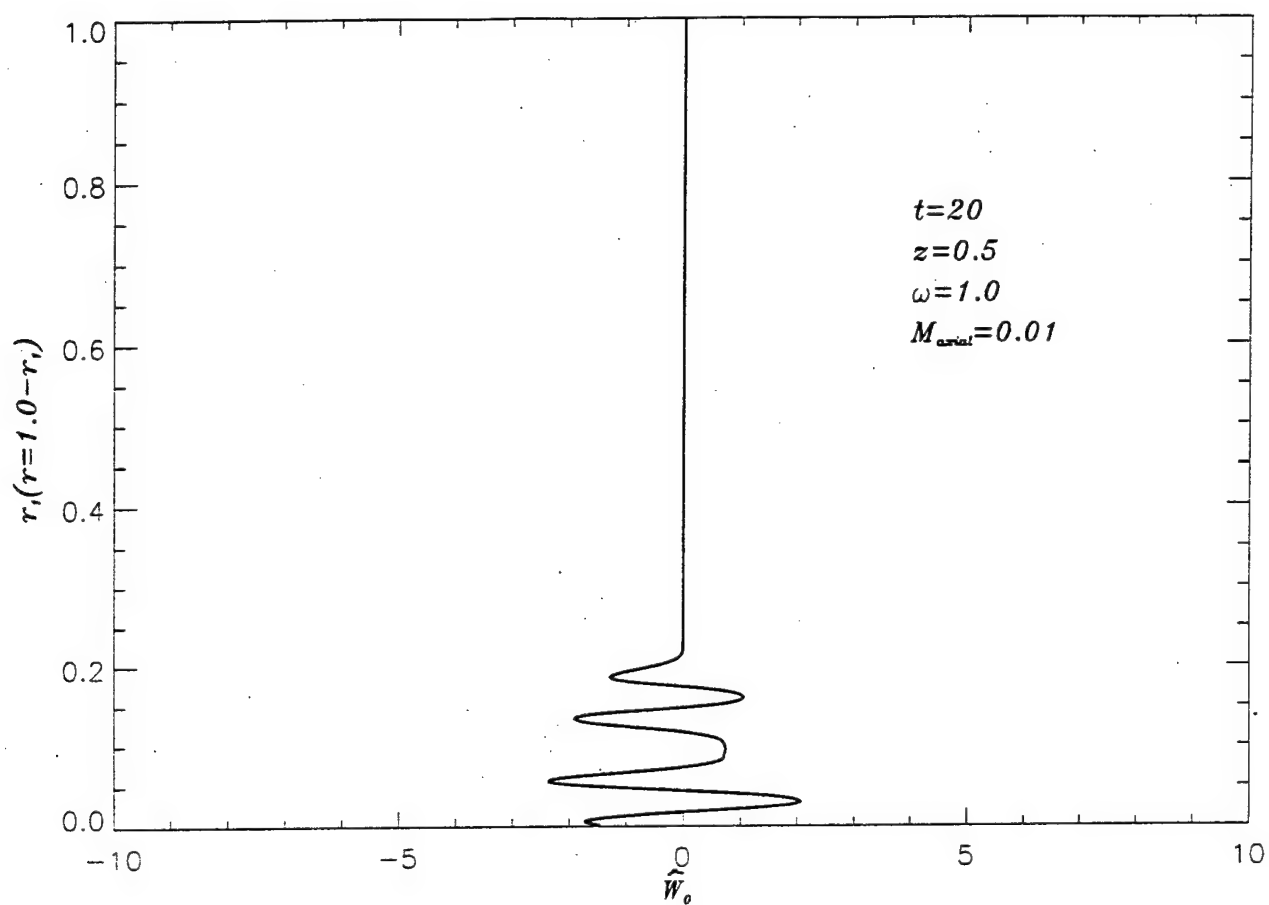


Fig. 6

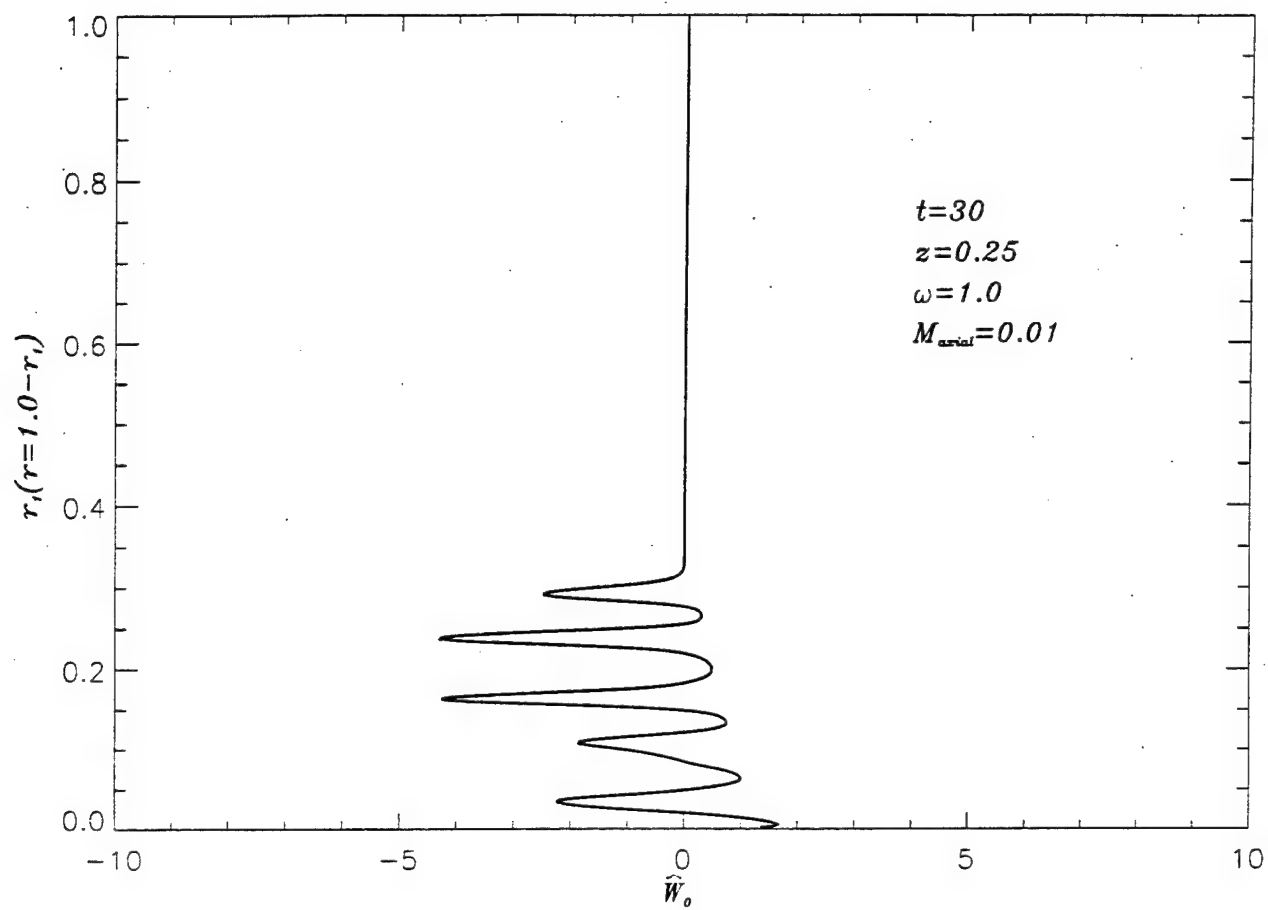


Fig. 7a

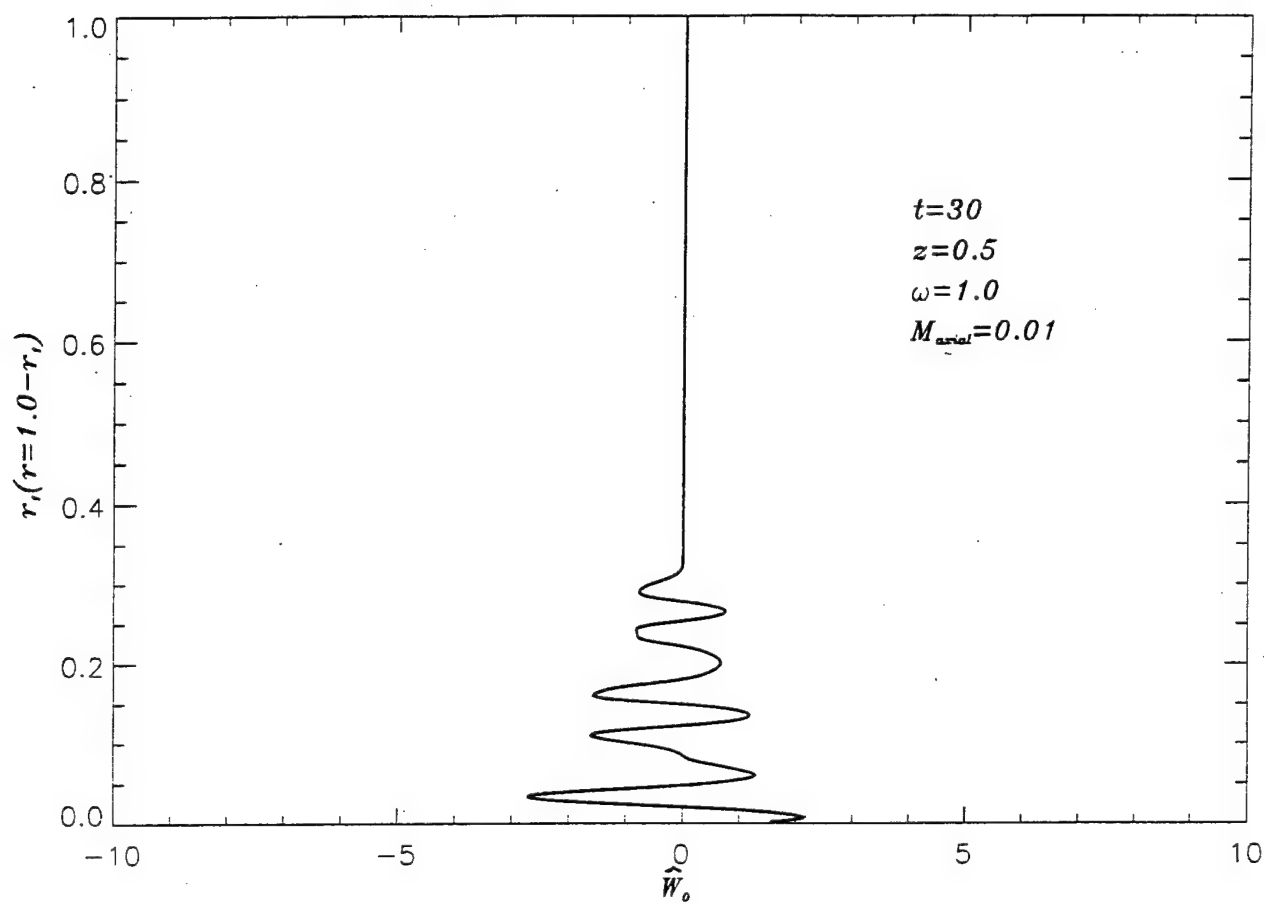


Fig. 76

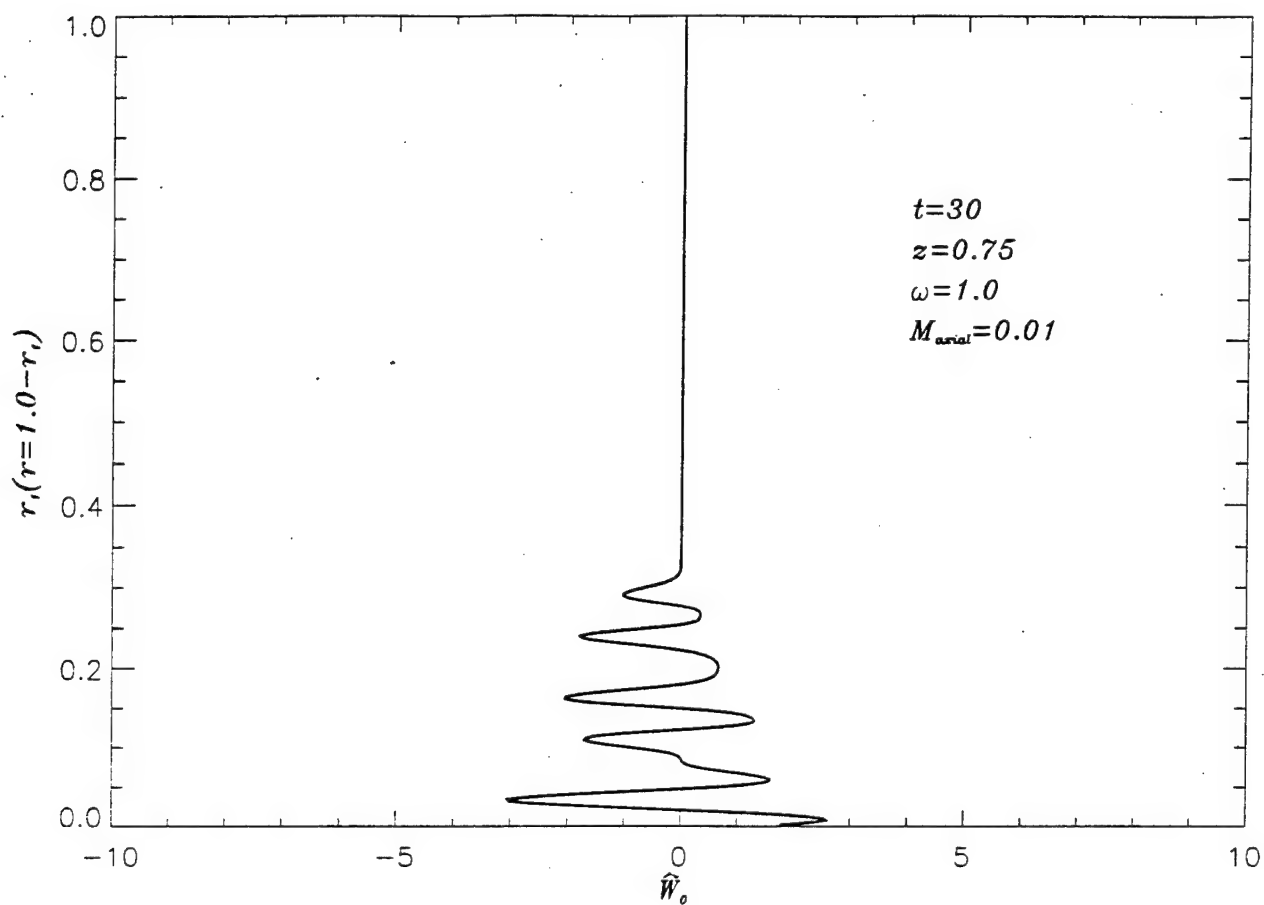


Fig. 7c



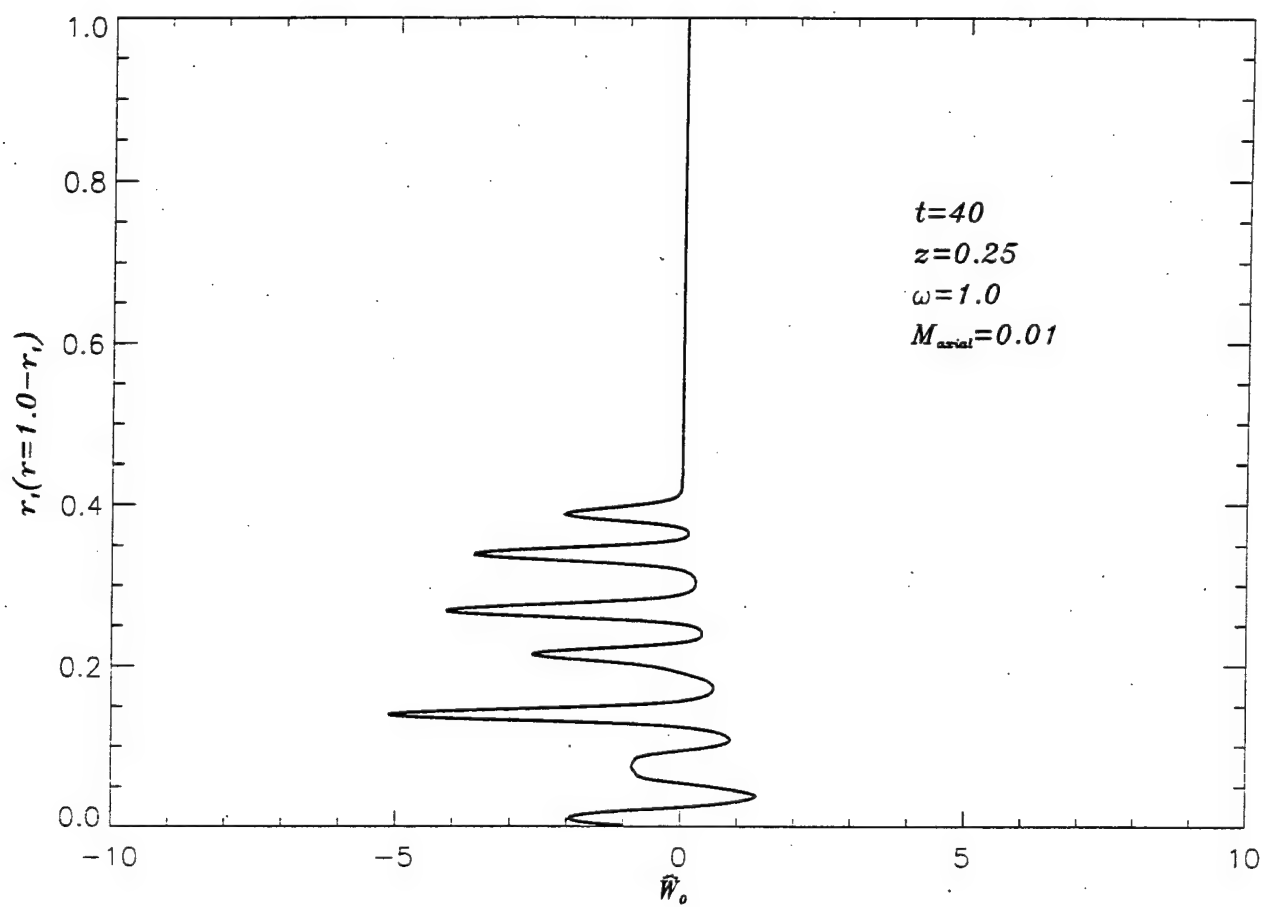


Fig. 8a

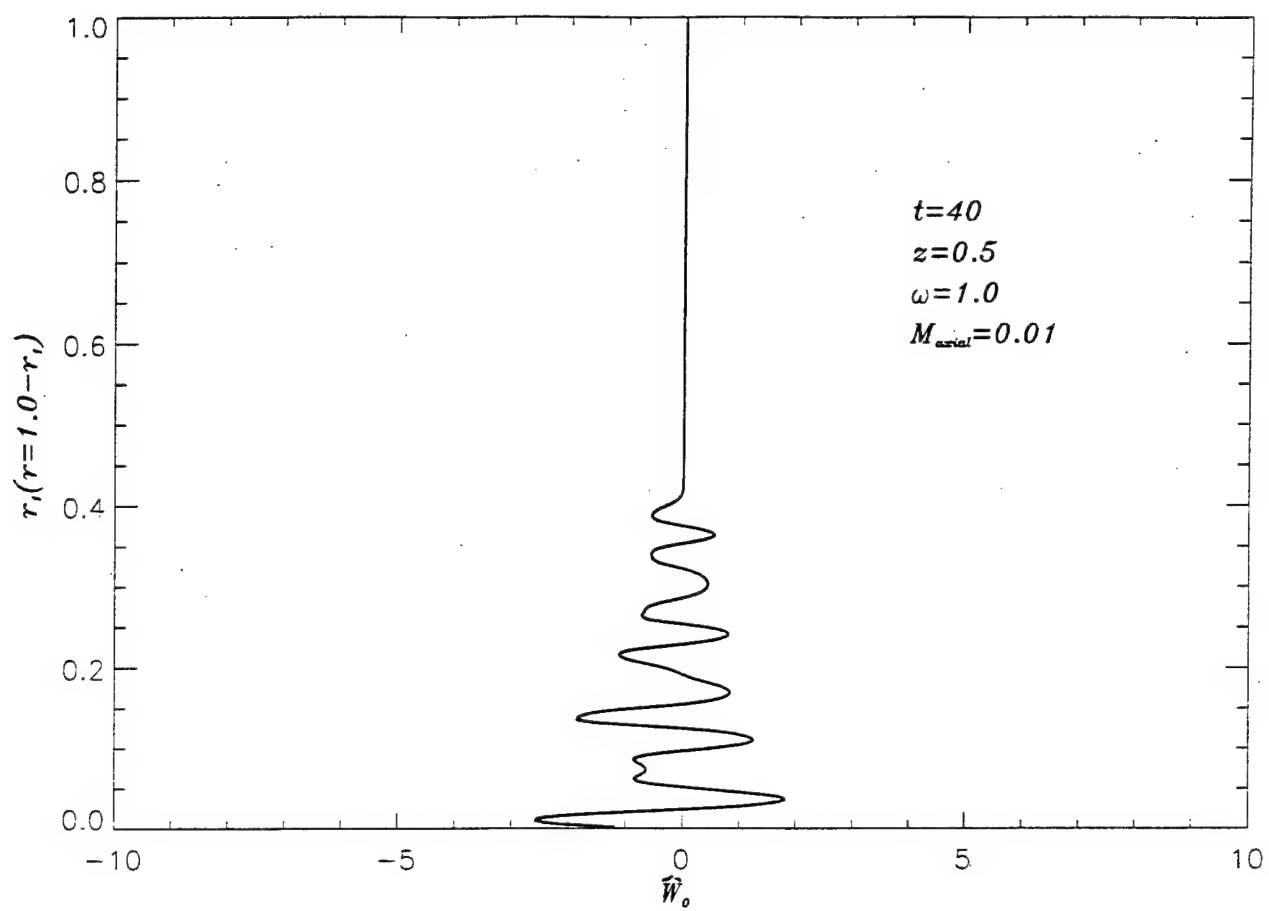


Fig. 86

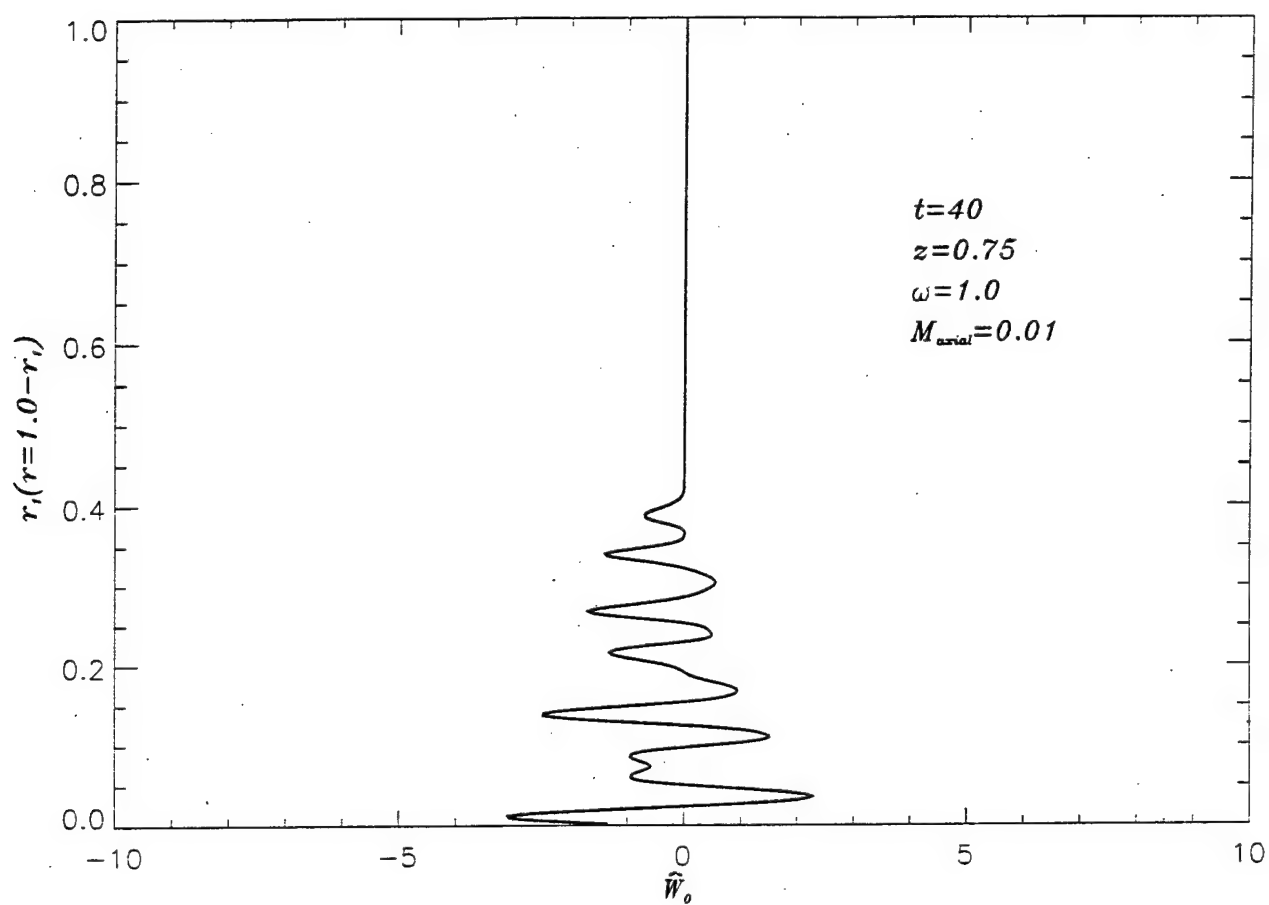
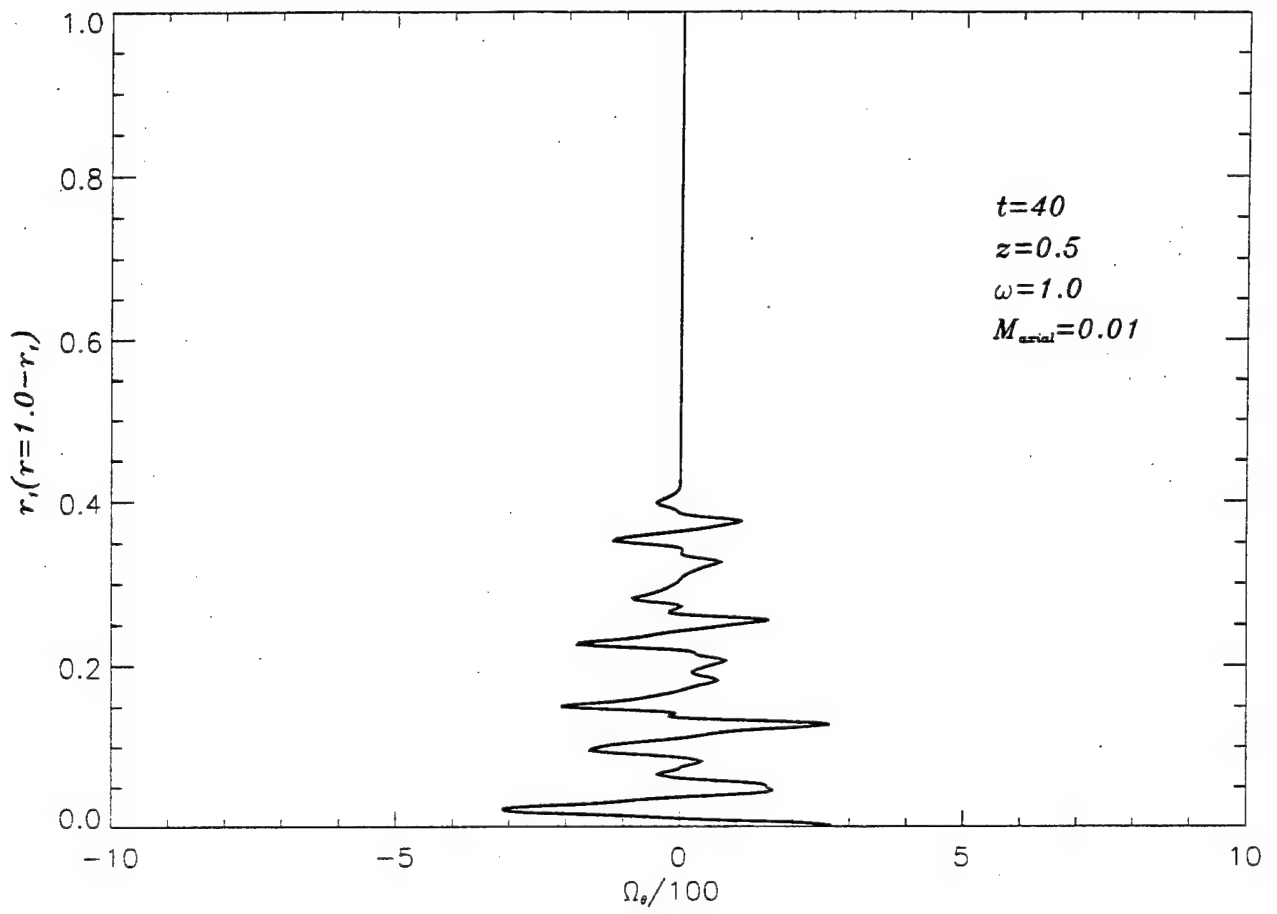


Fig. 8c



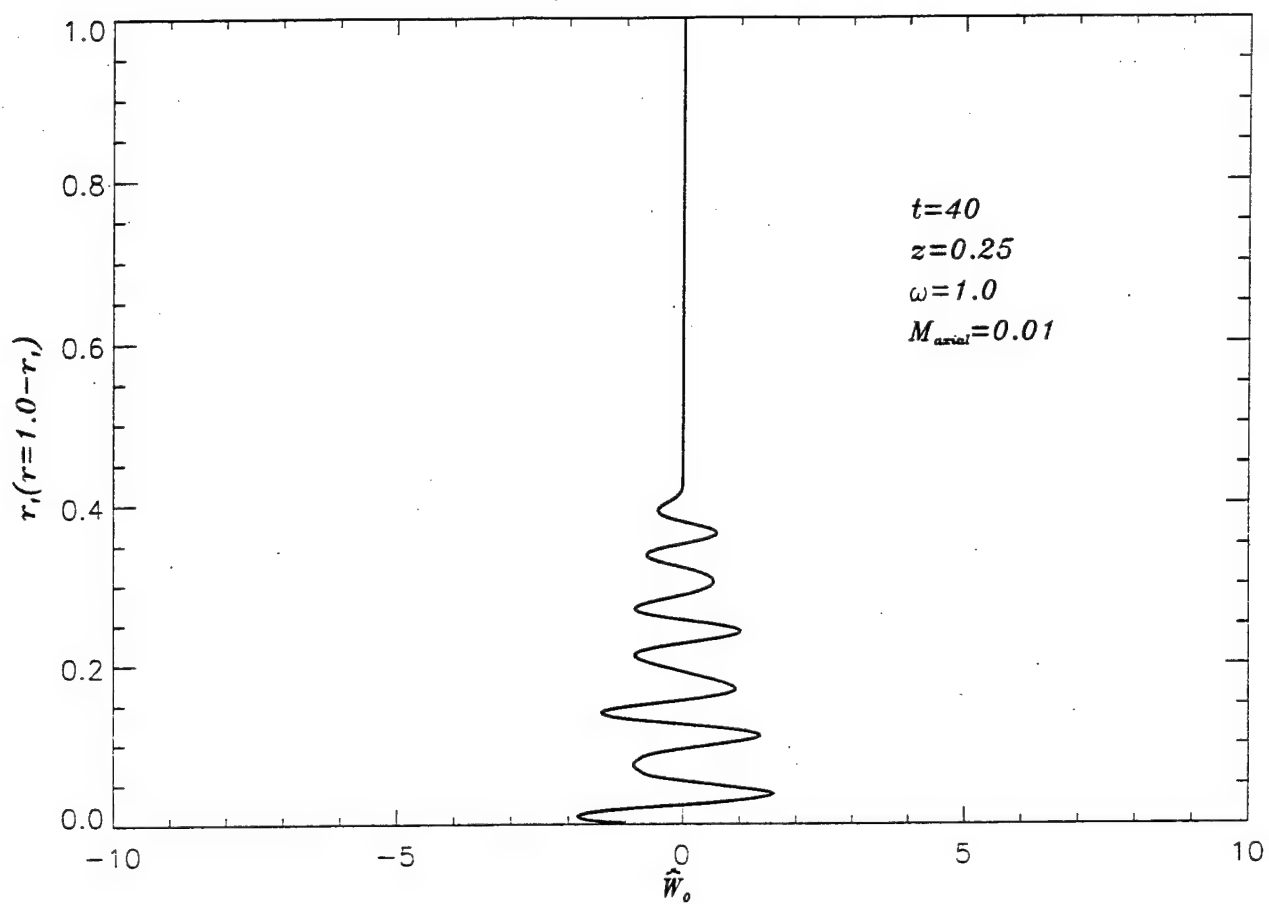


Fig. 10a

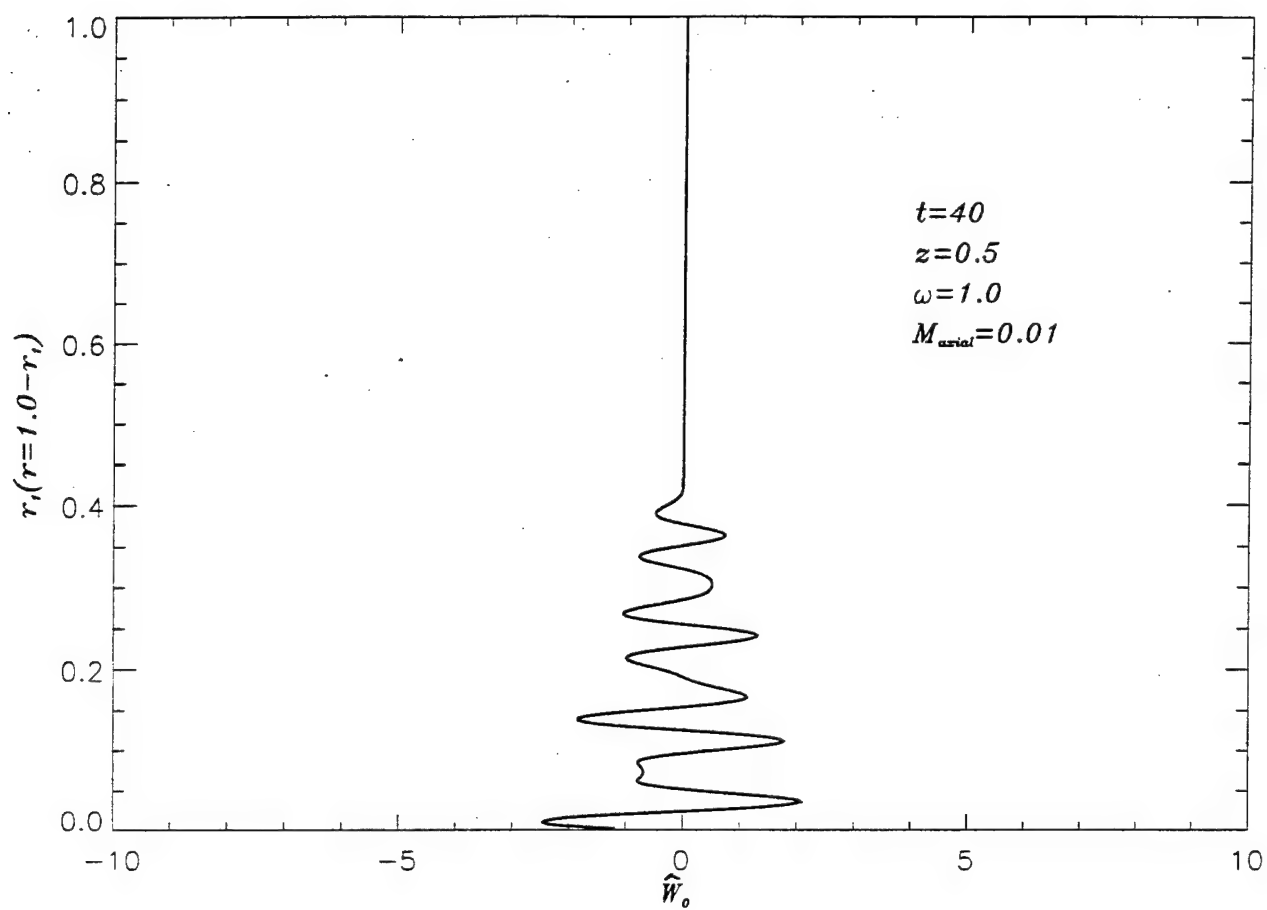


Fig. 10b

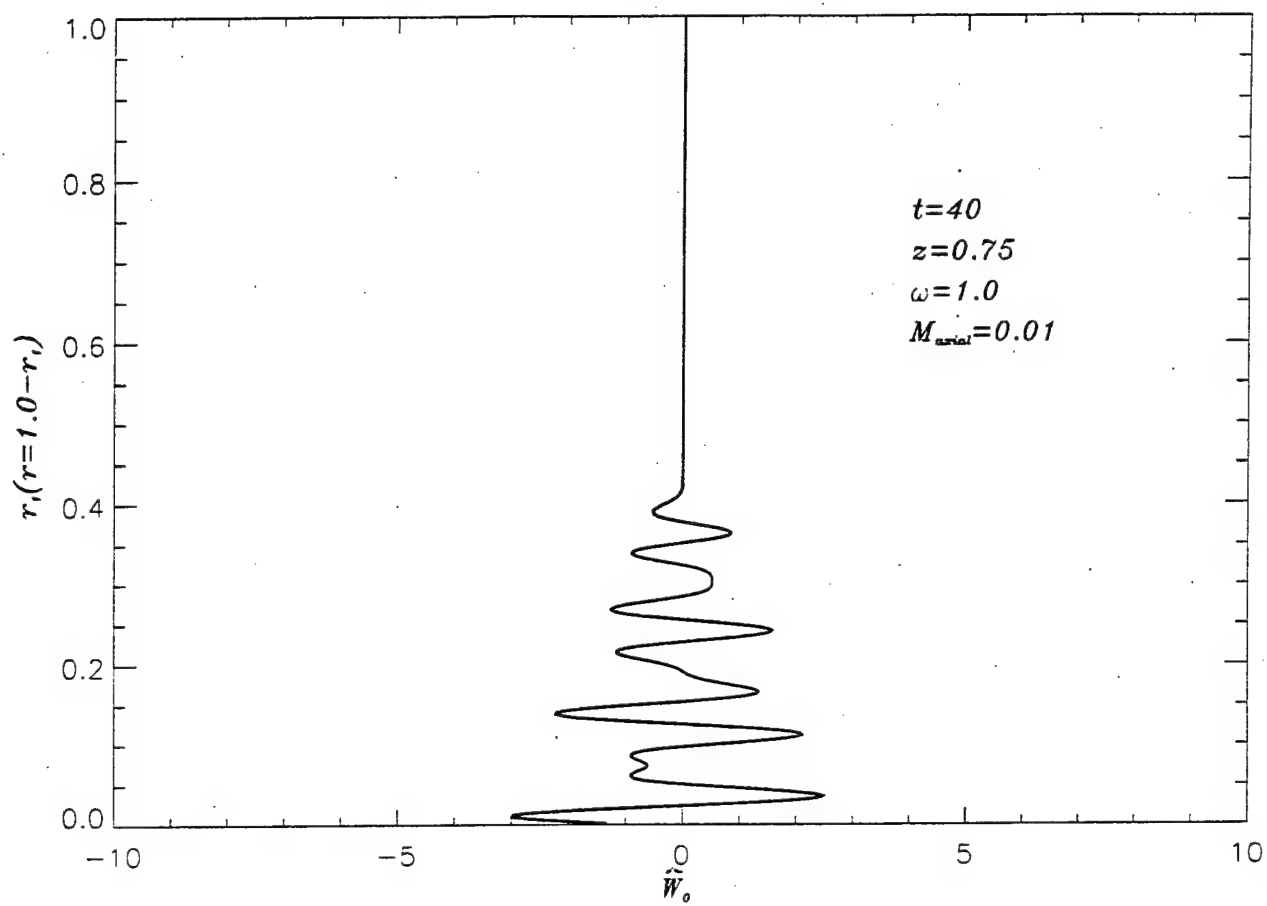


Fig 10C

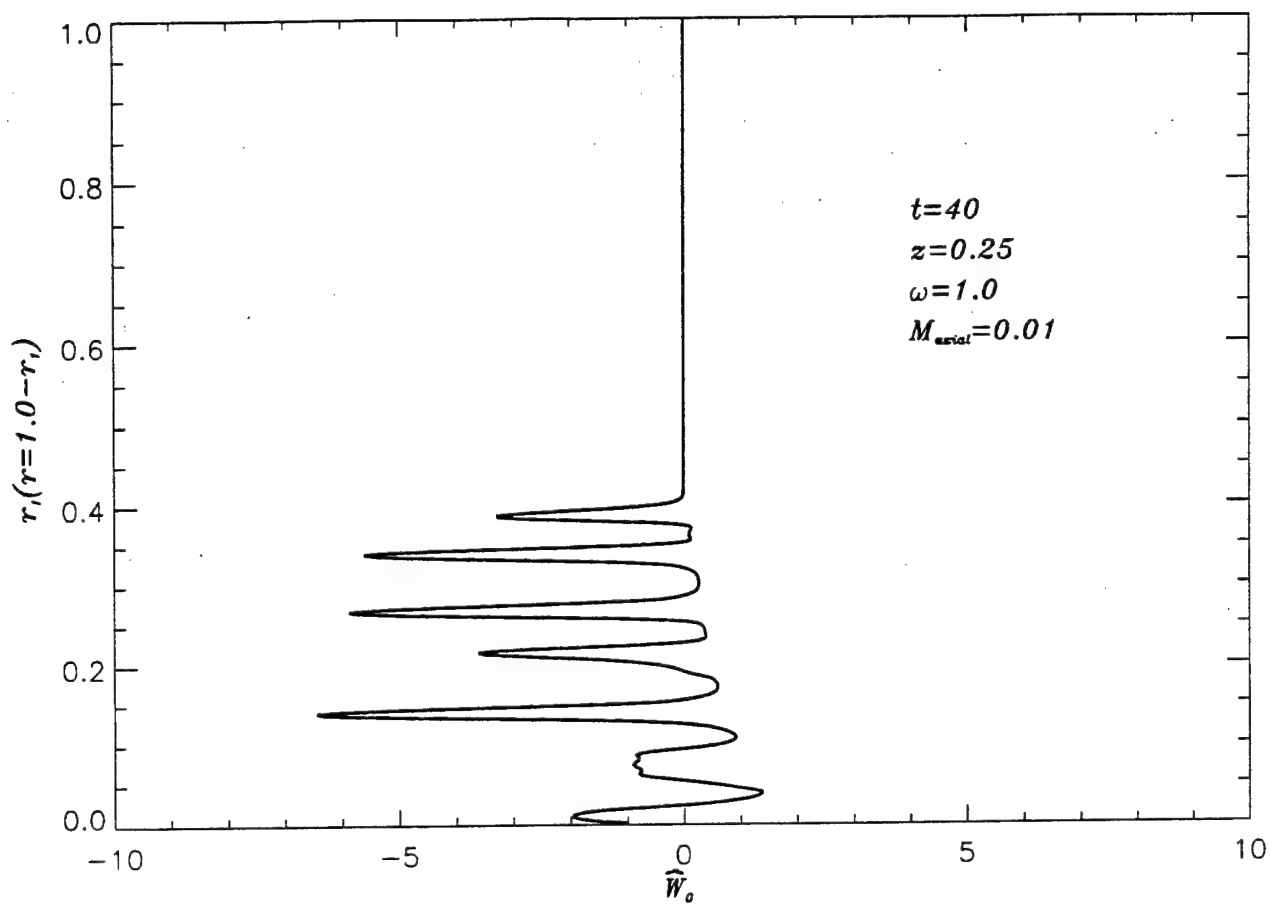


Fig. 11a



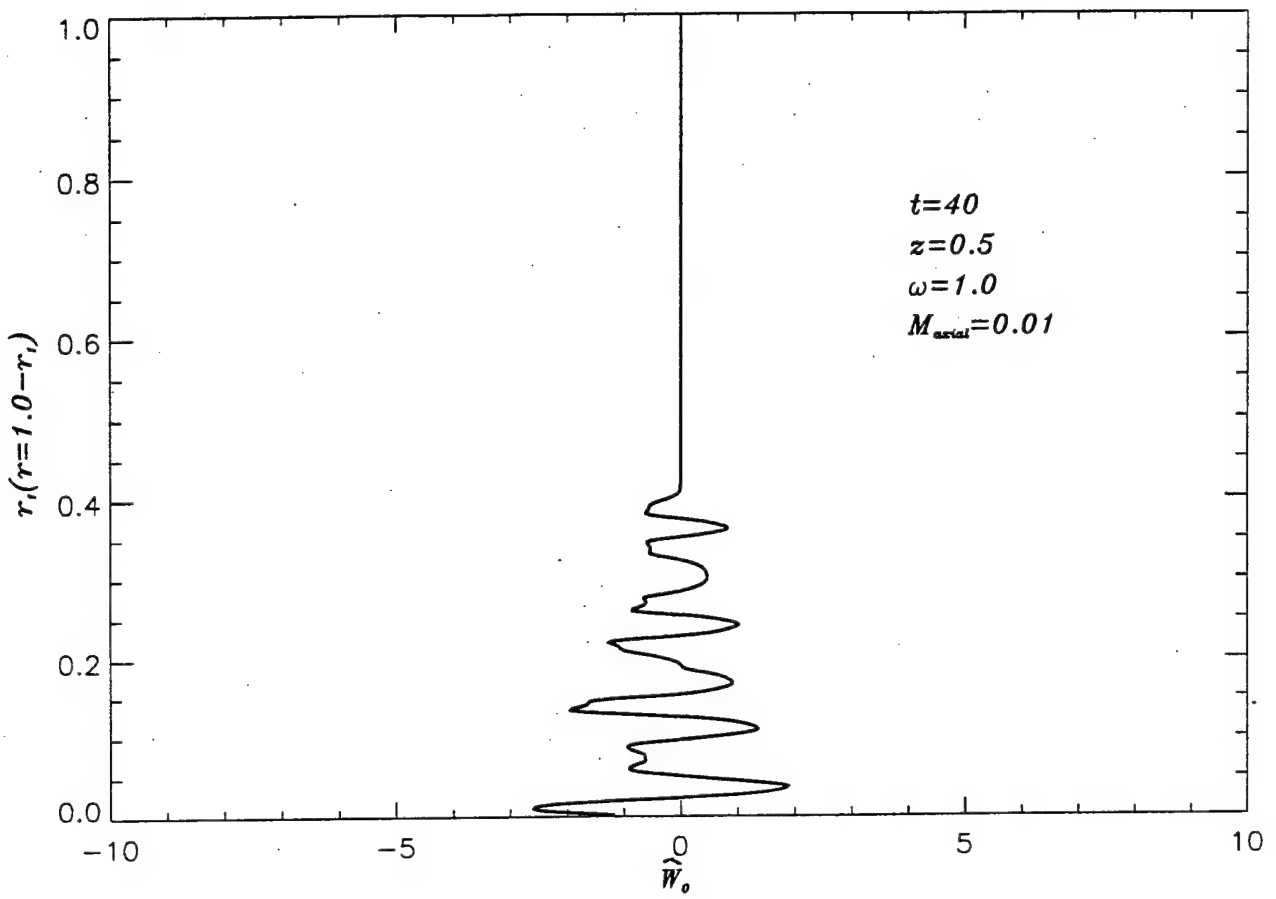


Fig. 116

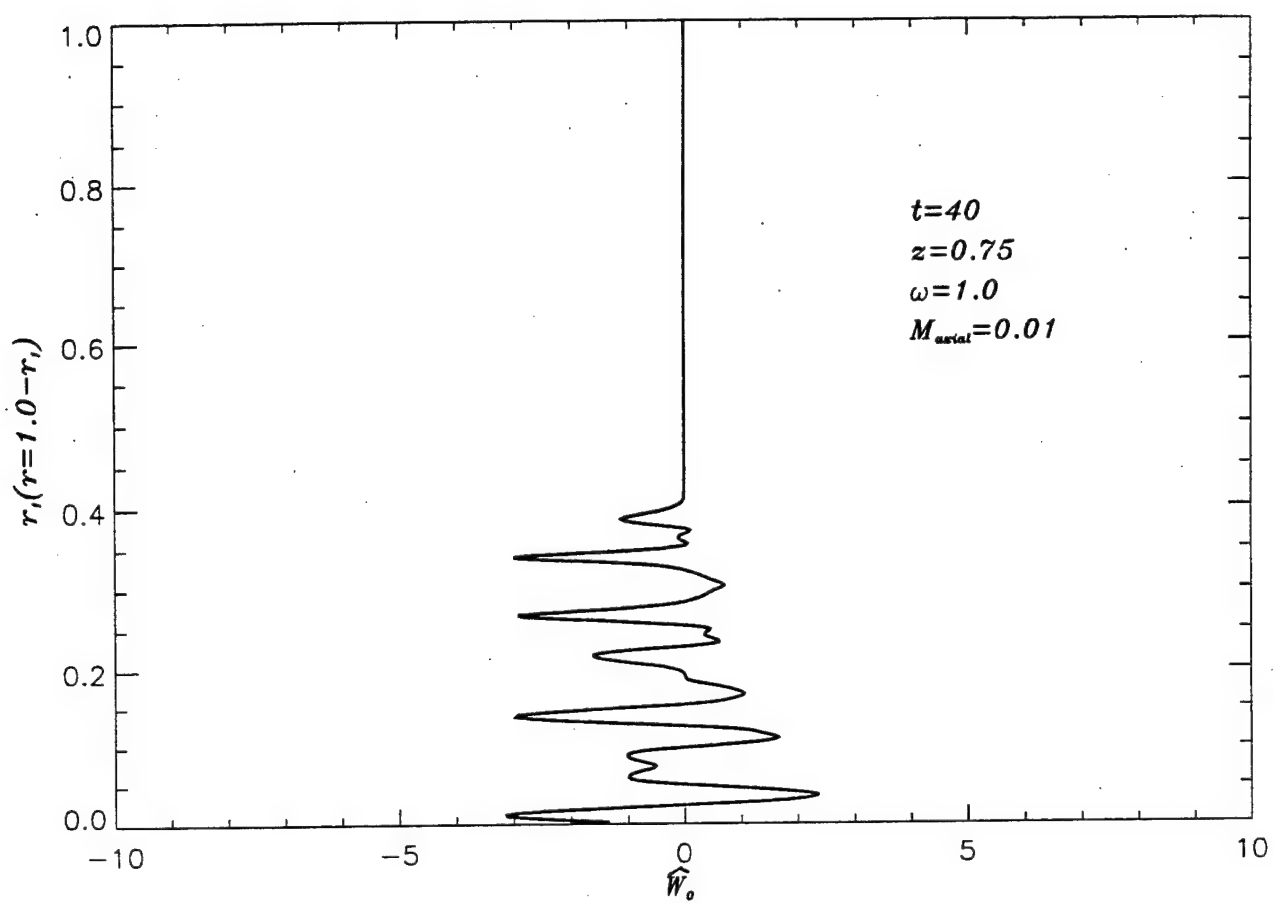


Fig. 11C

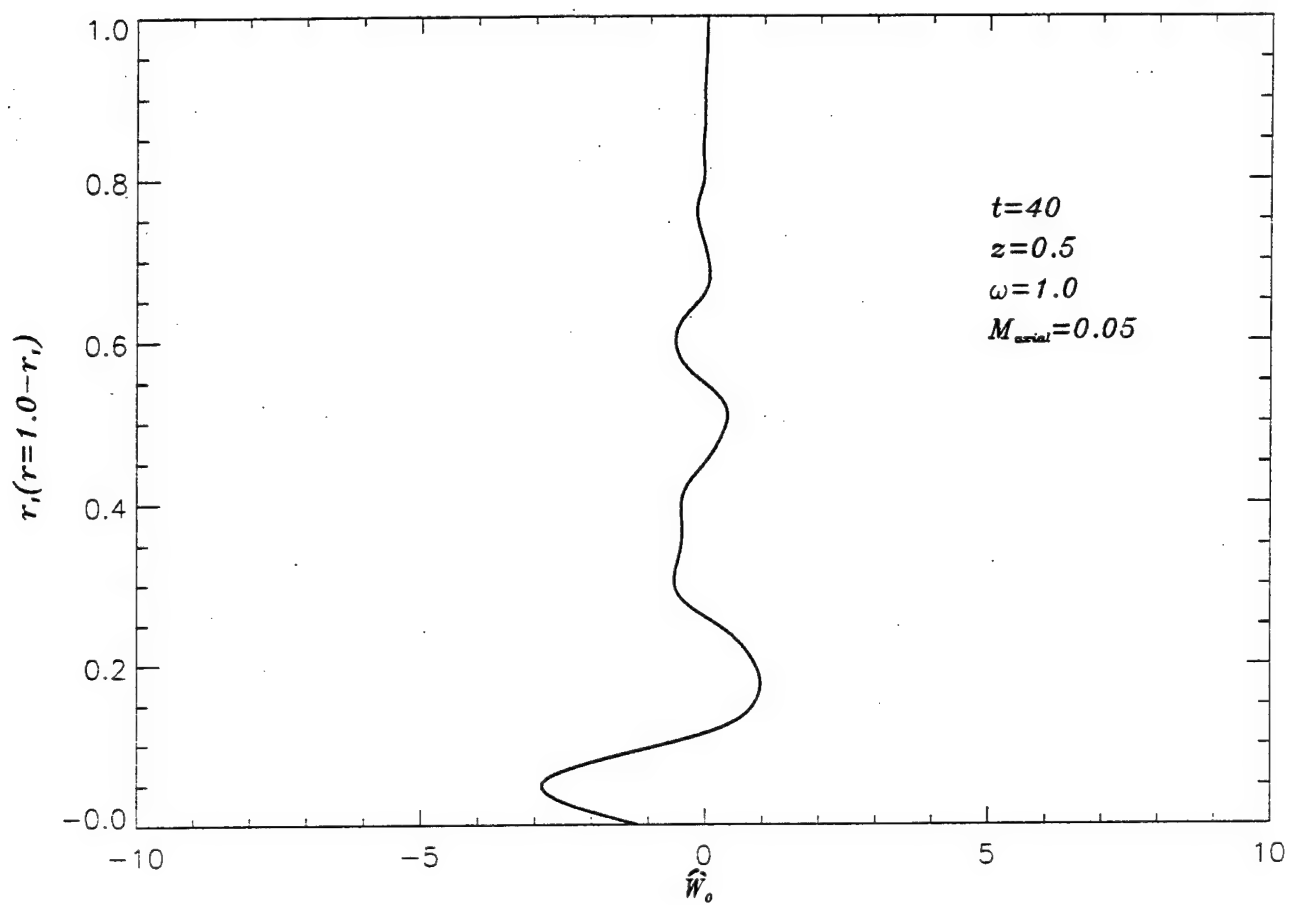


Fig. 12

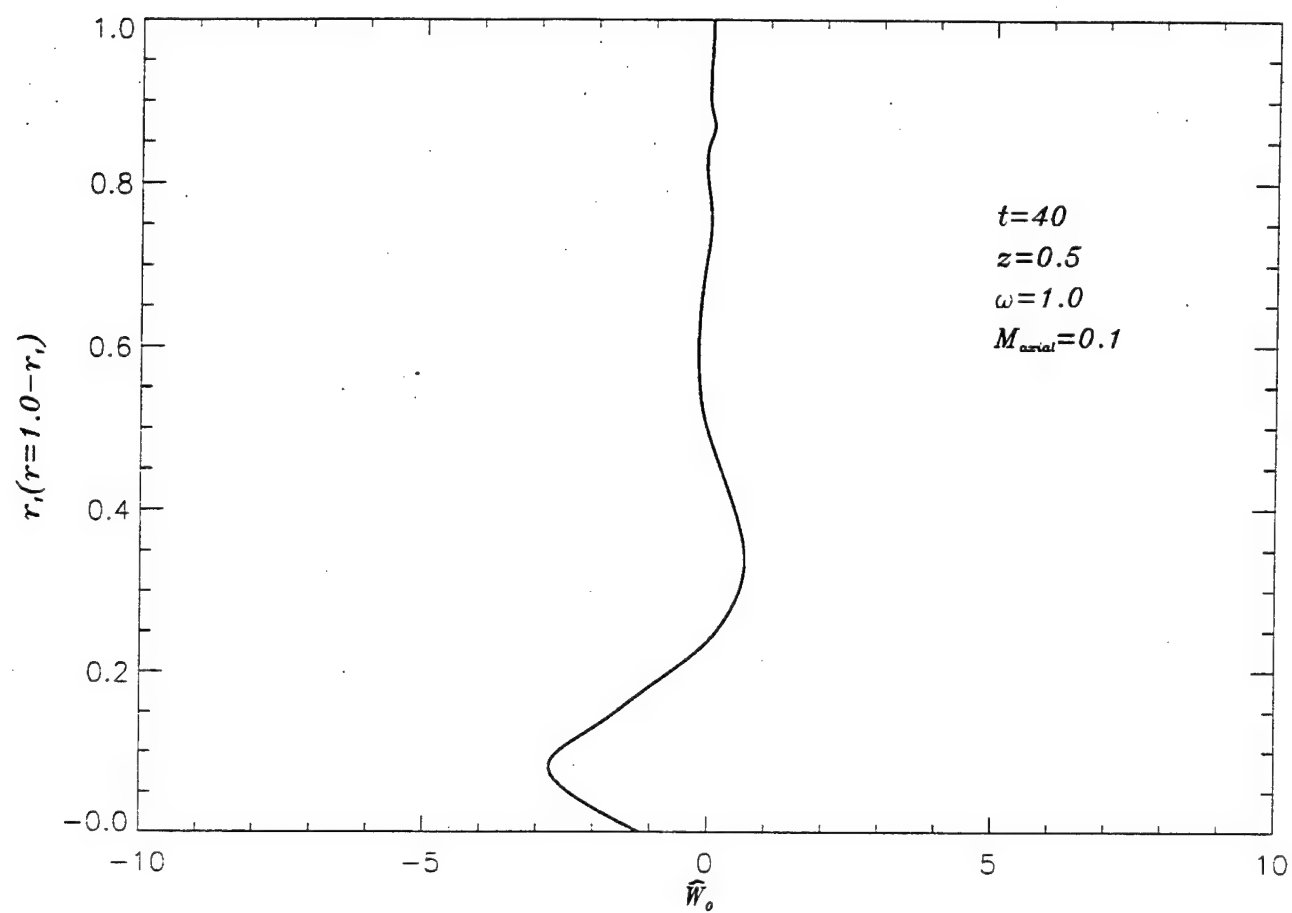


Fig. 13

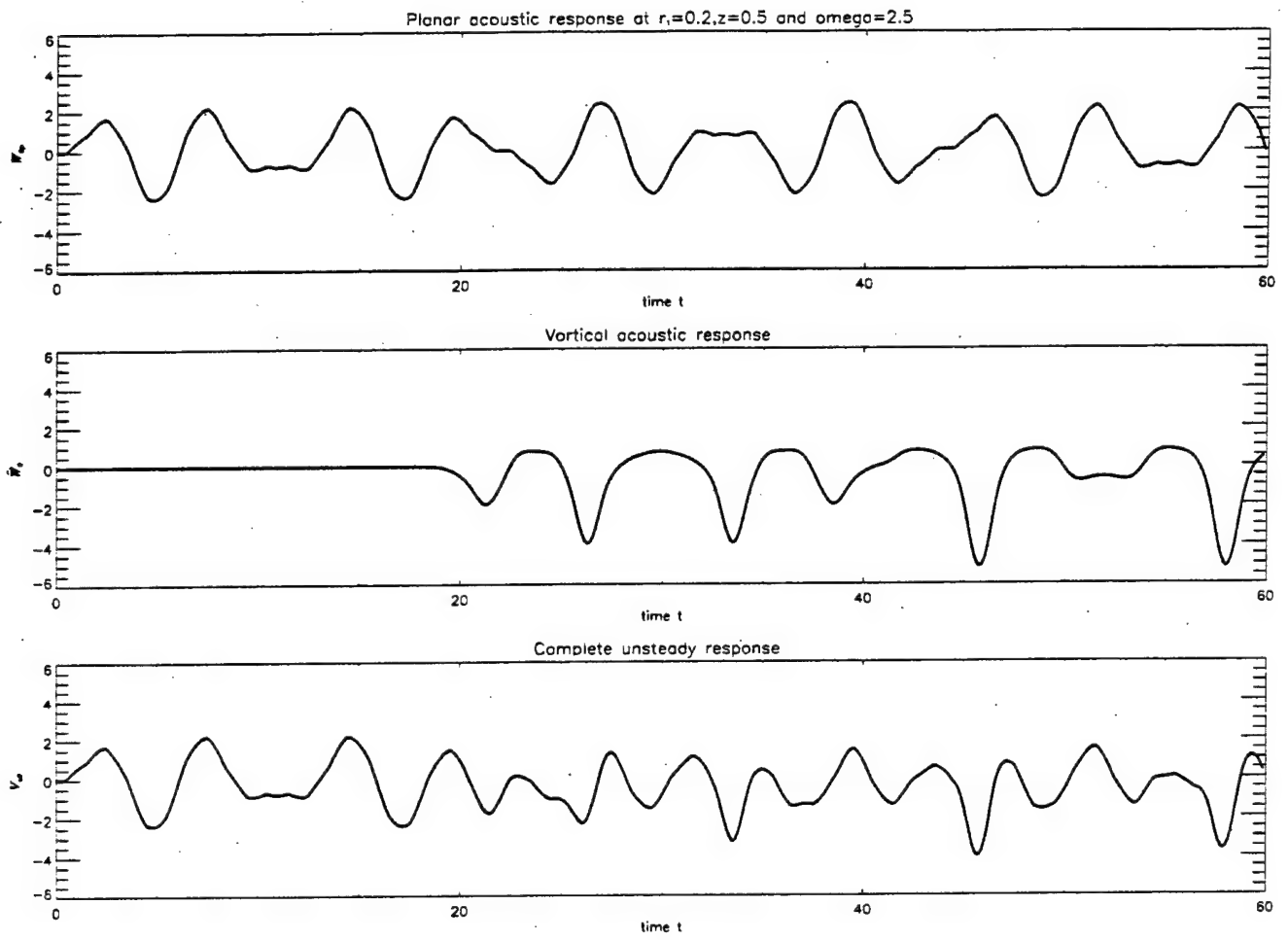


Fig. 14

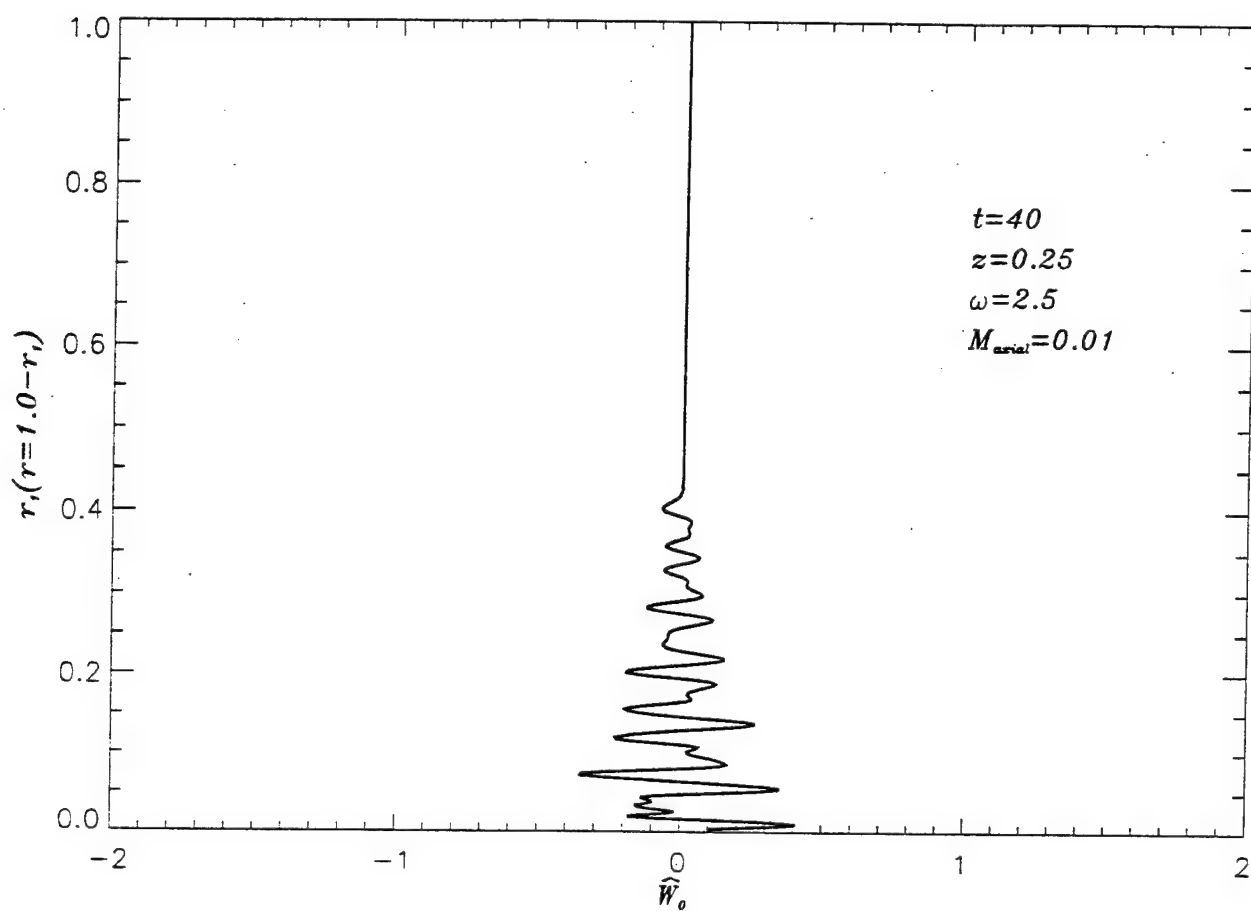


Fig. 15a

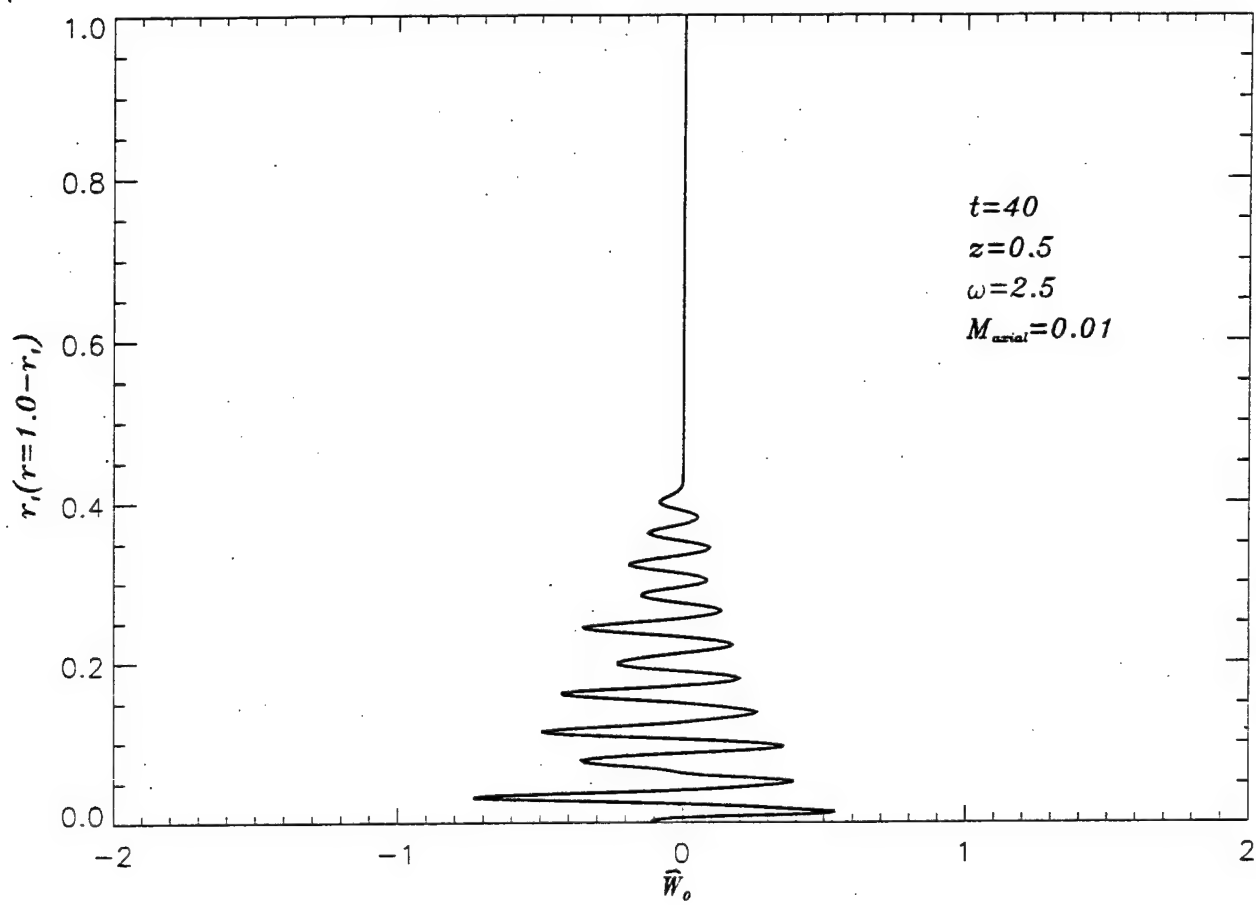


Fig. 156

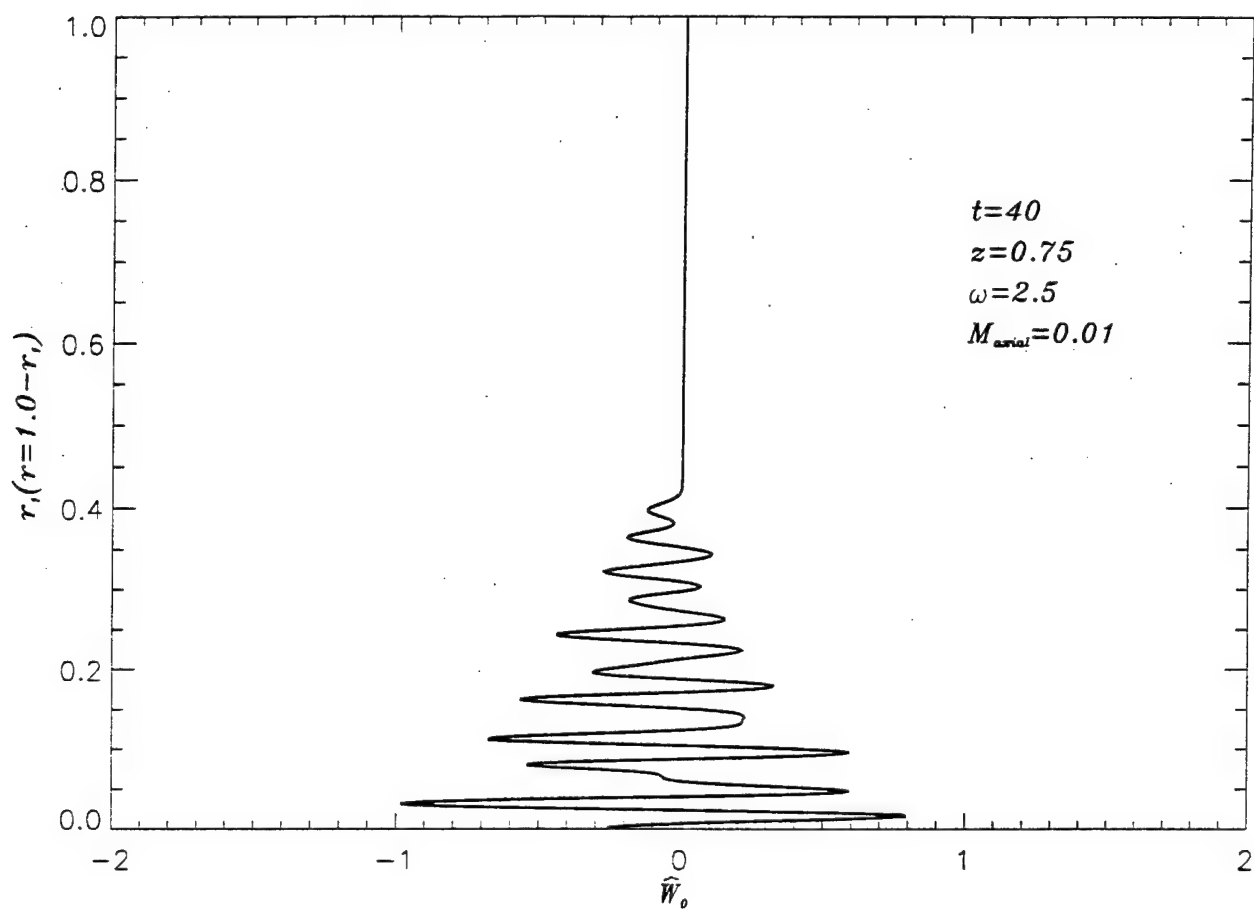


Fig. 15C



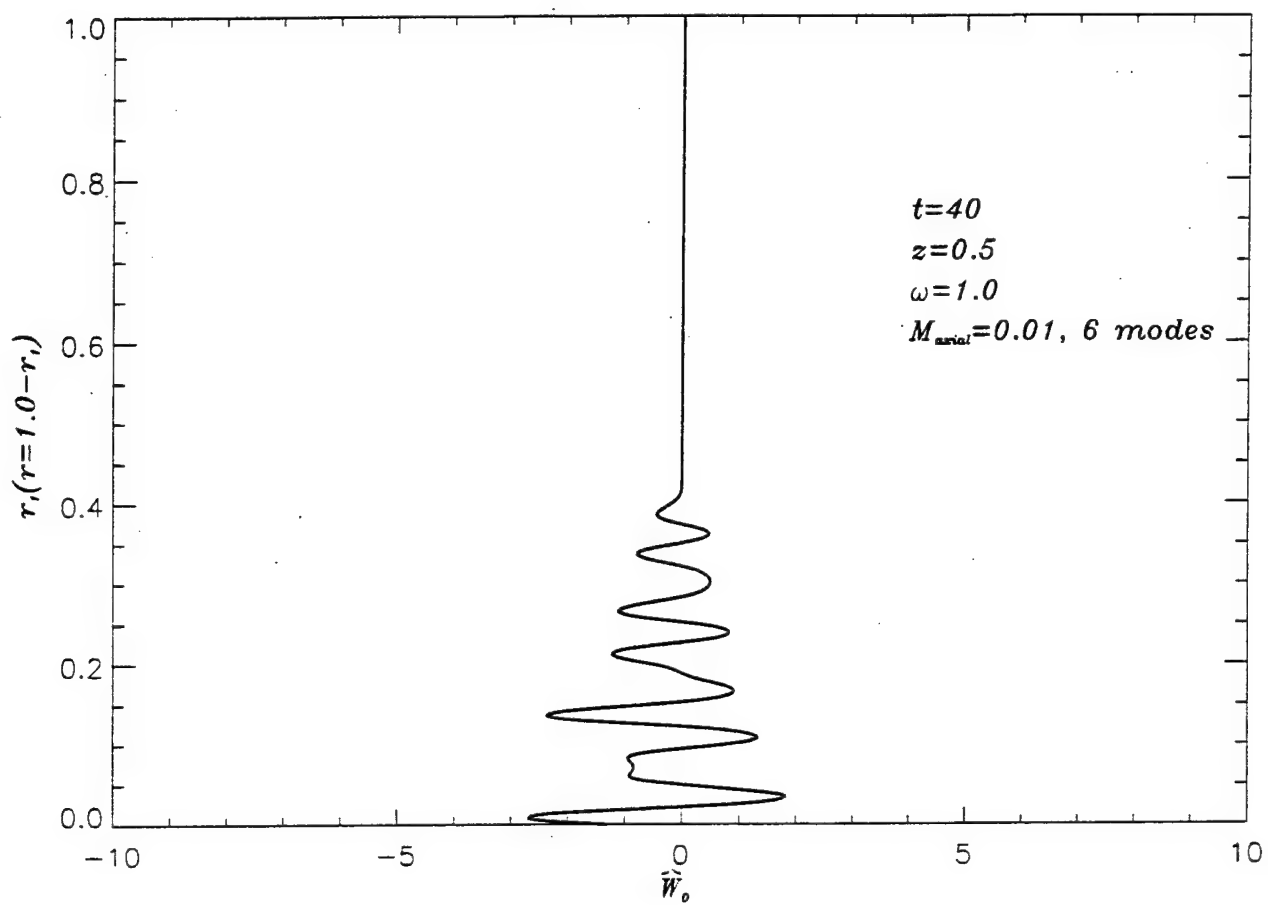


Fig. 16

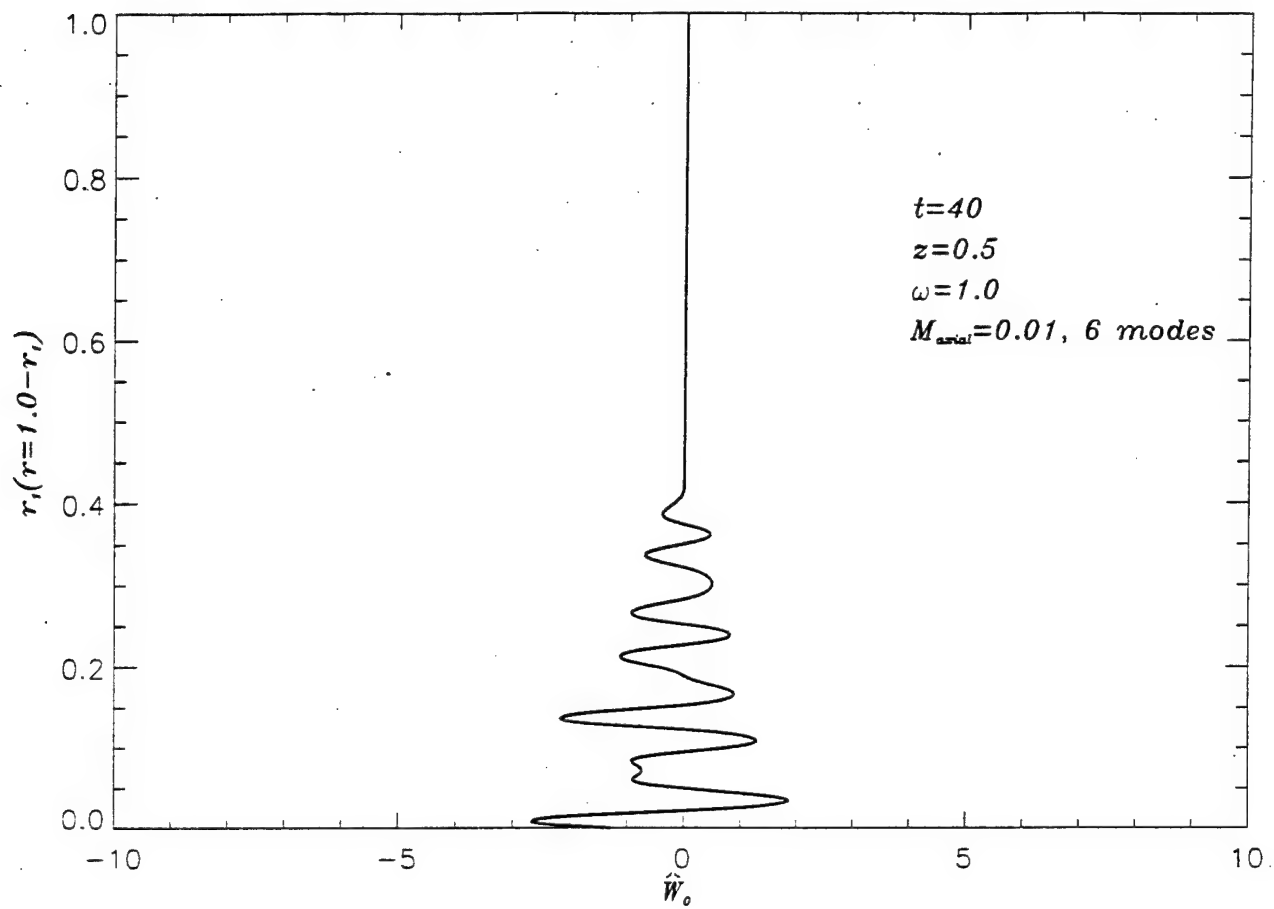


Fig. 17

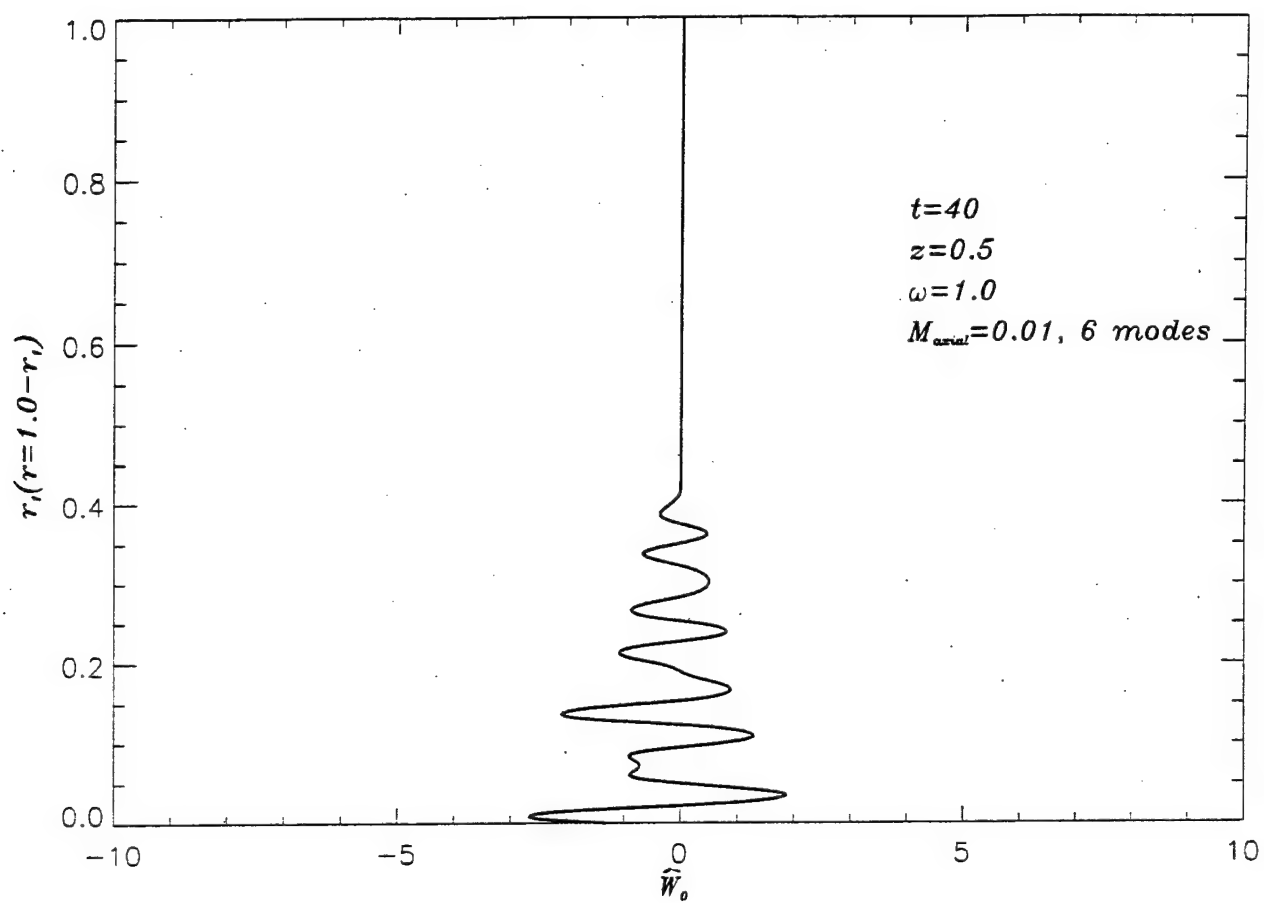


Fig. 18

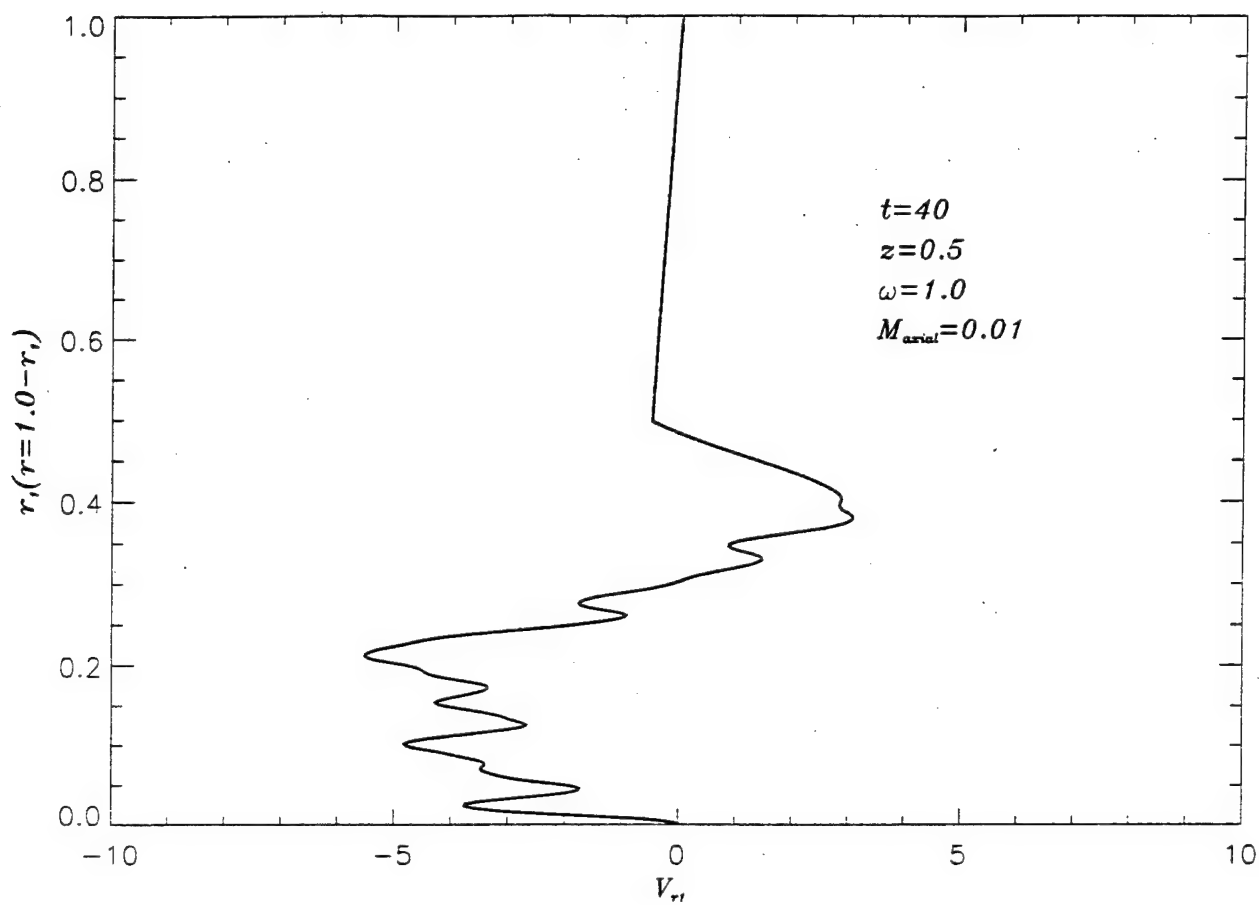


Fig. 19

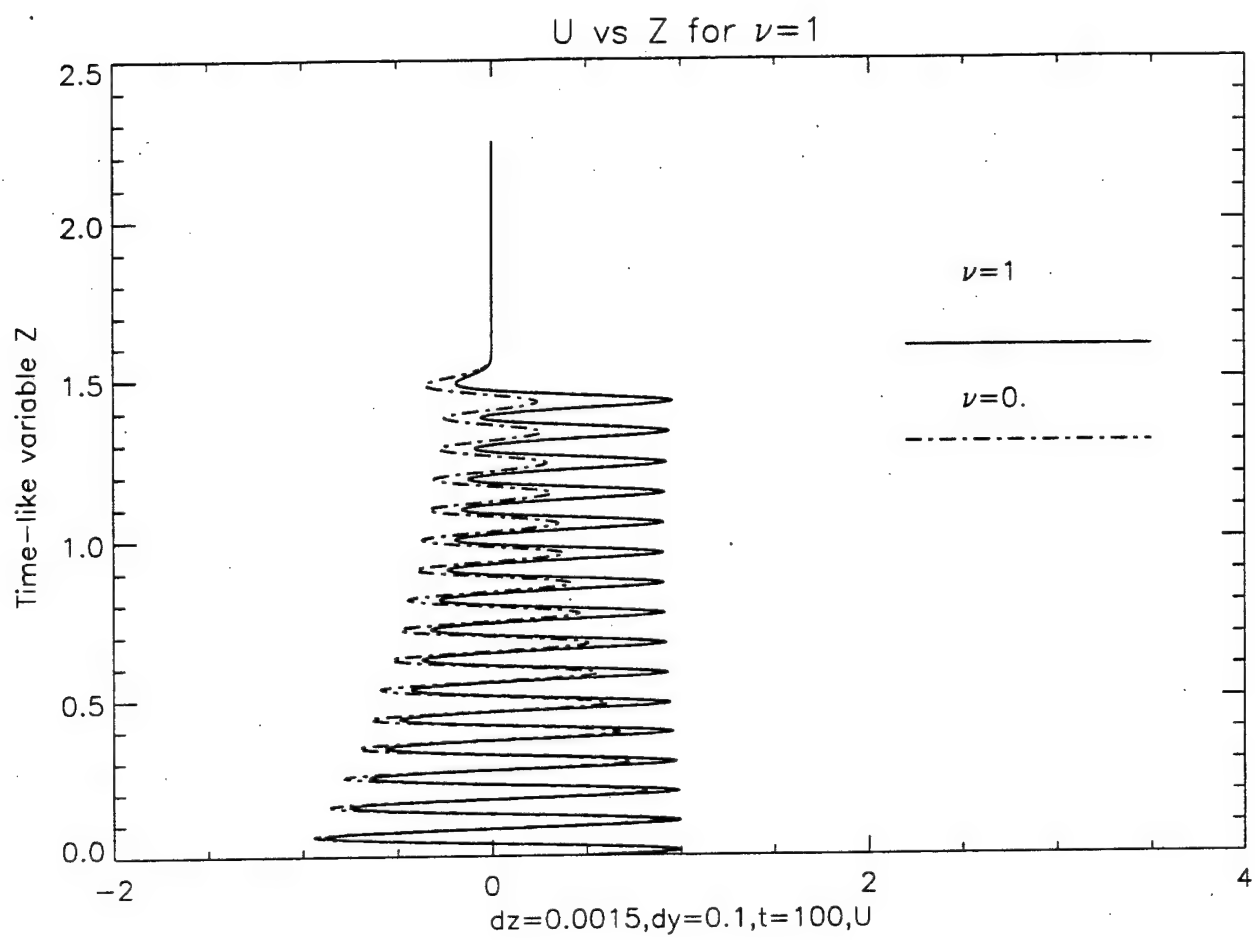


Fig. 20

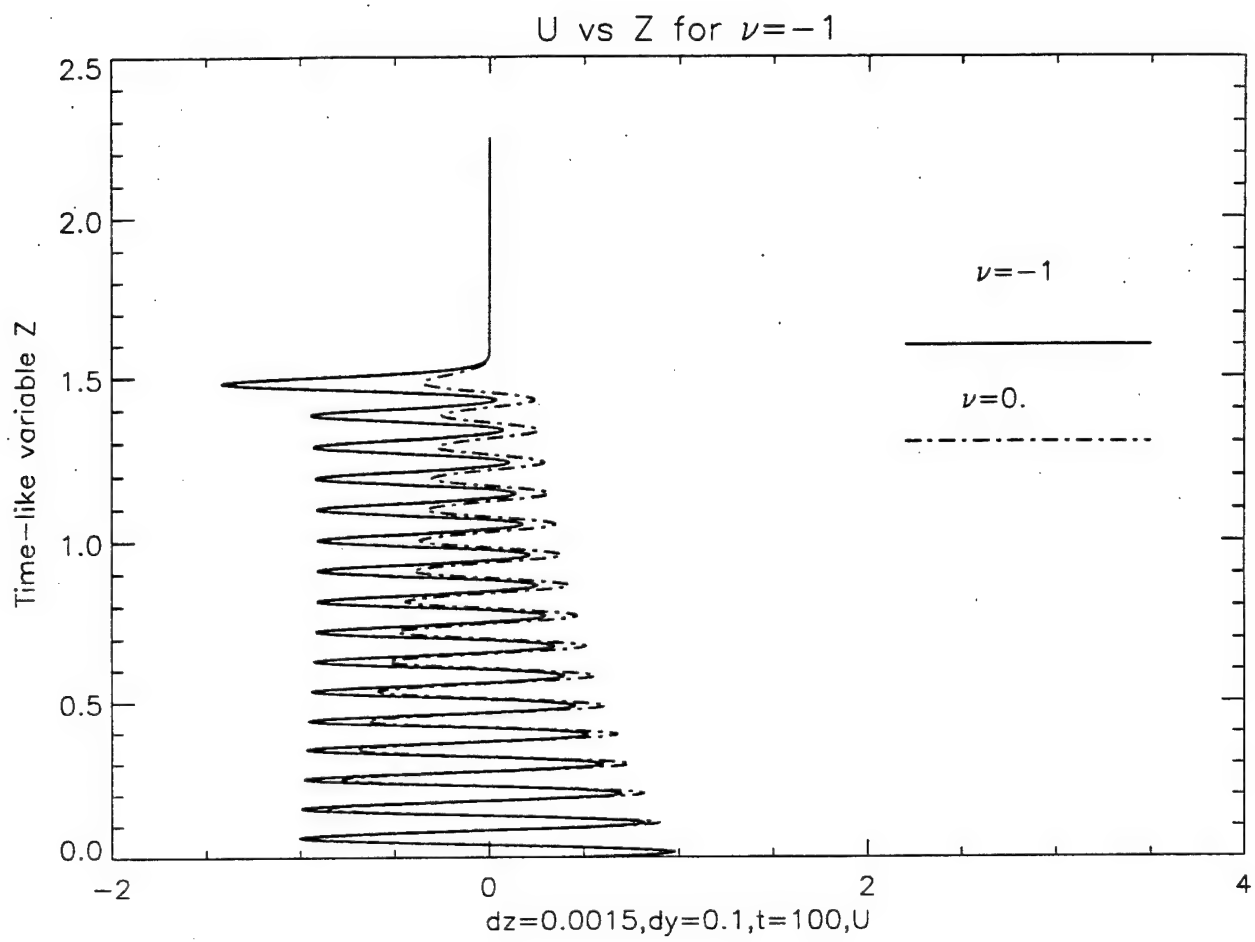


Fig. 21



AIAA 95-0603

UNSTEADY VORTICITY GENERATION AND  
EVOLUTION IN A MODEL OF A SOLID ROCKET  
MOTOR:  
SIDEWALL MASS ADDITION TRANSIENTS

K. Kirkkopru, D.R. Kassooy and Q. Zhao  
University of Colorado at Boulder  
Boulder, CO

**33rd Aerospace Sciences  
Meeting and Exhibit**  
January 9-12, 1995 / Reno, NV

# UNSTEADY VORTICITY GENERATION AND EVOLUTION IN A MODEL OF A SOLID ROCKET MOTOR: SIDEWALL MASS ADDITION TRANSIENTS

Kadir Kirkkopru\*, David R. Kassoy†, Qing Zhao‡

Department of Mechanical Engineering

University of Colorado at Boulder

Boulder, Colorado 80309

## Abstract

The two-dimensional, axisymmetric Navier-Stokes equations are solved numerically to study the effect of simulated propellant burning transients on the generation and evolution vorticity in a finite cylinder. A steady internal flow field driven by constant sidewall injection is perturbed by nonnegative axially distributed unsteady injection from sidewall, which simulates the unsteady mass input from propellant burning transients. The unsteady injection amplitude is chosen to be the same order of magnitude as that of the steady sidewall injection so that nonlinear effects have impact on the evolution of the vorticity field. Solutions to an initial value problem are used to show how vorticity is generated at the sidewall and then is convected into the chamber flow. The flow fields contain large instantaneous shear stress transients that are not considered in the traditional acoustic stability analyses.

## 1. Introduction

Solid propellant combustion in a rocket motor generates gaseous products that induce a low axial Mach number ( $M = O(10^{-2} - 10^{-1})$ ), large Re number ( $Re = O(10^4 - 10^6)$ ) internal shear flow in a long, narrow rocket motor chamber where the aspect ratio  $\delta \gg 1$ . The complete time-dependent shear flow is now known to include vorticity distributions (Vuillot and Avalon<sup>8</sup>, Flandro<sup>10</sup>, Kirkkopru et al.<sup>11</sup>, Tseng et al.<sup>16</sup>, and Zhao and Kassoy<sup>18</sup>) as well as the more familiar acoustic disturbances studied by many investigators in the past (Grad<sup>1</sup>, Culick<sup>3</sup>, Hart and McClure<sup>4</sup> and Williams<sup>9</sup>).

Brown et al.<sup>5,6</sup> and Brown and Shaeffer<sup>7</sup> conducted laboratory experiments in a cold flow rocket motor chamber analogue. Velocity measurements taken along

and across the cylindrical chamber show that there is a significant unsteady rotational flow component present everywhere. This type of vorticity is seen also in the study by Vuillot and Avalon<sup>8</sup> who used computational methods to solve the compressible Navier-Stokes equations in a channel with constant sidewall mass injection. The numerical results of Vuillot and Avalon<sup>8</sup> demonstrate that unsteady vorticity is not always confined to thin viscous acoustic boundary layers adjacent to the injecting wall, suggested in numerical studies of Baum and Levine<sup>12</sup> and Baum<sup>13</sup> and in the analytical study of Flandro<sup>10</sup>, Flandro and Roach<sup>14</sup> and in the related study, Smith et al.<sup>17</sup> attempted to simulate numerically the Brown et al.<sup>5,6</sup> experiments. They captured the essential features of the vortical structures observed by Brown et al.<sup>5,6</sup>, in spite of a numerical difficulty with the radial velocity distribution near the centerline of the chamber. Tseng and Yang<sup>15</sup> and Tseng et al.<sup>16</sup> included propellant combustion in the complete numerical solution of Navier-Stokes equations and studied the effect of combustion on the unsteady phenomena in an analogue of a rocket motor chamber. Flandro and Roach<sup>14</sup> developed an approximate model and analytical solution to describe vorticity generation at the injecting wall. The model is based on purely inviscid, linear equations. This work implies that there are two length scales for rotational effects, the tube radius and  $O(M)$  smaller length where significant local velocity variations occur. One may draw the conclusion from these experimental, numerical and analytical results that stability predictions based on the traditional acoustic analysis should be re-examined. Clearly, the presence of vortical structures in the internal flow field has significant consequences for the conceptual validity of traditional irrotational acoustic stability models where it is assumed that acoustic waves propagate through a quiescent chamber, and do not interact with sidewall gas injection.

Recently, Zhao and Kassoy<sup>18</sup> and Zhao et al.<sup>24</sup> provided an initial step in formulating a rational mathematical model for internal flow dynamics which incorporates both acoustic phenomena and vorticity distributions. Perturbation methods are used to derive systematic approximations to the complete compressible Navier-Stokes equations. An initial-boundary value

\* Research Associate, Program in Applied Math.

† Professor, member AIAA.

‡ Currently at NOAA, Boulder, CO.

Copyright ©1995 by the American Institute of Aeronautics and Astronautics, Inc. All rights reserved.



approach is used to formulate a generalized unsteady mathematical model capable of describing both non-resonant and resonant time history of solutions. The boundary disturbance is an  $O(M)$  axial, harmonic velocity variation on the closed end wall. The complete axial velocity is found from a superposition of three components of equal magnitude. First, the steady component arises from a solution to inviscid, rotational Euler equations known by Culick<sup>2</sup>. Secondly, there is a planar irrotational acoustic field, derived from a traditional linear wave equation which satisfies boundary conditions at the closed and open ends of the cylinder. Finally, when  $Re = O(\delta^2/M^2)$ , the rotational, weakly nonlinear viscous component varies on two disparate length scales, similar to those described in the study by Flandro and Roach<sup>14</sup>. Analysis shows that the vorticity, generated at the wall by an interaction between the injected fluid and the propagating planar acoustic disturbances, is convected out into the primarily inviscid core flow by the radial component of the injection induced flow field.

Fully computational methods are used by Kirkkopru et al.<sup>11</sup> to provide qualitative supporting evidence for the solutions described in Zhao et al.<sup>24</sup>. In this case the driving disturbance is a harmonic pressure transient applied on the downstream exit plane of the cylinder. Grid size and spatial distribution are chosen to accommodate the multiple lengthscale structure known from the study by Zhao et al.<sup>24</sup>. The unsteady rotational component of the axial velocity is extracted from the total value found from a MacCormack scheme. The solution properties and characteristics are identical to those found previously and support the basic concepts of vorticity generation and transport.

A closely related approach has been used in a new numerical effort to compute unsteady vorticity production and evolution in a finite cylinder with transient side wall injection that mimics unsteady burning of solid propellant surface in the rocket motor chamber. In this case the chamber flow disturbances are generated by a spatially distributed imposed harmonic transient component of the sidewall injection velocity. The disturbance quantity is super-imposed on a steady component of the same magnitude.

The flow field is described by axisymmetric, two-dimensional, laminar, compressible Navier-Stokes equations. The Navier-Stokes equations are solved by using the Two-Four method<sup>21</sup> which is a fourth-order variant of the fully-explicit MacCormack method. The unsteady rotational component of the axial velocity, extracted from numerical solutions, is used to describe the generation and evolution of the nonlinear unsteady vorticity field in the cylinder. The present computational results show that, as found before (Zhao et al.<sup>24</sup> and Kirkkopru et al.<sup>11</sup>), unsteady vorticity is generated at the injecting sidewall by an interaction between the injected fluid and an axial planar acoustic wave induced by the sidewall injection transients. In the present case,

the vorticity is convected away from the wall into the chamber by the more complicated spatially distributed unsteady injected flow field. In previous studies by Zhao et al.<sup>24</sup> and Kirkkopru et al.<sup>11</sup>, where the sidewall injection velocity is uniformly constant, the unsteady vorticity is convected away towards the centerline of the chamber by the constant radial velocity field. The core of the chamber is free of vorticity only during the early phases of the transient process, prior to the arrival of a well defined unsteady vorticity front. The radial location of the vorticity front varies with the axial location; unlike that in the previous studies for constant sidewall injection. This occurs because the transient injection distribution is axially dependent. The arrival times and the magnitude of vortical axial velocity found from the present computational solution agree quite well with predictions found from generally valid concepts developed in a parallel analytical study by Zhao et al.<sup>25</sup>. There is also an associated pressure field driven by the transient injection which has the characteristics of a traditional planar acoustic system.

The presence of rotational flow features imply that traditional acoustic balance theories, used widely to predict solid rocket motor chamber stability, must be reevaluated.

## 2. Computational Model

The flow field is described by the axisymmetric, two-dimensional, laminar, compressible Navier-Stokes equations, for a perfect gas, written in nondimensional conservative form:

$$\frac{\partial q}{\partial t} + \frac{\partial e}{\partial x} + \frac{\partial f}{\partial r} + \frac{h}{r} = 0 \quad (1)$$

where

$$\begin{aligned} q &= \begin{pmatrix} \rho \\ E_T \\ \rho u \\ \rho v \end{pmatrix} & e &= \begin{pmatrix} M\rho u \\ M[E_T + (\gamma - 1)p]u \\ M\rho u^2 + \frac{1}{\gamma M}p \\ M\rho uv \end{pmatrix} \\ f &= \begin{pmatrix} M\rho v \\ M[E_T + (\gamma - 1)p]v - \frac{\gamma M\delta^2}{Re}T_{,r} \\ M\rho uv - \frac{M\delta^2}{Re}u_{,r} \\ M\rho v^2 + \frac{\delta^2}{\gamma M}p \end{pmatrix} \\ h &= \begin{pmatrix} M\rho v \\ M[E_T + (\gamma - 1)p]v - \frac{\gamma M\delta^2}{Re}T_{,r} \\ M\rho uv - \frac{M\delta^2}{Re}u_{,r} \\ M\rho v^2 \end{pmatrix} \end{aligned} \quad (2)$$

and

$$E_T = \rho C_v T + \gamma(\gamma - 1)M^2 \frac{[u^2 + (v/\delta)^2]}{2} \quad (3)$$

is the total fluid energy.

The equation of state for a perfect gas is

$$p = \rho T. \quad (4)$$

Nondimensional variables, defined in terms of dimensional quantities denoted by a prime, are given by

$$\begin{aligned} x &= x'/L' & r &= r'/R' & u &= u'/U_R' \\ v &= v'/V_R' & \rho &= \rho'/\rho_0' & p &= p'/p_0' \\ T &= T'/T_0' & t &= t'/t_a' & C_v &= C_v'/C_{v0}' \end{aligned} \quad (5)$$

Characteristic length scales for the axial and radial directions are chosen to be the length of the tube  $L'$  and the radius of the tube  $R'$ , respectively. The known characteristic sidewall injection speed of the fluid  $V_R'$  is related to the characteristic mean axial speed  $U_R'$  through the global mass conservation relationship  $U_R' = \delta V_R'$  where  $\delta = L'/R'$  is the aspect ratio of the tube. Pressure is nondimensionalized with respect to the static pressure compatible with the injected fluid density and pressure,  $\rho_0'$  and  $T_0'$ , respectively. Time is nondimensionalized with respect to the tube axial acoustic time  $t_a' = L'/a_0'$  where  $a_0' = (\gamma p_0'/\rho_0')^{1/2}$  is the characteristic speed of sound. Here, the ratio of specific heats  $\gamma = 1.4$  is used in the present computations. The viscosity, specific heats and conductivity are treated as constants in this calculations because temperature variations are very small.

The following expressions

$$Re = \frac{\rho_0' U_R' L'}{\mu_0'} \quad Pr = \frac{\mu_0' C_{p0}'}{k_0'} \quad M = \frac{U_R'}{a_0'} \quad (6)$$

define the Reynolds number, the Prandtl number and the mean axial flow Mach number, respectively. In a typical solid rocket motor chamber  $Re \gg 1$ ,  $Pr = O(1)$  and  $M = O(10^{-2} - 10^{-1})$ .

The Navier-Stokes equations are simplified by ignoring the axial transport terms. Justification for the reduction is based on the asymptotic analysis in Zhao and Kassoy<sup>18</sup> and Zhao et al.<sup>24</sup> valid for  $M \ll 1$ ,  $\delta \gg 1$  and  $Re \gg 1$  provided that  $\delta^2/Re \ll 1$ . As a result the computation time is reduced significantly without sacrificing flow physics. Furthermore, the dissipative effects of the remaining transport terms are sufficient to avoid artificial damping terms needed in other similar computations<sup>14,17,20</sup>.

The Navier-Stokes equations are solved by using the Two-Four explicit, predictor-corrector scheme<sup>21</sup>. This method is highly phase-accurate and is therefore very suitable for wave propagation and wave interaction problems.

The size and the number of uniformly spaced grids are chosen to accommodate properly the local variations of flow variables in the axial and radial directions as suggested in the asymptotic analysis by Zhao et al.<sup>24</sup>.

### Steady and Unsteady Computations

A steady state flow solution is required as an initial condition for the transient flow computation. Boundary

conditions include an impermeable head end at  $x = 0$  ( $u = 0$ ), an assumed pressure node at the exit plane  $x = 1$  ( $p = 1$ ), a specified injection velocity ( $v = -1$ ), temperature ( $T = 1$ ), and no slip condition for the axial flow speed ( $u = 0$ ) on the sidewall at  $r = 1$  as well as symmetry conditions on the centerline,  $r = 0$ .

The analytically calculated velocity profiles for incompressible, rotational, inviscid flow in a long, narrow cylindrical tube (Culick<sup>2</sup>) are used as starting profiles for the steady, compressible, viscous flow computations. This approach reduces the computation time required to reach the final converged steady flow configuration relative to doing a complete transient solution by initiating wall injection at  $t = 0$ . In this calculation the solution converges to a steady state defined by the condition that the total injected mass is equal to the total exiting mass. Then the solution is run for an additional  $O(10^3)$  axial acoustic time to ensure that the steady state solution is stable. Results given in Fig. 1 show the steady normalized axial,  $u_s(x, r)/u_s(x, r = 0)$ , and radial velocity  $v_s(x, r)$  profiles at different axial locations,  $x = 0.025, 0.5$  and  $1.0$ , when  $M = 0.06$ ,  $\delta = 20$  and  $Re = 10^5$ , respectively. In these graphs, Culick<sup>2</sup> incompressible flow profiles which are invariant to axial location are nearly indistinguishable from the computed profiles. Small differences arise from the small but finite axial flow Mach number used in the computation. Low Mach number compressible flow theory implies  $O(M^2)$  differences between the Culick<sup>2</sup> solution for  $\delta \gg 1$  and the computational result.

A steady state flow solution for each Mach number and Reynolds number is obtained initially in order to prevent introducing unwanted noise into the unsteady computations.

Zhao et al.<sup>24</sup> have used formal asymptotic methods to show that the chamber flow is weakly viscous when the condition  $Re = O(\delta^2/M^2)$  is satisfied and when strong injection prevails. The latter condition implies that  $V_R' \gg U_R'/Re^{1/2}$ .<sup>19</sup> The primary viscous stresses are in the radial direction. Hence, it is useful to retain the radial transport terms in the Navier-Stokes equations. The steady flow solution is obtained faster and, at the same time, the largest important viscous effects in radial direction are responsible for physically meaningful damping, similar to the artificial damping terms that have been introduced in some earlier studies<sup>14,17,20</sup>.

Once a converged steady flow configuration for specified values of  $\delta$ ,  $M$  and  $Re$  is obtained, the flow is disturbed by adding an axially distributed unsteady sidewall injection component to the steady value. The total wall injection velocity is then given by

$$v(x, r = 1, t) = -[1 + A \cos(n\pi x/2)(1 - \cos \omega t)] \quad (7)$$

which can also be written in terms of a positive mean component  $1 + A \cos(n\pi x/2)$  and a fluctuating component proportional to  $\cos \omega t$ . Here  $\omega$  is the dimensionless angular frequency,  $A = O(1)$  is the amplitude of the unsteady wall injection and  $n$  is the spatial dependence

parameter. The total mass flow from the wall is always positive. The other boundary conditions are the same as those for the steady flow computations.

Unsteady computations are carried for several different axial Mach numbers and spatial dependence parameters. In this study the boundary driving frequency is  $\omega = 1$ . This is a relatively low frequency in the sense that the period  $t = 2\pi$  is larger than the time required for an acoustic wave to do a complete circuit of the chamber,  $t = 2$ .

### 3. Results and Discussion

The numerical code has been run approximately ten cycles after the injection transient is turned on in order to check if spurious numerical oscillations develop. For example, Fig. 2 shows the time variation of the centerline axial velocity at the midchamber ( $x = 0.5$ ) for flow parameters  $M = 0.1$ ,  $\delta = 20$ ,  $Re = 10^5$ ,  $A = 0.4$ ,  $n = 1$  and  $\omega = 1$ . It is noted that the value at  $t = 0$  corresponds to the steady state value of the centerline velocity at the midchamber. The solution appears to be quasi-steady almost immediately. This solution property can be attributed to the transient pressure field seen in Fig. 3. The result given at  $x = 0.5$  shows that pressure solution is almost purely planar ( $x$ -dependent only). For example, at  $x = 0.5$  and  $t = 60$ , for three radial locations,  $r = 0, 0.5$  and  $1$ , are  $p = 1.1480096, 1.1479678$  and  $1.1479073$ , respectively. The invariance to radial location results from the use of a large aspect ratio,  $\delta = 20$ . It should also be noted that the pressure deviation from the base value,  $O(0.1)$ , is fully compatible with the asymptotic prediction in Zhao et al.<sup>25</sup>.

The purely harmonic behavior in Fig. 3, seen in all similar computational results<sup>8,15,16</sup> is cause for concern because the analytical analogue to this study (Zhao et al.<sup>25</sup>) shows that a single eigenfunction of substantial amplitude should accompany the forced response. The eigenfunction arises from a solution to a linear acoustic equation driven by transient effects on the boundary. This is in contrast to the numerical solution which arises from a slightly viscous, weakly nonlinear mathematical system. It appears that there are at least two possible sources for the difference:

- (a) The nonlinear slightly viscous equations will not produce an eigenvalue-like response, or
- (b) The numerical boundary conditions at the exit plane do not represent wave reflections in an appropriate way.

These issues are the subject of the ongoing studies. It should be noted that acoustic wave viscous damping occurs on a time scale  $t \gg O(10^2)$ <sup>23</sup> for the Reynolds numbers considered here. Hence on the time scale  $t = O(10^2)$  damping cannot annihilate an eigenfunction response.

Following a procedure described by Lagerstrom<sup>22</sup>,

and similar to that employed by Flandro and Roach<sup>14</sup>, Zhao and Kassoy<sup>18</sup> and Zhao et al.<sup>24</sup>, the total unsteady axial flow speed may be divided into three parts

$$u(x, r, t) = u_S(x, r) + u_P(x, t) + u_V(x, r, t) \quad (8)$$

where  $u_S$  denotes the steady flow field which is known as an initial condition for unsteady computations. The second term  $u_P$  is the weakly viscous, slightly nonlinear analogue to the irrotational planar part of the flow field found by Zhao et al.<sup>24,25</sup>. It is found from the difference between the unsteady axial speed and the steady axial speed on the centerline of the tube. The remaining term  $u_V$ , defined as the vortical (rotational, nonplanar) part of the unsteady axial flow speed, is found from Eqn.(8) once  $u_S$  and  $u_P$  are calculated. Once again it is an analogue to analytically obtained rotational velocity field described by Zhao et al.<sup>24,25</sup>. It is used to describe the generation and evolution of the nonlinear unsteady vorticity field in the cylinder. Following the asymptotic analysis described by Zhao et al.<sup>24,25</sup>, one can show that the vortical part of the unsteady axial flow speed  $u_V$  vanishes at the centerline at all times.

Figure 4 shows the radial variation of the instantaneous unsteady axial vortical flow speed at midchamber ( $x = 0.5$ ) at three time values after the injection transient is initiated at the sidewall. The flow parameters are  $M = 0.1$ ,  $\delta = 20$  and  $Re = 10^5$ . The corresponding injection Mach number  $M_i = M/\delta = 0.005$ . The disturbance frequency is  $\omega = 1.0$ , a non-resonant frequency smaller than the first fundamental frequency of the tube,  $\omega_1 = \pi/2$ .

One observes a strong radial velocity gradient extending out about 0.35 units from the wall at  $t = 3.00$  (solid line). The unsteady vortical axial velocity field extends out to 0.65 radial units from the injecting wall when  $t = 6.00$ . At time  $t = 9.90$  the rotational flow field has spread throughout the chamber.

The spatial distribution of the vortical part of the unsteady axial flow velocity at each time may be explained in physical terms by considering an interaction between the total unsteady injected flow field and the axial planar acoustic wave induced and sustained by sidewall injection transients. The motion of a fluid particle injected radially into the tube from the sidewall at a specified axial location is affected by the harmonic variation with time of the local axial planar pressure gradient. For instance, Fig. 5 shows the time variation of the axial pressure gradient,  $\partial p/\partial x$ , at a point where  $x = 0.5$  and  $r = 0.95$  for the case being discussed above. As a result, a given fluid particle emanating from the wall will be accelerated alternately in the positive and negative axial directions as it is convected toward the axis of the cylinder by the unsteady radial flow field. Part of the fluid particle response is associated with irrotational acoustic effects. The rest is rotational, resulting from vorticity generation at the wall.

Figure 4 shows that by  $t = 10$ , unsteady vorticity fills the cylinder. But Fig. 3 shows no change in the

r-independent pressure field as vorticity fills the system. It follows that vorticity dynamics do not affect the pressure field, as predicted by the asymptotic analysis of Zhao et al.<sup>24,25</sup>. This provides an explanation why traditional acoustic theory yields transient pressure estimates that compare well with those found experimentally. Of course, the acoustic field will differ considerably from the acoustic theory as found by Brown et al.<sup>5,6</sup>.

Figure 6 shows the instantaneous spatial oscillation of vortical axial velocity at  $x = 0.5$  with respect to the radius when  $t = 2.96, 5.92$  and  $10.05$  for a smaller axial Mach number  $M = 0.06$  (corresponding to the weaker injection,  $M_{inj} = 0.003$ ) and for the same  $Re = 10^5$ . The forcing frequency  $\omega = 1.0$  is the same as for the previous case. The amplitude of the nonresonant injection transient disturbance is  $A = 0.4$ . The sharply defined region of large velocity gradient is seen in Fig. 6 at  $0.23$  units from the wall at  $t = 2.96$ . One notes that at  $t = 5.92$  the wavelength of the spatial oscillation of the vortical axial velocity field is smaller than that for the case when  $M = 0.1$ . This is an expected result because the total unsteady radial velocity field for  $M = 0.06$ , which transports the fluid particles into the cylinder, is characterized by a relatively lower speed than that for the  $M = 0.1$  case. Therefore, injected fluid particles are carried a shorter distance away from the sidewall towards the axis of the chamber in the same time interval, compared to that for the stronger injection speed case,  $M = 0.1$ . At  $t = 10.05$  one notes spatial oscillations fills the 70 percent of the cylinder.

Solution resolution requires 41 grid points in the axial direction and 101 grid points in the radial direction in the two cases discussed above. Figure 6 shows that near the injecting wall one wavelength of the spatial oscillation of the vortical axial velocity is represented by approximately 35-40 radial grid points. In contrast, near the centerline, where the wavelength is smaller, fewer but enough grid points per wavelength are available to resolve the velocity gradients.

The third case studied is for a smaller mean axial flow Mach number  $M = 0.02$  ( $M_{inj} = 0.001$ ),  $\delta = 20$ , slightly larger Reynolds number  $Re = 3.10^5$  and the forcing frequency  $\omega = 1.0$ . The results for the previous cases,  $M = 0.1$  and  $M = 0.06$ , imply that the number of radial grid points should be doubled for this weak injection case. There are 201 equally spaced grid points in the radial direction in order to represent the spatial variation of unsteady vortical axial velocity accurately. Figure 7 shows the instantaneous unsteady vortical axial velocity variation with respect to the radius at  $x = 0.5$  when  $t = 2.99, 4.93$  and  $10.00$ . It can be seen from this figure that axial velocity gradients are larger than those for larger Mach number cases presented previously. This implies that the absolute magnitude of the unsteady vorticity generated at the wall is much larger than that of the higher Mach number flows. This unsteady vorticity field is convected away

from the wall towards the center of the chamber by a relatively slower radial velocity component. Therefore, at  $t = 10.00$  only about 30 percent of the chamber is filled with the unsteady vorticity.

Figure 8 shows the instantaneous radial variation of vortical axial velocity at  $x = 0.5$  for larger times  $t = 10.00, 20.01, 30.02$  and  $40.02$ . The unsteady vorticity field spreads out towards the axis as time increases.

One should note here again that the wavelength of the oscillatory structure decreases as the centerline is approached. This occurs because of the slow-down in the convection process due to the decrease in the radial velocity component as the axis of the chamber is approached. The implication for mesh distributions is that there must be adequate spatial resolution throughout the cylinder, not just in an "acoustic boundary layer" near the injecting surface as used in a variety of earlier computations<sup>8,15,16</sup>. Of course this occurs because the injection velocity is large so that no thin localized viscous layer can exist.

Figures 9-11 show the instantaneous unsteady vorticity distribution throughout the chamber for three cases,  $M = 0.1, 0.06$  and  $0.02$ , discussed above, respectively. Corresponding times are  $t = 30.00, 29.56$  and  $30.02$ , respectively. The unsteady vorticity is computed from the following expression

$$\Omega = - \left[ \frac{\partial u_v}{\partial r} - \frac{1}{\delta^2} \frac{\partial (v - v_s)}{\partial x} \right] \quad (9)$$

The nondimensional vorticity is defined as  $\Omega = \Omega' / (U_R' / R')$  where  $\Omega'$  is the dimensional vorticity. As analysis of the present numerical results and the asymptotic analysis of Zhao et al.<sup>24</sup> show, the main contribution to the unsteady vorticity is brought by the first term in (9). It is seen from Figs. 9-11 that the magnitude of the instantaneous unsteady vorticity increases with decreasing mean flow Mach number. One should notice that the scales for  $\Omega$  are different in each of Figs. 9-11. Computation for the  $M = 0.02$  case is carried until and after the unsteady vorticity front reaches the centerline of the chamber.

Figure 12 shows the variation of the instantaneous unsteady vorticity variation with radial location at  $x = 0.5$  when  $t = 52.42$ . The presence of significant vorticity and hence shear stress near the sidewall is to be noted. The complete spatial distribution of the unsteady vorticity in the neighborhood of the centerline is shown in Fig. 13 where  $0 \leq r \leq 0.25, 0 \leq x \leq 1$  when  $t = 52.42$ . Here, it is shown that the unsteady vorticity fills the entire chamber and vorticity front has axial dependence.

Figure 14 provides the variation of the unsteady part of the radial speed,  $v - v_s$ , with radial location at  $t = 30.02$  and  $x = 0.5$  for  $M = 0.02, \delta = 20, Re = 3.10^5, n = 1, A = 0.4$  and  $\omega = 1$ . Here,  $v_s$  is the steady radial velocity associated with constant wall injection. This corresponds to the axial velocity result in Fig. 8. Our result is well converged throughout the cylinder, unlike

that found by Flandro and Roach<sup>14</sup> and Smith et al.<sup>17</sup> where unusual solution behavior occurred along the axis.

When the sidewall injection transient is spatially dependent the radial location of the vorticity front seen for example in Figs. 7 and 8 varies with the axial location, unlike that in the previous studies for constant sidewall injection<sup>18-24</sup>. Figures 15-18 show the total spatial variation of the instantaneous unsteady vorticity distribution throughout the cylinder at times  $t = 7.48, 14.96, 22.44$  and  $29.92$ , respectively, when the spatial dependence parameter  $n = 3$  in (7). In this case,  $M = 0.02$ ,  $\delta = 20$ ,  $Re = 3.10^5$ ,  $\omega = 1$  and  $A = 0.5$ . The observed spatially dependent front configurations imply that there will be much more complicated front morphologies if the sidewall injection transients have sufficient spatial complexity. As a result, one may find intermittent regions of strongly rotational unsteady flow on an axial traverse at a fixed radial distance from the wall, reminiscent of turbulent structures.

The amplitude of the unsteady vorticity distributions is  $O(M^{-1})$  larger than that of the Culick<sup>2</sup> steady solution as predicted by Zhao et al.<sup>24,25</sup>. This implies that there will exist a relatively large transient axial shear stresses on the sidewall surface, particularly for smaller  $M$  values. One can speculate that these large transient shear stresses will impact the burning rate of a solid propellant which is the source of the "injected" fluid used in the present model. Perhaps there is a direct relationship between the effect of the surface shear stress transients, predicted in the present work, and erosive burning concepts used in the solid rocket engineering literature<sup>2</sup>.

#### 4. Summary and Conclusions

Unsteady vorticity generation and evolution due to simulated propellant burning transients in an idealized rocket motor chamber are studied in the context of an initial boundary value problem. The nearly complete compressible Navier-Stokes equations are solved numerically. An axially distributed harmonically varying sidewall injection component is superimposed on a similar magnitude steady sidewall injection in order to simulate mass addition from irregular and nonuniform solid propellant burning.

In this study, instantaneous values of flow variables are used rather than time averaged values as presented in studies by Tseng and Yang<sup>15</sup>, Flandro and Roach<sup>14</sup>, Smith et al.<sup>17</sup> and Tseng et al.<sup>16</sup>. Hence, the time evolution of unsteady vorticity creation and propagation can be investigated in contrast to the aforementioned studies where instantaneous information is lost due to the time averaging process.

The computational analysis shows that axial planar acoustic waves induced and sustained by the sidewall injection transients interact with the sidewall injection

induced flow in the chamber to generate unsteady vorticity on the sidewall. This time-dependent vorticity is subsequently convected into the entire chamber by the unsteady radial flow field. The core of the chamber is free of vorticity only during the early phases of the transient process, prior to the arrival of a well defined vorticity front (see, for example, Figs. 7, 15-18).

The unsteady vorticity wave front radial location varies in the axial direction in contrast to that in the previous studies with constant sidewall injection flow field subject to either endwall or exit flow disturbances (Figs. 15-18). This occurs because the injection transient is axially dependent in this work, a reasonable modelling effort that reflects the transient and nonuniform propellant burning in solid rocket motors. Moreover, the enhanced sidewall injection due to the superimposed component causes the unsteady vorticity to spread more rapidly into the chamber than that for the constant sidewall injection cases studied before. The absolute magnitude of the unsteady vorticity is  $O(1/M)$ . This implies that large transient shear stresses impact on the solid propellant surface, probably influencing the burning rate directly.

These results and the asymptotic analysis by Zhao et al.<sup>24</sup> suggest that the flow pattern is fundamentally viscous when the condition  $Re = O(\delta^2/M^2)$  is satisfied. This condition is also satisfied by the numerical solutions of Smith et al.<sup>17</sup> and Tseng et al.<sup>16</sup>. In contrast, Flandro and Roach<sup>14</sup> describes a quasi-steady analytical result, derived from a fully inviscid model, which cannot be applied directly to the weakly viscous problems.

It is noted that the pressure field is independent of the unsteady vorticity distribution in the chamber. Therefore, one may imagine that the acoustic pressure predictions obtained from traditional acoustic stability theories, used widely for scientific and engineering purposes, yield reasonable estimates. However, it is unlikely that velocity and shear stress predictions are accurate, given the irrotational basis of acoustic theories.

There is now a considerable body of evidence (Brown et al.<sup>5,6</sup>, Vuillot and Avalon<sup>8</sup>, Kirkkopru et al.<sup>11</sup>, Flandro and Roach<sup>14</sup>, Tseng and Yang<sup>15</sup>, and Zhao et al.<sup>24,25</sup>) in support of the presence of an unsteady vorticity distribution within a physically reasonable model of a solid rocket motor chamber. The presence of unsteady vorticity throughout the domain suggests that traditional irrotational acoustic theories, used largely to predict solid rocket motor flow stability, should be reexamined.

#### Acknowledgement

This work is supported by the Air Force Office of Scientific Research through a grant AFOSR 89-0023.

## References

1. Grad, H., "Resonance Burning in Rocket Motors," *Comm. Pure Appl. Math.*, **2**, 79-102, 1949.
2. Culick, F.E.C., "The Blowhard problem - Inviscid Flows with Surface Injection," *AIAA J.*, **4**, 1462-1463, 1966.
3. Culick, F.E.C., "Some Recent Results for Nonlinear Acoustics in Combustion Chambers," AIAA 90-3927, Aeroacoustics Conference, October, 1990.
4. Hart, R.W. and McClure, F.T., "Theory of Acoustic Instability in Solid Propellant Rocket Combustion," *10th International Symposium on Combustion*, Combustion Ins., Pittsburg, PA, 1047-1065, 1965.
5. Brown, R.S., Blackner, A.M., Willoughby, P.G. and Dunlap, R., "Coupling Between Acoustic Velocity Oscillations and Solid Propellant Combustion," *J. Propulsion and Power*, **2**, 428-437, 1986.
6. Brown, R.S., Blackner, A.M., Willoughby, P.G. and Dunlap, R., "Coupling Between Velocity Oscillations and Solid Propellant Combustion," AIAA 86-0531, AIAA Aerospace Sciences Meeting, January, 1986.
7. Brown, R.S. and Shaeffer, C.W., "Oscillatory Internal Flow Field Studies," AFOSR Contractors Meeting in Propulsion, La Jolla, California, June, 1992.
8. Vuillot, F. and Avalon, G., "Acoustic Boundary Layers in Solid Propellant Rocket Motors Using Navier-Stokes Equations," *J. Propulsion*, **7**, No 2, 231-239, 1991.
9. Williams, F.A., *Combustion Theory*, Benjamin/Cummings, Menlo Park, 1985.
10. Flandro, G.A., "Solid Propellant Admittance Correction," *J. Sound and Vibration*, **36**, 297-312, 1974.
11. Kirkkopru, K., Kassoy, D.R. and Zhao, Q., "Unsteady Vorticity Generation and evolution in a Model of a Solid Rocket Engine Chamber," submitted to AIAA J., 1994.
12. Baum, J.D. and Levine, J.N., "Numerical Investigation of Acoustic Refraction," *AIAA J.*, **25**, 1577-1586, 1987.
13. Baum, J.D., "Energy Exchange Mechanisms Between the Mean and Acoustic Fields in a Simulated Rocket Combustor," AFOSR Contractors Meeting, Atlanta, GA, June, 1990.
14. Flandro, G.A. and Roach, R.L., "Effects of Vorticity Production on Acoustic Waves in a Combustion Chamber," Final Technical Report, AFOSR-90-0159, 1992.
15. Tseng, I.S. and Yang, V., "Interactions of Homogeneous Propellant Combustion and Acoustic Waves in a Solid Rocket Motor, AIAA 92-0101, AIAA Aerospace Sciences Meeting, Reno, Nevada, January, 1992.
16. Tseng, C., Tseng, I.S., Chu, W. and Yang, V., "Interactions Between Acoustic Waves and Premixed Flames in Porous Chambers," AIAA 94-3328, Joint Propulsion Conference, Indianapolis, Indiana, June, 1994.
17. Smith, T.M., Roach, R.L. and Flandro, G.A., "Numerical Study of the Unsteady Flow in a Simulated Solid Rocket Motor," AIAA 93-0112, Aerospace Sciences Meeting, Reno, Nevada, January 11-14, 1993.
18. Zhao, Q. and Kassoy, D.R., "The Generation and Evolution of Unsteady Vorticity in a Solid Rocket Engine Chamber," AIAA 94-0779, Aerospace Sciences Meeting, Reno, Nevada, January, 1994.
19. Cole, J.D. and Aroesty, J., "The Blowhard Problem-Inviscid Flows with Surface Injection," *Int. J. Heat Mass Transfer*, **11**, 7, 1167-1183, 1968.
20. Lupaglazoff, N. and Vuillot F., "Two-Dimensional Numerical Simulation of the Stability of a Solid Propellant Rocket Motor," AIAA 91-0205, Aerospace Sciences Meeting, Reno, Nevada, January, 1991.
21. Gottlieb, D. and Turkel, E., "Dissipative Two-Four Methods for Time-Dependent Problems," *J. of Mathematics of Computation*, **30**, 136, 703-723, 1976.
22. Lagerstrom, P.A., in *Theory of Laminar Flows*, Section B, Moore, F.K., ed., Princeton University Press, 1964.
23. Landau, L.D. and Lifshitz, E.M., *Fluid Mechanics*, Pergamon Press, New York, 1959.
24. Zhao, Q., Kassoy, D.R. and Kirkkopru, K., "Nonlinear Unsteady Vorticity Generation in a Model of a Solid Rocket Engine Chamber," submitted to *J. Fluid Mech.*, 1994.
25. Zhao, Q., Kassoy, D.R. and Kirkkopru, K., "Nonlinear Vorticity Generation by Acoustic Wave Interaction with an Injected Gas," in preparation, 1994.

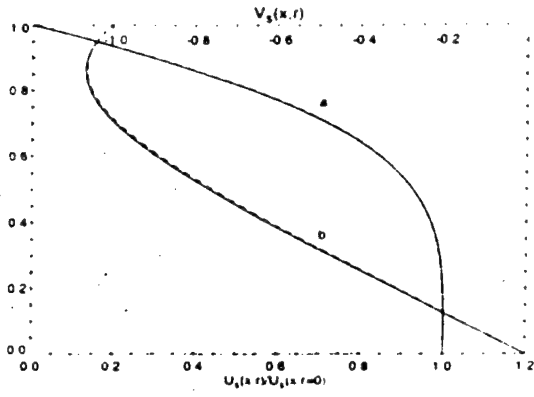


Figure 1: Normalized steady axial velocity (a) and steady radial velocity (b) profiles at  $x = 0.025$  (solid line), 0.5 (dotted line) and 1 (dashed line) for  $M = 0.06$ ,  $Re = 10^5$  and  $\delta = 20$ .

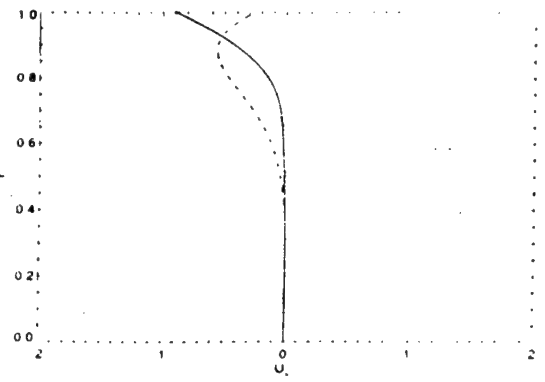


Figure 4: The radial variation of  $u_r$  at  $x = 0.5$  when  $t = 3$  (solid line),  $t = 6$  (dashed line) and  $t = 9.9$  (dotted line) for  $M = 0.1$ ,  $\delta = 20$ ,  $Re = 10^5$ ,  $\omega = 1$ ,  $A = 0.4$ , and  $n = 1$ .

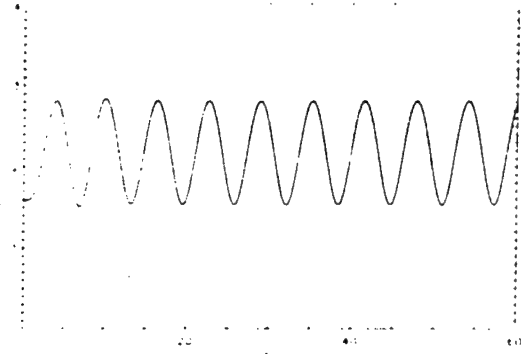


Figure 2: The time history of the centerline axial velocity at  $x = 0.5$  for  $M = 0.1$ ,  $\delta = 20$ ,  $Re = 10^5$ ,  $\omega = 1$ ,  $A = 0.4$ , and  $n = 1$ .

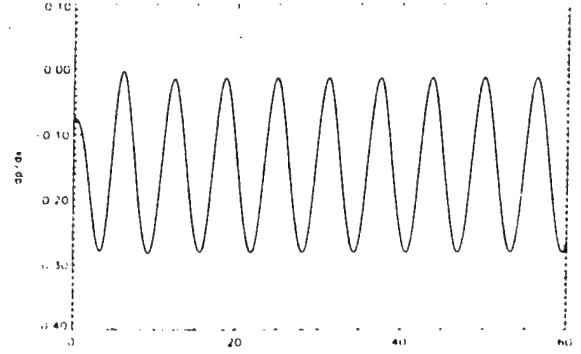


Figure 5: The time history of axial pressure gradient,  $\partial p / \partial x$ , at  $x = 0.5$ ,  $r = 0.95$  for  $M = 0.1$ ,  $\delta = 20$ ,  $Re = 10^5$ ,  $\omega = 1$ ,  $A = 0.4$ , and  $n = 1$ .

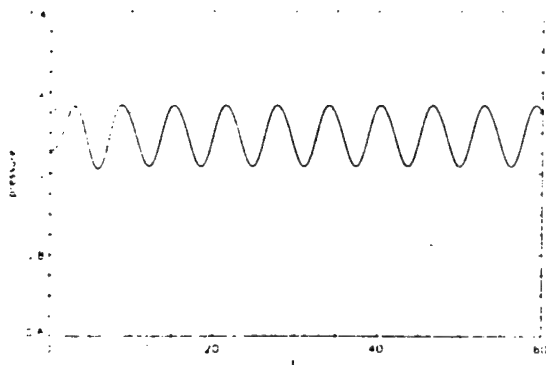


Figure 3: The time history of pressure at  $x = 0.5$  for  $M = 0.1$ ,  $\delta = 20$ ,  $Re = 10^5$ ,  $\omega = 1$ ,  $A = 0.4$ , and  $n = 1$ .

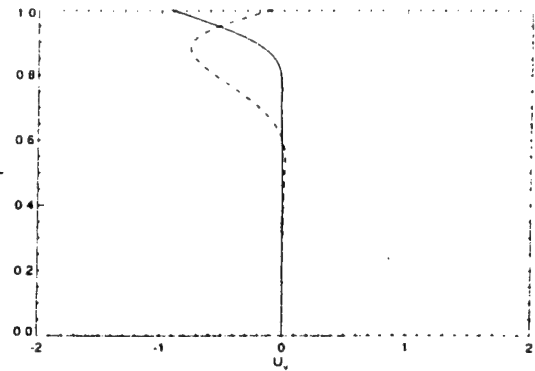


Figure 6: The radial variation of  $u_r$  at  $x = 0.5$  when  $t = 2.96$  (solid line),  $t = 5.92$  (dashed line) and  $t = 10.05$  (dotted line) for  $M = 0.06$ ,  $\delta = 20$ ,  $Re = 10^5$ ,  $\omega = 1$ ,  $A = 0.4$ , and  $n = 1$ .



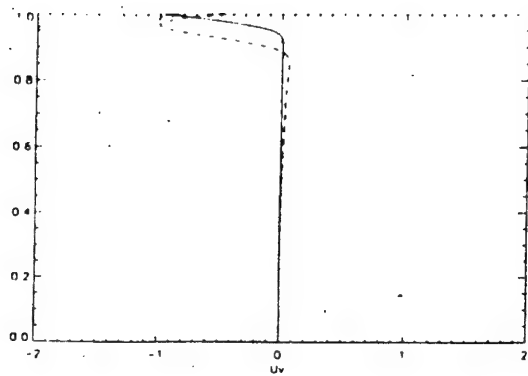


Figure 7: The radial variation of  $u_v$  at  $x = 0.5$  when  $t = 2.99$  (solid line),  $t = 4.93$  (dashed line) and  $t = 10.00$  (dotted line) for  $M = 0.02$ ,  $\delta = 20$ ,  $Re = 3.10^5$ ,  $\omega = 1$ ,  $A = 0.4$ , and  $n = 1$ .

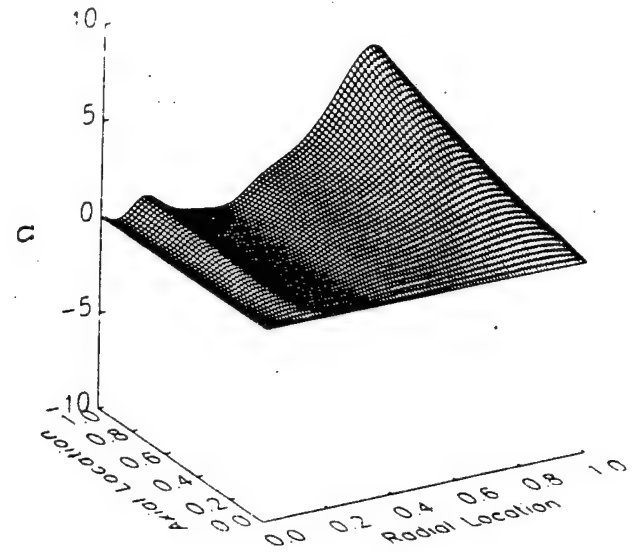


Figure 9: Spatial variation of the unsteady distribution,  $\Omega$ , as a function of axial location and radial location at  $t = 30$  for  $M = 0.1$  and  $\delta = 20$ .

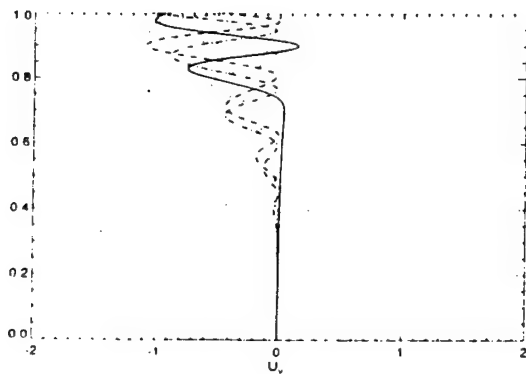


Figure 8: As Fig.7 but for  $t = 10.00$  (solid line),  $t = 20.01$  (dashed line),  $t = 30.02$  (dotted line) and  $t = 40.02$  (dash-dot line).

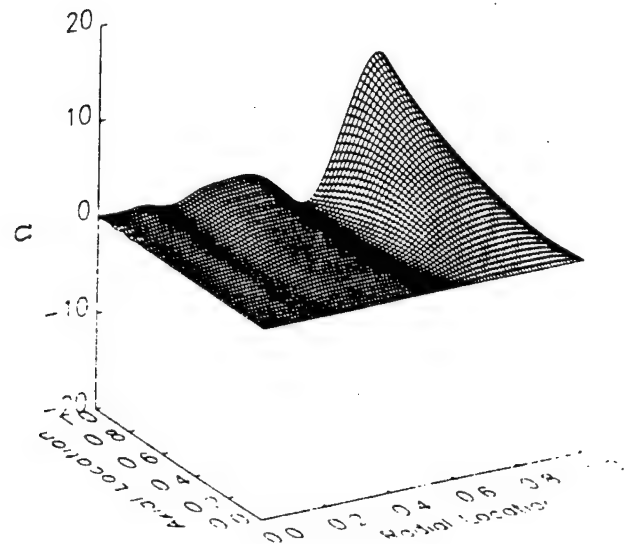


Figure 10: As Fig.9 but at  $t = 29.56$  and for  $M = 0.06$ . Note the different scale in  $\Omega$ .



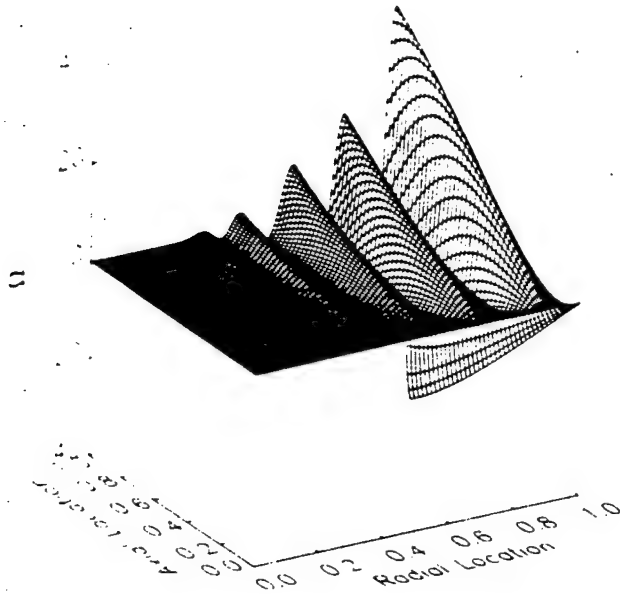


Figure 11: As Fig.9 but at  $t = 30.02$  and for  $M = 0.02$ . Note the different scale in  $\Omega$ .

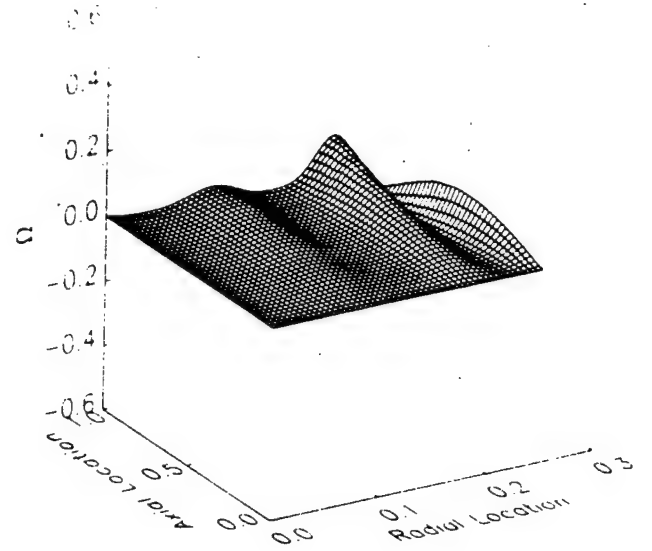


Figure 13: Unsteady vorticity variation in the region where  $0 \leq x \leq 1$ ,  $0 \leq r \leq 0.25$  for the same parameters and time in Fig.12.

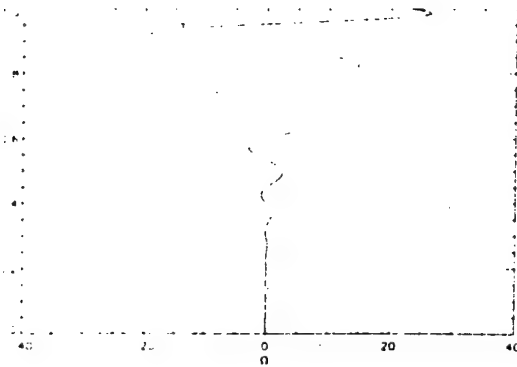


Figure 12: Radial variation of  $\Omega$  at  $x = 0.5$  when  $t = 52.42$  for  $M = 0.02$ ,  $Re = 3.10^5$ ,  $\omega = 1$ ,  $A = 0.4$  and  $n = 1$ .

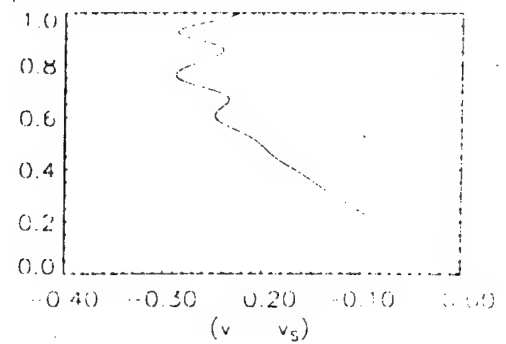


Figure 14: The instant radial variation of  $(v - v_s)$  at  $x = 0.5$  when  $t = 30.02$  for the same flow parameters as those in Fig.8.

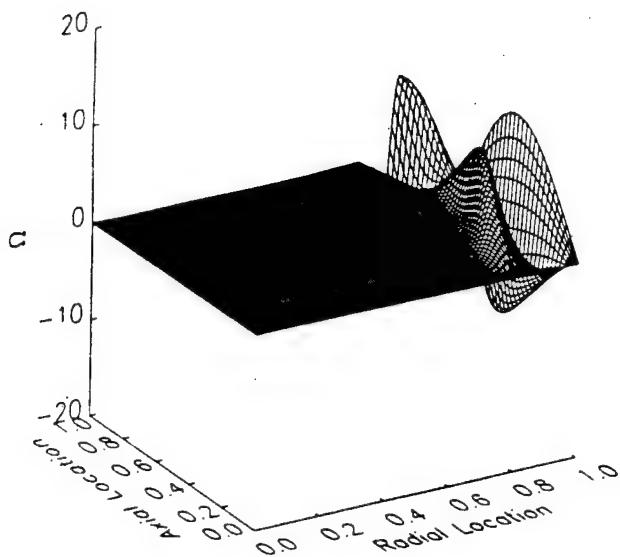


Figure 15: Instantaneous unsteady vorticity variation throughout the cylindrical chamber at  $t = 7.48$  for  $M = 0.02$ ,  $\delta = 20$ ,  $Re = 3.10^5$ ,  $\omega = 1.$ ,  $A = 0.5$  and  $n = 3$ . The net mean injection speed from (8) is always positive.

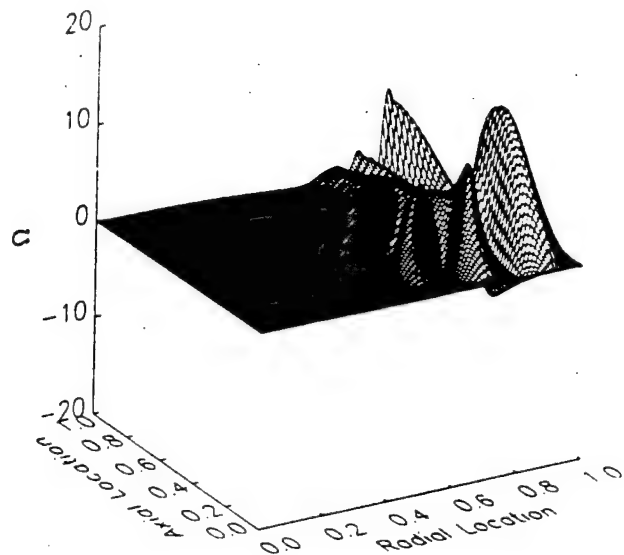


Figure 17: As Fig.15 but at  $t = 22.44$ .

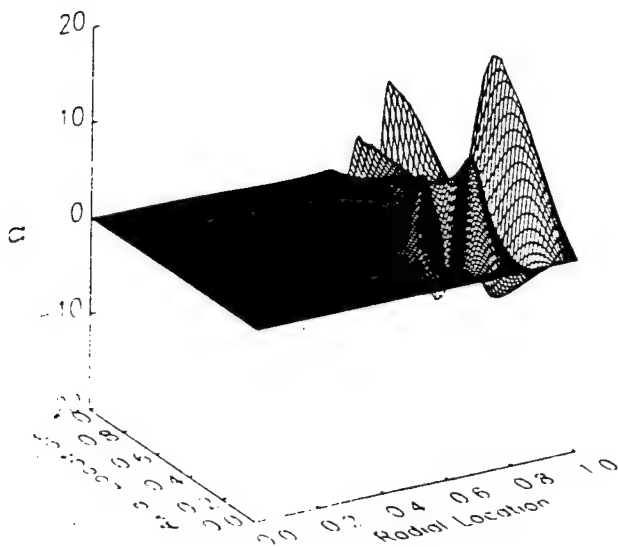


Figure 16: As Fig.15 but at  $t = 14.96$ .

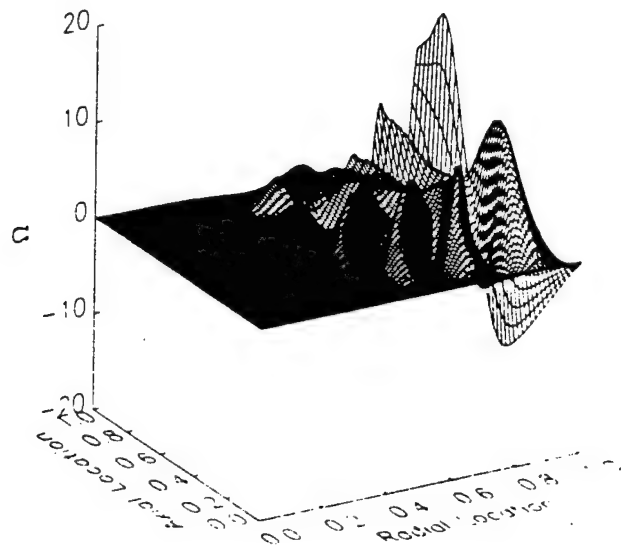


Figure 18: As Fig.15 but at  $t = 29.92$ .

## NONLINEAR OSCILLATIONS IN A RESONANT GAS COLUMN: AN INITIAL-BOUNDARY-VALUE STUDY\*

MENG WANG<sup>†</sup> AND DAVID R. KASSOY<sup>‡</sup>

**Abstract.** Acoustic resonance in a gas column driven by a vibrating piston is studied in terms of an initial-boundary-value formulation. If the boundary opposite to the piston face permits acoustic energy leakage, the linear solution prevails and describes the evolution to periodic, quasi-steady oscillations at the piston frequency. Resonant amplification of the wavefield may occur only if the opposite boundary is either closed (a rigid wall) or ideally open (an isobaric exit). A multiple-timescale perturbation analysis, based on Fourier eigenfunction representations, is used to find weakly nonlinear solutions that provide unique physical insights in terms of acoustic modal interactions and transient waveform evolution to limit cycles. It is shown that quadratic modal interactions in a closed system lead to persistent shock appearance and relatively small limiting amplitudes, whereas cubic mode-coupling dominates in an open system and stronger shocks are created intermittently. Finite-difference solutions support these conclusions. The initial-value approach employed enables the prediction of shock waves in parameter regimes where no shock has been found by earlier investigators using a quasi-steady formulation.

**Key words.** nonlinear acoustics, weak shock, perturbation methods, multiple scales, open- and closed-system resonance

**AMS subject classifications.** 76N15, 76Q05, 35C20, 35L, 34E

**1. Introduction.** This paper presents a theoretical investigation of the evolution of planar acoustic disturbances driven by a vibrating piston at one boundary of a perfect gas. Detailed results from a weakly nonlinear analysis for linear resonant driving frequencies are obtained when the opposite boundary is either closed or isobaric. A comparative analysis is used to demonstrate that the mathematical essentials, the character of the nonlinear phenomena, as well as the gasdynamic properties, differ fundamentally in the two cases.

Forced acoustic oscillations play a significant role in a variety of practical systems, ranging from rocket engine combustors (Williams, 1985) to pulse combustors (Margolis, 1993), for example. In these semiconfined configurations the flow is multidimensional and coupled with specific driving mechanisms. Acoustic stability analyses for rocket engines are often based on eigenfunctions for a closed chamber with rigid walls (Culick, 1976a, 1976b; Lores and Zinn, 1973), implying that velocity disturbances normal to the surfaces of the control volume vanish. In reality, such disturbances are present in chamber outflow and transverse gas injection from the burning propellant. The consequences of the approximation are difficult to evaluate. In particular, one is concerned about the accuracy of a nonlinear formulation based on eigenfunctions that do not satisfy realistic boundary conditions, both in terms of long-time amplitude predictions and the details of the flow dynamics, particularly the appearance of shock waves.

\* Received by the editors January 13, 1993; accepted for publication (in revised form) May 10, 1994. This research was supported by Air Force Office of Scientific Research grant AFOSR-89-0023.

<sup>†</sup>Center for Combustion Research, Department of Mechanical Engineering, University of Colorado, Boulder, Colorado 80309-0427. Present address: Center for Turbulence Research, NASA Ames Research Center/Stanford University, MS 202A-1, Moffett Field, California 94035.

<sup>‡</sup>Center for Combustion Research, Department of Mechanical Engineering, University of Colorado, Boulder, Colorado 80309-0427.

In comparison, a recent study of a combustion-driven acoustic resonator (model pulse combustor) by Margolis (1993) employs eigenfunctions that are compatible with a semiconfined chamber, open at one end to a constant pressure field. A formal perturbation procedure is carried out to demonstrate that the nonlinear wavefield characteristics are fundamentally different from those obtained in an analysis based on closed-system eigenfunctions. The resulting evolution equations for wave amplitudes are shown to involve cubic mode-coupling, instead of the usual quadratic coupling.

The present study is motivated by the need for an explanation of the explicit effect of boundary conditions on wavefield evolution in acoustic chambers. The resonance tube offers an ideal model problem because of its simple geometry and simple source mechanism (piston motion). Furthermore, aside from its relevance to engineering applications, the investigation of oscillations in acoustic resonators possesses its own scientific significance. It has been an active area of research in nonlinear acoustics for over three decades.

Experimental evidence (Lettau, 1939; Saenger and Hudson, 1960) shows that in a closed tube, a piston vibrating in a narrow frequency band around each resonance frequency can amplify the gas oscillations to the extent that shock waves develop. The latter travel back and forth between the piston surface and the rigid tube end. In order to explain this fascinating observation, Betchov (1958) and Saenger and Hudson (1960) constructed theoretical models based on the existence of a propagating shock discontinuity. The solutions, obtained using the method of characteristics, describe periodic limit cycle behavior. Chester's (1964) theory provides more generality in the sense that shock waves appear as a natural outcome of the solution when the piston frequency approaches one of the resonant frequencies. Outside these narrow resonant frequency bands, the solution is continuous but not purely harmonic. This work was further extended by Keller (1976) to include the effect of boundary layer friction of arbitrary strength. Other related studies concerning closed resonance tubes can be found in, for example, Eninger and Vincenti (1973), Merkli and Thomann (1975), Zaripov and Ilhamov (1976), and Ochmann (1985).

Jimenez (1973) and Seymour and Mortell (1973a, 1973b) conducted studies of acoustic resonance in both closed and open tubes to determine the periodic motions of the gas. A reflexion coefficient (or admittance) is used to characterize the acoustic response of the tube-end, ranging from a velocity node (closed) to a pressure node (ideally open). Limit cycle amplitudes and waveforms are predicted as a function of the reflexion coefficient and the forcing frequency. In both open- and closed-end resonance cases, shock waves are found to exist in certain parameter ranges. However, the limiting amplitudes for the two cases are dramatically different, of  $O(\epsilon^{1/3})$  and  $O(\epsilon^{1/2})$ , respectively, where  $\epsilon$  denotes the maximum piston Mach number.

It is noted that nearly all the earlier investigators consider only quasi-steady oscillations, with the notable exception of Ochmann (1985), whose formulation is sufficiently general to include transient effects. In his study of a closed resonance tube excited by distributed forcing, the method of averaging is employed to describe the slowly varying wave amplitude. Ochmann derives an infinite system of coupled nonlinear ordinary differential equations for the coefficients of a Fourier series solution. The Fourier system is summable when transformed into characteristic coordinates, which leads to an inhomogeneous Burgers equation.

More recently, Wang and Kassoy (1990a, 1990b) have developed a mathematical technique that combines a formal multiple-scale perturbation procedure with Fourier series expansions to study wavefield evolution in a cylinder subject to extensive piston compression and expansion. The problem differs fundamentally from the resonance

tube problem in the sense that the piston displacement is not small, and thus the variation in the mean gas state must be described. Acoustic disturbances, either caused by a rapid piston acceleration or specified as an initial nonequilibrium distribution, evolve into weak shocks on the timescale of one piston stroke. The evolution equations describing acoustic modal interactions contain quadratic nonlinear terms and are infinitely coupled, resembling those obtained by Ochmann (1985) and Culick (1976a). Adequate modal resolution ensures that the Fourier summations can resolve weak shock formation and, to some extent, subsequent evolution.

In the present paper, the techniques developed by Wang and Kassoy (1990a, 1990b) are employed and extended in order to investigate the piston-driven resonances in a gas column subject to a variety of boundary conditions at the far end. Our objective is to examine the effect of eigenfunction choice, compatible with the boundary condition, on the resulting wave evolution. In particular, we want to determine the mathematical and physical consequences of using a particular set of eigenfunctions to describe solution evolution. Relative to the studies of Jimenez (1973) and Seymour and Mortell (1973a, 1973b), the present analysis has the advantage of being fully transient, based on an initial-boundary-value formulation. As a result, not only the long-time solutions, but also the evolution processes en route to limit cycles, are revealed.

A linear theory is developed first using an arbitrary boundary admittance, of the type proposed by Seymour and Mortell (1973a). The solution describes the damping of acoustic transients which leads to harmonic steady oscillations if the acoustic admittance is positive and finite. The main focus of the paper is, however, a comparative study of open- vs. closed-system resonance phenomena. Modal evolution equations containing quadratic or cubic nonlinearities, characteristic of processes in closed and open systems, respectively, are derived and evaluated numerically. In contrast to the conventional stability analysis, adequate modal resolution is used in order to obtain the complete solution behavior, reflective of detailed nonlinear wave/shock structures. In addition, a finite-difference calculation is conducted to verify and extend the perturbation results.

Since no periodicity requirement is imposed, in contrast to previous quasi-steady studies, our solution allows the spontaneous evolution of all the possible waveforms. In particular, weak shocks of relatively large strength are found to form and disappear alternately in an ideally open system (isobaric exit) driven at the linearly resonant frequency. Under the same circumstance no shock has been predicted by Jimenez (1973) and Seymour and Mortell (1973a, 1973b). The sensitivity of wave magnitudes and characteristics to the imposed boundary condition, demonstrated through this study, suggests the importance of using accurate eigenfunctions in modeling acoustically active systems.

**2. Problem formulation.** We consider forced, one-dimensional acoustic wave motion in a gas contained in a region  $0 \leq x^* \leq L^*$ . At the left end of the region, a piston executes small harmonic vibrations with velocity  $U^* \sin(\omega^* t^*)$ . The physical conditions at  $L^*$  are represented by a real admittance function that permits partial reflection of outgoing waves. The gas is initially stationary and has a reference state  $(p_0^*, \rho_0^*, T_0^*)$ , with the associated sound speed  $c_0^* = (\gamma p_0^* / \rho_0^*)^{1/2}$ . An acoustic disturbance travels across the region on the acoustic timescale  $t_a^* = L^* / c_0^*$ .

In terms of the dimensionless variables

$$(1) \quad p = \frac{p^*}{p_0^*}, \quad \rho = \frac{\rho^*}{\rho_0^*}, \quad T = \frac{T^*}{T_0^*}, \quad u = \frac{u^*}{c_0^*}, \quad x = \frac{x^*}{L^*}, \quad t = \frac{t^*}{t_a^*},$$

the equations describing the motion of an ideal gas with constant properties can be written as (Wang and Kassoy, 1990a)

$$(2) \quad \rho_t + (\rho u)_x = 0,$$

$$(3) \quad u_t + uu_x + \frac{p_x}{\gamma p} = 0,$$

$$(4) \quad p = \rho^\gamma, \quad T = \rho^{\gamma-1},$$

where the subscripts  $t$  and  $x$  denote partial derivatives. Transport terms are ignored because the timescale for damping is very long with respect to the acoustic time variable  $t$ , for gradients on the length scale  $L^*$  (Landau and Lifshitz, 1959). Only very short wavelength disturbances will be affected by viscous and thermal diffusion. Other flow regions where transport effects are not negligible include shock zones and acoustic boundary layers, of the type described by Wang and Kassoy (1992). The former can be treated as a mathematical discontinuity in the inviscid study, and the latter are not considered in the one-dimensional problem formulation.

As a consequence of the transport-free assumption, (4) implies that the flow field is isentropic if the solution is continuous (no shocks present). This approximation is not restrictive for gradients with a characteristic length scale  $L^*$  as long as the acoustic Reynolds number  $R_A = c_0^* L^* / \nu_0^* \gg 1$ . If a weak shock appears, then one must consider weak (discontinuous) solutions to (2)–(4), and recognize that entropy changes are proportional to the third power of the shock strength (Whitham, 1974). Although relatively small, these changes will accumulate if a repeatedly reflected shock processes the gas in a closed container. Eventually, on a sufficiently long timescale, entropy changes will be significant, and the model in (2)–(4) will be inadequate.

The initial and boundary conditions are

$$(5) \quad t = 0; \quad p = \rho = T = 1, \quad u = 0,$$

$$(6) \quad x = -\frac{\epsilon}{\omega} \cos(\omega t); \quad u = \epsilon \sin(\omega t), \quad x = 1; \quad u = \frac{\sigma}{\gamma} (p - 1),$$

in which the dimensionless frequency of piston vibration  $\omega = \omega^* t_a^*$ ,  $\epsilon = U^* / c_0^*$  is the maximum Mach number of the piston, characteristic of flow speeds in the absence of resonance, and  $\sigma$  is the acoustic admittance discussed below. The perturbation analyses presented in the subsequent sections are focused on the limit  $\epsilon \rightarrow 0$ . Furthermore, it is assumed that  $\omega = O(1)$ , so that the piston displacement is of  $O(\epsilon)$ , small relative to the length of the gaseous region.

The second boundary condition in (6) involves an acoustic admittance  $\sigma$  which provides a general relationship between the velocity fluctuation and the excess (acoustic) pressure on the outflow boundary. This type of boundary condition, conventionally used for linear acoustic systems, was extended by Seymour and Mortell (1973a, 1973b) and Jimenez (1973) to characterize boundary responses to nonlinear wave phenomena. In this study we consider only values of  $\sigma$  that are real, positive, and invariant to frequency and time. Negative values of admittance imply acoustic energy input through the boundary; and complex values imply a time delay in velocity response to the pressure disturbance, which can be accommodated by using a time-lag constant in real-valued derivations (Williams, 1985). Finally, one notices that when  $\sigma = 0$ ,  $u = 0$  at  $x = 1$ , and a rigid wall is present. In contrast,  $\sigma \rightarrow \infty$  corresponds to an isobaric exit which is sometimes referred to as being “ideally open.”

**3. Linear oscillation.** First, a linear perturbation study is carried out to (i) obtain general linear solutions describing piston-induced acoustic transients as well as evolution to quasi-steady oscillations; (ii) discover physical conditions, in terms of the acoustic admittance  $\sigma$  and driving frequency  $\omega$ , under which resonant wave amplifications may occur; and (iii) determine the timescales for wave nonlinearization and the limiting amplitudes in resonant systems, to be used as a basis for an intricate weakly nonlinear analysis in the subsequent section.

In the linear regime an  $O(\epsilon)$  piston oscillation initiates in the gas both mechanical and thermodynamical disturbances of similar magnitude. By applying the scale transformations

$$(7) \quad u = \epsilon \bar{u}, \quad \rho = 1 + \epsilon \bar{\rho},$$

to (2)–(6), the lowest-order approximate system for the induced acoustic velocity can be derived as

$$(8) \quad \bar{u}_{tt} - \bar{u}_{xx} = 0,$$

$$(9) \quad t = 0; \quad \bar{u} = \bar{u}_t = 0,$$

$$(10) \quad x = 0; \quad \bar{u} = \sin(\omega t), \quad x = 1; \quad \bar{u}_t = -\sigma \bar{u}_x.$$

The solution to (8)–(10), found from Laplace transform techniques, can be put into the form

$$(11) \quad \bar{u} = \bar{u}_{QS} + \bar{u}_{TR},$$

$$(12) \quad \bar{u}_{QS} = \frac{1}{\sin^2(\omega) + \sigma^2 \cos^2(\omega)} \{ -\sigma \sin(\omega x) \cos(\omega t) \\ + [\sin(\omega) \sin(\omega(1-x)) + \sigma^2 \cos(\omega) \cos(\omega(1-x))] \sin(\omega t) \},$$

$$(13) \quad \bar{u}_{TR} = \sum_{n=-\infty}^{\infty} \frac{i\omega}{\lambda_n^2 - \omega^2} \sin(\lambda_n x) e^{i\lambda_n t},$$

provided that the denominators do not vanish. The corresponding density disturbance can be readily obtained by integrating the lowest approximation to continuity equation (2).

Equation (12) describes a quasi-steady gas oscillation at the forced frequency of the piston. The transient part, denoted by  $\bar{u}_{TR}$  in (13), arises from residuals of the integrand in the complex Laplace inversion formula at singular points

$$(14) \quad \tan(\lambda_n) = i\sigma,$$

which defines the eigenvalues for the Fourier series. Note that  $\lambda_n$  is a complex quantity in general even for real values of  $\sigma$ , due to the mixed derivatives in the boundary condition (10). The real and imaginary parts of  $\lambda_n$  can be solved explicitly from (14) to obtain

$$(15) \quad \lambda_n^{(r)} = \begin{cases} n\pi, & 0 \leq \sigma < 1, \\ (n - \frac{1}{2})\pi & \sigma > 1, \end{cases} \quad n = 1, 2, \dots,$$

$$(16) \quad \lambda_n^{(i)} = -\frac{1}{2} \ln \left| \frac{1 - \sigma}{1 + \sigma} \right|.$$

As a result, (13) can be put into a more illuminating form,

$$(17) \quad \bar{u}_{TR} = \frac{\omega}{2} e^{-\lambda^{(i)}(t+x)} \sum_{n=-\infty}^{\infty} \frac{e^{i[\lambda_n^{(r)}(t+x) - \phi_n]}}{|\lambda_n^2 - \omega^2|} - \frac{\omega}{2} e^{-\lambda^{(i)}(t-x)} \sum_{n=-\infty}^{\infty} \frac{e^{i[\lambda_n^{(r)}(t-x) - \phi_n]}}{|\lambda_n^2 - \omega^2|},$$

where the phase angle ( $0 \leq \phi_n < 2\pi$ ) is determined from

$$(18) \quad e^{i\phi_n} = \frac{[(\lambda_n^{(r)})^2 - (\lambda^{(i)})^2 - \omega^2] + i[2\lambda_n^{(r)}\lambda^{(i)}]}{|\lambda_n^2 - \omega^2|}.$$

Clearly, (17) represents an infinite number of pairs of counterpropagating waves, whose amplitudes attenuate exponentially with time if  $\lambda^{(i)} > 0$  or, equivalently,  $0 < \sigma < \infty$ . In physical terms a finite-admittance surface acts as an energy sink for all the oscillatory modes, and only the mode at the forced frequency is sustained due to the continuous boundary work input from the piston. An important implication of this result is that the wave system remains linear always, because the eigenmodes do not survive, and hence no significant deformation in waveform can be accumulated on long timescales by weakly nonlinear effects.

Another distinct effect of the boundary energy loss is to render the acoustic wavefield nonresonant across the entire spectrum of the piston-excitation frequency. It can be shown that, for  $0 < \sigma < \infty$ , the solution described by (11), (12), and (17) has positive-definite denominators and is therefore always bounded. An interesting special case arises for  $\sigma = 1$ , which corresponds to a nonreflecting outflow boundary. In this case the expression for  $\bar{u}$  reduces to a simple traveling wave solution of the form  $\sin[\omega(t-x)]$ .

In contrast, for the cases of  $\sigma = 0$  (rigid endwall) and  $\sigma \rightarrow \infty$  (isobaric exit), no acoustic energy exchange with the end boundary exists; the damping coefficient  $\lambda^{(i)}$  vanishes; and therefore the transient responses represented by the infinite series persist. We can derive the following from (11)–(18):

$$(19) \quad \sigma = 0; \quad \bar{u} = \frac{\sin[\omega(1-x)] \sin(\omega t)}{\sin(\omega)} - \sum_{n=1}^{\infty} \frac{2\omega}{\lambda_n^2 - \omega^2} \sin(\lambda_n x) \sin(\lambda_n t)$$

and

$$(20) \quad \sigma \rightarrow \infty; \quad \bar{u} = \frac{\cos[\omega(1-x)] \sin(\omega t)}{\cos(\omega)} - \sum_{n=1}^{\infty} \frac{2\omega}{\lambda_n^2 - \omega^2} \sin(\lambda_n x) \sin(\lambda_n t),$$

where  $\lambda_n = \lambda_n^{(r)}$  is defined by (15). In reality, of course, transport effects which are excluded in the present analysis eventually damp out the acoustic transient modes on the timescale  $t_d = O(R_A/n^2)$ , and the solutions converge to quasi-steady solutions (the first terms on the right-hand side of (19) and (20)) in the absence of resonance. Except for large mode numbers,  $t_d \gg 1$  and is larger than the characteristic nonlinearization time for a system with an  $O(\epsilon)$  piston Mach number.

Acoustic systems described by (19) and (20) are prone to resonance phenomena as the frequency of the acoustic driver coincides with one of the eigenvalues ( $\omega = n\pi$  and  $(n - 1/2)\pi$ , respectively). To avoid singularities and accommodate modal amplification, new solutions are derived directly from (8)–(10) for the two special cases:

$$(21) \quad \bar{u} = \begin{cases} (1-x) \sin(\omega t) - \sum_{n=1}^{\infty} \frac{2\omega}{\lambda_n} \Theta_n(t) \sin(\lambda_n x), & \sigma = 0, \\ x \sin(\omega t) - \sum_{n=1}^{\infty} \frac{2\omega}{\lambda_n} \Theta_n(t) \sin(\lambda_n x), & \sigma \rightarrow \infty, \end{cases}$$



where

$$(22) \quad \Theta_n = \begin{cases} \frac{\lambda_n \sin(\lambda_n t) - \omega \sin(\omega t)}{\lambda_n^2 - \omega^2}, & \omega \neq \lambda_n, \\ \frac{1}{2\omega} \sin(\omega t) + \frac{t}{2} \cos(\omega t), & \omega = \lambda_n. \end{cases}$$

It is to be noted that although the solutions for the closed and ideally open resonant systems bear remarkable resemblance in form, the results are quite different because of the different eigenvalues (cf. (15)).

The linear growth with time of the resonant mode, shown explicitly in (22), will be limited ultimately by nonlinear effects. In order to determine the limiting amplitudes and the timescales on which nonlinear damping offsets the resonant amplification, it is necessary to use a perturbation expansion for  $u$  and  $\rho$  in powers of  $\epsilon$ , with (21) and (22) as leading-order solutions. The analysis is carried out to higher orders based on the governing system (2)–(6), and the fastest growing secular terms at each order are determined. The following hold for  $\epsilon \rightarrow 0$  and  $t \rightarrow \infty$ .

(i) For a closed resonant system with a rigid endwall ( $\sigma = 0$ ),

$$(23) \quad u(t \rightarrow \infty; x) \sim -\epsilon t \cos(\omega t) \sin(\omega x) - \epsilon^2 t^3 \frac{\gamma - 1}{24} \omega \cos(2\omega t) \sin(2\omega x) + O(\epsilon^3 t^5).$$

The asymptotic expansion breaks down as  $t = O(\epsilon^{-1/2})$ , at which point the second- and third-order terms have the same magnitude as the leading-order term. The limiting amplitude  $u = O(\epsilon^{1/2})$ .

(ii) For an ideally open resonant system with an isobaric end ( $\sigma \rightarrow \infty$ ),

$$(24) \quad u(t \rightarrow \infty; x) \sim -\epsilon t \cos(\omega t) \sin(\omega x) - \epsilon^2 t^2 \omega \sin(2\omega t) \sum_{n=1}^{\infty} \frac{[\lambda_n^2 + 2(\gamma - 3)\omega^2] \sin(\lambda_n)}{(\lambda_n^2 - 4\omega^2)^2} \sin(\lambda_n x) + \epsilon^3 t^4 \omega \frac{(\gamma - 2)(\gamma - 3)}{32} [3 \sin(\omega t) \sin(\omega x) - \sin(3\omega t) \sin(3\omega x)] + \dots$$

Unlike case (i), as  $t = O(\epsilon^{-2/3})$ , the magnitude of the third term becomes comparable with that of the first term, and the limiting wave magnitude is thus characterized by  $u = O(\epsilon^{1/3})$ . This is of course based on the assumption that the growth rate of the third term remains the same after its magnitude catches up with that of the second term at  $t = O(\epsilon^{-1/2})$ . A formal proof can be obtained by rederiving the asymptotic series on the latter timescale.

It should be noted again for both cases that on the timescales for nonlinearization, transport property damping will be negligible, particularly if the resonance occurs in one of the lower-order modes ( $n$  not too large). The above results also illustrate a distinct advantage of the current initial-boundary-value approach over the more traditional steady-oscillation analysis. Here, both the limiting amplitudes and the timescales for the resonant systems to reach the limiting amplitudes are obtained through a relatively simple linear analysis.

Finally, we remark that the two cases discussed above are highly idealized and extreme. In practical terms, if the admittance function lies in a small neighborhood of zero or infinity, and when the frequency of excitation becomes sufficiently close to

one of the resonant frequencies, strong wave amplification resulting from elongated beats also renders the linear solutions inappropriate for large  $t$ . The weakly nonlinear analysis presented in the next section will again be limited to the idealized cases to reduce the mathematical complexity. Nonetheless, it is conceptually straightforward to incorporate the effect of small deviations from the linear resonant frequency and the critical admittance values (0 and  $\infty$ ) by introducing additional small parameters used by Jimenez (1973) and Seymour and Mortell (1973a, 1973b).

#### 4. Weakly nonlinear analysis

**4.1 Resonant oscillations: The closed endwall.** The nonuniformity which occurs at  $t = O(\epsilon^{-1/2})$  in the linear asymptotic solution (23) suggests that

$$(25) \quad \tau = \epsilon^{1/2} t$$

constitutes a second important time variable for a two-timescale, weakly nonlinear study of resonance in a closed system. As is standard in multiple-scale formulations, the ordinary time derivative must be replaced by

$$(26) \quad \left( \frac{\partial}{\partial t} \right)_x = \left( \frac{\partial}{\partial t} \right)_{\tau, x} + \epsilon^{1/2} \left( \frac{\partial}{\partial \tau} \right)_{t, x},$$

and  $t$  and  $\tau$  are treated as though they were independent of one another despite the relation (25). In addition, since the system mass is conserved, it is more efficient to conduct the analysis in terms of the Lagrangian coordinate

$$(27) \quad s = \int_{\epsilon x_p(t)}^x \rho(\hat{x}, t) d\hat{x},$$

in which the piston face  $x = \epsilon x_p(t)$  and the endwall  $x = 1$  are represented by  $s = 0$  and  $s = 1$ , respectively. Since, as will be shown later, the displacement of the gas particle is at most of  $O(\epsilon^{1/2})$ , there is practically no need to distinguish between the two coordinates in the leading-order results except near the piston surface.

In the  $(s, t, \tau)$  space the governing equations (2)–(4) and boundary conditions (6) become

$$(28) \quad \rho_t + \epsilon^{1/2} \rho_\tau + \rho^2 u_s = 0,$$

$$(29) \quad u_t + \epsilon^{1/2} u_\tau + \rho^{\gamma-1} p_s = 0,$$

$$(30) \quad s = 0; \quad u = \epsilon \sin(\omega t), \quad s = 1; \quad u = 0.$$

The velocity is zero on the right boundary because  $\sigma = 0$ . Given the asymptotic behavior displayed in (23), the proper expansions for velocity and density on the timescale  $\tau$  are

$$(31) \quad u = \epsilon^{1/2} u_1 + \epsilon u_2 + \dots, \quad \rho = 1 + \epsilon^{1/2} p_1 + \epsilon p_2 + \dots.$$

These expansions are used in (28)–(30) to derive the leading-order, linear, homogeneous equation system

$$(32) \quad \rho_{1t} + u_{1s} = 0, \quad u_{1t} + \rho_{1s} = 0,$$

$$(33) \quad s = 0; \quad u_1 = 0, \quad s = 1; \quad u_1 = 0.$$

One notices that the  $O(\epsilon)$  piston-driving function in (30) does not appear at this order, although it is the source of the excited disturbances. The two equations in (32) can be combined to generate a single second-order linear wave equation for  $u_1$ ,

$$(34) \quad u_{1tt} - u_{1ss} = 0.$$

The general solution satisfying (33) takes the form

$$(35) \quad u_1 = \sum_{n=1}^{\infty} [\alpha_n(\tau) \cos(n\pi t) + \beta_n(\tau) \sin(n\pi t)] \sin(n\pi s),$$

where  $\alpha_n$  and  $\beta_n$  are slowly varying coefficients characterizing the evolution of the wave amplitude, to be determined from next-order considerations as well as initial conditions. Equation (35) can be used to integrate (32) to generate

$$(36) \quad \rho_1 = \sum_{n=1}^{\infty} [-\alpha_n(\tau) \sin(n\pi t) + \beta_n(\tau) \cos(n\pi t)] \cos(n\pi s).$$

In deriving (36), the integration constant  $\beta_0(\tau)$  representing the bulk Fourier mode has been set to zero. This can be justified by using the physical requirement that the spatially averaged density,  $\int_0^1 \rho ds$ , should remain constant (equal to the initial value of 1) to the present order. Bulk density variations associated with the piston displacement occur on the short acoustic time  $t$  and appear at the next order. Alternatively, we may retain  $\beta_0$  in (36) and determine its value together with  $\alpha_n$  and  $\beta_n$  from next-order equations. The latter approach generates identical results but increases the algebraic complexity.

The next-order velocity equation system, derived from (28)–(31), is given by

$$(37) \quad u_{2tt} - u_{2ss} = 2 \left[ \rho_{1\tau s} - \frac{\gamma+1}{4} (\rho_1^2)_{ss} \right],$$

and

$$(38) \quad s=0; \quad u_2 = \sin(\omega t), \quad s=1; \quad u_2 = 0.$$

The transformation

$$(39) \quad u_2 = w_2 + (1-s) \sin(\omega t)$$

is employed to homogenize the boundary conditions, so that

$$(40) \quad w_{2tt} - w_{2ss} = 2 \left[ \rho_{1\tau s} - \frac{\gamma+1}{4} (\rho_1^2)_{ss} \right] + \omega^2 (1-s) \sin(\omega t),$$

$$(41) \quad s=0; \quad w_2 = 0, \quad s=1; \quad w_2 = 0.$$

Our objective is to identify and eliminate terms in the forcing function that contribute to the resonant growth in  $w_2$  and hence  $u_2$ . To this end, a Fourier sine series solution of the form

$$(42) \quad w_2 = \sum_{n=1}^{\infty} T_n(t, \tau) \sin(n\pi s)$$

is substituted into (40) to convert the partial differential equation into a set of ordinary differential equations,

$$(43) \quad T_{n\tau\tau} + (n\pi)^2 T_n = 2 \int_0^1 \left\{ \left[ \rho_{1\tau s} - \frac{\gamma+1}{4} (\rho_1^2)_{ss} \right] + \omega^2 (1-s) \sin(\omega t) \right\} \sin(n\pi s) ds,$$

based on orthogonality properties of Fourier series. The integral on the right-hand side of (43) is evaluated using (36); and following a systematic procedure developed in a related study (Wang and Kassoy, 1990a), harmonic terms of frequency  $n\pi$ , responsi-

ble for causing  $O(t)$  secular growth, are collected and suppressed by setting their coefficients equal to zero. As a result one obtains the amplitude evolution equations

(44)

$$\alpha'_k = \frac{\gamma+1}{16} k\pi \left[ 2 \sum_{n=1}^{\infty} (\alpha_n \alpha_{k+n} + \beta_n \beta_{k+n}) - \sum_{n=1}^{k-1} (\alpha_n \alpha_{k-n} - \beta_n \beta_{k-n}) \right] - \delta_{\nu k},$$

(45)

$$\beta'_k = \frac{\gamma+1}{16} k\pi \left[ 2 \sum_{n=1}^{\infty} (\alpha_n \beta_{k+n} - \alpha_{k+n} \beta_n) - \sum_{n=1}^{k-1} (\alpha_{k-n} \beta_n + \alpha_n \beta_{k-n}) \right]$$

for  $k = 2, 3, \dots$ . If  $k = 1$ , the second summation in both equations must be replaced by zero. The quantity  $\delta_{\nu k}$  is the Kronecker delta arising from the piston driving at the resonant frequency  $\omega = \nu\pi$ .

Solutions described by (35) and (36) based on results from (44) and (45) are quite general in the sense that more general initial conditions than those in (5) can be accommodated. Given an arbitrary initial disturbance  $u(t=0) = \epsilon^{1/2} u_i(s)$  and  $\rho(t=0) = 1 + \epsilon^{1/2} \rho_i(s)$ , it follows from (35) and (36) that

$$(46) \quad \alpha_n(0) = 2 \int_0^1 u_i(s) \sin(n\pi s) ds, \quad \beta_n(0) = 2 \int_0^1 \rho_i(s) \cos(n\pi s) ds.$$

The nonlinear evolution of the prescribed initial disturbance and its interaction with the piston-generated disturbances can be traced. If the forcing term  $\delta_{\nu k}$  is dropped from (44), the results simply describe the nonlinear relaxation of the specified initial disturbance in a region of constant volume.

In the present study we focus on the resonant evolution of disturbances initiated purely by piston excitation. In this case  $\alpha_k(0) = \beta_k(0) = 0$ ; and (45), which is homogeneous, implies that  $\beta_k(\tau) \equiv 0$ . The amplitude evolution equations reduce to

$$(47) \quad \alpha'_k = \frac{\gamma+1}{16} k\pi \left( 2 \sum_{n=1}^{\infty} \alpha_n \alpha_{k+n} - \sum_{n=1}^{k-1} \alpha_n \alpha_{k-n} \right) - \delta_{\nu k}.$$

The quadratic mode-coupling exhibited in (44), (45), and (47) is characteristic of nonlinear interactions in closed acoustic systems (Wang and Kassoy, 1990a, 1990b). This mechanism enables acoustic energy to be transferred from lower modes, especially the forced resonant mode, to higher frequency modes, so that the amplitude growth of any particular mode may be limited. Compressive wavefronts steepen to form shock waves, and rarefaction wavefronts flatten out. The weak solutions to the Euler equations evolve to limit cycles because there is an inherent balance between energy input by the driving piston and internal dissipation by the shock. This is supported by numerical calculations to be discussed in §5. Entropy changes induced by the  $O(\epsilon^{1/2})$  shock occur at the  $O(\epsilon^{3/2})$  level and have no impact on the present asymptotic solutions for  $\tau = O(1)$ .

It can be shown that the results derived in this section are equivalent to those obtained by Ochmann (1985) using the method of averaging. The purpose of revisiting this problem is to demonstrate that useful insights can be extracted from the multiple-scale procedure, and that the approach can be employed in the investigation of more complex modal interactions arising in an open-ended resonant system. In addition, a systematic truncation strategy is developed to evaluate reduced versions of the infinitely coupled amplitude equation system by numerical means. Spatially

resolved solutions are found from summations of sufficient numbers of Fourier modes. These solutions, not available in Ochmann's work, are presented in §5 and employed in a comparative study of the effect of boundary conditions, and hence system eigenfunctions, on the evolution of acoustic phenomena in open- and closed-ended resonant systems.

**4.2 Resonant oscillations: The isobaric exit.** In a resonant system with an isobaric exit boundary, Eulerian variables are used because the system mass varies with time. The multiple-scale formulation is carried out in terms of the time variables  $t$  and

$$(48) \quad \tau = \epsilon^{2/3} t$$

through the transformation

$$(49) \quad \left( \frac{\partial}{\partial t} \right)_x = \left( \frac{\partial}{\partial t} \right)_{\tau, x} + \epsilon^{2/3} \left( \frac{\partial}{\partial \tau} \right)_{t, x},$$

implied by (24) and the subsequent discussion. As a consequence of the relatively long growth time  $\tau$ , the pertinent asymptotic expansions for  $u$  and  $\rho$  at the expected limit cycle are now

$$(50) \quad u = \epsilon^{1/3} u_1 + \epsilon^{2/3} u_2 + \epsilon u_3 + \dots,$$

$$(51) \quad \rho = 1 + \epsilon^{1/3} \rho_1 + \epsilon^{2/3} \rho_2 + \epsilon \rho_3 + \dots.$$

In analogy with the closed system, the leading-order solution can be put into the form

$$(52) \quad u_1 = \sum_{n=1}^{\infty} [\alpha_n(\tau) \cos(\lambda_n t) + \beta_n(\tau) \sin(\lambda_n t)] \sin(\lambda_n x),$$

$$(53) \quad \rho_1 = \sum_{n=1}^{\infty} [-\alpha_n(\tau) \sin(\lambda_n t) + \beta_n(\tau) \cos(\lambda_n t)] \cos(\lambda_n x),$$

which satisfies the same homogeneous system as (32) and (33) except that at  $x = 1$ , the disturbance density, instead of velocity, is zero because of the isobaric condition ( $\sigma \rightarrow \infty$  in (6)) and the isentropic approximation (4). Consequently, the correct eigenvalues have the form  $\lambda_n = (n - 1/2)\pi$  for  $n = 1, 2, \dots$ . The slowly varying amplitude functions  $\alpha_n$  and  $\beta_n$  in (52) and (53) are again to be determined from higher-order considerations.

The relations in (49)–(51) can be applied to (2)–(6) to find the next two ordered equation sets,

$$(54) \quad \rho_{2t} + u_{2x} = -(\rho_1 u_1)_x,$$

$$(55) \quad u_{2t} + \rho_{2x} = -u_1 u_{1x} - (\gamma - 2) \rho_1 \rho_{1x},$$

$$(56) \quad \rho_{3t} + u_{3x} = -\rho_{1\tau} - (\rho_1 u_2 + \rho_2 u_1)_x,$$

$$(57) \quad u_{3t} + \rho_{3x} = -u_{1\tau} - \frac{(\gamma - 2)(\gamma - 3)}{6} (\rho_1^3)_x - [u_1 u_2 + (\gamma - 2) \rho_1 \rho_2]_x,$$

together with boundary conditions

$$(58) \quad x = 0; \quad u_2 = 0, \quad u_3 = \sin(\omega t), \quad x = 1; \quad \rho_2 = \rho_3 = 0.$$

The left boundary condition, imposed at  $x = 0$  instead of the actual piston location, is consistent with the accuracy of the perturbation scheme because the piston displacement is of  $O(\epsilon)$  small (cf. (6)). It can be formally derived based on a Taylor series expansion of the exact condition  $u(\epsilon x_p, t) = \epsilon \sin(\omega t)$ , in the limit process  $\epsilon \rightarrow 0$ .

A suitable combination of (54) and (55) gives

$$(59) \quad u_{2tt} - u_{2xx} = - \left( u_1^2 + \frac{\gamma-1}{2} \rho_1^2 \right)_{xt},$$

which must be solved subject to boundary conditions derived from (54) and (58),

$$(60) \quad x = 0; \quad u_2 = 0, \quad x = 1; \quad u_{2x} = \frac{1}{2} (u_1^2)_t|_{x=1}.$$

If the transformation

$$(61) \quad u_2 = w_2 + \frac{x}{2} (u_1^2)_t \Big|_{x=1}$$

is substituted into (59) and (60), we obtain

$$(62) \quad w_{2tt} - w_{2xx} = - \left( u_1^2 + \frac{\gamma-1}{2} \rho_1^2 \right)_{xt} - \frac{x}{2} (u_1^2)_{ttt} \Big|_{x=1}$$

and a set of homogeneous boundary conditions for  $w_2$ . A general solution can be written as

$$(63) \quad u_2 = \frac{x}{2} (u_1^2)_t \Big|_{x=1} + \sum_{n=1}^{\infty} T_n(t, \tau) \sin(\lambda_n x),$$

where

$$(64) \quad T_n = \delta_n(\tau) \cos(\lambda_n t) + \gamma_n(\tau) \sin(\lambda_n t) + \int_0^t R_n(\hat{t}, \tau) \cos[\lambda_n(\hat{t} - t)] d\hat{t},$$

$$(65) \quad R_n = 2\lambda_n \int_0^1 \left( u_1^2 + \frac{\gamma-1}{2} \rho_1^2 \right) \cos(\lambda_n x) dx - \sin(\lambda_n) \left[ \frac{1}{\lambda_n^2} (u_1^2)_{tt} + 2u_1^2 \right] \Big|_{x=1}.$$

The functions  $\delta_n$  and  $\gamma_n$ , whose explicit forms are not needed in the determination of  $\alpha_n$  and  $\beta_n$ , are the second-order counterparts of the latter. An integration of (55) with respect to  $x$ , combined with the requirement that  $\rho_2|_{x=1} = 0$ , gives the corresponding density disturbance

$$(66) \quad \rho_2 = \frac{1-x^2}{4} (u_1^2)_{tt} \Big|_{x=1} - \frac{1}{2} [u_1^2 - u_1^2|_{x=1} + (\gamma-2)\rho_1^2] + \sum_{n=1}^{\infty} \frac{T_n(t, \tau)}{\lambda_n} \cos(\lambda_n x).$$

One might expect that the evolution equations governing the leading-order Fourier coefficients  $\alpha_n$  and  $\beta_n$  should result from eliminating secular growth terms in the second-order solution (63)–(66), as is usually the case with two-scale expansions. Here, however, both  $u_2$  and  $\rho_2$  are found to be bounded as  $t \rightarrow \infty$ , a conclusion drawn through a careful analysis of the solution structure. Evidently, the only plausible source of resonant growth lies in the particular solution associated with the integral in

(64), whose integrand contains triple products of harmonic functions of  $\hat{t}$  (cf. (65), (52), and (53)). These product terms are convertible into single functions such as  $\cos[(\lambda_k \pm \lambda_m \pm \lambda_n)\hat{t}]$  or  $\sin[(\lambda_k \pm \lambda_m \pm \lambda_n)\hat{t}]$ . Since the algebraic combinations of three arbitrary eigenvalues are never zero, the integral remains harmonic in  $t$  always.

The fact that the second-order equations provide no clue toward a definitive leading-order solution may be explained from another perspective: the growth of the wave amplitude must be intimately related to the boundary driving effect, which manifests itself only at the next order. Therefore, secular relations have to be sought through an extension of the perturbation scheme to the third order. Margolis (1993) confronts similar issues in his study of a combustion-driven tube.

The third-order analogues of (59) and (60), derived from (56)–(58), are

$$(67) \quad u_{3tt} - u_{3xx} = E(t, \tau, x),$$

$$(68) \quad x = 0; \quad u_3 = \sin(\omega t), \quad x = 1; \quad u_{3x} = -(\rho_1 u_2 + \rho_2 u_1)_x,$$

where

$$(69) \quad E = 2\rho_{1\tau x} + (\rho_1 u_2 + \rho_2 u_1)_{xx} - \left[ \frac{(\gamma-2)(\gamma-3)}{6} \rho_1^3 + u_1 u_2 + (\gamma-2)\rho_1 \rho_2 \right]_{xx}.$$

Again, a transformation defined by

$$(70) \quad u_3 = w_3 + \sin(\omega t) - x(\rho_1 u_2 + \rho_2 u_1)_{x=1}$$

renders the boundary conditions homogeneous for  $w_3$ , and the differential equation becomes

$$(71) \quad w_{3tt} - w_{3xx} = \omega^2 \sin(\omega t) + x(\rho_1 u_2 + \rho_2 u_1)_{x=1} + E(t, \tau, x).$$

As a result, a Fourier-series solution of the form

$$(72) \quad w_3 = \sum_{n=1}^{\infty} \Theta_n(t, \tau) \sin(\lambda_n x)$$

exists. We now insert (72) into (71), multiply both sides by  $\sin(\lambda_k x)$ , and integrate over the interval  $[0, 1]$ . This leads to

$$(73) \quad \Theta_{ktt} + \lambda_k^2 \Theta_k = 2 \int_0^1 \left[ \omega^2 \sin(\omega t) + x(\rho_1 u_2 + \rho_2 u_1)_{x=1} + E(t, \tau, x) \right] \sin(\lambda_k x) dx.$$

If (69) is substituted into (73) and integration by parts is carried out, more explicit representations of the forcing terms can be obtained, giving

$$(74) \quad \begin{aligned} \Theta_{ktt} + \lambda_k^2 \Theta_k = & \frac{\omega^2 \sin(\omega t)}{\lambda_k} - 2\lambda_k \int_0^1 \rho_{1\tau} \cos(\lambda_k x) dx \\ & + \sin(\lambda_k) \left( 2 + \frac{1}{\lambda_k^2} \frac{\partial^2}{\partial t^2} \right) (\rho_1 u_2 + \rho_2 u_1)_{x=1} \\ & + \lambda_k \frac{\partial}{\partial t} \int_0^1 \left[ \frac{(\gamma-2)(\gamma-3)}{6} \rho_1^3 + u_1 u_2 + (\gamma-2)\rho_1 \rho_2 \right] \cos(\lambda_k x) dx \\ & - \lambda_k^2 \int_0^1 (\rho_1 u_2 + \rho_2 u_1) \sin(\lambda_k x) dx. \end{aligned}$$

Equation (74) describes the forced motion of a collection of linear oscillators, each associated with an  $O(\epsilon)$  acoustic mode. Nonhomogeneous terms on the right-hand side contain both the effect of piston driving (the first term) and the time-evolution of various combinations of lower-order acoustic variables. The appearance of  $\rho_{1\tau}$  in the second forcing term is particularly encouraging, since it provides the  $\tau$ -derivatives of  $\alpha_k$  and  $\beta_k$ , an imperative ingredient in the desired evolution equations. First- and second-order solutions developed in this section are used to evaluate the right-hand side of (74). Resonance is then suppressed by equating to zero the coefficients of all the terms proportional to  $\sin(\lambda_k t)$  and  $\cos(\lambda_k t)$ . This labor-intensive procedure, involving triple products of Fourier series, leads to

$$\begin{aligned}
 \alpha'_k = \frac{\lambda_k}{16} & \left\{ \sum_{j=1}^{k-1} \sum_{l=1}^j \Lambda_{jkl}^a [\alpha_{k-j}(\alpha_l \beta_{j-l+1} + \alpha_{j-l+1} \beta_l) + \beta_{k-j}(\alpha_l \alpha_{j-l+1} - \beta_l \beta_{j-l+1})] \right. \\
 & + \sum_{j=1}^{\infty} \sum_{l=1}^j \Lambda_{jkl}^b [\alpha_{k+j}(\alpha_l \beta_{j-l+1} + \alpha_{j-l+1} \beta_l) - \beta_{k+j}(\alpha_l \alpha_{j-l+1} - \beta_l \beta_{j-l+1})] \\
 & + \sum_{j=k}^{\infty} \sum_{l=1}^j \Lambda_{jkl}^c [\alpha_{j-k+1}(\alpha_l \beta_{j-l+1} + \alpha_{j-l+1} \beta_l) - \beta_{j-k+1}(\alpha_l \alpha_{j-l+1} - \beta_l \beta_{j-l+1})] \\
 & + 2 \sum_{j=1}^{k-1} \sum_{l=1}^{\infty} \Lambda_{jkl}^d [\alpha_{k-j}(\alpha_l \beta_{l+j} - \alpha_{l+j} \beta_l) + \beta_{k-j}(\alpha_l \alpha_{l+j} + \beta_l \beta_{l+j})] \\
 & + 2 \sum_{j=1}^{\infty} \sum_{l=1}^{\infty} \Lambda_{jkl}^e [\alpha_{k+j}(\alpha_l \beta_{l+j} - \alpha_{l+j} \beta_l) - \beta_{k+j}(\alpha_l \alpha_{l+j} + \beta_l \beta_{l+j})] \\
 & + 2 \sum_{j=k}^{\infty} \sum_{l=1}^{\infty} \Lambda_{jkl}^f [\alpha_{j-k+1}(\alpha_l \beta_{l+j} - \alpha_{l+j} \beta_l) - \beta_{j-k+1}(\alpha_l \alpha_{l+j} + \beta_l \beta_{l+j})] \Big\} \\
 & - \delta_{\nu k},
 \end{aligned}
 \tag{75}$$

$$\begin{aligned}
 \beta'_k = \frac{\lambda_k}{16} & \left\{ \sum_{j=1}^{k-1} \sum_{l=1}^j \Lambda_{jkl}^a [-\alpha_{k-j}(\alpha_l \alpha_{j-l+1} - \beta_l \beta_{j-l+1}) + \beta_{k-j}(\alpha_l \beta_{j-l+1} + \alpha_{j-l+1} \beta_l)] \right. \\
 & + \sum_{j=1}^{\infty} \sum_{l=1}^j \Lambda_{jkl}^b [\alpha_{k+j}(\alpha_l \alpha_{j-l+1} - \beta_l \beta_{j-l+1}) + \beta_{k+j}(\alpha_l \beta_{j-l+1} + \alpha_{j-l+1} \beta_l)] \\
 & + \sum_{j=k}^{\infty} \sum_{l=1}^j \Lambda_{jkl}^c [-\alpha_{j-k+1}(\alpha_l \alpha_{j-l+1} - \beta_l \beta_{j-l+1}) \\
 & \quad \quad \quad - \beta_{j-k+1}(\alpha_l \beta_{j-l+1} + \alpha_{j-l+1} \beta_l)] \\
 & + 2 \sum_{j=1}^{k-1} \sum_{l=1}^{\infty} \Lambda_{jkl}^d [-\alpha_{k-j}(\alpha_l \alpha_{l+j} + \beta_l \beta_{l+j}) + \beta_{k-j}(\alpha_l \beta_{l+j} - \alpha_{l+j} \beta_l)] \\
 & + 2 \sum_{j=1}^{\infty} \sum_{l=1}^{\infty} \Lambda_{jkl}^e [\alpha_{k+j}(\alpha_l \alpha_{l+j} + \beta_l \beta_{l+j}) + \beta_{k+j}(\alpha_l \beta_{l+j} - \alpha_{l+j} \beta_l)] \\
 & + 2 \sum_{j=k}^{\infty} \sum_{l=1}^{\infty} \Lambda_{jkl}^f [-\alpha_{j-k+1}(\alpha_l \alpha_{l+j} + \beta_l \beta_{l+j}) - \beta_{j-k+1}(\alpha_l \beta_{l+j} - \alpha_{l+j} \beta_l)] \Big\},
 \end{aligned}
 \tag{76}$$



where the coefficients  $\Lambda_{jkl}^a$  through  $\Lambda_{jkl}^f$ , defined explicitly in the Appendix, are constants depending only on the subscript indices and the parameter  $\gamma$ , the ratio of specific heats of the gas. The Kronecker delta in (75) again signifies acoustic excitation by the piston when  $\omega = \lambda_p$ .

The infinite system of coupled differential equations described by (75) and (76) involves double sums of cubic modal interaction terms, in comparison to single sums of quadratic interaction terms exhibited in (44) and (45) for a closed resonant system. The increased mathematical complexity arises from the derivation of the evolution equations in terms of the first three expansion orders instead of the usual two. As in Margolis's (1993) related study, it is concluded that third-order nonlinear effects, characterized by cubic mode-coupling, are the dominant mechanism for wavefield evolution in an ideally open system.

Another point to notice is that, unlike the evolution equations for closed systems, no simplification can be achieved for (75) and (76) if  $\alpha_k(0) = \beta_k(0) = 0$ , because neither family of the Fourier coefficients vanishes identically. On the other hand, a nonequilibrium initial state in the gas column can be treated in the same fashion as in (46), if  $n\pi$  is replaced by the appropriate eigenfunction  $\lambda_n$ , and  $u_i$  and  $\rho_i$  are construed as the initial values of the  $O(\epsilon^{1/3})$  quantities in the perturbation expansions (50) and (51).

The formulation described here is based on the isentropic equations in (2)–(4) and the expansions in (50) and (51). If an  $O(\epsilon^{1/3})$  shock forms, it is conceivable that  $O(\epsilon)$  entropy production will occur. The third-order equations, represented by (56) and (57), may have to be altered to accommodate entropy-induced state changes subsequent to the appearance of a shock. In that circumstance the isentropic condition is unique at  $O(\epsilon)$  on each side of the moving shock. This has the effect of changing the relationship between  $p_3$  and  $\rho_3$  by an additive quantity that is time- and space-dependent in general. The effect of this additional consideration on the resonance suppression conditions used to derive (75) and (76) is unknown, and should be more thoroughly examined in the future.

## 5. Numerical solutions

**5.1. Solution techniques.** The asymptotic results derived in the previous section form the basis for a comparative study of piston-driven acoustic resonance phenomena in closed and open systems. Were one interested in circumstances that promoted shock-free flows, it would be useful to follow the solution approach used by Culick (1990) and Margolis (1993), involving a severe truncation of the infinitely coupled system of amplitude equations to a level tractable by analytical means. The truncated system typically includes four to six equations with two to three modes, based on which the existence and stability of limit cycles are determined using the concept of nonlinear dynamical systems. This mathematically elegant approach provides accurate assessments of nonlinear acoustic stability behavior only when large wave number spatial resolution is not required. It is incapable of describing the detailed wavefield structure, particularly the appearance and evolution of steep-fronted waves including shocks, the primary concern of the present study.

As an alternative, one can truncate the amplitude equation system at a sufficiently high level and integrate the resulting coupled ordinary differential equations numerically, so that the global solution behavior is described accurately based on Fourier modal summations. This second approach has been employed successfully in related studies to trace the evolution of acoustic and weak shock waves (Culick, 1976b; Wang and Kassoy, 1990a, 1990b), and is adopted here once again.

The first step in the numerical evaluation is to develop truncated versions of (44) and (45) for the closed system and of (75) and (76) for the ideally open case. If it is desired to include  $N$  modes in the calculations,  $2N$  coupled equations for  $\alpha_k$  and  $\beta_k$  have to be solved simultaneously. All the infinite summations must be replaced with finite summations in order to close the mathematical systems. Thus, in (44) and (45), the infinite sums are replaced by sums of  $N - k$  modes, whereas in both (75) and (76), the appropriate upper limits for the infinite sums are, in the order of their appearance in each equation,  $N - k$ ,  $N$ ,  $N - j$ ,  $N - k$ ,  $N - j$ ,  $N - j$ , and  $N - 1$ . The truncation level  $N$  is determined ideally by the need for accurate representations of steep-fronted shock phenomena. Pragmatic considerations of computational time have limited the total number of modes to  $N \leq 200$  for the closed-system case and  $N \leq 25$  for the open case.

Numerical integrations are carried out by utilizing a standard IMSL library subroutine, IVPRK, which is based on fifth- and sixth-order Runge-Kutta methods. The routine adjusts the step sizes automatically in accordance with the specified global error tolerance, which is set to be  $10^{-4}$ . This error is sufficiently small in view of the larger truncation errors in approximating the infinite systems. Once the first  $N$  Fourier coefficients  $\alpha_k$  and  $\beta_k$  are evaluated, the time and spatial variations of the acoustic velocity and density can be calculated based on (35) and (36) (closed system) or (52) and (53) (open system). It is observed that the computational values for  $\alpha_k$  and  $\beta_k$  become increasingly inaccurate as  $k$  approaches  $N$ , because the truncation prevents the cascade of energy to higher wavenumber modes. Consequently, only the first  $\frac{1}{2}N$  to  $\frac{3}{4}N$  terms are actually utilized in the finite Fourier series summations used to find the solutions described in the next section.

Results obtained from the multiple-scale perturbation analysis are compared with finite-difference solutions based on the MacCormack scheme, a predictor-corrector type of hyperbolic system solver with second-order accuracy in both space and time, capable of capturing shock waves (Anderson, Tannehill, and Pletcher, 1984). To increase shock resolution and damp out the associated Gibbs phenomena, the flux-corrected-transport (FCT) technique (Book, Boris, and Hain, 1975) is incorporated into the numerical code. In the results presented below, 201 spatial grid points are typically used, and numerical experiments show that a Courant number of 0.985 generates the best results.

In order to apply the scheme, conservative versions of the governing partial differential equations must be used. The present computations are based on (2)–(4) for an open resonant system and their Lagrangian analogue for a closed system, so that each solution is comparable to the appropriate perturbation result. The oscillatory left boundary is mapped exactly into a fixed point  $s = 0$  in the Lagrangian coordinate and hence imposes no special difficulty; in the Eulerian coordinate, on the other hand, the piston is located at  $x = 0$ , an approximation compatible with that employed in the perturbation analysis.

**5.2. Closed-system solutions.** Figures 1(a) and 1(b) display the resonant growth of the scaled acoustic velocity  $\hat{u}$  ( $u = \epsilon^{1/2} \hat{u}$ ) and density  $\hat{\rho}$  ( $\rho = 1 + \epsilon^{1/2} \hat{\rho}$ ), respectively, at a fixed Lagrangian coordinate  $s = \frac{1}{4}$  in a closed resonant system. The gas, initially static, is being driven by a piston that operates at the fundamental frequency  $\omega = \pi$  ( $\nu = 1$ ) with a dimensionless velocity amplitude of  $\epsilon = 0.01$ . The characteristic gas velocity (really Mach number) is thus  $O(0.1)$  in value. Solid lines represent the lowest-order perturbation approximations calculated from (35) and (36) based on a summation of 50 Fourier modes from an  $N = 100$  calculation, whereas the dashed

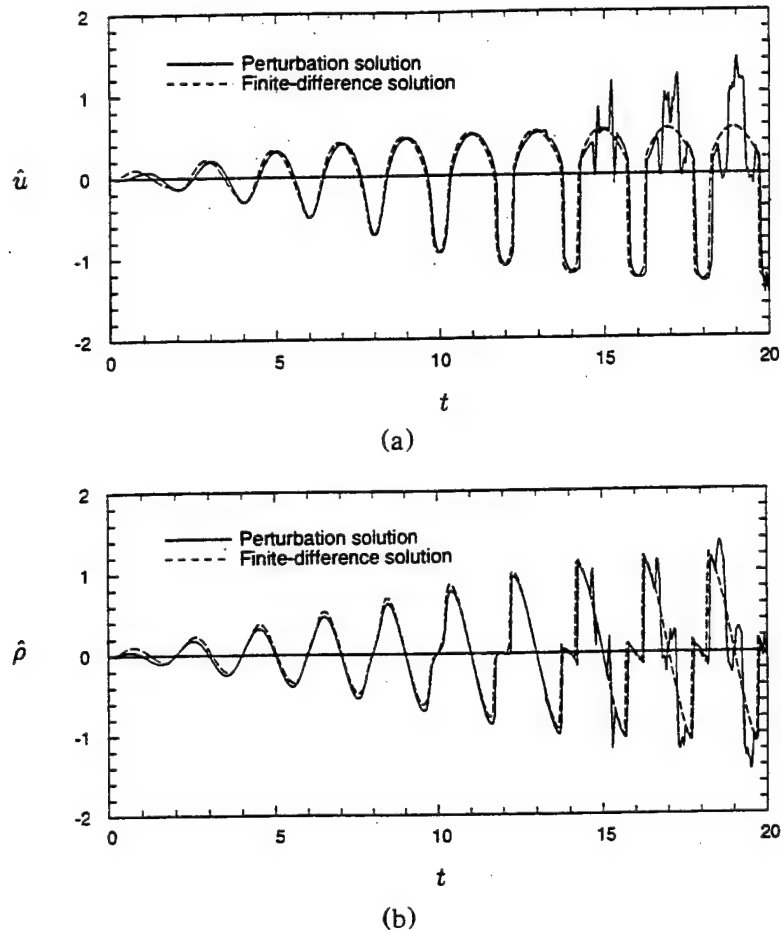


FIG. 1. Time variations of (a) the scaled acoustic velocity  $\hat{u}$  ( $u = \epsilon^{1/2}\hat{u}$ ); (b) the scaled acoustic density  $\hat{p}$  ( $p = 1 + \epsilon^{1/2}\hat{p}$ ) at Lagrangian coordinate  $s = \frac{1}{4}$  in a closed resonant system, driven by piston motion  $u_p = \epsilon \sin(\pi t)$ . The solid lines represent the lowest-order perturbation approximations  $u_1$  and  $p_1$ , calculated from (35) and (36), respectively, and the dashed lines represent finite-difference solutions using the MacCormack scheme. The maximum piston Mach number  $\epsilon = 0.01$ .

lines denote the computational solutions obtained using the MacCormack scheme. The agreement between the two types of solutions prior to shock formation is quite good, and easily within the limits expected for the perturbation and complete solutions. Both exhibit an initial period of linear amplification which leads to severe waveform deformation as nonlinear effect accumulates. Finally, steep line segments appear at  $t \approx 12$ , implying the occurrence of a weak shock wave. Subsequent to shock formation, the MacCormack solution describes the shock extremely well. On the other hand, spurious spikes appear in the Fourier-based perturbation curves, although the latter still capture some useful features such as the shock position and strength.

The appearance of spurious signals in Fig. 1 is caused by the poor convergence of Fourier series associated with discontinuous functions (Gibbs phenomenon). In fact, the Fourier coefficients  $\alpha_k$  and  $\beta_k$  behave like  $1/k$  for discontinuous functions, compared to  $1/k^r$  ( $r \geq 2$ ) for those that are continuous. Errors involved in truncating the infinite evolution system (44)–(45) become significant and accumulate rapidly

during numerical integration. A more quantitative error analysis can be found in Wang and Kassoy (1990b). As with all Fourier-based spectral methods, increasing modal-resolution is ineffective for accuracy improvement when discontinuities are present. Numerical experiments conducted with increasingly large mode numbers produce little change in the magnitude of erroneous spikes. Nonetheless, sharper shock descriptions are obtained with an increased modal truncation level, due to the inclusion of higher wavenumber components.

Once a shock appears, it traverses the gas repeatedly as it reflects from solid walls at both ends. The time intervals between two neighboring passages are unequal because the observation of the shock occurs at a location three times farther away from the right boundary than from the left. Each shock passage brings about a positive density jump (cf. Fig. 1b), but the sign of the velocity jump is dependent on the direction of propagation (cf. Fig. 1a). As time progresses, the oscillatory amplitude growth is seen to become saturated, and a limit cycle is approached, as is demonstrated more clearly in the longer-time result of Fig. 2. The latter shows the same acoustic velocity as plotted in Fig. 1a computed over an extended time using the MacCormack scheme.

Insights about the physical phenomena occurring in the limit-cycle can be gained by using an energy perspective. Figure 3 depicts the instantaneous acoustic energy input by the piston  $\hat{p}\hat{u}|_{x=0}$  (the lower curve), and the cumulative acoustic energy input (the upper curve), both calculated using the MacCormack scheme. Evidently, the piston velocity is basically in phase with the local pressure disturbance, and therefore the boundary work is predominantly positive. In the limit cycle, the energy input per unit cycle is seen to be a constant. Since the right end of the system is a reflector, the only way to remove mechanical energy is through shock dissipation, which is also a constant per cycle because the shock amplitude is a periodic function of time. One may conclude that the limit-cycle shock oscillation in a closed system is supported by a balance between piston energy input and shock damping.

**5.3. Open-system solutions.** Acoustic resonance in an open system is profoundly different from that found in a closed system. First, the magnitudes of the limiting amplitude and nonlinear growth-time are worth emphasizing. Based on the scale relations described in the previous sections, an  $O(\epsilon)$  acoustic driver can excite

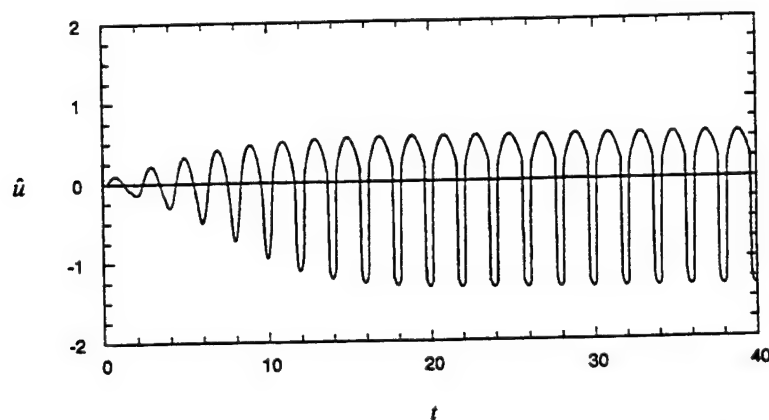


FIG. 2. The same acoustic velocity as depicted in Fig. 1(a) plotted over extended time, to demonstrate the evolution to limit cycle. The results are obtained using the MacCormack scheme.

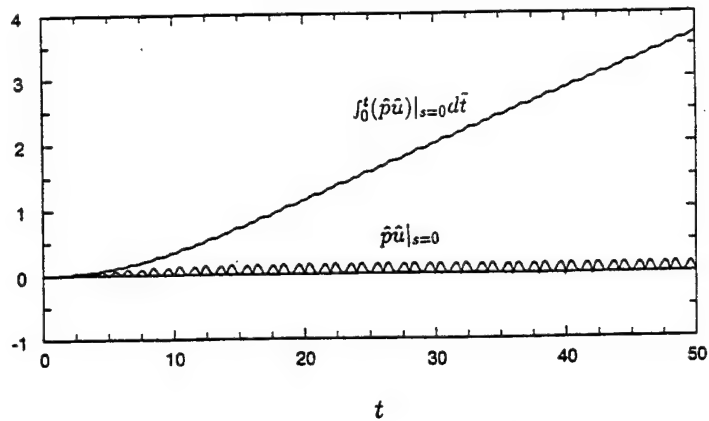


FIG. 3. Instantaneous (lower curve) and cumulative (upper curve) acoustic energy input into the closed resonant system by a vibrating piston, calculated based on finite-difference solutions under conditions identical to those in Fig. 1.

$O(\epsilon^{1/3})$  oscillations over  $t = O(\epsilon^{-2/3})$  in an open system, relative to the maximum amplitude of  $O(\epsilon^{1/2})$  and the growth-time of  $O(\epsilon^{-1/2})$  in a closed system. Other unique features of open-system oscillations are revealed by the following example calculations, conducted for  $\epsilon = 0.08$  ( $\epsilon^{1/3} = 0.2$ ) and  $\nu = 1$  ( $\omega = \pi/2$ ) and with zero initial conditions.

The time-evolution of the acoustic velocity at  $x = \frac{1}{4}$  is plotted in Figs. 4(a) and 4(b), based on the summation of 10 Fourier modes from an  $N = 15$  computation, and the MacCormack solution, respectively. These time-response curves are the result of resonant growth and nonlinear waveform deformation to generate steep-fronted waves. The two types of solutions agree well when the solutions are smooth, and deviate more substantially as large gradient structures develop. The differences are due to the relatively poor convergence properties of truncated Fourier series representations of steep-fronted waves.

To examine the effect of Fourier modal truncation, perturbation solutions using 5, 10, and 18 Fourier mode summations from  $N = 8, 15$ , and 25 calculations, respectively, are plotted in Fig. 5 in terms of acoustic velocity and density at  $x = \frac{1}{4}$ . The results of finite-difference calculations are depicted as dotted lines for comparison. The time range is shorter than that in Fig. 4, so that details of nonlinear distortion of the time-response curves can be viewed with clarity. Near  $t = 40$ , the three finite Fourier series summations produce results that are essentially indistinguishable from one another to the graphical accuracy, and closely resemble the finite-difference solutions, indicating satisfactory convergence of the series. The quantitative difference between the two solution types are within the error bound expected for the perturbation approximation, which, given  $\epsilon^{1/3} = 0.2$ , can be as large as 20%. As time evolves, the time-response curves contain steep gradients and sharp corners that are poorly represented by the Fourier modal summations. The truncation errors involved in approximating the infinite evolutionary system (75)–(76) become severe, rendering the numerical solutions less accurate. Furthermore, it is observed by comparing the numerical data from the three truncation levels that accuracy improvement with increased modal resolution is fairly marginal. This is again due to the fact that Gibbs phenomenon cannot be eliminated with finite modal summations (unless some strong damping mechanisms are introduced into the inviscid system to prevent

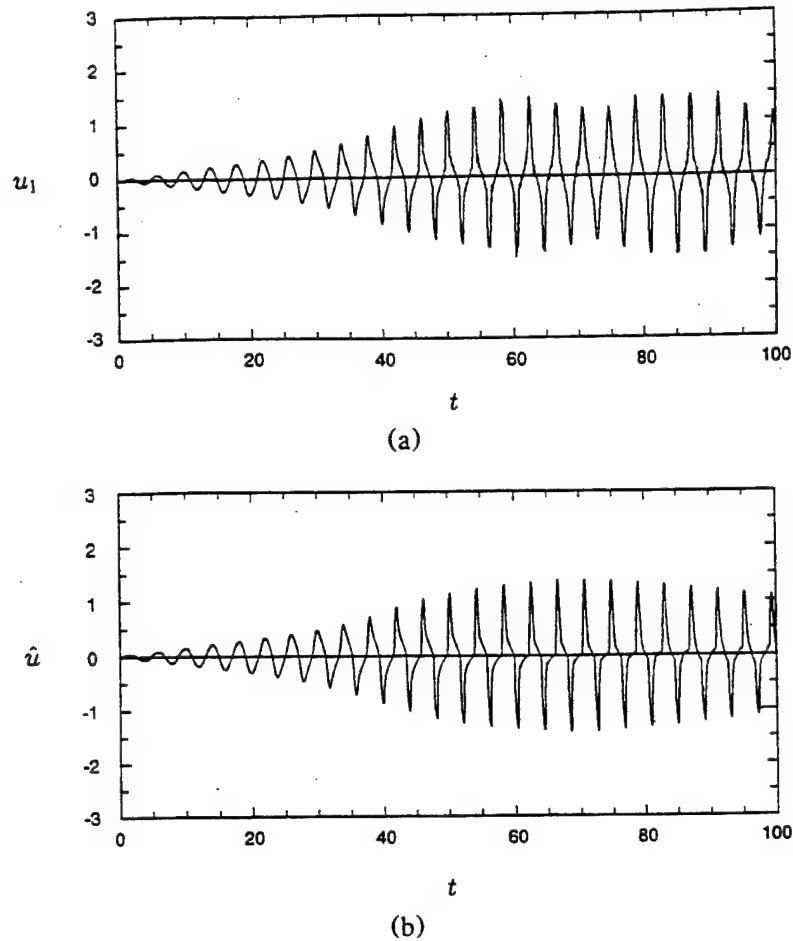


FIG. 4. Time variations of the scaled acoustic velocity  $\hat{u}$  ( $u = \epsilon^{1/3}\hat{u}$ ) at  $x = \frac{1}{4}$  in an open resonant system (isobaric exit), driven by piston motion  $u_p = \epsilon \sin((\pi/2)t)$ . The maximum piston Mach number  $\epsilon = 0.008$ . (a) Leading-order perturbation solution  $u_1$  calculated from (52); (b) finite-difference solution.

the generation of small-scale structures unresolvable by the highest Fourier mode). Despite the apparent deficiency, both Figs. 4 and 5 indicate that some useful features, such as the oscillatory amplitudes and relative phase, are preserved by the truncated modal solutions.

An interesting point to notice from Fig. 4 is that shortly after the formation of steep wavefronts, the oscillatory amplitudes reach a maximum and then decline instead of maintaining a constant value. A longer-time calculation based on the MacCormack method, illustrated in Fig. 6 for the acoustic velocity at  $x = \frac{1}{2}$ , shows beat-like patterns of nonlinear amplitude evolution. The peak-to-valley ratio of the envelope decreases with time, and it is expected that eventually the system relaxes to an equilibrium oscillation of constant amplitude. However, we do not have sufficient numerical accuracy to extend the computation reliably to the time required in order to support this assertion.

The unusual character of the time-response curves in Figs. 4–6 can be better understood by examining the time variation of the spatial wave structure. In Fig. 7 the results of the finite-difference calculation are used to plot the velocity distribution at

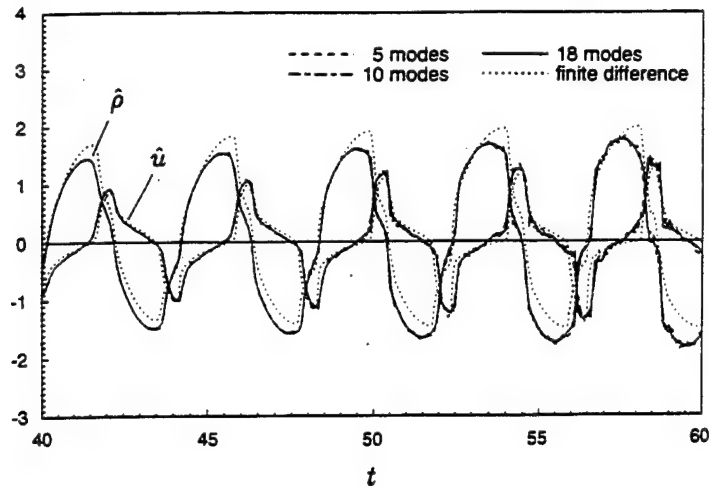


FIG. 5. Comparison of leading-order perturbation solutions based on summations of 5, 10, and 18 Fourier modes and the finite-difference solution obtained using the MacCormack scheme. Plotted are the scaled acoustic velocity  $\hat{u}$  ( $u = 1 + \epsilon^{1/3}\hat{u}$ ) and density  $\hat{\rho}$  ( $\rho = 1 + \epsilon^{1/3}\hat{\rho}$ ) as a function of time at  $x = \frac{1}{4}$ , under conditions identical to those in Fig. 4.

a sequence of times starting from  $t_1 \approx 60.14$ . The direction of propagation at each instant is indicated by a small arrow. At  $t_1$  we observe a compression wavefront propagating leftward. It reflects from the piston face to the right, and subsequently steepens to form a weak shock ( $t_2$ ). Compression signals emitted from the piston cause the shock strength to increase ( $t_3$ ). When the shock hits the isobaric right boundary, its phase is changed by  $\pi$  and a rarefaction wave appears ( $t_4$ ). During the next round-trip to the piston and back, the rarefaction wavefront gradient decreases until  $t_7$ . Then, upon reflection of the rarefaction wave from the isobaric boundary, a compression wavefront reappears ( $t_8$ ), leading to the formation of another shock. The passage of the rapidly evolving waveform is responsible for the drastically varying rates of change displayed in Figs. 4–6. One notices after-shock oscillations in Fig. 7 that arise from the computational scheme even though the FCT approach was carefully employed. The Fourier series-based calculations give the same quantitative behavior, but with relatively poor shock resolution because only a limited number of modes are available.

The intermittent occurrence of the weak shock in an open system discovered in this study is particularly interesting. According to Seymour and Mortell (1973b) and Jimenez (1973), there exist no shocked periodic solutions for an ideally open tube driven at the linearly resonant frequency (cf. the origin in Jimenez's Fig. 9). In other words, the limit-cycle solution for this parameter combination consists of smooth functions only. The results of our initial-boundary-value study suggest that en route to a limit-cycle, characterized by slow, periodic amplitude modulation, weak shocks are generated intermittently.

The mechanism which limits the wave amplitude from growing indefinitely in an ideally open system is fundamentally different from that in a closed one. While the effect of shock dissipation may still play a role, the preeminent factor is a shift in the relative phase between the piston velocity and the local acoustic pressure, resulting in negative boundary work at times, as demonstrated in Fig. 8. It is believed that this occurs because the relatively large amplitude disturbances alter the wavespeed

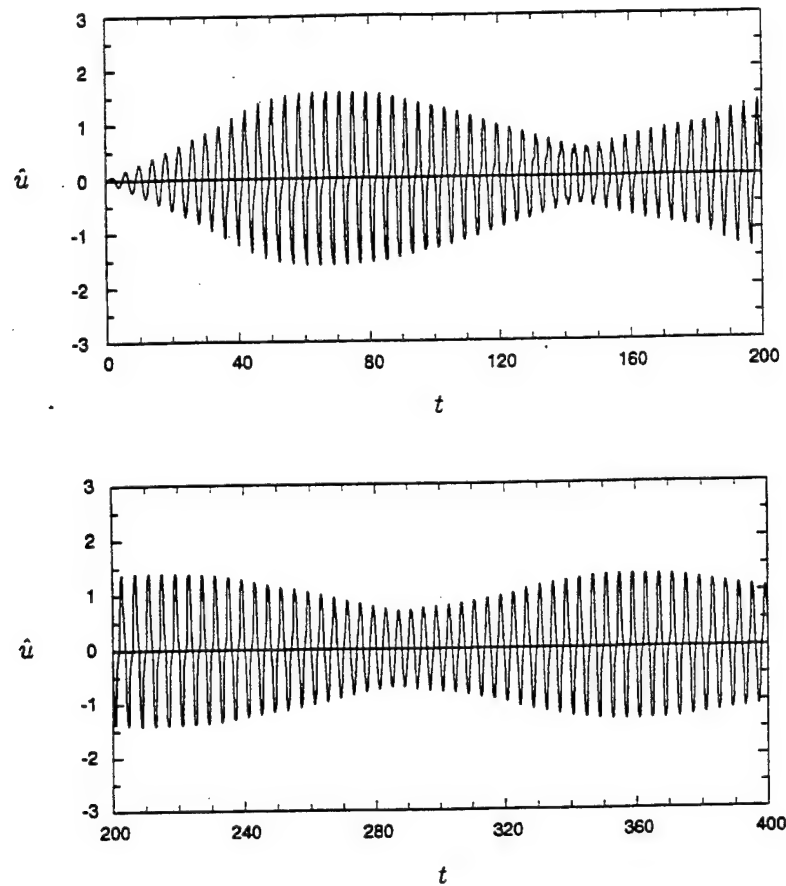


FIG. 6. Long-time evolution of the scaled acoustic velocity  $\hat{u}$  ( $u = \epsilon^{1/3}\hat{u}$ ) at  $x = \frac{1}{2}$  in an open-ended resonant system, under identical operating conditions as in Fig. 4. The results are obtained using the MacCormack finite-difference scheme.

substantially due to nonlinear effects, so that the system resonant frequency deviates from the linear resonant frequency at which the piston operates. When the piston work is mostly negative during a cycle, the net effect is a decrease in the total acoustic energy and hence the wave amplitudes. However, a smaller amplitude oscillation pushes the nonlinear resonant frequency closer to the piston frequency, and wave amplification ensues. This type of negative feedback generates the slow amplitude modulation exhibited in Fig. 6. It is anticipated that the piston-generated net work should be zero after each period once a limit-cycle is reached.

**6. Discussion.** The results presented for closed- and open-ended systems are based on the model in (2)–(4) which includes purely isentropic relationships among the thermodynamic variables. Given the magnitudes of the nonlinear disturbances, this model provides accurate  $p$ - $\rho$  relationships with respect to the perturbation results, at least until the weak shock forms. Subsequently the mathematically weak solutions are capable of predicting the acoustic energy damping caused by entropy generation in the shock (Smoller, 1983; Wang and Kassoy, 1990b). However, one must be aware that entropy accumulation and spatial variation arising from repeated passages of time-varying shocks on timescales  $t \gg O(1)$  may alter the state relations



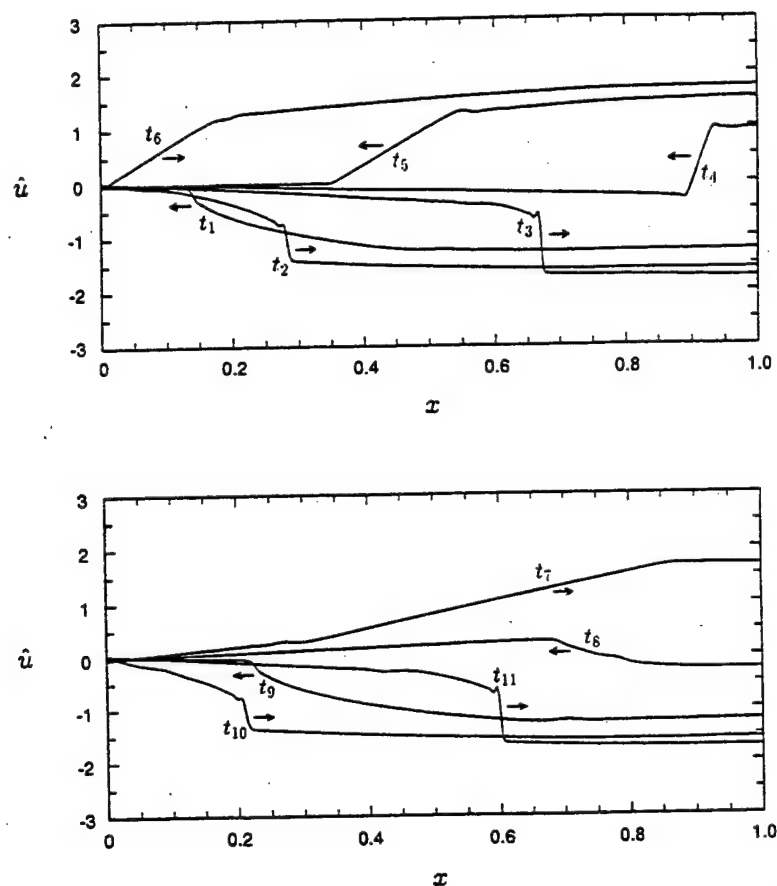


FIG. 7. Spatially distributed velocity profiles at a sequence of times starting from  $t_1 = 60.14$ , with an increment  $\Delta t \approx 0.05$ , in the open-ended resonant system described in the caption for Fig. 4. The solutions are obtained using the MacCormack finite-difference scheme.

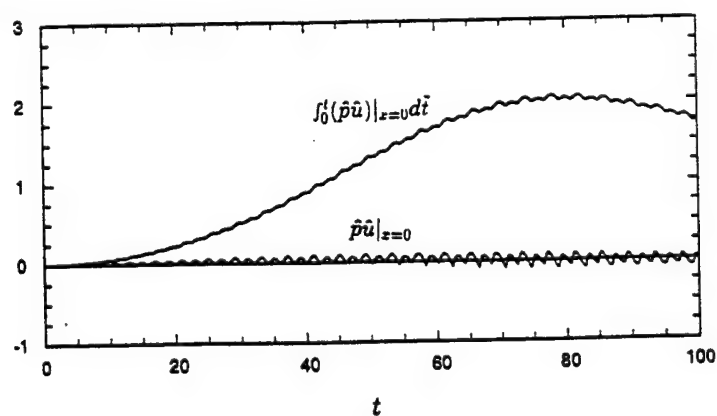


FIG. 8. Instantaneous (lower curve) and cumulative (upper curve) acoustic energy input into the open-ended resonant system by a vibrating piston, obtained from finite-difference solutions under operating conditions identical to those in Fig. 4.

sufficiently to invalidate, at least formally, the use of a single isentropic relationship throughout the entire region. Rather, one may have to account for small entropy changes across the shock and the accumulated effect of these changes by employing distinct isentropic results on either side of the propagating shock. These effects, not addressed definitively either here or in previous work focused on resonant systems, should be considered more fully in the future in order to evaluate the accuracy of the long-time solution presented here.

The mathematical models employed in this study are paradigms for investigating the impact of specific boundary conditions on an idealized physical system. In particular, the isobaric end-condition imposed in the open tube analysis is a crude approximation to what is found in a laboratory experiment, since it precludes acoustic energy loss at the open end. The nonlinear boundary condition proposed by Wijngaarden (1968) and its variants provide a much more realistic alternative, because they contain adjustable parameters modeling certain physical effects (jet-like outflow and sink-like inflow) at the tube exit. Investigations along this line can be found in, for example, Keller (1977), Disselhorst and van Wijngaarden (1980), and the references therein.

It should be recognized that the time-history of shock formation and subsequent gasdynamic evolution in the open-ended tube (cf. Fig. 7) is valid formally only for the pressure-node boundary condition associated with an infinite value of the admittance constant  $\sigma$ . Jimenez (1973) and Seymour and Mortell (1973b) demonstrate that the long-time, quasi-steady waveform varies substantially as the acoustic admittance at the open end changes from infinity to large but finite values. Unfortunately, their analyses do not provide insights into the solution trajectories nor, therefore, into the evolution of wave systems leading to the assumed quasi-steady solutions.

Closed-system eigenfunctions are frequently employed in the study of stability characteristics of rocket engine chambers (Culick, 1990). These systems are characterized by axial outflow through a nozzle as well as by transverse injection of gaseous combustion products at the propellant surface. Hence, the imposition of a closed boundary condition, particularly at the downstream end of the chamber prior to the nozzle, is a significant approximation that has uncertain consequences. The resulting basic amplitude equations contain only quadratic nonlinear effects like those found in the present study of a closed system. In contrast, Margolis's (1993) nonlinear stability study of an open-ended pulse combustor, and that done here for an open resonant system, show that the appropriate basic amplitude equations should contain only cubic nonlinearities. Clearly, the flow dynamics produced for the open-ended system are quite different from those for the fully closed system. This suggests that the accuracy of predictions obtained from the rocket engine stability studies should be tested in order to determine the quantitative and qualitative impact of approximate eigenfunctions on the detailed evolutionary responses of the system.

As a related matter, it is important to recognize that if steep-fronted waves are created or appear spontaneously in an inviscid system, a modal description of their evolution requires a high-order truncation. In this sense results of limit cycle analyses based only on a few lower-order modes preclude the appearance of shocks at any time. If a particular system is likely to develop compression waves, a higher-order truncation of a modal analysis is recommended.

Finally, we conclude this section by commenting on the relative merits of the perturbation and finite-difference methods as applied to the present problem. The MacCormack scheme is used because it captures shock waves in an efficient way. However, it is difficult to ascertain the physical origins of the observed phenomena directly from the numerical output. On the other hand, the multiple-scale perturba-

tion analysis and the individual steps leading to the derivation of the amplitude equations can be interpreted physically to discover the origin of the predicted events. The powerful scaling laws discovered in the perturbation scheme allow us to predict a priori the limiting amplitudes and nonlinear growth times in an order of magnitude sense. The analytical solution forms (35), (36), (52), and (53) give explicit representations of standing waves (or, equivalently, pairs of counterpropagating traveling waves) with slowly modulating amplitudes. The amplitude evolution equations derived (cf. (44), (45), (75), and (76)) reveal the unique characters of closed- and open-system acoustics in terms of quadratic and cubic modal interactions, and demonstrate how acoustic energy is transferred from the forced mode to other modes. Since these mode-coupling equations are independent of the amplitude parameter  $\epsilon$ , once they are truncated and solved numerically, one can obtain complete solutions for any  $\epsilon$  by means of simple Fourier summations. The results demonstrate that the truncated systems can describe the evolving wavefields adequately until shock formation. However, the persistent appearance of shock phenomena undermines the effectiveness of the Fourier series solutions, and in this case the finite-difference method provides a useful remedy. This study exemplifies how analytical and computational approaches can complement one another to generate insightful and reliable solutions.

**7. Summary.** In this paper the evolution of acoustic oscillations driven by a small amplitude vibrating piston is examined theoretically using an initial-boundary-value approach. Single- and multiple-scale perturbation techniques employing Fourier eigenfunction summations, as well as finite-difference calculations, are employed to obtain solutions. The primary objective is to elucidate the effect of the far-end boundary condition on the time-evolution and maximum amplitudes of the forced acoustic disturbances.

When physical conditions at the far-end boundary are characterized by a positive and finite acoustic admittance, an  $O(\epsilon)$  piston Mach number produces gasdynamic disturbances of the same order of magnitude. The lowest-order linear solution describes the exponential decay of acoustic transients, which leads to periodic, quasi-steady oscillations at the frequency of the driving piston.

Linear resonant amplification is possible only when the admittance function approaches zero (closed end) or infinity (isobaric exit). Under resonant conditions the linear perturbation scheme is extended to higher orders to determine the wave nonlinearization time at which nonlinear effects suppress the linear amplitude growth. It is found that in a closed resonant system the wave growth time is of  $O(\epsilon^{-1/2})$  and the limiting amplitude is of  $O(\epsilon^{1/2})$ . In comparison, in an open system, the growth time and limiting amplitude are of  $O(\epsilon^{-2/3})$  and  $O(\epsilon^{1/3})$ , respectively.

Based on the above scales, a weakly nonlinear analysis using multiple-timescale expansions is used to study the nonlinear wave evolution under resonant conditions for  $t \gg O(1)$ . The solutions are expressed in terms of Fourier summations of standing wave modes with slowly modulating amplitude functions. The latter are described by an infinite system of coupled ordinary differential equations. These equations are derived from a second-order perturbation analysis in a closed system and contain quadratic modal interactions. In an open system one must use a third-order analysis to obtain the amplitude evolution equations containing cubic modal interactions. As a result, solution behavior is drastically different for the two cases.

The closed-system solution describes the formation of weak shock waves and their repeated reflections from both boundaries leading to a limit cycle. In contrast, shocks occur only intermittently in an open-ended system, disappearing upon each reflection from the isobaric boundary. It should be noted that the transient solution

described here accommodates shocks in an open-ended resonant system because spontaneous evolution of all waveforms is permitted. No such shocks have been predicted by earlier investigators using a purely periodic solution form to describe the limit cycle.

The perturbation-based results are supported and extended by a computational solution based on the MacCormack finite-difference method. The numerical solutions are remarkably similar to those found from the weakly nonlinear, fully transient analysis.

**Appendix.** The coefficients  $\Lambda_{jkl}^a - \Lambda_{jkl}^f$  appearing in (75) and (76) are defined as follows:

$$\begin{aligned} \Lambda_{jkl}^a = 2j\pi(-1)^j & \left[ I_{k-j,k}^a - I_{k,k-j}^a + \frac{j\pi}{2} (I_{k-j,k}^b + (\gamma-2)H_{k-j,k}^a) + \frac{(-1)^j}{\lambda_k} \right] \\ & - I_{l,j-l+1,k-j,k}^d - (\gamma-2)H_{l,j-l+1,k-j,k}^c \\ (A1) \quad & + 2 \sum_{n=1}^{\infty} \Phi_{n,l,j-l+1} \left[ -\frac{(-1)^{n+j}}{\lambda_k} + I_{n,k-j,k}^c - I_{n,k,k-j}^c \right. \\ & \left. + \frac{j\pi}{\lambda_n} (I_{k-j,n,k}^c + (\gamma-2)H_{k-j,n,k}^b) \right], \end{aligned}$$

$$\begin{aligned} \Lambda_{jkl}^b = 2j\pi(-1)^j & \left[ I_{k+j,k}^a - I_{k,k+j}^a - \frac{j\pi}{2} (I_{k+j,k}^b + (\gamma-2)H_{k+j,k}^a) + \frac{(-1)^j}{\lambda_k} \right] \\ & + I_{l,j-l+1,k+j,k}^d + (\gamma-2)H_{l,j-l+1,k+j,k}^c \\ (A2) \quad & + 2 \sum_{n=1}^{\infty} \Phi_{n,l,j-l+1} \left[ -\frac{(-1)^{n+j}}{\lambda_k} + I_{n,k+j,k}^c - I_{n,k,k+j}^c \right. \\ & \left. - \frac{j\pi}{\lambda_n} (I_{k+j,n,k}^c + (\gamma-2)H_{k+j,n,k}^b) \right], \end{aligned}$$

$$\begin{aligned} \Lambda_{jkl}^c = 2j\pi(-1)^j & \left[ -I_{j-k+1,k}^a - I_{k,j-k+1}^a + \frac{j\pi}{2} (I_{j-k+1,k}^b - (\gamma-2)H_{j-k+1,k}^a) - \frac{(-1)^j}{\lambda_k} \right] \\ & - I_{l,j-l+1,j-k+1,k}^d + (\gamma-2)H_{l,j-l+1,j-k+1,k}^c \\ (A3) \quad & + 2 \sum_{n=1}^{\infty} \Phi_{n,l,j-l+1} \left[ \frac{(-1)^{n+j}}{\lambda_k} - I_{n,j-k+1,k}^c - I_{n,k,j-k+1}^c \right. \\ & \left. + \frac{j\pi}{\lambda_n} (I_{j-k+1,n,k}^c - (\gamma-2)H_{j-k+1,n,k}^b) \right], \end{aligned}$$

$$\Lambda_{jkl}^d = 2j\pi(-1)^j \left[ -I_{k-j,k}^a + I_{k,k-j}^a - \frac{j\pi}{2} (I_{k-j,k}^b + (\gamma-2)H_{k-j,k}^a) - \frac{(-1)^j}{\lambda_k} \right]$$

$$(A4) \quad -I_{l,l+j,k-j,k}^{e} - (\gamma - 2)H_{l,l+j,k-j,k}^d + 2 \sum_{n=1}^{\infty} \Psi_{n,l,l+j} \left[ \frac{(-1)^{n+j}}{\lambda_k} - I_{n,k-j,k}^c + I_{n,k,k-j}^c - \frac{j\pi}{\lambda_n} (I_{k-j,n,k}^c + (\gamma - 2)H_{k-j,n,k}^b) \right],$$

$$(A5) \quad \Lambda_{jkl}^e = 2j\pi(-1)^j \left[ -I_{k+j,k}^a + I_{k,k+j}^a + \frac{j\pi}{2} (I_{k+j,k}^b + (\gamma - 2)H_{k+j,k}^a) - \frac{(-1)^j}{\lambda_k} \right] + I_{l,l+j,k+j,k}^e + (\gamma - 2)H_{l,l+j,k+j,k}^d + 2 \sum_{n=1}^{\infty} \Psi_{n,l,l+j} \left[ \frac{(-1)^{n+j}}{\lambda_k} - I_{n,k+j,k}^c + I_{n,k,k+j}^c + \frac{j\pi}{\lambda_n} (I_{k+j,n,k}^c + (\gamma - 2)H_{k+j,n,k}^b) \right],$$

$$(A6) \quad \Lambda_{jkl}^f = 2j\pi(-1)^j \left[ I_{j-k+1,k}^a + I_{k,j-k+1}^a - \frac{j\pi}{2} (I_{j-k+1,k}^b - (\gamma - 2)H_{j-k+1,k}^a) + \frac{(-1)^j}{\lambda_k} \right] - I_{l,l+j,j-k+1,k}^e + (\gamma - 2)H_{l,l+j,j-k+1,k}^d + 2 \sum_{n=1}^{\infty} \Psi_{n,l,l+j} \left[ -\frac{(-1)^{n+j}}{\lambda_k} + I_{n,j-k+1,k}^c + I_{n,k,j-k+1}^c - \frac{j\pi}{\lambda_n} (I_{j-k+1,n,k}^c - (\gamma - 2)H_{j-k+1,n,k}^b) \right],$$

where

$$(A7) \quad \Phi_{lmn} = \frac{(-1)^{l+m+n} \lambda_l^2 (\lambda_m + \lambda_n)}{(\lambda_m + \lambda_n)^2 - \lambda_l^2} \left[ \frac{3 - \gamma}{(\lambda_m - \lambda_n)^2 - \lambda_l^2} + \frac{\gamma + 1}{(\lambda_m + \lambda_n)^2 - \lambda_l^2} + \frac{4\lambda_l^2 - 2(\lambda_m + \lambda_n)^2}{\lambda_l^4} \right],$$

$$(A8) \quad \Psi_{lmn} = \frac{(-1)^{l+m+n} \lambda_l^2 (\lambda_m - \lambda_n)}{(\lambda_m - \lambda_n)^2 - \lambda_l^2} \left[ \frac{3 - \gamma}{(\lambda_m + \lambda_n)^2 - \lambda_l^2} + \frac{\gamma + 1}{(\lambda_m - \lambda_n)^2 - \lambda_l^2} + \frac{4\lambda_l^2 - 2(\lambda_m - \lambda_n)^2}{\lambda_l^4} \right],$$

(A9)

$$I_{mn}^a = \int_0^1 x \cos(\lambda_m x) \sin(\lambda_n x) dx,$$

(A10)

$$I_{mn}^b = \int_0^1 (1-x^2) \sin(\lambda_m x) \sin(\lambda_n x) dx,$$

(A11)

$$I_{lmn}^c = \int_0^1 \sin(\lambda_l x) \cos(\lambda_m x) \sin(\lambda_n x) dx,$$

(A12)

$$I_{klmn}^d = \int_0^1 \left\{ (3-\gamma) \cos[(\lambda_k - \lambda_l)x] - (\gamma-1) \cos[(\lambda_k + \lambda_l)x] - 2(-1)^{k+l} \right\} \\ \times \sin(\lambda_m x) \sin(\lambda_n x) dx,$$

(A13)

$$I_{klmn}^e = \int_0^1 \left\{ -(3-\gamma) \cos[(\lambda_k + \lambda_l)x] + (\gamma-1) \cos[(\lambda_k - \lambda_l)x] - 2(-1)^{k+l} \right\} \\ \times \sin(\lambda_m x) \sin(\lambda_n x) dx,$$

(A14)

$$H_{mn}^a = \int_0^1 (1-x^2) \cos(\lambda_m x) \cos(\lambda_n x) dx,$$

(A15)

$$H_{lmn}^b = \int_0^1 \cos(\lambda_l x) \cos(\lambda_m x) \cos(\lambda_n x) dx,$$

(A16)

$$H_{klmn}^c = 2 \int_0^1 \left\{ \frac{(3-\gamma)}{3} \cos[(\lambda_k - \lambda_l)x] - \frac{\gamma}{3} \cos[(\lambda_k + \lambda_l)x] - (-1)^{k+l} \right\} \\ \times \cos(\lambda_m x) \cos(\lambda_n x) dx,$$

(A17)

$$H_{klmn}^d = 2 \int_0^1 \left\{ -\frac{(3-\gamma)}{3} \cos[(\lambda_k + \lambda_l)x] + \frac{\gamma}{3} \cos[(\lambda_k - \lambda_l)x] - (-1)^{k+l} \right\} \\ \times \cos(\lambda_m x) \cos(\lambda_n x) dx.$$

The above equations are in a relatively primitive form that fostered algebraic accuracy in the course of a laborious derivation. Undoubtedly, more compact formulas could be derived. To find numerical solutions of (75) and (76), explicit expressions for the integrals in (A9)–(A17) have been obtained, which are used in combination with (A1)–(A8) to compute the coefficients.

**Acknowledgment.** We are grateful to Professor N. Rott of Stanford University for his shared interest in the subject, and for providing references unknown to us previously.

#### REFERENCES

- D. A. ANDERSON, J. C. TANNEHILL, AND R. H. PLETCHER (1984), *Computational Fluid Mechanics and Heat Transfer*, McGraw-Hill, New York.
- R. BETCHOV (1958), *Nonlinear oscillations of a column of gas*, Phys. Fluids, 1, pp. 205–212.

- D. L. BOOK, J. P. BORIS, AND K. HAIN (1975), *Flux-corrected transport II: Generalizations of the method*, J. Comp. Phys., 18, pp. 248-283.
- W. CHESTER (1964), *Resonant oscillations in closed tubes*, J. Fluid Mech., 18, pp. 44-64.
- F. E. C. CULICK (1976a), *Nonlinear behavior of acoustic waves in combustion chambers I*, Acta Astronautica, 3, pp. 715-734.
- (1976b), *Nonlinear behavior of acoustic waves in combustion chambers II*, Acta Astronautica, 3, pp. 735-757.
- (1990), *Some recent results for nonlinear acoustics in combustion chambers*, AIAA 13th Aeroacoustic Conference, AIAA Paper 90-3927.
- J. H. M. DISSELHORST AND L. VAN WUNGAARDEN (1980), *Flow in the exit of open pipes during acoustic resonance*, J. Fluid Mech., 99, pp. 293-319.
- J. E. ENINGER AND W. G. VINCENTI (1973), *Nonlinear resonant wave motion of a radiating gas*, J. Fluid Mech., 60, pp. 161-186.
- J. JIMENEZ (1973), *Nonlinear gas oscillations in pipes; Part 1. Theory*, J. Fluid Mech., 59, pp. 23-46.
- J. KELLER (1976), *Resonant oscillations in closed tubes: The solution of Chester's equation*, J. Fluid Mech., 77, pp. 279-304.
- (1977), *Resonant oscillations in open tubes*, J. Appl. Math. Phys. (ZAMP), 28, pp. 237-263.
- L. D. LANDAU AND E. M. LIFSHITZ (1959), *Fluid Mechanics*, Pergamon Press, Elmsford, NY.
- E. LETTAU (1939), *Messungen an Schwingungen von Gassäulen mit steilen Fronten in Rohrleitungen*, Deutsche Kraftfahrtforschung, 39, pp. 1-10.
- M. E. LORES AND B. T. ZINN (1973), *Nonlinear longitudinal combustion instability in rocket motors*, Combust. Sci. Tech., 7, pp. 245-256.
- S. B. MARGOLIS (1993), *Nonlinear stability of combustion-driven acoustic oscillations in resonance tubes*, J. Fluid Mech., 253, pp. 67-104.
- P. MERKLI AND H. THOMANN (1975), *Thermoacoustic effects in a resonance tube*, J. Fluid Mech., 70, pp. 161-177.
- M. OCHMANN (1985), *Nonlinear resonant oscillations in closed tubes—An application of the averaging method*, J. Acoust. Soc. Amer., 77, pp. 61-66.
- R. A. SAENDER AND G. E. HUDSON (1960), *Periodic shock waves in resonating gas columns*, J. Acoust. Soc. Amer., 32, pp. 961-970.
- B. R. SEYMOUR AND M. P. MORTELL (1973a), *Resonant acoustic oscillations with damping: Small rate theory*, J. Fluid Mech., 58, pp. 353-373.
- (1973b), *Nonlinear resonant oscillations in open tubes*, J. Fluid Mech., 60, pp. 733-749.
- J. SMOLLER (1983), *Shock Waves and Reaction-Diffusion Equations*, Springer-Verlag, Berlin.
- E. STUHLTRÄGER AND H. THOMANN (1986), *Oscillations of a gas in an open-ended tube near resonance*, J. Appl. Math. Phys. (ZAMP), 37, pp. 155-175.
- M. WANG AND D. R. KASSOY (1990a), *Dynamic compression and weak shock formation in an inert gas due to fast piston acceleration*, J. Fluid Mech., 220, pp. 267-292.
- (1990b), *Evolution of weakly nonlinear waves in a cylinder with a movable piston*, J. Fluid Mech., 221, pp. 27-52.
- (1992), *Transient acoustic processes in a low Mach number shear flow*, J. Fluid Mech., 238, pp. 509-536.
- G. B. WHITHAM (1974), *Linear and Nonlinear Waves*, John Wiley, New York.
- L. VAN WUNGAARDEN (1968), *On the oscillations near and at resonance in open pipes*, J. Engrg. Math., II, pp. 225-240.
- F. A. WILLIAMS (1985), *Combustion Theory*, 2nd ed., Benjamin/Cummings, New York.
- R. G. ZARIPOV AND M. A. ILHAMOV (1976), *Nonlinear gas oscillations in a pipe*, J. Sound Vibrations, 46, pp. 245-257.

# **Unsteady Vorticity Generation and Evolution in a Model of a Solid Rocket Motor**

**K. Kirkkopru, D. R. Kassoy, Q. Zhao**

Reprinted from

## **Journal of Propulsion and Power**

Volume 12, Number 4, Pages 646-654



*A publication of the*  
American Institute of Aeronautics and Astronautics, Inc.  
1801 Alexander Bell Drive, Suite 500  
Reston, VA 22091



# Unsteady Vorticity Generation and Evolution in a Model of a Solid Rocket Motor

Kadir Kirkkopru,\* David R. Kassoy,† and Qing Zhao‡  
University of Colorado, Boulder, Colorado 80309

The cylindrical, axisymmetric Navier–Stokes equations are solved numerically to study the generation and evolution of vorticity in an injection-induced transient shear flow. An initially steady internal flowfield driven by constant sidewall injection is disturbed by positive transient sidewall injection, which simulates the unsteady mass input from propellant burning variations. The disturbance amplitude is as large as that of the steady sidewall injection to ensure that nonlinear effects influence the vorticity field evolution. Initial value solutions show that relatively intense vorticity is generated at the sidewall and eventually fills the cylinder with a rotational flow. Although the pressure response is essentially that found in acoustic stability theory, the axial and radial velocity components contain large local radial velocity gradients that cannot be predicted from acoustic theory alone.

## I. Introduction

SOLID propellant combustion in a rocket motor generates gaseous products that induce a low axial Mach number [ $M = \mathcal{O}(10^{-2} - 10^{-1})$ ], large flow Reynolds number [ $Re = \mathcal{O}(10^4 - 10^6)$ ] internal shear flow in a cylindrical chamber where the aspect ratio is  $\delta \gg 1$ . Inert flows with these characteristics can be generated by injecting gas through the porous sidewall of a cylinder. Flow transients are then induced by specified time-dependent boundary conditions applied on some surface or on the exit plane. The complete time-dependent shear flow is now known to include vorticity distributions,<sup>1–8</sup> as well as the more familiar acoustic disturbances studied by many investigators in the past.<sup>9–12</sup>

Brown et al.<sup>1,2</sup> and Brown and Shaeffer<sup>3</sup> conducted laboratory experiments in a cold flow rocket motor chamber analogue. Velocity measurements taken along and across the cylindrical chamber show that there is a significant unsteady rotational flow component present everywhere. This type of vorticity is seen also in the study by Vuillot and Avalon<sup>4</sup> who used computational methods to solve the compressible Navier–Stokes equations in a channel with constant sidewall mass injection. Both results demonstrate that for sufficiently large wall injection rates unsteady vorticity need not be confined to thin viscous acoustic boundary layers adjacent to the injecting wall, like those observed in the numerical studies of Baum and Levine<sup>13</sup> and Baum<sup>14</sup> and in the acoustic boundary-layer analysis of Flandro.<sup>5</sup>

Flandro and Roach<sup>15</sup> and Smith et al.<sup>16</sup> describe numerical simulations of the Brown et al.<sup>1,2</sup> experiments. Significant radial gradients in the axial velocity are seen about halfway out toward the centerline. They capture the qualitative features of the spatial vorticity distributions observed by Brown et al.<sup>1,2</sup>

Flandro and Roach<sup>15</sup> describe an initial attempt at developing an analytically based model of the Brown and co-worker experiments. A more complete version is given in Flandro,<sup>17</sup>

where a theory is developed for coexisting transient vorticity and acoustic waves throughout a cylindrical chamber. The steady, inviscid rotational Culick<sup>18</sup> solution, associated with a uniform injection Mach number  $M_i \ll 1$ , is disturbed by a smaller  $\mathcal{O}(\epsilon)$  acoustic velocity that varies harmonically in time. Perturbation methods are used to derive inviscid, linear, small disturbance equations for the rotational part of the axial velocity. The momentum equation itself can be used to show that the amplitude of the vorticity generated at the injection surface is  $\mathcal{O}(\epsilon/M_i^2)$  relative to the vorticity associated with the steady Culick<sup>18</sup> profiles. Hence, for sufficiently large values of  $\epsilon$ , the transient vorticity can be more intense than that of the steady Culick velocity components. Calculated axial velocity variation with radius is qualitatively similar to the spatial oscillations observed experimentally by Brown et al.<sup>1,2</sup>

Tseng and Yang<sup>19</sup> and Tseng et al.<sup>7</sup> provide a computational model for a premixed laminar flame adjacent to a cylindrical porous surface through which a combustible mixture is injected. The flame is a surrogate for solid propellant combustion in a rocket chamber. Prescribed boundary disturbances are the sources of transients in the flowfield. In this reactive model of a chamber, flow vorticity appears in the vicinity of the wall and the adjacent flame.

Roh and Yang<sup>20</sup> have done a similar computation for combustion processes associated with double-base solid propellants. Longer run times and better spatial resolution lead to the appearance of vorticity through 75% of the half-height of the rectangular chamber.

Zhao et al.<sup>21</sup> as well as Zhao and Kassoy<sup>8</sup> use a systematic asymptotic analysis to formulate an initial boundary value description of vorticity production in a low Mach number ( $M \ll 1$ ), weakly viscous internal flow ( $Re \gg 1$ ), sustained by mass addition through the sidewall of a long, narrow cylinder ( $\delta \gg 1$ ). A hard blowing condition (characteristic injection speed is much larger than the characteristic axial speed divided by  $Re^{1/2}$  (Ref. 22)) is used. An  $\mathcal{O}(M)$  axial acoustical disturbance, generated by a prescribed harmonically time-dependent closed endwall velocity, interacts with the basically inviscid rotational steady flow to produce unsteady vorticity at the injecting sidewall. Baroclinicity and volume dilatation are higher-order sources of unsteady vorticity production in this nearly isothermal flow. The complete axial velocity is found from a superposition of three components of equal magnitude. First, the steady component is described by a weakly rotational, steady solution to inviscid Euler equations known by Culick.<sup>18</sup> Secondly, there is a planar irrotational acoustic field,

Received Dec. 27, 1994; revision received Feb. 19, 1995; accepted for publication Feb. 20, 1996. Copyright © 1996 by the American Institute of Aeronautics and Astronautics, Inc. All rights reserved.

\*Research Associate, Program in Applied Math; currently at Department of Mechanical Engineering, Istanbul Technical University, Istanbul, Turkey.

†Professor, Department of Mechanical Engineering. Member AIAA.

‡Graduate Student, Department of Mechanical Engineering; currently at Applicon, Inc., Boulder, CO 80301.

derived from a traditional linear wave equation that satisfies boundary conditions at the closed and open ends of the cylinder. Finally, when  $Re = O(\delta^2/M^2)$ , the strongly rotational, weakly viscous, nonlinear component varies simultaneously on the length scale of the tube radius  $O(1)$  and on an  $O(M)$  smaller scale similar to those described in the study by Flandro and Roach.<sup>15</sup> Mathematical formulas are used to prove that the vorticity is generated at the wall by an interaction between the injected fluid and the time-dependent axial pressure gradient. It is then diffused on the short  $O(M)$  radial length scale and convected subsequently toward the axis by the radial component of the injection-induced flowfield. Initially, the intense wall-generated vorticity is separated from the weakly rotational flow of the Culick<sup>18</sup> solution by a sharply defined front that convects in the radial direction at the local radial speed. Eventually, the wall-generated rotational flow fills the entire cylinder.

Computational methods are used by Kirkkopru et al.<sup>6</sup> to provide qualitative supporting evidence for the solutions described in Zhao et al.<sup>21</sup> In this case the driving disturbance is a harmonic pressure transient applied on the exit plane of the cylinder, like that used by Vuillot and Avalon.<sup>4</sup> Grid size and spatial distributions are chosen to accommodate the small length scale velocity variations throughout the cylinder known from the study by Zhao et al.<sup>21</sup> In analogy with the analytical effort, the unsteady rotational component of the axial velocity is extracted from the numerically generated total value. The initial-boundary value solution properties and characteristics are similar to those found from the asymptotic analysis in Ref. 21.

The objective of the present work is to compute unsteady vorticity production and evolution in a finite cylinder with spatially distributed, transient injection from the sidewall. The latter mimics unsteady burning of a solid propellant surface. The two-four method<sup>23</sup> is used to obtain solutions to the unsteady, compressible Navier-Stokes equations in a cylindrical axisymmetric geometry. Parametric values for  $Re$ ,  $M$ , and  $\delta$  are chosen to ensure that the hard blowing condition of Cole and Aroesty<sup>22</sup> ( $\delta^2/Re \ll 1$ ) is met and that the analytically derived weakly viscous condition  $Re = O(\delta^2/M^2)$  is satisfied. Grid points are distributed in the radial direction to resolve  $O(M)$  length scale velocity variations throughout the cylinder as predicted by the asymptotic study.<sup>21</sup> The unsteady rotational component of the axial velocity  $u_v$ , extracted from the numerical solutions, is used to describe the generation and evolution of the nonlinear unsteady vorticity field in the cylinder. The present computational results show that unsteady vorticity is generated at the injecting sidewall by an interaction between the injected fluid and the axial pressure gradient arising from a planar acoustic wave field induced by the sidewall injection transients. In the present case, the vorticity is convected away from the wall into the chamber by the spatially distributed unsteady injected flowfield. In previous studies by Zhao et al.<sup>21</sup> and Kirkkopru et al.,<sup>6</sup> where the sidewall injection velocity is spatially uniform and constant, the unsteady vorticity is convected by the simpler steady radial velocity field. For sufficiently short times, a well defined front separates the relatively low vorticity chamber core flow from a region of more intense unsteady vorticity generated initially at the wall. The radial location of the vorticity front varies with axial location because the transient sidewall injection distribution is axially dependent.

Fully resolved, time-dependent results enable one to understand the source and evolution of unsteady vorticity in the system, its ultimate distribution, and the length scales on which it is important. These insights are difficult to extract from the cited previous work because 1) the radial spatial variations in the numerical solutions are not adequately resolved, and 2) the numerical results are frequently presented in time-averaged form, so that the information about the transient evolution of the field variables is lost.

## II. Computational Model

The flowfield is described by the cylindrical, axisymmetric, laminar, compressible Navier-Stokes equations, for a perfect gas, written in nondimensional conservative form:

$$\frac{\partial q}{\partial t} + \frac{\partial e}{\partial x} + \frac{\partial f}{\partial r} + \frac{h}{r} = 0 \quad (1)$$

where

$$q = \begin{bmatrix} \rho \\ E_T \\ \rho u \\ \rho v \end{bmatrix} \quad e = \begin{bmatrix} M\rho u \\ M[E_T + (\gamma - 1)p]u \\ M\rho u^2 + \frac{1}{\gamma M} p \\ M\rho uv \end{bmatrix}$$

$$f = \begin{bmatrix} M\rho v \\ M[E_T + (\gamma - 1)p]v - \frac{\gamma M \delta^2}{RePr} T_r \\ M\rho uv - \frac{M \delta^2}{Re} u_r \\ M\rho v^2 + \frac{\delta^2}{\gamma M} p \end{bmatrix} \quad (2)$$

$$h = \begin{bmatrix} M\rho v \\ M[E_T + (\gamma - 1)p]v - \frac{\gamma M \delta^2}{RePr} T_r \\ M\rho uv - \frac{M \delta^2}{Re} u_r \\ M\rho v^2 \end{bmatrix}$$

$$E_T = \rho C_v T + \gamma(\gamma - 1)M^2 \frac{[u^2 + (v/\delta)^2]}{2} \quad (3)$$

is the total fluid energy.

The equation of state for a perfect gas is

$$p = \rho T \quad (4)$$

Nondimensional variables, defined in terms of dimensional quantities denoted by a prime, are given by

$$\begin{aligned} x &= x'/L' & r &= r'/R' & u &= u'/U_R' \\ v &= v'/V_R' & \rho &= \rho'/\rho_0' & p &= p'/p_0' \\ T &= T'/T_0' & t &= t'/t_a' & C_v &= C_v'/C_{v,0}' \end{aligned} \quad (5)$$

Characteristic length scales for the axial and radial directions are chosen to be the length of the tube  $L'$  and the radius of the tube  $R'$ , respectively. The known characteristic sidewall injection speed of the fluid  $V_R'$  is related to the characteristic axial speed  $U_R'$  through the global mass conservation relationship  $U_R' = \delta V_R'$ , where  $\delta = L'/R'$  is the aspect ratio of the tube. Pressure is nondimensionalized with respect to the static pressure compatible with the injected fluid density and temperature,  $\rho_0'$  and  $T_0'$ , respectively. Time is nondimensionalized with respect to the tube axial acoustic time  $t_a' = L'/a_0'$ , where  $a_0' = (\gamma p_0'/\rho_0')^{1/2}$  is the characteristic speed of sound. Here, the ratio of specific heats  $\gamma = 1.4$  is used in the present computations. The viscosity, specific heats, and conductivity are treated as constants in these calculations, because temperature variations are very small.

The following expressions define the flow Reynolds number, the Prandtl number, and the characteristic axial flow Mach number, respectively:

$$Re = \frac{\rho'_0 U'_R L'}{\mu'_0} \quad Pr = \frac{\mu'_0 C'_{p0}}{k'_0} \quad M = \frac{U'_R}{a'_0} \quad (6)$$

Note that the acoustic Reynolds number  $Re_A = Re/M$ , and the injection Mach number  $M_i = M/\delta$ . In a typical solid rocket motor chamber  $Re = \mathcal{O}(10^4 - 10^6)$ ,  $Pr = \mathcal{O}(1)$ ,  $M = \mathcal{O}(10^{-2} - 10^{-1})$ , and  $\delta = \mathcal{O}(10)$ .

The Navier-Stokes equations are simplified by ignoring the axial transport terms. Justification for the reduction is based on the asymptotic analysis in Zhao and Kassoy<sup>8</sup> and Zhao et al.<sup>21</sup> valid for  $M \ll 1$ ,  $\delta \gg 1$ , and  $Re \gg 1$  provided that the hard blowing condition  $\delta^2/Re \ll 1$  is satisfied. As a result, the computation time is reduced significantly without sacrificing flow physics. Furthermore, the dissipative effects of the remaining transport terms are sufficient to avoid artificial damping terms needed in other similar computations.<sup>15,16,24</sup>

The Navier-Stokes equations are solved by using the two-four explicit, predictor-corrector scheme,<sup>23</sup> which is a fourth-order variant of the fully explicit MacCormack scheme. This method is highly phase-accurate and is therefore very suitable for wave propagation and wave interaction problems. The number of conditions specified on a boundary are equal to the number of characteristics pointing into the computational domain.<sup>7</sup> The remaining numerically required conditions are extrapolated from the computational domain to the boundary.

The size and the number of uniformly spaced grids are chosen to accommodate properly the local variations of flow variables in the axial and radial directions as suggested in the asymptotic analysis by Zhao et al.<sup>21</sup>

A steady-state flow solution is required as an initial condition for the transient flow computation. Boundary conditions include an impermeable head end at  $x = 0$  ( $u = 0$ ), an assumed pressure node at the exit plane  $x = 1$  ( $p = 1$ ), a specified injection velocity ( $v = -1$ ), temperature ( $T = 1$ ), and a no-slip condition for the axial flow speed ( $u = 0$ ) on the sidewall at  $r = 1$  as well as symmetry conditions on the centerline,  $r = 0$ .

The analytically calculated velocity profiles for incompressible, rotational, inviscid flow in a long, narrow cylindrical tube (Culick<sup>18</sup>) are used as starting profiles for the steady, compressible, viscous flow computations. This approach reduces the computation time required to reach the final converged steady flow configuration relative to doing a complete transient solution by initiating wall injection at  $t = 0$ . In this calculation the solution converges to a steady state defined by the condition that the total injected mass is equal to the total exiting mass. Then the solution is run for as much as  $\mathcal{O}(10)$  additional axial acoustic times to ensure that the steady-state solution is stable. Results given in Fig. 1 show the steady normalized axial,  $u_s(x, r)/u_s(x, r=0)$ , and radial velocity  $v_s(x, r)$  profiles at different axial locations,  $x = 0.025, 0.5$ , and  $1.0$ , when  $M = 0.06$ ,  $\delta = 20$ , and  $Re = 10^5$ , respectively. In these graphs, Culick<sup>18</sup> incompressible flow profiles that are invariant to axial location are nearly indistinguishable from the computed profiles. Small differences arise from the small but finite axial flow Mach number used in the computation. Low Mach number compressible flow theory implies  $\mathcal{O}(M^2)$  differences between the Culick<sup>18</sup> solution for  $\delta \gg 1$  and the computational result.

A steady-state flow solution for each Mach number and Reynolds number is obtained initially to prevent introducing unwanted noise into the unsteady computations.

Zhao et al.<sup>21</sup> have used formal asymptotic methods to show that the chamber flow is weakly viscous when the condition  $Re = \mathcal{O}(\delta^2/M^2)$  is satisfied and when strong injection ( $\delta^2/Re \ll 1$ ) prevails. The latter condition implies that  $V'_R \gg U'_R/Re^{1/2}$  (Ref. 22). The asymptotic theory shows that the primary viscous stresses are in the radial direction. Hence, it is useful to

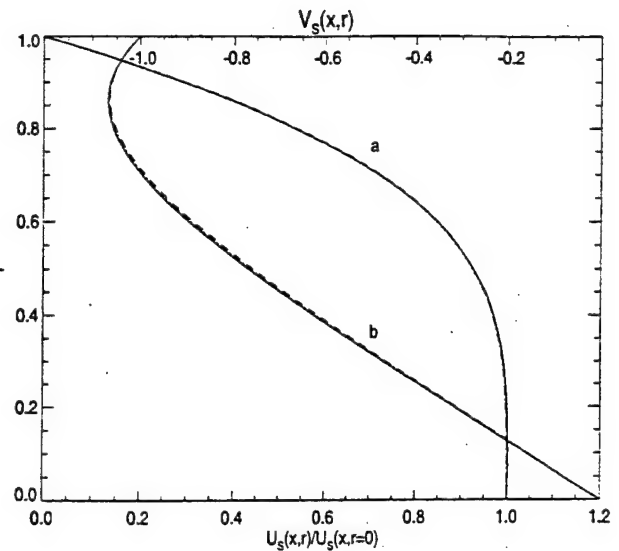


Fig. 1 a) Normalized steady axial velocity and b) steady radial velocity profiles at  $x = 0.025$  (solid line),  $0.5$  (dotted line), and  $1$  (dashed line) for  $M = 0.06$ ,  $Re = 10^5$ , and  $\delta = 20$ .

ignore the axial transport effects and retain only the radial transport terms in the reduced Navier-Stokes equations. The steady flow solution is obtained faster and, at the same time, the largest important viscous effects in radial direction are responsible for physically meaningful damping, similar to the artificial damping terms that have been introduced in some earlier studies.<sup>15,16,24</sup>

Once a converged steady flow configuration for specified values of  $\delta$ ,  $M$ , and  $Re$  is obtained, the flow is disturbed by adding an axially distributed unsteady sidewall injection component to the steady value. The total wall injection velocity is then given by

$$v(x, r = 1, t) = -[1 + A \cos(n\pi x/2)(1 - \cos \omega t)] \quad (7)$$

which can also be written in terms of a positive mean component  $1 + A \cos(n\pi x/2)$  and a fluctuating component proportional to  $\cos \omega t$ . Here  $\omega$  is the dimensionless angular frequency,  $A = \mathcal{O}(1)$  is the amplitude of the unsteady wall injection, and  $n$  is the spatial dependence parameter. The total mass flow from the wall is always positive. The other boundary conditions are the same as those for the steady flow computations.

Unsteady computations are carried out for several different axial Mach numbers and spatial dependence parameters. In this study the boundary driving frequency is  $\omega = 1$ . This is a relatively low frequency in the sense that the period  $t = 2\pi$  is larger than the time required for an acoustic wave to do a complete circuit of the chamber,  $t = 2$ .

### III. Results and Discussion

The numerical code has been run approximately 10 cycles after the injection transient is turned on to check if spurious numerical oscillations develop. For example, Fig. 2 shows the time variation of the centerline axial velocity at the midchamber ( $x = 0.5$ ) for flow parameters  $M = 0.1$ ,  $\delta = 20$ ,  $Re = 10^5$ ,  $A = 0.4$ ,  $n = 1$ , and  $\omega = 1$ . Note that the value at  $t = 0$  corresponds to the steady-state value of the centerline velocity at the midchamber. The solution appears to be quasisteady almost immediately. This solution property can be attributed to the transient pressure field seen in Fig. 3. The result given at  $x = 0.5$  shows that pressure solution is almost purely planar ( $x$  dependent only). For example, at  $x = 0.5$  and  $t = 60$  for three radial locations,  $r = 0, 0.5$ , and  $1$ ,  $p = 1.1480096, 1.1479678$ , and  $1.1479073$ , respectively. The invariance to radial loca-

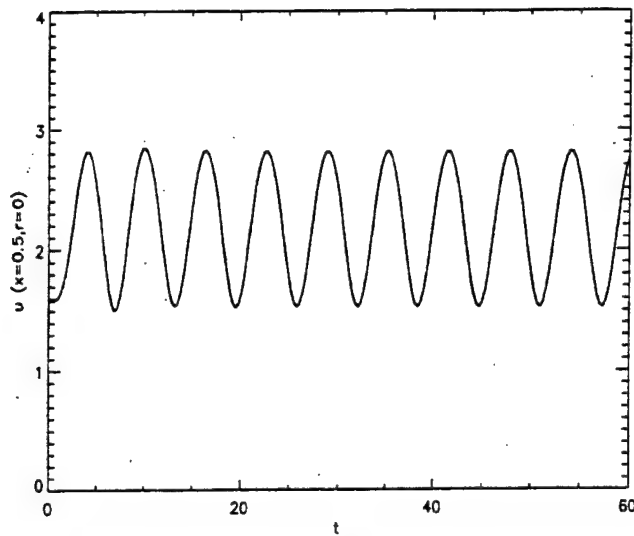


Fig. 2 Time history of the centerline axial velocity at  $x = 0.5$  for  $M = 0.1$ ,  $\delta = 20$ ,  $Re = 10^5$ ,  $\omega = 1$ ,  $A = 0.4$ , and  $n = 1$ .

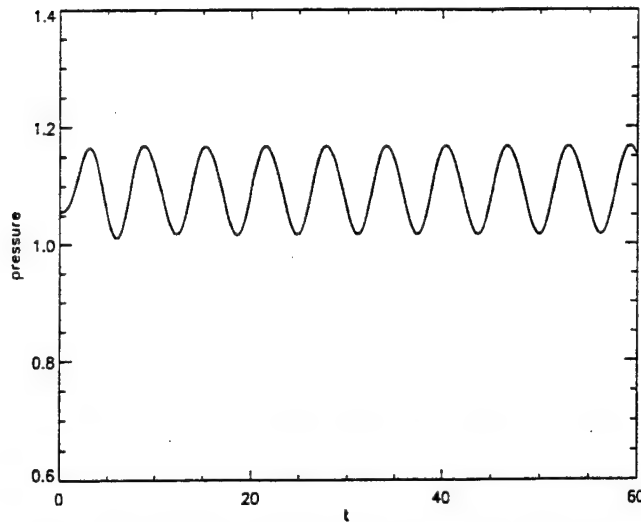


Fig. 3 Time history of pressure at  $x = 0.5$  for  $M = 0.1$ ,  $\delta = 20$ ,  $Re = 10^5$ ,  $\omega = 1$ ,  $A = 0.4$ , and  $n = 1$ .

tion results from the use of a large aspect ratio  $\delta = 20$ . Also note that the pressure deviation from the base value,  $\mathcal{O}(10^{-1})$ , is fully compatible with the asymptotic prediction in Zhao et al.<sup>25</sup>

The purely harmonic behavior in Fig. 3, seen in all similar computational results,<sup>4,7,19</sup> is cause for concern because the analytical analogue to this study<sup>25</sup> shows that a single eigenfunction of substantial amplitude should accompany the forced response. The eigenfunction arises from a solution to a linear, acoustic equation driven by transient effects on the sidewall boundary. In contrast, the numerical solution arises from a slightly viscous, weakly nonlinear mathematical system. It appears that there are at least two possible sources for the difference:

- 1) The finite difference form of the nonlinear, slightly viscous equations will not produce an eigenvalue-like response.
- 2) The numerical boundary conditions at the exit plane do not account for wave reflections in an appropriate way.

These issues are the subject of the ongoing studies. Note that acoustic wave planar viscous damping occurs on a time scale  $t \gg \mathcal{O}(10^2)$  (Ref. 26) for the Reynolds numbers consid-

ered here. Hence, on the time scale  $t = \mathcal{O}(10^2)$  planar damping cannot annihilate an eigenfunction response.

Following a procedure described by Lagerstrom,<sup>27</sup> and similar to that employed by Flandro and Roach,<sup>15</sup> Zhao and Kassoy,<sup>8</sup> and Zhao et al.,<sup>21</sup> the total unsteady axial flow speed may be divided into three parts

$$u(x, r, t) = u_s(x, r) + u_p(x, t) + u_v(x, r, t) \quad (8)$$

where  $u_s$  denotes the steady flowfield that is known as an initial condition for the unsteady computations. The second term  $u_p$  is the weakly viscous, slightly nonlinear analogue to the irrotational planar part of the flowfield found by Zhao et al.<sup>21</sup> and Zhao.<sup>25</sup> It is found from the difference between the unsteady axial speed and the steady axial speed on the centerline of the tube. The remaining term  $u_v$ , defined as the rotational (non-planar) part of the unsteady axial flow speed, is found from Eq. (8) after  $u_s$  and  $u_p$  are calculated. Once again, it is an analogue to the analytically obtained rotational velocity field described by Zhao et al.<sup>21</sup> and Zhao<sup>25</sup> and is used to describe the generation and evolution of the nonlinear unsteady vorticity field in the cylinder. Following the asymptotic analysis described by Zhao et al.<sup>21</sup> and Zhao<sup>25</sup> one can show that the rotational part of  $u_v$  vanishes at the centerline for all times.

Figure 4 shows the radial variation of the instantaneous unsteady axial rotational flow speed  $u_v$  at midchamber ( $x = 0.5$ ) for three time values after the injection transient is initiated at the sidewall. The flow parameters are  $M = 0.1$ ,  $\delta = 20$ , and  $Re = 10^5$ . The corresponding injection Mach number  $M_i = M/\delta = 5 \times 10^{-3}$ . The disturbance frequency is  $\omega = 1.0$ , a nonresonant frequency smaller than the first fundamental frequency of the tube,  $\omega_1 = \pi/2$ .

One observes a radial velocity gradient (hence vorticity) extending out about 0.35 units from the wall ( $r = 1$ ) at  $t = 3.00$  (solid line) and to about 0.65 radial units when  $t = 6.00$ . At  $t = 9.90$  the numerical data themselves show that the rotational flowfield has spread throughout the chamber.

The spatial distribution of the rotational part of the unsteady axial flow velocity at each time may be explained in physical terms by considering an interaction between the total unsteady injected flowfield and the axial planar acoustic wave induced and sustained by sidewall injection transients. The motion of a fluid particle injected radially into the tube from the sidewall at a specified axial location is affected by the harmonic variation with time of the local axial planar pressure gradient. For instance, Fig. 5 shows the time variation of the axial pressure

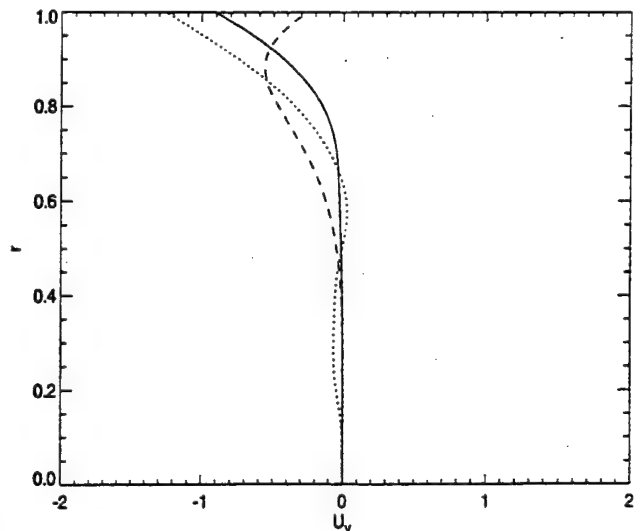


Fig. 4 Radial variation of  $u_v$  at  $x = 0.5$  when  $t = 3$  (solid line),  $t = 6$  (dashed line), and  $t = 9.9$  (dotted line) for  $M = 0.1$ ,  $\delta = 20$ ,  $Re = 10^5$ ,  $\omega = 1$ ,  $A = 0.4$ , and  $n = 1$ .

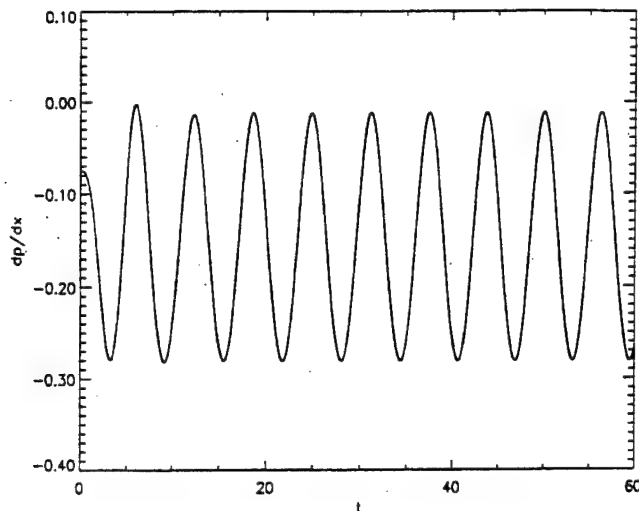


Fig. 5 Time history of axial pressure gradient,  $\partial p/\partial x$ , at  $x = 0.5$ ,  $r = 0.95$  for  $M = 0.1$ ,  $\delta = 20$ ,  $Re = 10^5$ ,  $\omega = 1$ ,  $A = 0.4$ , and  $n = 1$ .

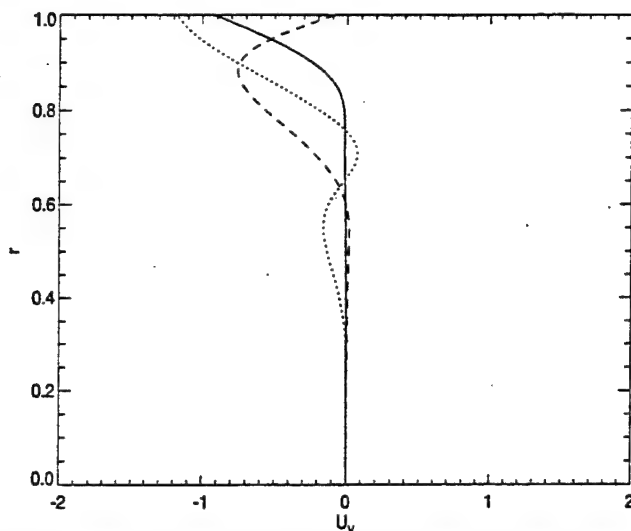


Fig. 6 Radial variation of  $u_r$  at  $x = 0.5$  when  $t = 2.96$  (solid line),  $t = 5.92$  (dashed line), and  $t = 10.05$  (dotted line) for  $M = 0.06$ ,  $\delta = 20$ ,  $Re = 10^5$ ,  $\omega = 1$ ,  $A = 0.4$ , and  $n = 1$ .

gradient,  $\partial p/\partial x$ , at a point where  $x = 0.5$  and  $r = 0.95$  for the case being discussed previously. As a result, a given fluid particle emanating from the wall will be accelerated alternately in the positive and negative axial directions as it is convected toward the axis of the cylinder by the unsteady radial flowfield. Part of the fluid particle response is associated with irrotational acoustic effects. The rest is rotational, resulting from vorticity generation at the wall.

Figure 4 shows that by  $t = 10$  unsteady vorticity has filled the cylinder. But Fig. 3 shows no change in the  $r$ -independent pressure field as vorticity fills the system. It follows that the presence of vorticity does not affect the pressure field, as predicted by Flandro and Roach<sup>15</sup> and in the asymptotic analysis of Zhao et al.<sup>21</sup> and Zhao.<sup>25</sup> This provides an explanation of why traditional acoustic stability theory yields transient pressure estimates that compare well with those found experimentally, although the acoustic velocity field will differ considerably from that observed by Brown et al.<sup>1,2</sup>

Figure 6 shows the instantaneous spatial variation of  $u_r$  at  $x = 0.5$  with respect to the radius when  $t = 2.96$ ,  $5.92$ , and  $10.05$  for a smaller axial Mach number  $M = 0.06$  (corresponding to the weaker injection,  $M_i = 3 \times 10^{-3}$ ) and for the same  $Re = 10^5$ . The forcing frequency  $\omega = 1.0$  is the same as for

the previous case. The amplitude of the nonresonant injection transient disturbance is  $A = 0.4$ . The sharply defined region of large velocity gradient is seen in Fig. 6 out to about 0.23 units from the wall at  $t = 2.96$ . One notes that at  $t = 5.92$  the wavelength of the spatial oscillation of  $u_r$  is smaller than that for the case when  $M = 0.1$ . This is an expected result because the total unsteady radial velocity field for  $M = 0.06$ , which transports the fluid particles into the cylinder, is characterized by a relatively lower speed than that for the  $M = 0.1$  case. Injected fluid particles are carried a shorter distance away from the sidewall towards the axis in a given time interval, relative to that for the stronger injection speed case,  $M = 0.1$ . At  $t = 10.05$  one notes that spatial oscillations are present about 0.7 radial units from the wall.

Solution resolution requires 41 grid points in the axial direction and 101 grid points in the radial direction in the two cases discussed previously. Figure 6 shows that near the injecting wall one wavelength of the spatial oscillation of  $u_r$  is represented by approximately 35–40 radial grid points. In contrast, near the centerline, where the wavelength is smaller, fewer but an adequate number of grid points per wavelength are available to resolve the velocity gradients.

The third case studied is for a smaller characteristic axial flow Mach number  $M = 0.02$  ( $M_i = 10^{-3}$ ),  $\delta = 20$ , slightly larger Reynolds number  $Re = 3 \times 10^5$ , and the forcing frequency  $\omega = 1.0$ . The results for the previous cases,  $M = 0.1$  and  $M = 0.06$ , imply that the number of radial grid points should be doubled for this weak injection case. There are 201 equally spaced grid points in the radial direction to represent the spatial variation of  $u_r$  accurately. Figure 7 shows the instantaneous variation of  $u_r$  with respect to the radius at  $x = 0.5$  when  $t = 2.99$ ,  $4.93$ , and  $10.00$ . It can be seen from this figure that axial velocity gradients are larger than those for larger Mach number cases presented previously. This implies that the absolute magnitude of the unsteady vorticity generated at the wall is much larger than that of the higher Mach number flows. This unsteady vorticity field is convected away from the wall towards the center of the chamber by a relatively slower radial velocity component. Therefore, at  $t = 10.00$  only about 30% of the chamber is filled with the unsteady vorticity.

Figure 8 shows the instantaneous radial variation of  $u_r$  at  $x = 0.5$  for larger times,  $t = 10.00$ ,  $20.01$ ,  $30.02$ , and  $40.02$ . The computational data can be used to infer that the unsteady vorticity field spreads out toward the axis as time increases, so that eventually the entire cylinder is filled with an intense

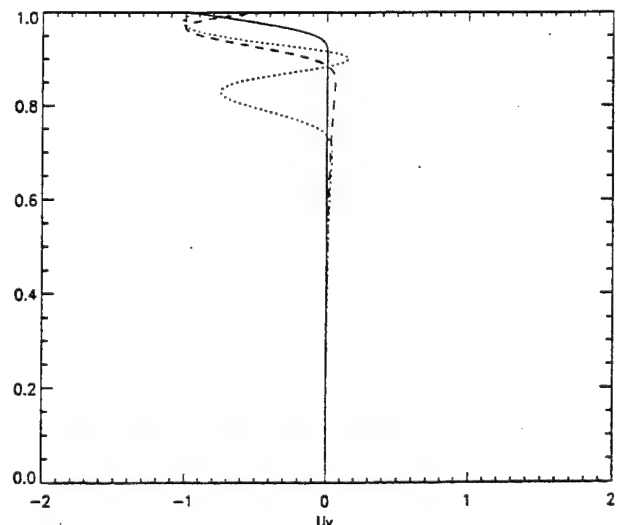


Fig. 7 Radial variation of  $u_r$  at  $x = 0.5$  when  $t = 2.99$  (solid line),  $t = 4.93$  (dashed line), and  $t = 10.00$  (dotted line) for  $M = 0.02$ ,  $\delta = 20$ ,  $Re = 3 \times 10^5$ ,  $\omega = 1$ ,  $A = 0.4$ , and  $n = 1$ .



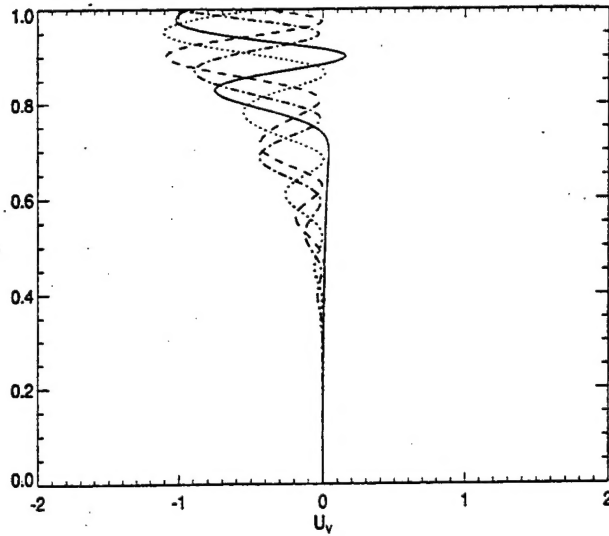


Fig. 8 Same as Fig. 7, but for  $t = 10.00$  (solid line),  $t = 20.01$  (dashed line),  $t = 30.02$  (dotted line), and  $t = 40.02$  (dash-dot line).

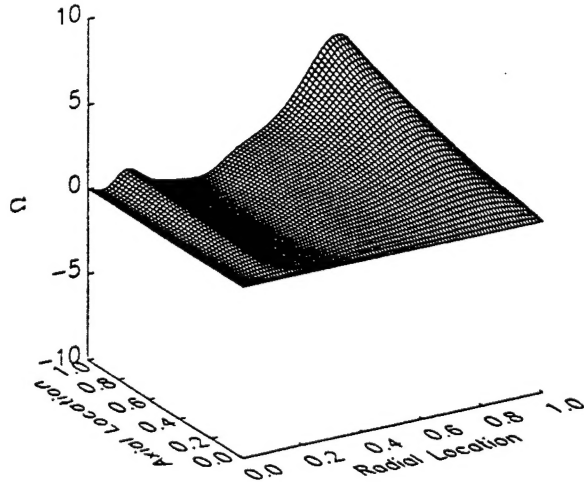


Fig. 9 Spatial variation of the unsteady distribution  $\Omega$  as a function of axial location and radial location at  $t = 30$  for  $M = 0.1$  and  $\delta = 20$ .

level of vorticity, approximately  $\mathcal{O}(1/M)$  larger than that associated with the  $u_s$  velocity field.

Here again, the wavelength of the oscillatory structure decreases as the centerline is approached. This occurs because the rate of radial convection is reduced as the radial velocity component decreases toward zero near the axis of the chamber. The implication for mesh distributions is that there must be adequate spatial resolution throughout the cylinder, not just in an acoustic boundary layer near the injecting surface as used in a variety of earlier computations.<sup>4,7,19</sup> Of course, this necessity arises because the injection velocity is sufficiently large to preclude the existence of a thin localized viscous layer like that considered by Flandro.<sup>5</sup>

Figures 9–11 show the instantaneous unsteady vorticity distribution throughout the chamber for three cases,  $M = 0.1$  ( $t = 30.00$ ),  $0.06$  ( $t = 29.56$ ), and  $0.02$  ( $t = 30.02$ ), discussed earlier, where one notes significant variation in the axial direction. The unsteady vorticity is computed from

$$\Omega = - \left[ \frac{\partial u_v}{\partial r} - \frac{1}{\delta^2} \frac{\partial(v - v_s)}{\partial x} \right] \quad (9)$$

defined as  $\Omega = \Omega'/(U'_R/R')$ , where primed quantities are di-

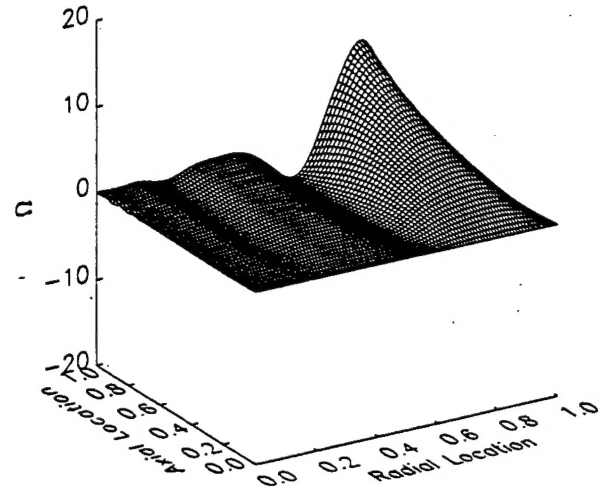


Fig. 10 Same as Fig. 9 but at  $t = 29.56$  and  $M = 0.06$ . Note the different scale in  $\Omega$ .

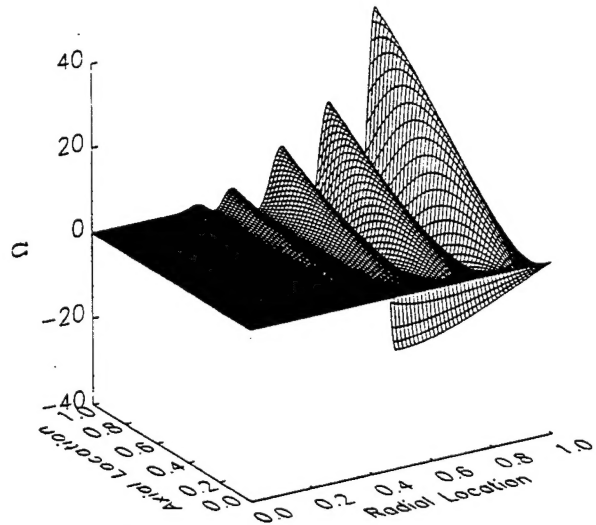


Fig. 11 Same as Fig. 9 but at  $t = 30.02$  and  $M = 0.02$ . Note the different scale in  $\Omega$ .

mensional. The numerical results and the asymptotics of Zhao et al.<sup>21</sup> show that the main contribution to  $\Omega$  is brought by the first term in Eq. (9). A comparison of Figs. 9–11, with significantly varying vertical scales, shows that the magnitude of  $\Omega$  increases with decreasing values of  $M$ . The distribution of vorticity extends out to axis for the two larger Mach numbers in Figs. 9 and 10. Figure 11 shows a succession of wave-like morphologies extending to about  $r = 0.3$ .

Long-time results ( $t = 52.42$ ) for the  $M = 0.02$  case are given in Figs. 12 and 13 to show that unsteady vorticity eventually fills the entire cylinder, even for a relatively small Mach number. Although the graphical representation of  $\Omega$  in Fig. 12 appears to imply that there is no vorticity close to the axis, the enlarged scale result in Fig. 13 demonstrates the presence of vorticity waves close to  $r = 0$ .

Figure 14 provides the radial variation of the unsteady part of the radial speed,  $v - v_s$ , at  $t = 30.02$  and  $x = 0.5$  for  $M = 0.02$ ,  $\delta = 20$ ,  $Re = 3 \times 10^5$ ,  $n = 1$ ,  $A = 0.4$ , and  $\omega = 1$ . The steady radial velocity  $v_s$ , associated with constant wall injection, is shown as curve b in Fig. 1. The result in Fig. 14 corresponds to the axial velocity result in Fig. 8. A study of the numerical data shows that the vorticity front is located about 0.7 radial units from the wall. One may observe considerable spatial variation in the radial speed of the fluid toward the axis when  $0.5 \leq r \leq 1$ .

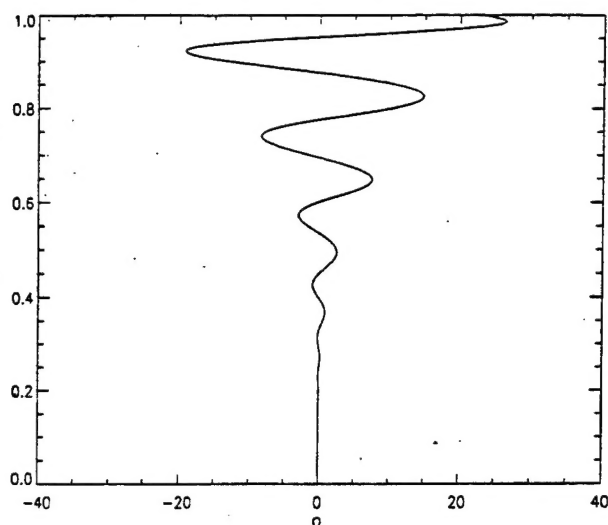


Fig. 12 Radial variation of  $\Omega$  at  $x = 0.5$  when  $t = 52.42$  for  $M = 0.02$ ,  $Re = 3 \times 10^5$ ,  $\omega = 1$ ,  $A = 0.4$ , and  $n = 1$ .

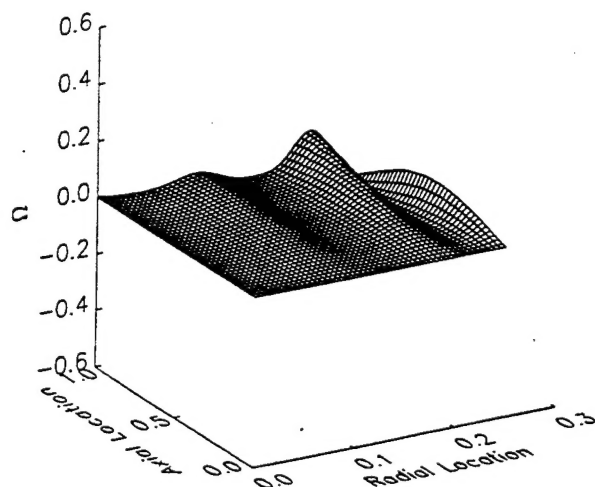


Fig. 13 Unsteady vorticity variation in the region where  $0 \leq x \leq 1$ ,  $0 \leq r \leq 0.25$  for the same parameters and time in Fig. 12.

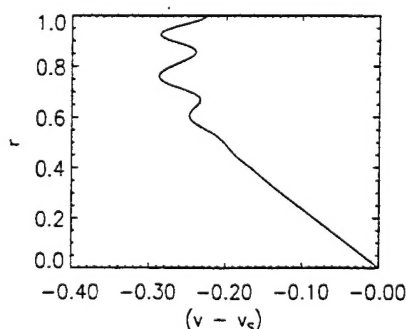


Fig. 14 Instant radial variation of  $(v - v_s)$  at  $x = 0.5$  when  $t = 30.02$  for the same flow parameters as those in Fig. 8.

A more complex wall injection pattern is used to find the results in Figs. 15–18 for the case  $n = 3$  in Eq. (7). The vorticity distribution  $\Omega$  is given for  $t = 7.48$ ,  $14.96$ ,  $22.44$ , and  $29.92$  when  $M = 0.02$ ,  $\delta = 20$ ,  $Re = 3 \times 10^5$ ,  $\omega = 1$ , and  $A = 0.5$ . Note that the morphology of the surfaces is considerably more complex than those in Figs. 9–11 and 13 for  $n = 1$ . These graphs show at a fixed radial location that  $\Omega$  increases monotonically with axial position when the instantaneous wall injection speed decreases monotonically as  $x$  increases [ $n = 1$

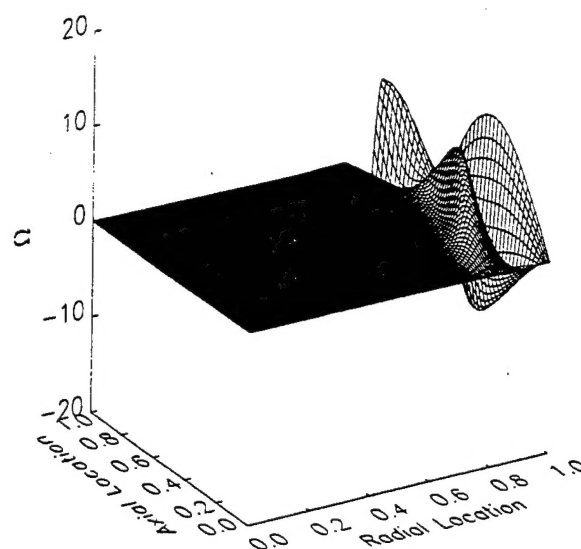


Fig. 15 Instantaneous unsteady vorticity variation throughout the cylindrical chamber at  $t = 7.48$  for  $M = 0.02$ ,  $\delta = 20$ ,  $Re = 3 \times 10^5$ ,  $\omega = 1$ ,  $A = 0.5$ , and  $n = 3$ . The net mean injection speed in Eq. (7) is always positive.

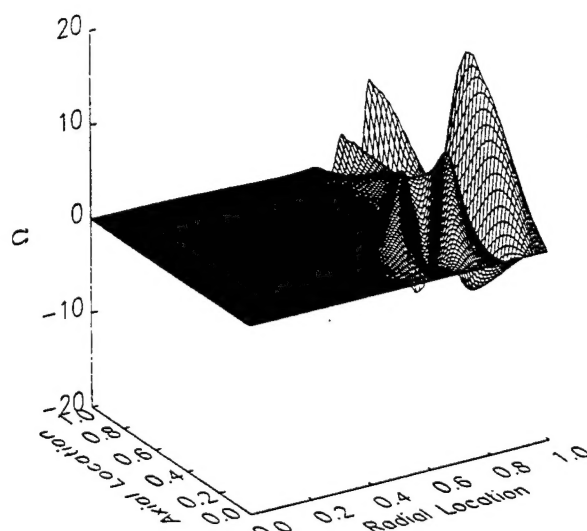
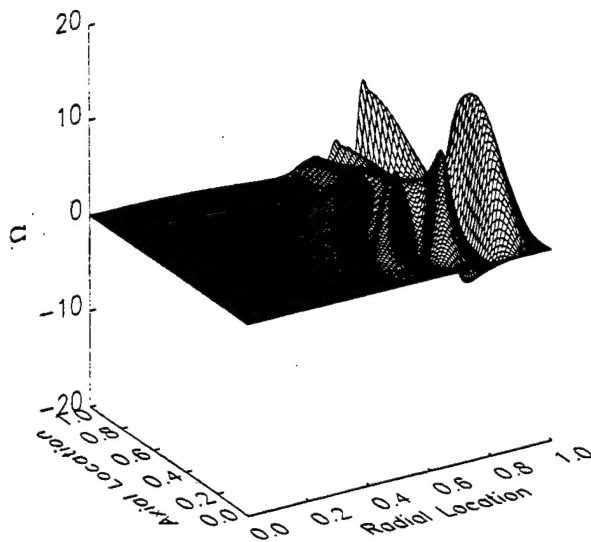
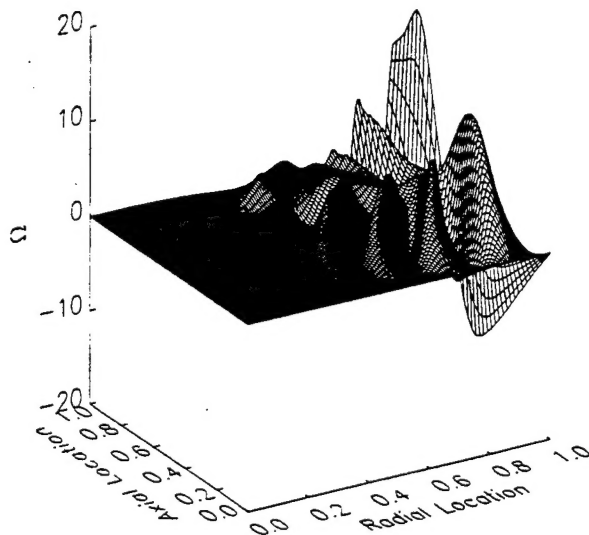


Fig. 16 Same as Fig. 15 but at  $t = 14.96$ .

in Eq. (7)]. The relative increase in the radial gradient of  $u_v$  with increasing  $x$  can be explained in terms of the vorticity generating interaction between the harmonically varying axial pressure gradient (see Fig. 5) and the fluid injected at a given axial location. In particular, the magnitude of the radial gradient of  $u_v$  at the wall depends directly on the radial distance traveled by a fluid particle exiting from the injecting surface during one cycle in  $\partial p / \partial x$ . Downstream, more slowly moving injected fluid particles will be accelerated and decelerated by the variation in  $\partial p / \partial x$  on a shorter radial length scale than those upstream. As a result the radial gradient of  $u_v$  is relatively larger at downstream locations.

In contrast, the corrugated appearance of the surfaces in Figs. 15–18 arises from the variability of the injection speed along the cylinder surface. One may also observe that the radial location of the front is dependent on axial position and reflects the characteristics of the sidewall injection distribution with axial coordinate in  $x$ . This implies that the front morphologies can be quite complex if the injection distribution is spatially irregular and complex.

The amplitude of the unsteady vorticity distributions is  $O(M^{-1})$  larger than that of the Culick<sup>18</sup> steady solution, a result

Fig. 17 Same as Fig. 15 but at  $t = 22.44$ .Fig. 18 Same as Fig. 15 but at  $t = 29.92$ .

predicted by the Zhao et al.<sup>21</sup> and Zhao<sup>25</sup> asymptotic theory. This implies that there will exist a relatively large transient axial shear stress on the sidewall surface, particularly for smaller  $M$  values. One can speculate that these large transient shear stresses will impact the burning rate of a solid propellant that is the source of the injected fluid used in the present model. Perhaps there is a direct relationship between the effect of the surface shear stress transients, predicted in the present work, and erosive burning concepts used in the solid rocket engineering literature.<sup>12</sup>

#### IV. Summary and Conclusions

Unsteady vorticity generation and evolution caused from simulated propellant burning transients in an idealized rocket motor chamber are studied in the context of an initial boundary value problem. An axially distributed, harmonically varying sidewall injection component is superimposed on a similar magnitude steady sidewall injection to simulate spatially variable, time-dependent mass addition from solid propellant burning.

The nearly complete compressible Navier-Stokes equations are solved numerically, using a grid distribution that resolves locally large radial gradients of the axial velocity across the diameter of the cylinder. Instantaneous values of the flow var-

iables are presented to describe the time evolution of unsteady vorticity creation and propagation. This provides an alternative to the studies by Tseng and Yang,<sup>19</sup> Flandro and Roach,<sup>15</sup> Smith et al.,<sup>16</sup> and Tseng et al.,<sup>17</sup> where an acoustic-based time-averaging approach is used to study mean spatial distributions.

The computational analysis shows that axial planar acoustic waves induced and sustained by the sidewall injection transients interact with the sidewall injection induced flow in the chamber to generate unsteady vorticity on the sidewall. This time-dependent vorticity is subsequently convected into the entire chamber by the unsteady radial flowfield. For sufficiently short times, there is a well-defined front that separates the intense transient vorticity generated at the injecting surface from the relatively weak vorticity in the initial steady shear flow.

The instantaneous radial location of the front varies in the axial direction when the wall injection is spatially distributed. In contrast, flows generated by uniform constant sidewall injection, subject to either endwall or exit flow disturbances, have instantaneous front locations that are invariant in the axial direction.<sup>6,8,21</sup>

The maximum amplitude of the intense vorticity, generated at the wall and convected subsequently into the cylinder by the radial component of the flow velocity, scales approximately like  $1/M$  (see Figs. 9–11) as predicted by the formal asymptotic analysis in Ref. 25, in the model of Flandro and Roach<sup>15</sup> and Flandro.<sup>17</sup> Near the sidewall, where the rotational part of the axial velocity  $u_r$  is relatively small, one finds a large radial gradient as seen in Fig. 8. It is conceivable that these large transient gradients will persist to the surface of a burning solid propellant in a real rocket chamber and the resulting axial shear stresses may affect the characteristics of the combustion process.

The results presented here satisfy the order of magnitude equality  $Re = O(\delta^2/M^2)$  derived by Zhao and Kassoy<sup>8</sup> and Zhao et al.<sup>25</sup> for flows that are weakly, but pervasively viscous. This condition is also satisfied approximately by the parameters used in the computational solutions of Smith et al.<sup>16</sup> and Tseng et al.<sup>7</sup> Note that the equality satisfies the hard-blowing condition of Cole and Aroesty,<sup>22</sup>  $Re/\delta^2 \gg 1$ , so that no thin localized viscous acoustic boundary layer can exist adjacent to the injecting surface. Rather, in this case of a confined geometry the viscous effect is present at a relatively low level across the entire cylinder on the  $O(M)$  length scale of the axial velocity radial gradient.

There is now a considerable body of evidence<sup>1,2,4,6,17,19–21,25</sup> in support of the presence of an intense unsteady vorticity distribution within a physically reasonable model of a solid rocket motor chamber. In principle, the basic rotationality of the flowfield should impact traditional irrotational acoustic stability theories. The latter appear to predict acoustic pressure fields seen in solid rocket engines, but are unlikely to give accurate descriptions of axial and radial velocity fields that possess significant rotationality as seen in the work by Brown et al.<sup>12</sup>

#### Acknowledgment

This work is supported by the U.S. Air Force Office of Scientific Research through Grant AFOSR 89-0023.

#### References

1. Brown, R. S., Blackner, A. M., Willoughby, P. G., and Dunlap, R., "Coupling Between Acoustic Velocity Oscillations and Solid Propellant Combustion," *Journal of Propulsion and Power*, Vol. 2, No. 5, 1986, pp. 428–437.
2. Brown, R. S., Blackner, A. M., Willoughby, P. G., and Dunlap, R., "Coupling Between Velocity Oscillations and Solid Propellant Combustion," AIAA Paper 86-0531, Jan. 1986.
3. Brown, R. S., and Shaeffer, C. W., "Oscillatory Internal Flow Field Studies," U.S. Air Force Office of Scientific Research Contractors Meeting in Propulsion, La Jolla, CA, June 1992.



- <sup>4</sup>Vuillot, F., and Avalon, G., "Acoustic Boundary Layers in Solid Propellant Rocket Motors Using Navier-Stokes Equations," *Journal of Propulsion and Power*, Vol. 7, No. 2, 1991, pp. 231-239.
- <sup>5</sup>Flandro, G. A., "Solid Propellant Admittance Correction," *Journal of Sound and Vibration*, Vol. 36, No. 3, 1974, pp. 297-312.
- <sup>6</sup>Kirkkopru, K., Kassoy, D. R., and Zhao, Q., "Unsteady Vorticity Generation and Evolution in a Long Narrow Cylinder with Sidewall Injection," *Physics of Fluids* (submitted for publication).
- <sup>7</sup>Tseng, C., Tseng, I. S., Chu, W., and Yang, V., "Interactions Between Acoustic Waves and Premixed Flames in Porous Chambers," AIAA Paper 94-3328, June 1994.
- <sup>8</sup>Zhao, Q., and Kassoy, D. R., "The Generation and Evolution of Unsteady Vorticity in a Solid Rocket Engine Chamber," AIAA Paper 94-0779, Jan. 1994.
- <sup>9</sup>Grad, H., "Resonance Burning in Rocket Motors," *Communications on Pure and Applied Mathematics Composites*, Vol. 2, No. 3, 1949, pp. 79-102.
- <sup>10</sup>Culick, F. E. C., "Some Recent Results for Nonlinear Acoustics in Combustion Chambers," AIAA Paper 90-3927, Oct. 1990.
- <sup>11</sup>Hart, R. W., and McClure, F. T., "Theory of Acoustic Instability in Solid Propellant Rocket Combustion," *10th International Symposium on Combustion*, The Combustion Inst., Pittsburgh, PA, 1965, pp. 1047-1065.
- <sup>12</sup>Williams, F. A., *Combustion Theory*, Benjamin/Cummings, Menlo Park, CA, 1985.
- <sup>13</sup>Baum, J. D., and Levine, J. N., "Numerical Investigation of Acoustic Refraction," *AIAA Journal*, Vol. 25, No. 12, 1987, pp. 1577-1586.
- <sup>14</sup>Baum, J. D., "Energy Exchange Mechanisms Between the Mean and Acoustic Fields in a Simulated Rocket Combustor," U.S. Air Force Office of Scientific Research Contractors Meeting, Atlanta, GA, June 1990.
- <sup>15</sup>Flandro, G. A., and Roach, R. L., "Effects of Vorticity Production on Acoustic Waves in a Combustion Chamber," Final Tech. Rept., U.S. Air Force Office of Scientific Research 90-0159, 1992.
- <sup>16</sup>Smith, T. M., Roach, R. L., and Flandro, G. A., "Numerical Study of the Unsteady Flow in a Simulated Solid Rocket Motor," AIAA Paper 93-0112, Jan. 1993.
- <sup>17</sup>Flandro, G. A., "Effects of Vorticity on Rocket Combustion Stability," *Journal of Propulsion and Power*, Vol. 11, No. 4, 1995, pp. 607-625.
- <sup>18</sup>Culick, F. E. C., "Rotational Axisymmetric Mean Flow and Damping of Acoustic Waves in a Solid Propellant Rocket," *AIAA Journal*, Vol. 4, No. 8, 1966, pp. 1462-1464.
- <sup>19</sup>Tseng, I. S., and Yang, V., "Interactions of Homogeneous Propellant Combustion and Acoustic Waves in a Solid Rocket Motor," AIAA Paper 92-0101, Jan. 1992.
- <sup>20</sup>Roh, T. S., and Yang, V., "Transient Combustion Responses of Solid Propellants to Acoustic Disturbances in Rocket Motors," AIAA Paper 95-0602, Jan. 1995.
- <sup>21</sup>Zhao, Q., Kassoy, D. R., and Kirkkopru, K., "Nonlinear Unsteady Vorticity Generation in a Model of a Solid Rocket Engine Chamber," *Journal of Fluid Mechanics* (to be published).
- <sup>22</sup>Cole, J. D., and Aroesty, J., "The Blowhard Problem-Inviscid Flows with Surface Injection," *International Journal of Heat and Mass Transfer*, Vol. 11, No. 7, 1968, pp. 1167-1183.
- <sup>23</sup>Gottlieb, D., and Turkel, E., "Dissipative Two-Four Methods for Time-Dependent Problems," *Journal of Mathematics of Computation*, Vol. 30, No. 136, 1976, pp. 703-723.
- <sup>24</sup>Lupaglazoff, N., and Vuillot, F., "Two-Dimensional Numerical Simulation of the Stability of a Solid Propellant Rocket Motor," AIAA Paper 91-0205, Jan. 1991.
- <sup>25</sup>Zhao, Q., "Nonlinear Acoustic Processes in Solid Rocket Engines," Ph.D. Dissertation, Univ. of Colorado, Boulder, CO, 1994.
- <sup>26</sup>Landau, L. D., and Lifshitz, E. M., *Fluid Mechanics*, Pergamon, New York, 1959.
- <sup>27</sup>Lagerstrom, P. A., *Theory of Laminar Flows*, edited by F. K. Moore, Sec. B, Princeton Univ. Press, Princeton, NJ, 1964.

Approved for public release,  
distribution unlimited

AIR FORCE  
OFFICE OF  
SCIENTIFIC  
RESEARCH  
ATLANTA, GA  
30333-6155